UNIVERSITAT POLITÈCNICA DE VALÈNCIA

Instituto Universitario Mixto de Tecnología Química

(UPV-CSIC)

DIVALENT METAL ORGANIC FRAMEWORKS AS HETEROGENEOUS OXIDATION CATALYSTS

Doctoral Thesis

Anna Nowacka

Supervisor:

Dr. Francesc X. Llabrés i Xamena

September 2019

Valencia

Francesc X. Llabrés i Xamena, Tenured Scientist at the Instituto Universitario Mixto de Tecnología Química (UPV-CSIC), hereby

CERTIFY: That the thesis entitled "**Divalent Metal Organic Frameworks as Heterogeneous Oxidation Catalysts**" has been carried out under my supervision by Mrs. Anna Elzbieta Nowacka at the Instituto Universitario Mixto de Tecnología Química

Dr. Francesc X. Llabrés i Xamena

Acknowledgements

The opportunity to study at ITQ and the completion of the work presented here would not have been possible without the contributions from many people whom I had the pleasure to meet during those 4 years of constant growing as a person and a scientist.

First, I would like to express my deep gratitude to Xesc, for his excellent supervision and guidance throughout the course of my Ph.D studies. He has always been available and his door was always open for discussing issues and giving advice.

Thanks are also owed to our collaborators that contribute to the chapters of this thesis: Pol Briantais and Carmelo Prestipino form Institut Sciences Chimiques de Rennes, UMR-CNRS in France, for collaboration in Chapter 3 and 4. Marco Moroni and Simona Galli from Dipartimento di Scienza e Alta Tecnologia Como in Italy, Miguel Palomino form ITQ and Corrado Di Nicola form Scuola di Scienze e Tecnologie, Università di Camerino in Italy for participation in Chapter 5.

Professional help provided by the people working in Electron Microscopy Service UPV: Alicia, Ximo, José Luiz, Merche and Manolo is also valued during many hours at SEM and TEM.

Secondly, acknowledgement is given to prof. Dirk de Vos and Carlos Marquez for their guidance and help as well as for the rest of group members that created amazing atmosphere during my secondment in KU Leuven.

Thirdly, I would like to acknowledge DEFect NETwork, Materials Science and Engineering European Training Network (ETN) Marie Skłodowska-Curie Actions (MSCA) for the founding of this project

I would like to thank my laboratory colleagues and other ITQ members that are dear to me for their friendship and fun times shared during the all 4 years.

Przede wszystkim dziękuję całej mojej rodzinie, za Waszą miłość i wsparcie w dążeniu do celów. To dzięki Wam mogę być tym kim jestem dziś. Dziękuję również Tobie mój najdroższy, za Twoją miłość i wiarę, że wszystko czym żyjemy teraz, prowadzi nas we wspólnym kierunku.

THANK YOU GRACIAS DZIĘKUJĘ

This present moment, since it knows
neither past nor future, is itself timeless,
and that which is timeless is eternal.
Thus, eternal life belongs to those who live in the present

Ken Wilber

Resumen

Se ha desarrollado un método de síntesis “verde” de compuestos metal orgánicos en medio acuoso, a temperatura y presión ambientes, fácilmente escalable y con tiempos de cristalización muy cortos (10 min). El método se ha aplicado con éxito a la síntesis de trimesatos de metales divalentes isoreticulares y con fórmula general $M_3(BTC)_2{\cdot}12\ H_2O$ ($M = Ni^{2+}$, Co^{2+}, Cu^{2+} y Zn^{2+}; BTC = trimesato). La estructura de estos materiales presenta dos tipos de centros metálicos (“puente” y “terminales”) en proporción 2 a 1, ambos con coordinación octaédrica y unidos a 4 moléculas de H_2O y a dos oxígenos carboxilato del ligando. Usando este método de síntesis, se han preparado también series de compuestos bimetálicos isoreticulares de Co-Ni y Co-Zn en todo el rango de concentraciones, así como compuestos de Mn-Ni con una concentración máxima de Mn^{2+} del 50%. Mediante la combinación de difracción de rayos X (en polvo y de monocristal) y microscopía EDX/SEM se ha demostrado que los compuestos bimetálicos forman verdaderas disoluciones sólidas (no meras mezclas de fases) y que los iones metálicos se distribuyen homogéneamente en todo el cristal. Además, el análisis detallado de la variación de los parámetros de celda con la composición en compuestos Co-Ni y Co-Zn aporta fuertes evidencias de que los iones Co^{2+} ocupan preferentemente las posiciones “terminales”. Así, la composición química del material determina el grado de aislamiento de los iones Co2+ en una matriz formada por iones Ni^{2+} (o Zn^{2+}) y ligandos trimesato, lo que es de gran relevancia en determinadas reacciones catalíticas. En el caso de compuestos bimetálicos Mn-Ni, el análisis de los parámetros de celda con la composición no son concluyentes, aunque no se puede descartar que exista también una ocupación preferencial de las posiciones “terminales” por los iones Mn2+.

Se ha evaluado la actividad de los compuestos preparados como catalizadores para la oxidación aeróbica de cumeno (CM) a cumeno hidroperóxido (CHP). El compuesto monometálico de Co^{2+}, Co-BTC, presentó una elevada actividad, aunque la selectividad a

CHP obtenida fue relativamente baja (69%), ya que los iones Co^{2+} catalizan también la descomposición del CHP formado. Una buena estrategia para optimizar esta selectividad consistió en aislar los iones Co^{2+} en una matriz de Ni-BTC (que es inerte tanto para la oxidación de CM como para la descomposición de CHP). Así, al disminuir la concentración de iones Co^{2+} en compuestos bimetálicos Co-Ni se observó un aumento de la selectividad a CHP de hasta el 91% para el material con un 5% de Co. Se ha calculado que estadísticamente el 73% de los iones Co^{2+} en este material se encuentran aislados, por lo que la descomposición/sobreoxidación del CHP se ve muy limitada.

Usando una variación del método de síntesis, se han obtenido también compuestos isoreticulares de Co^{2+} en los que los ligandos trimesato se han reemplazado parcialmente por ligandos isoftálico o 5-aminoisoftálico. Al utilizar estos compuestos como catalizadores para la oxidación aeróbica de CM, se ha observado que la introducción de este segundo ligando (y en particular del 5-aminoisoftálico) en la red metal-orgánica facilita la descomposición del CHP formado y aumenta la selectividad final a 2-fenil-2-propanol (PP). Esto se ha atribuido a la creación de defectos puntuales en la red del material, que presentan una mayor actividad para la descomposición de CHP.

Siguiendo con la oxidación de CM como reacción modelo, se ha evaluado la actividad catalítica de compuestos isoreticulares de cobalto con ligandos bispirazolato funcionalizados con distintos grupos (CoBPZ, CoBPZ-NO_2 y CoBPZ-NH_2). En este caso se ha observado una clara influencia del ligando utilizado sobre la actividad catalítica y la selectividad a CHP o PP del material. Mientras que el Co-BPZ presenta una baja conversión de CM y una elevada selectividad a CHP, Co-BPZ-NH_2 presenta las características opuestas: una elevada velocidad de reacción pero una baja selectividad a CHP. En este último caso, el producto mayoritario formado es el PP. Por su parte, el material Co-BPZ-NO_2 presenta unas características intermedias. Las diferencias observadas se han atribuido al papel de los grupos amino en el Co-BPZ-NH_2, que aumentan la adsorción del CHP en el material y facilitan su descomposición posterior a PP. Por tanto, los resultados presentados en este capítulo demuestran el potencial de la introducción de grupos funcionales en los ligandos del MOF como estrategia para modular la reactividad del material resultante.

Por último, el estudio de MOFs de cationes divalentes como catalizadores de oxidación se ha completado con una reacción de síntesis de quinazolina mediante acoplamiento oxidativo de bencilamina y 2-aminoacetofenona usando TBHP como oxidante. Como catalizadores para esta reacción se ha utilizado el trimesato de cobre, HKUST-1, así como materiales isoreticulares con ligandos mixtos obtenidos al reemplazar parcialmente el trimesato por 5-hidroxiisophthalico (OH-isoftálico). Los materiales con ligandos mixtos presentan un sistema jerárquico de micro- y mesoporos, en el que el volumen de mesoporos representa hasta un 40% del volumen total de poros. La creación de estos mesoporos resulta claramente visible en forma de profundas grietas en la superficie externa, que corren paralelas a las aristas de los microcristales octahédricos. Al aumentar el grado de incorporación del segundo ligando, estas grietas se vuelven más profundas y las aristas de los octaedros se redondean progresivamente. La creación de un sistema jerárquico de mesoporos se traduce en una mayor actividad catalítica en la síntesis de quinazolina, lo que se ha atribuido a una mejora de la difusión de este producto voluminoso desde el interior de los poros del material hacia el exterior.

Abstract

A “green” synthesis method has been developed for the preparation of metal organic frameworks in aqueous media, which is easily scalable, at room temperature, ambient pressure and very short crystallization times (10 min). This method has been successfully applied to the synthesis of isoreticular divalent metal trimesates of general formula $M_3(BTC)_2 \cdot 12\ H_2O$ (M = Ni^{2+}, Co^{2+}, Cu^{2+} y Zn^{2+}; BTC = trimesate). The structure of these compounds features two types of metal centers (“bridging” and “terminal”) in a 2 to 1 ratio, both with octahedral coordination and linked to 4 water molecules and 2 carboxylate oxygens of the ligand. Using this method, two series of bimetallic isoreticular compounds of Co-Ni and Co-Zn have also been prepared in all range of compositions, as well as bimetallic Mn-Ni compounds up to a maximum concentration of 50% of Mn^{2+}. A combined X-ray diffraction (powder and single crystal) and EDX/SEM has shown that these bimetallic compounds form true solid solutions (not simple mixture of phases) and that both ions distribute homogeneously throughout the crystal. A detailed analysis of the variation of cell parameters with the composition strongly suggests that Co2+ ions occupy preferentially the “terminal” positions of the framework. Thus, the chemical composition of the bimetallic compound determines the degree of isolation of Co2+ ions in a matrix formed by Ni^{2+} (or Zn^{2+}) and trimesate ligands, which is of high interest for certain catalytic reactions. IN the case of bimetallic Mn-Ni compounds, the analysis of the cell parameters with composition is not conclusive, although a preferential occupation of the “terminal” sites by Mn^{2+} cannot be excluded.

The materials obtained with the above method have been evaluated as catalysts for the aerobic oxidation of cumene (CM) to cumene hydroperoxide (CHO). The monometallic Co^{2+} compound, Co-BTC, showed a high catalytic activity, but a relatively low selectivity to CHP 69%), since the Co^{2+} ions can also catalyze the decomposition of the formed CHP. A good strategy to optimize the CHP selectivity consisted in isolating the Co^{2+}

ions into a Ni-BTC (which is inert for both CM oxidation and CHP decomposition). In this way, as the concentration of Co^{2+} ions in the bimetallic Co-Ni compound decreases, a parallel increase of the CHP selectivity was observed, up to 91% for the material with 5% of Co. In this compound, 73% of the total Co^{2+} ions are statistically isolated, so that decomposition/overoxidation of CHP is unlikely to occur.

By using a variation of the above synthesis method, additional isoreticular Co^{2+} compounds have been prepared in which the trimesate ligands have been partially replaced by either isophthalic or 5-aminoisophthalic. When these compounds were used as catalysts for the aerobic oxidation of cumene, we observed that the introduction of this second ligand (in particular in the case of 5-aminoisophthalic) into the framework facilitates decomposition of CHP and increases the final selectivity to 2-phenyl-2-propanol (PP). This has been attributed to the progressive creation of point defects in the framework, having a higher activity for CHP decomposition.

Following with the aerobic oxidation of CM as model reaction, we evaluated the catalytic activity of isoreticular cobalt compounds having bispyrazolate ligands bearing differnent functional groups (CoBPZ, CoBPZ-NO_2 and CoBPZ-NH_2). In this case, there is a clear influence of the ligand used on the catalytic activity of the material and the obtained selectivity to CHP or PP. While CoBPZ showed a low CM conversion and high CHP selectivity, the opposite properties are obtained for the Co-BPZ-NH_2: i.e., a high reaction rate but a low CHP selectivity. In this latter case, the major product of the reaction was PP. Meanwhile, CoBPZ-NO_2 has characteristics that are intermediate between these two materials. The observed differences are attributed to the role of the amino groups in CoBPZ-NH_2, increasing the adsorption of CHP on the material thereby facilitating its decomposition to PP. Therefore, the results presented in this chapter show the potential of introducing functional groups in the organic linkers of the MOF as a way to modulate the reactivity of the final material.

Finally, the evaluation of divalent MOFs as oxidation catalysts has been completed by addressing the synthesis of quinazoline through the oxidative coupling reaction of benzylamine and 2-aminoacetophenone using TBHP as oxidant. As catalysts for this reaction we have used a copper trimesate, HKUST-1, as well as isoreticular mixed-ligand compounds obtained by partially replacing trimesate ligands by 5-hydroxyisophthalic (OH-isophthalic). The mixed-ligand compounds present a hierarchical microporous-mesoporous system in which mesopores account for up to 40% of the total pore volume of the solid. Creation of such mesopores is clearly evidenced by the formation of deep trenches running parallel to the edges of the octahedral crystallites. Upon increasing the amount of the second linker incorporated, these trenches become deeper and the edges of the octahedral more rounded. The creation of a hierarchical system of mesopores translates into a higher catalytic activity for quinazoline synthesis. This has been attributed to an improved diffusion of this bulky compound from inside the pores of the MOF to the exterior.

Resum

S’ha desenvolupat un mètode de síntesi “verda” de compostos metall orgànics en medi aquós, a temperatura i pressió ambients, fàcilment escalable i amb temps de cristal·lització molt curts (10 min). El mètode s’ha aplicat amb èxit a la síntesi de trimesats de metalls divalents isoreticular i amb fórmula general $M_3(BTC)_2 \cdot 12\ H_2O$ (M = Ni^{2+}, Co^{2+}, Cu^{2+} y Zn^{2+}; BTC = trimesat). L’estructura d’aquests materials presenta dos tipus de centres metàl·lics (“pon” i “terminals”) en una proporció de 2 a 1, ambdós amb coordinació octaèdrica i units a 4 molècules d’aigua i a 2 oxígens carboxilat del lligand. Emprant aquest mètode de síntesi, s’han preparat també sèries de compostos bimetàl·lics isoreticular de Co-Ni i Co-Zn en tot el rang de concentracions, així com compostos de Mn-Ni amb una concentració màxima de Mn^{2+} del 50%. Mitjançant l’ús combinat de difracció de raigs X (en pols i de monocristall) i microscòpia EDX/SEM s’ha demostrat que els compostos bimetàl·lics formen vertaderes dissolucions sòlides (no simples mescles de fase) i que els ions metàl·lics es distribueixen homogèniament en tot el cristall. A més, l’anàlisi detallat de la variació dels paràmetres de cel·la amb la composició de compostos Co-Ni i Co-Zn aporta fortes evidències de que els ions Co^{2+} ocupen preferentment les posicions “terminals”. Així, la composició química del material determina el grau d’aïllament dels ions Co^{2+} en una matriu formada per ions Ni^{2+} (o Zn^{2+}) i lligands trimesat, el que és de gran rellevància en determinades reaccions catalítiques. En el cas de compostos bimetàl·lics Mn-Ni, l’anàlisi del paràmetres de cel·la amb la composició no són concloents, encara que no es pot descartar que existeixi també una ocupació preferent de les posicions “terminals” per part dels ions Mn^{2+}.

S’ha avaluat l’activitat dels compostos preparats com a catalitzador per a l’oxidació aeròbica de cumè (CM) a cumè hidroperòxid (CHP). El compost monometàl·lic de Co^{2+}, Co-BTC, presenta una elevada activitat, encara que la selectivitat a CHP obtinguda és relativament baixa (69%), ja que els ions Co^{2+} catalitzen també la descomposició del

CHP format. Una bona estratègia per optimitzar aquesta selectivitat consisteix en aïllar els ions Co^{2+} en una matriu de Ni-BTC (que és inert tant per a l'oxidació de CM com per a la descomposició de CHP). Així, a mesura que disminueix la concentració d'ions Co^{2+} en compostos bimetàl·lics Co-Ni s'observa un augment de la selectivitat a CHP de fins el 91% per al material amb un 5% de cobalt. S'ha calculat que estadísticament el 73% dels ions Co^{2+} d'aquest material es troben aïllats, de manera que la descomposició/sobreoxidació del CHP es veu molt limitada.

Emprant una variació del mètode de síntesi, s'han obtingut també compostosisoreticulars de Co^{2+} en els que els lligands trimesat s'han reemplaçat parcialment per lligands isoftàlic o 5-aminoisoftàlic. Quan aquest compostos s'usen com a catalitzadors per a l'oxidació aeròbica de CM, sobserva que la introducció d'aquest segon lligand (i en particular del 5-aminoisoftàlic) en la xarxa metallorgànica es facilita la descomposició del CHP format i augmenta la selectivitat final a 2-fenil-2-propanol (PP). Això s'ha atribuït a la creació de defectes puntuals en la xarxa del material, que presenten una major activitat per a la descomposició del CHP.

Seguint amb l'oxidació de CM com a reacció model, s'ha avaluat l'activitat catalítica de compostosisoreticulars de cobalt amb lligands bispirazolat funcionalitzats amb distints grups (CoBPZ, CoBPZ-NO_2 i CoBPZ-NH_2). En aquest cas s'ha observat una clara influència del lligand utilitzat sobre l'activitat catalítica i la selectivitat a CHP o PP del material. Mentre que el CoBPZ presenta una baixa conversió de CM i una elevada selectivitat a CHP, CoBPZ-NH_2 presenta les característiques oposades: una elevada velocitat de reacció però una baixa selectivitat a CHP. En aquest últim cas, el producte majoritari format és el PP. Per la seva part, el material CoBPZ-NO_2 presenta unes característiques intermèdies. Les diferències observades s'han atribuït al paper dels grups amino en el CoBPZ-NH_2, que augmenta l'adsorció del CHP en el material i faciliten la seva descomposició posterior a PP. Per tant, els resultats presentats en aquests capítol demostren el potencial de la introducció de grups funcionals en els lligands del MOF como una estratègia per modular la reactivitat del material resultant.

Per últim, l’estudi de MOFs amb cations divalent como a catalitzadors d’oxidació s’ha completat amb una reacció de síntesi de quinazolina mitjançant acoblament oxidatiu de benzilamina i 2-aminoacetofenona emprant TBHP como a oxidant. Com a catalitzadors per aquesta reacció s’ha utilitzat el trimesat de coure, HKUST-1, així com materials isoreticular amb lligands mixtes obtinguts reemplaçant parcialment el trimesat per 5-hidroxiisoftàlic (OH-isoftàlic). Els materials amb lligands mixtes presentes un sistema jeràrquic de micro- i mesoporus en el que el volum de mesoporus representa fins a un 40% del volum total de porus. La creació d’aquests mesoporus resulta clarament visible en forma de profunds solcs en la superfície externa, que corren paral·lels a les arestes dels microcristalls octaèdrics. Quan s’augmenta el grau d’incorporació del segon lligand, aquests solcs es fan més profunds i les arestes s’arrodoneixen progressivament. La creació d’un sistema jeràrquic de mesoporus es traduexi en una major activitat catalítica en la síntesis de quinazolina, el que s’ha atribuït a una millora de la difusió d’aquest producte voluminós des de l’interior del porus del material cap a l’exterior.

Abbreviation

BTC – 1,3,5-benzenetricarboxylic acid
CP – Coordination polymer
CUS – Coordinatively Unsaturated Sites
DMF - N,N-Dimethylformamide
FE-SEM - Field Emission Scanning Electron Microscopy
FTIR - Fourier-transform infrared spectroscopy
HKUST - The Hong Kong University of Science and Technology
ICP-OES - Inductively Coupled Plasma - Optical Emission Spectrometery
IRMOF – Isoreticular MOF
MIL - Materials of Institut Lavoisier
MOF- Metal-organic Framework
PSM – Post Synthetic Modification
SBU – secondary Building Unit
STEM – scanning transmission electron microscopy
TGA - Thermogravimetric Analysis
TBHP - tert-Butyl hydroperoxide
TOF - turnover frequency
TON – Turnover number
UiO - Universitetet i Oslo
XRD – X-ray Diffraction
ZIF - Zeolitic imidazolate framework

Index

Chapter 1

General introduction and objectives

1.1. General introduction

1.1.1. What are Metal-Organic Frameworks?

Metal-organic frameworks (MOFs), also known as porous coordination polymers (PCPs) are a very promising class of crystalline porous materials consisting of metal ions or cluster (inorganic nodes) coordinated to multidentate organic molecules (ligands) to form 1D, 2D or 3D pore structure. Early reports dedicated to this type of materials date from the late 1950s[1,2] and early 1960s[3–7], however the real boost of this field was observed in the end of the 1990s, when MOFs were rediscovered by groups of Robson[8,9], Kitgawa[10], Yaghi[11] and Ferey[12] followed by many others. Thanks to their structural diversity, stability and functional flexibility, MOFs allow the creation of materials with tailored properties and have become one of the exciting research areas in Chemistry. The ever growing numbers of articles containing metal-organic framework concept is showed in Figure 1.1.

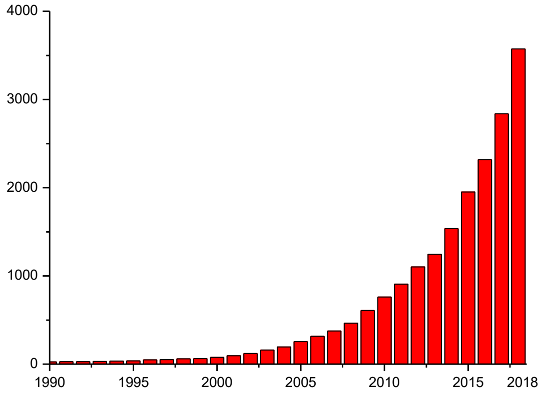

Figure 1.1 Number of publication on MOFs per year from 1990 to 2018 (data obtained from SciFinder on May 21, 2019)

MOFs can be produced by many different synthesis methods, both traditional and more specific ones, like microwave, ultrasonic, mechanochemical and electrochemical processing. The possibility to vary the structure porosity (increase even up to 98Å), topology and elemental composition by the choice of initial building units has led to many application in fields like gas adsorption[13,14] and separation[15], catalysis[16–18], photocatalysis[19,20] and many others, covered in many reviews[21,22]. The above mentioned features of MOFs, including high surface area and tuneable porosity, are main aspects that differ them from Zeolites and exceed their properties in many ways. However, Zeolites are still rank above in terms of thermal stability.

The big diversity in MOFs is also reflected by the variety of nomenclature. A large number of abbreviations are commonly in use to name these compounds, which can cause additional confusion and misunderstandings. This is why attempts have been made to systematize the definitions used in this field[23,24] followed by IUPAC recommendations for nomenclature[25]. There, the use of accurate and careful topology description for MOFs is advised, which can allow comparing materials from different publications much easier and more efficient. Topology descriptions should use the symbols or codes from Reticular Chemistry Structural Resource (RCSR) database, which are composed of three letters and should be additional to common practice of giving important new compounds nicknames names based on their place of origin. By now, apart from simple numeration e.g. MOF-5, MOF-74, MOF-177 the most famous classes are UiO (Universitetet i Oslo), MIL (Materials of Institut Lavoisier), HKUST (Hong Kong University of Science and Technology), etc. Figure 1.2 shows the examples of two of the most famous MOFs: HKUST-1, which forms a **tbo** net, and MOF-5 that has **pcu** topology.

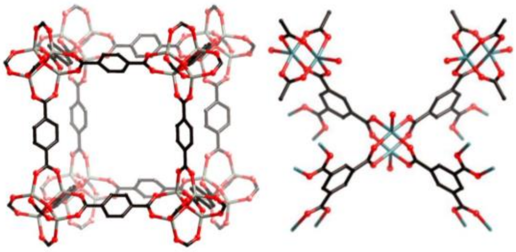

Figure 1.2 Archetypical MOFs: (*Left*) The zinc and carboxylate-based MOF-5, where each [Zn_4O] unit is bridged by six benzene-1,4-dicarboxylates. (*Right*) HKUST-1 with coppe(II) paddlewheel dimers bridged by benzene-1,3,5-tricarboxylates. Hydrogen atoms are not shown. Grey: Zn; turquoise: Cu; black: C; red: O.[25] Adapted from Pure Appl. Chem., Vol. 85, No. 8, pp. 1715–1724, 2013 ©IUPAC;

One of the most famous subgroup inside MOFs are ‘zeolite imidazolate frameworks’ (ZIFs), where metal ions (Fe,Co,Zn,Cu etc.) are surrounded by tetrahedral imidazole rings. Most common way of naming these materials is by using the abbreviation ZIF followed by a number, as in ZIF-8[26].

1.1.2. Synthesis of MOFs

1.1.2.1 Methods of crystalization

The potential applications of MOFs, related to their porous nature gain attention among engineers and material scientist. Various research background has without doubts contributed to wide range of applications. However, before the MOF with designed specific properties will be used, appropriate synthesis conditions (solvents, pH, temperature, concentration, solvents polarity) and materials (inorganic salt, organic ligands) should be carefully chosen. Various methods and approaches towards understanding the formation of MOFs have been reviewed[27,22].

Solvothermal approach

Solvothermal synthesis is one of the most common synthesis method. The synthesis often takes place under high pressure and temperature in the presence of organic solvents and/or aqueous solvents and mineralizers (in case of hydrothermal reaction).

Those syntheses are commonly carried out in tightly capped vessels, either Teflon-lined stainless steel autoclave or glass flasks, placed inside an oven to generate autogenous pressure[28]. This increases the solubility and interaction of reactants in the solvent during the synthesis procedure. Alcohols and dimethylformamide (DMF) are among the most common solvents used in the synthesis of MOFs. In some cases, addition of amine such as trimethylamine can favor deprotonation of the organic ligand, which accelerate the synthesis rate[29]. In small scale, high-throughput solvothermal syntheses are a powerful tool leading to accelerate the discovery of new MOF structures and to optimize synthesis procedures[30,31]. Despite of huge popularity, solvothermal synthesis have also few limitations. Usually this type of synthesis can take from few hours up to days depending on the precursor used. Moreover, in many cases solvent is adsorbed strongly inside the pores, requiring high temperature activation[32].

Employing ionic liquids in ionothermal synthesis helped to improve classical solvothermal synthesis in terms of safety concerns[33], by eliminating high pressure from the process. Ionic liquids are salts that melt below the temperature used in the synthesis (423-493 K) and can serve as both solvent and structure-directing agent for the dissolution of starting precursors as it was demonstrated in the case of Zn-BTC[34] and NH_2-MIL-53[35].

Microwave and sonochemical synthesis

Microwave assisted and sonochemical synthesis of MOFs are alternative methods to conventional solvothermal synthesis. So far, microwave (MW) irradiation has been used mostly for the inorganic or organic solid state materials synthesis and polymer curing[36–38]. Currently, both methods are used with success also for synthesis of MOFs[39,40]. Main advantages of those methods are reduction of crystal size for production of nanosized materials[41,42], as well as phase selective synthesis[43], where formation of the kinetically favored phase can be observed due to the very fast kinetics of nucleation and crystallization under MW heating and shorter crystallization time. In many cases physical and textural properties of materials obtained by MW and solvothermal methods are very similar. MIL-100-Cr was the first MOF material successfully synthesized by MW irradiation[44]. In this method MIL-100 was synthesized at 493 K in 20 times shorter time, as compared to conventional electric heating method at the same temperature. This improvement was possible thanks to fast dissolution of the precursors, especially metallic chromium, acceleration of the condensation of the oxygen-metal networks and reduction of the nucleation period. Similar observation was obtained for other MOFs: MIL-101-Cr[45], MOF-5[46], Cu-BTC[47] and MIL-53-Fe[48].

Sonochemical technique was applied for the first time to synthesized MOF-5[49] resulting, like in the case of MW in smaller crystal size and reduced synthesis time comparing to convective heating.

Electrochemical synthesis

The electrochemical synthesis of MOFs was reported for the first time by BASF's researchers[50]. They established synthesis procedures for Cu- and Zn- based MOFs with various linkers [1,3,5-H_3BTC, 1,2,3-H_3BTC, H_2BDC and H_2BDC-$(OH)_2$]. In this method metal ions, rather than metal salts are continuously introduced through anodic dissolution to reaction mixture, where dissolved organic linker and conducting salt are present. Use of protic solvents helps to prevent metal deposition on the cathode forming H_2 in the process. Big advantage of this process its industrial friendly aspect like possibility to run continuous reaction with high yield solid content compared to normal batch synthesis. Researchers form BASF extended their work for ZIFs family and reported procedures for $Zn(MIm)_2$ and $Zn(BIm)_2$[51]. Despite of high surface area obtained for most of the materials, the main drawback is poor quality of those materials, which is assigned to the incorporation of linker molecules and/or the conducting salt in the pores during crystallization[27].

Mechanochemical synthesis

Mechanochemical synthesis is considered as a green alternative for solvothermal synthesis due two main advantages. Firstly, the process goes under solvent free conditions and secondly, faster reaction time which usually oscillate around 10-60 min with quantitative yields and can be easily scale up[52]. Mechanochemical method proceeds by grinding (using ball mill) metal precursor and organic ligand in the solid state to produce discrete coordination complexes with reorientation of intramolecular bonds leading to chemical reaction[22]. HKUST-1 and MOF-14 were successfully synthesized by this method with high surface areas[53]. Moreover, this green-chemistry approach leads to framework structures where adsorbed guest molecules can be easily removed, leaving a free pore access for other applications. This method was later extended by Liquid-assisted grinding (LAG) and of ion- and liquid- assisted grinding (ILAG) in order to improve reactivity of unreactive or low-yielding systems[54].

Room temperature synthesis

Room temperature synthesis is an attractive method, which offers a simple rapid and high-yield way to prepare MOF materials. Since it does not require any energy source to trigger nucleation and crystal growth, it is considered as "green" alternative for solvothermal reaction. MOFs can be simply obtained by mixing together starting materials, however in some cases addition of the base i.e. trimethylamine in order to deprotonate the linker) is requiring[55,56]. Other methods use for the synthesis salts of organic linkers[57], which will be described in more details in Chapter 3.

Solvent evaporation

Another alternative synthesis method is called solvent evaporation. Shortly, in this method mixed reactants are transferred into beaker and sealed with a parafilm. Crystal growth is initiated either by saturating the solution, which can be achieved by cooling of the solution or removal of excess solvent. As an example, Zhang et al. have synthesized copper(II)–lanthanide(III) MOF using a solvent evaporation method[58].

1.1.2.2 Purification and activation

Seemingly simple synthesis of MOFs often brings challenges in terms of phase-pure, non-catenated and "activated" materials, especially in the high surface area regime[59].

Purity of the material is one of the most important factors in catalysis as presence of by-products can mimic the activity and also lower the sorption capacity of the MOF. One of the methods to separate mixture of MOF phases i.e. catenated and non-catenated is density separation[60], where mixed organic solvents are applied. Moreover, catenation can be controlled by concentration[61], temperature[62], use of templating solvents or molecules[63,64], solvent-assisted linker exchange (SALE)[63] etc.. The crystalline impurities can be detected by X-ray powder diffraction and amorphous by-products can be revealed by thermogravimetric or elemental analysis. It is also worth to notice, that all steps necessary for purification and activation of the MOFs are strongly depending on its chemical and thermal stability. Activation (removal of unreacted linker or solvents from the pores) of the MOF is crucial to achieve high porosity. However, in many cases, this process leads to structural collapse due to strong host-guest interaction, especially when high temperatures are needed. High activation temperature was successfully applied for Cr-MIL-53[65] and Al-MIL-53[66] where unreacted ligand could be removed by heating in air at 300°C. In case of less stable materials the solvent molecules can be first exchanged with more volatile compounds like methanol or dichloromethane[67], which can be removed without thermal treatment.

1.1.3. Application of MOFs in catalysis

Every year new MOFs structures are discovered. Unlimited possibilities in terms of designing new functionalities has significantly expanded the application of these materials, as covered in recent years by many reviews[68–70]. High adsorption capacities of MOFs and pore tunability are important advantages for gas storage, separation and molecular sensing[71–76]. Synthesis of bio-compatible scaffolds found their way in medical applications like drug storage, drug delivery and also as potential imaging agents[77–81]. Magnetic, semi-conductor and proton MOFs have perspective application as sensors, in electronic applications, in magnetic refrigeration, or in quantum computing[82,83]. Compatibilization of MOFs with either organic or inorganic materials lead to creation of advanced composites with applications varying form (opto)electronic devices[84] to food packaging materials[85] and membrane separation[86]. Finally, the hybrid nature of MOF materials and tuneable properties point at MOFs as very promising heterogeneous catalysts[87–93].

Lewis acid catalysed reactions

Based on those positive features, MOFs have been used in many different types of reactions. As solid Lewis/Brønsted acid MOFs can act as general catalyst for reactions promoted by these sites. Typical reactions catalyzed by Lewis and/or Brønsted acids sites are isomerizations. Reaction like α-pinene oxide or citronellal isomerization are well-studied reactions in fine chemistry. They are also used to estimate the nature (type and strength) of the Brønsted or Lewis acid sites of the catalyst. Briefly, in the isomerization of α-pinene oxide Lewis acid sites catalyse the formation of campholenic aldehyde while Brønsted acidity lowers the selectivity towards this product. Dirk de Vos and co-workers examined the acid properties of HKUST-1[94]. The results clearly showed that HKUST-1 possess hard Lewis acid sites. Similar tests were performed by Vermoortele et al. over MIL-100(Fe)[95] after post-synthetic treatment. Either $HClO_4$ or CF_3COOH were used to activate the MOF. The level of defects created after acid treatment were measured by the catalytic performance in the α-pinene oxide isomerization. It was observed that both, conversion and selectivity to campholenic aldehyde decreased, which can be attributed to the increased amout of protonated carboxylate ligands inside cages of MOF, which serves as weak Brønsted acid sites. Other types of Lewis acid reactions where MOFs showed activity are benzaldehyde cyanosilylation[96,97], esterification[98], Prins reaction[99], Strecker reaction[100,101], CO_2 cyclization reaction[102–105], Friedel-Crafts substitution[106–109] reaction and many others.

Base catalysed reaction

C-C forming reactions are important in fine chemicals and pharmaceuticals synthesis; however stoichiometric amounts of base are often required. Normally alkali, alkali earth, ammonium or organic basic salts are used as a soluble base catalyst. This requires additional synthetic steps of neutralization and separation from the reaction mixture. Therefore, design of MOFs as base heterogeneous catalyst that can simplify the separation process is of great interest. The most common reaction for testing basic properties of the catalyst is Knoevenagel reaction. Gascón et al.[110] showed that MOFs with non-coordinated amino groups like IRMOF-3 and amino-functionalized MIL-53, can be use a stable solid basic catalysts in the Knoevenagel condensation of ethyl cyanoacetate and ethyl acetoacetate with benzaldehyde. Interesting example was also reported by Vermoortele et al.[111], that have described the use of UiO-66-NH_2 as a bifunctional acid-base catalyst for the cross-aldol condensation of benzaldehyde and heptanal to produce jasminaldehyde. It was proposed that the amino functional groups on the ligands act as basic sites, while the acid sites are created in situ by controlled dehydratation of the catalyst, creating coordination vacancies shared by three metal cations (Zr^{4+}) in the inorganic cluster.

Oxidation reactions

Selective oxidation reactions are important due to possibility of functionalize C-C bonds. MOFs thanks to their diversity of transition metal presence in the structure i.e., Cr, Mn, Fe, Co, Co and even Ti, are often used as oxidation catalysts[112,113,92]. Asefa et al.[114], reported cobalt based MOF $[Co(OBA)_2(H_2O)_2]$ (H_2oba = 4,4'-oxydibenzoic acid) as highly active catalyst, for olefin epoxidation reactions. In another example copper-based MOFs were used by Pombeiro for selective oxidation of cyclopentane and cyclohexane[115]. Also in our group several MOFs have been reported as selective catalyst for aerobic oxidation of hydrocarbons i.e. MIL-101(Cr)[116] for indane oxidation to respective alcohol/ketone mixture, $[Cu(2\text{-pymo})_2]$ and $[Co(BzIM)_2]$ (2-pymo = 2-hydroxypyrimidinolate; BzIM = benzimidazolate) for tetraline, cumene and ethylbenzene oxidation[117,118].

Reduction reactions

Selective reduction of carbonyl group of an α,β-unsaturated ketone in an important reaction in the perfume, flavouring, agrochemical and pharmaceutical industries. The product of this reaction, allylic alcohols, find a wide range of applications, for example as intermediates in the synthesis of fine chemicals[119–122]. Meerwein-Ponndorf-Verley (MPV) is one of the reduction method where MOFs attracted interest as heterogeneous catalysts. UiO-66 and MOF-808 were shown good performance in reducing the carbonyl group without affecting the CC double bond[123,124].

1.1.4. Tunability of structural properties of MOFs

1.1.4.1 Isoreticular strategy

As it has been described above, MOFs possess features that makes them perfect candidates for heterogeneous catalysis: high surface area, permanent and ordered porosity and most of all, an endless possibility for tuning their physical and chemical properties.

One of the strategies to create new MOFs is the so-called isoreticular concept (one that has the same framework topology), which originally was introduced by Yaghi et al.[61]. In this work IRMOF isoreticular family (based on MOF-5), were constructed from Zn_4O as inorganic building block and various linear dicarboxylic organic linker molecules. Sixteen different materials having the same topology were obtained, which proved the possibility not only for organic linker functionalization, with the groups like -Br, $-NH_2$, $-OC_3H_7$, $-OC_5H_{11}$, $-C_2H_4$ and $-C_4H_4$, but also expansion of the pore size in IRMOF-0, IRMOF-1, IRMOF-10 and IRMOF-16, which contain alkyne, phenyl, biphenyl and triphenyl respectively (see Figure 1.3)

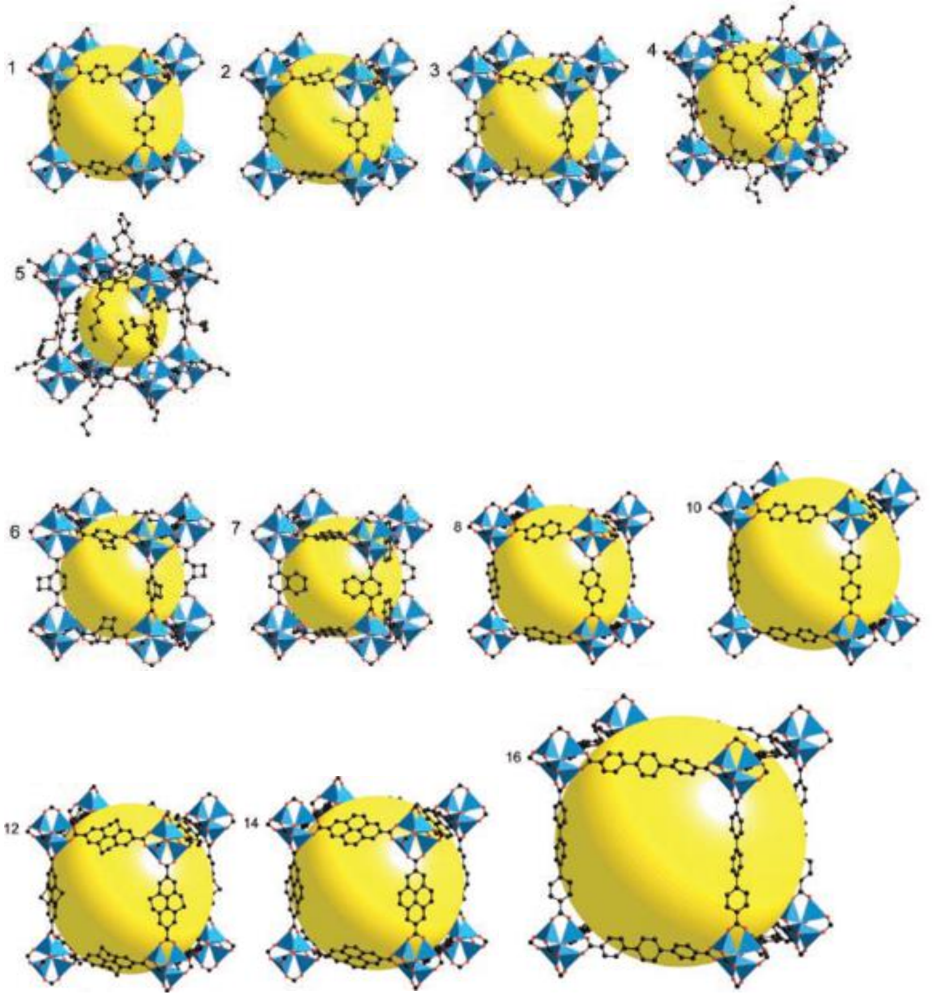

Figure 1.3 Serie of IRMOF. Zn (blue polyhedral), O (red spheres), C (black spheres), Br (green spheres in 2), Amino-group (blue spheres in 3). The large tallow spheres represent the largest van der Waals spheres that would fit in the cavities without touching the frameworks. All hydrogen atoms have been omitted, and only one orientation of disordered atoms is shown for clarity. Adopted from Science 2002,295, 469-472 with permission from The American Association for the Advancement of Science

Another example of isoreticular MOF family is UiO-66, containing hexameric $Zr_6O_4(OH)_4^{12+}$ clusters as inorganic building blocks and linear dicarboxylic acids. These compounds show remarkable stability, and high surface area, which increase upon extending the linkers to two and three benzene ring dicarboxylic acids in UiO-66, UiO-67 and UiO-68 (from 1187m^2/g to 3000 and 4170 m^2/g, respectively)[125] (see Figure 1.4)

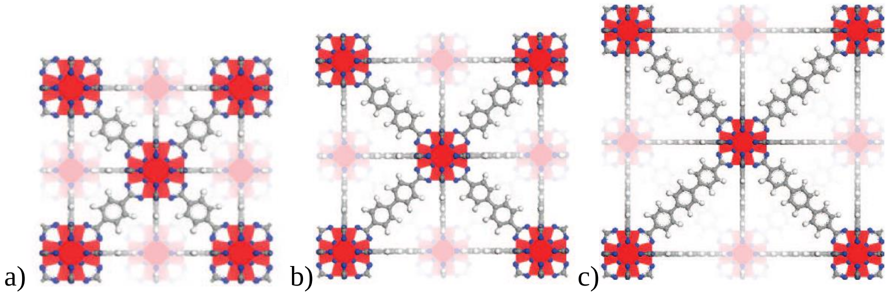

Figure 1.4 a)UiO-66; b)UiO-67; c)UiO-68. Zr (red), O (blue), C (gray), H(white) respectively. Adapted with permission from Journal of the American Chemical Society 2008, 42, 13850-13851 Copyright 2008, American Chemical Society

This topology can also be obtain using fumaric acid[126] (by now the smallest molecule used) and terphenyldicarboxylic acid[127] (as the biggest). Further extension of ligand, results in formation of interpenetrated frameworks with UiO-66 topology[128]. As in previous example of MOF-5, UiO-66 family was also investigate in terms of ligand functionalization[129,130].

Highly diverse and widely studied isoreticular family of MIL-53 topology, with dynamic porosity, usually referred to as “breathing” properties, is a good example not only for changing organic linker, but also replacing inorganic building units. Originally, MIL-53, reported by G. Ferey et al.[65], was the first three-dimensional chromium(III) dicarboxylate with general formula $M^{III}(OH)(O_2C\text{-}C_6H_4\text{-}CO_2)$. This trivalent chromium metal ion, can be easily replaced by other metals like: Al^{3+} [66], Sc^{3+} [131], Fe^{3+} [132], In^{3+} [133], Ga^{3+} [134]. As in the previous examples, MIL-53 topology was also explored in terms of pore dimension, with fumaric acid[135] and 4,4’-biphenyl dicarboxylic acid[136] and furthermore functionalization of terephthalic acid[132,137,138].

In the literature many examples of isoreticular approach can be found on tuning the materials properties in order to achieved low density crystals by the use of long struts[139-141], more complex interpenetrated structures[142-144], substitution of metal[145] and finally - ligand functionalization[146-149]. All this aspects can play an important role in applications of MOF materials in catalysis[150] and adsorption. For instance, $Cu_3(BTC)_2$ (BTC = 1,3,5-benzentricarboxylate), well known as HKUST-1, as a member of an isostructural series of Cr, Fe, Ni, Zn, Mo, and Ru analogues, where investigated in terms of CO_2-metal interaction for CO_2 storage/separation[151]. Despite of unexpected high adsorption enthalpy for $Ni_3(BTC)_2$ material (affected by donor guest molecules), results suggested that incorporation of more electropositive divalent metals in $M_3(BTC)_2$ analogues, could lead to increase its CO_2 affinity at low coverage. Other very common way to enhanced CO_2 affinity and selectivity include organic ligand functionalization with amines or other basic groups[152,153,154].

W. Lin et al. and co-workers used isoreticular nature of chiral metal-organic frameworks (CMOFs), constructed from $[Zn_4(_{\mu 4}\text{-}O)(O_2CR)_6]$, to incorporate well-defined Mn-Salen catalyst into framework and by introducing spacers of different lengths to tune open channel dimensions[155]. Results showed, that the larger open channel dimensions can increase the epoxidation reaction rate, by overcoming diffusion limits of reactant and product molecules.

F. Bigdeli et al.[156] and co-workers perform investigation on isoreticular MOF family ($[Zn(oba)(4\text{-}bpmb)_{0.5}]_n{\cdot}(DMF)_{1.5}$(TMU-6), $[Zn(oba)(R\text{-}4\text{-}bpmb)_{0.5}]_n{\cdot}(DMF)_{1.5}$(R-TMU-6), $[Zn(oba)(4\text{-}bpmn)_{0.5}]_n{\cdot}(DMF)_{1.5}$(TMU-21) and $[Zn(oba)(R\text{-}4\text{-}bpmn)_{0.5}]_n{\cdot}(DMF)_{1.5}$ (R-TMU-21)) containing N-donor ligands with various basicity character (see Figure 1.5). All materials were tested in the Knoevenagel condensation, showing that R-TMU-21 (possessing higher basicity ligand, among tested materials) has the highest catalytic activity - 100% conversion vs. 62% obtain on TUM-6. Moreover, R-TMU-21 exhibit good stability for a few cycles with no leaching detected.

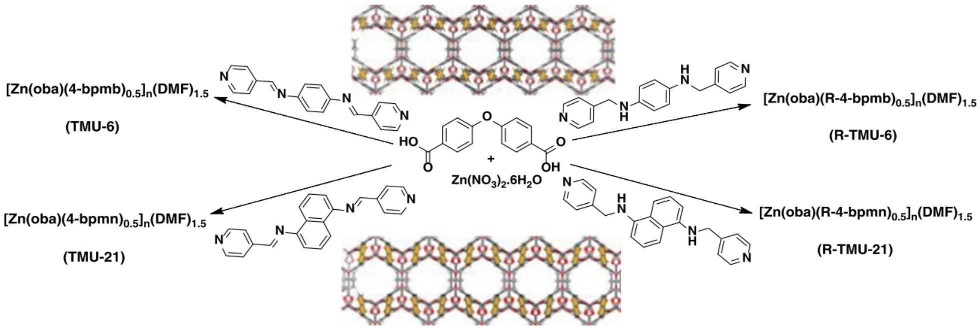

Figure 1.5 Isoreticular family of TMU MOFs. Adapted from Inorganic Chemistry Communications 2016,72,122-127. Copyright 2016 Published by Elsevier B.V.

Other possibility of designing MOFs is introduction of chiral catalytic centers in use of asymmetric (enantioselective) catalysis[157] for enantiomerically pure drugs synthesis. Moreover, multifunctional catalyst can be design in order to perform one-pot synthesis, which involve few catalytic steps (cascade, domino or tandem reactions). This can lead to more selective, cost efficient and environmentally friendly synthesis, avoiding separation and purification of intermediate products and in overall avoiding generation of waste by-products.

1.1.4.2 Mixed metal approach

The simultaneous incorporation of different building blocks in the crystal lattice, which possess the same or similar coordination geometry (structure) and connectivity, can lead to the construction of mixed component MOFs called MIX-MOFs[158]. Such a combination can lead to materials with new functionality and unusual properties.

Introduction of another metal into the MOF structure can be achieved by post synthetic modification (PSM) on parent MOF containing single metal[159] or by directly mixing metal precursors during synthesis procedure (one-step approach). To successfully synthesize mix-metal MOF with homogeneous distribution, features like columbic charge, ionic radius and behaviour of the co-incorporated metals have to be considered.

In PSM method[160] partial replacement of metal in the native material can be performed by bringing the solid into contact with a solution containing required second metal precursor. One of the first examples was reported by Dincă et al., where metal cations with the same or different oxidation states than 2+ were substituted in MOF-5 crystal. Mixed metal MOF-5 analogues containing Ce^{2+}, Mn^{2+}, and Fe^{2+} as well as Ti^{3+}, V^{3+} and Cr^{3+} were obtained by PSM. In another report, Ti^{4+} was introduced by PSM into UiO-66(Zr)[161].

Due to its simplicity, one-pot synthesis of mixed metal MOF have been also reported[162]. Using this one-step approach, Yaghi and co-workers presented MOFs containing more than two kinds of metal ion[163]. Microcrystalline MOF-74 containing 2 (Mg and Co), 4 (Mg, Co, Ni, and Zn), 6 (Mg, Sr, Mn, Co, Ni, and Zn), 8 (Mg, Ca, Sr, Mn, Fe, Co, Ni, and Zn), and 10 (Mg, Ca, Sr, Ba, Mn, Fe, Co, Ni, Zn, and Cd) different kinds of divalent metals were obtained. True solid solution and heterogeneous metal distribution was confirmed by X-ray diffraction, scanning electron microscopy, N_2 adsorption, elemental analysis and energy-dispersive X-ray spectroscopy. However, control of incorporation level of each metal still remained a challenge.

Mixed metal materials have found many applications in catalysis. A series of isostructural three-dimensional MOFs CPO-27-M or MOF-74-M with different metal ions (M = Co, Mg, Mn, Ni and Zn) were tested in the cyanosilylation of aldehydes with trimethylsilylcyanide[164]. Among tested materials CPO-27-Mn showed the highest activity with size selectivity towards aldehyde substrates. Also mixed-valence MOF materials were used as heterogeneous catalyst for phenol degradation[165] and aerobic oxidation[166]. Mixed metal materials have a huge potential to fulfil one of the ambitions of heterogeneous catalysis - development of multifunctional catalysts by incorporation of more than one type of active site, which can be use in cascade or tandem reactions[167,168]. For instance, trivalent metal cations Al^{3+}, Cr^{3+} and Fe^{3+} were separately introduced into MIL-100(Sc,M)[169] (M= Al, Cr, Fe) and tested in Lewis acid + oxidation tandem catalytic process. It was showed that incorporation of Fe^{3+} into MIL-100(Sc) significantly improved conversion in overall process. Encapsulated palladium nanoparticles in Pd@MIL-101[170] were also reports as successful material for menthol synthesis tandem reaction. Many other examples were collected in the review[171].

1.1.4.3 Mixed linker approach

Introduction of second ligand can be achieved by one-pot synthesis (by direct mixture of two linker solutions) or by PSM[159]. Among mixed-ligand MOFs three kinds of substitution can be distinguished[172]. One undergoes an isomorphous substitution with new ligand that possess a similar size and directionality, but bears new functional group. The second kind of mixed-linker MOFs have structurally different organic building units (called defective linkers), which leads to formation of defects without affecting general integrity of the crystalline material. Finally, the third group represents the mixed-ligand MOFs which lead to formation of new structures, which cannot be achieved otherwise.

Isomorphus substitution

Mixed-linker materials that undergo isomorphous substitution can be used for pore engineering and functionalization (introduction of active sites). Hereafter, we present few examples of this transformation and its use in catalysis.

A series of MIXMOFs based on MOF-5 was synthesized by the partial replacement of benzene-1,4-dicarboxylate (BDC) linkers by functionalized 2-aminobenzene-1,4-dicarboxylate (ABDC) using one-pot method. Their activity was tested for the synthesis of propylene carbonate.[173] The amount of amino groups was tuned by choosing the appropriate BDC/ABDC linker ratio, which in turn exhibited different activity. In another example, a series of mixed ligand zirconium-based MOFs were synthesized containing ABDC as the primary linker and 2-X-1,4- benzenedicarboxylate (X-BDC, X = H, F, Cl, Br) as a secondary linker, and their activity was evaluated as visible light photocatalyts in oxidation of benzyl alcohol[174]. Mixed ligand catalyst with halogenated linkers (X-BDC, X = F, Cl, Br) led to a four- to five-fold enhancement of the activity of the corresponding Zr-MOFs for benzyl alcohol oxidation in comparison to UiO-66-NH_2–H. An interesting example of using mixed ligand MOFs was reported by Ranocchiari et al.[175]. Here, Zn-based MOFs containing NH_2-BPDC (BPDC= 4,4'-biphenyl dicarboxylate) as an active component and an inert linker with methyl (MeBPDC) or diphenylphosphoryl (DPP) groups (DPP-BPDC). The strategy of using mixed linkers, resulted in a bifunctional material, where amino functionalised group acts as an active centre for the Knoevenagel condensation and the second linker (Me or DPP) tunes the pore opening by changing the size within the pores. Mixed linker materials, with the same topology can be also obtained by PSM exchange[176], as in the case of mixed metal MOFs or could be based on performing an organic transformation at the organic linker. In this latter case, only a portion of the original linkers inside the MOF is reacted. Examples include the nitration[174] or sulfonation[177] of the terephthalate linker in MIL-101.

Defective linker substitution

Introduction of defective linker into the MOF structure is recently the most intensively studied method that can also introduce new properties in the material, useful for catalysis. One of the pioneer work in this field was done by Baiker and co-workers, who reported a mixed-linker MOF based on the HKUST-1 structure, where BTC linkers were partially substituted by defective linker, pyridine-3,5-dicarboxylate (PyDC), with partially missing one carboxylate group[178]. According to structural analysis up to 50% of defective PyDC could be incorporated without significantly affecting the crystal structure of the solid. Introduction of PyDC led to alteration of the electronic structure of the MOF, with remarkable consequences in their catalytic properties for the hydroxylation of toluene. Different selectivities toward the desired ortho- and para-cresol and other oxidation products (benzaldehyde, benzyl alcohol, methylbenzoquinone) were observed for $Cu_3(BTC)_2$ and $Cu_3(BTC)_2$-PyDC. Analogous approach was employed to introduce structural defects and modify the metal sites in the mixed-valence $Ru^{II/III}$ $[Ru_3(BTC)_2Cl_{1.5}]$ structural analogue of HKUST-1, with partly missing carboxylate groups at the Ru_2 paddle-wheels. Incorporation of (PyDC) led to formation of isoreticular derivative material, with new coordinatively unsaturated sites and partial reduction of the Ru sites at the defective paddle-wheel moieties that trigged novel reactivity. Hence, the MOFs with modified Ru sites were highly active in the reduction of 1-octene using molecular hydrogen as a reducing agent as compared with the parent MOF[179]. Besides HKUST-1 analogues, a series of defect engineered MOF-808 was recently reported in our group[180]. Improvement of the catalytic activity in Meerwein–Ponndorf–Verley (MPV) reduction of carbonyl compounds for defect-engineered MOF-808-IP (IP=isophthalic acid) and MOF-808-Pydc (Pydc = pyridine dicarboxylic acid) was observed, which was assigned to the occurrence of less crowded Zr^{4+} sites in defected MOF-808. In another example, two cobalt-based MOFs TMU-10 - constructed form OBA ligand (OBA=4,4’-oxybisbenzoic acid) and mixed-ligand TMU-12[181] - constructed form OBA and pyrazine ligands, were examined in terms of its activity in the desulfurization of DBT (dibenzothiophene). Results showed that incorporation of the second ligand increased catalytic activity, compared to TUM-10, due to the difference in their coordination to Co centers and void space.

Many other mixed-linker materials with defective linker substitution were found useful in catalytic reactions like Knoevenagel[182,183], Henry reaction for carbon–carbon bond formation[184], Aldol reaction[185], oxidative amidation[186] and many others[187,188].

New architectures

By judicious selection of ligands having different connectivity, new mixed-ligands MOFs can be prepared that cannot be obtained otherwise by using the individual ligands alone. In turn, their pore architectures can be further modified in terms of pore shapes, sizes and opening windows of the channels in order to form new structures. High stability of these structures, allows for PSM of the SBU or the linker which can also be applied to modify the structures and functions[189]. One of the important group in mixed-ligand MOFs family are pillared-layered MOFs, which are constructed from infinite layers pillared by linear bidentate linkers through dative bonds or supramolecular interactions. Those materials often consist of bipyridine and polycarboxylate ligands[190–192]. Another groups within this construction approach are rod-spacer MOFs[193,194] and cluster based mixed-ligand MOFs[195]

1.1.4.4 Encapsulation

MOFs have emerged as a new class of heterogeneous catalyst, in which they serve as hosts for encapsulated active guest species[196] such as polyoxometalates (POMs)[197], metalloporphyrins[198] and nanoparticles (metal and metal oxide) MNPs. Incorporation of polyoxometalates (POMs) inside MOFs as catalyst gives many economically and environmentally advantages. Maksimchuk et al. incorporated Ti and Co Keggin anions into the large cavities of MIL-101 and tested their catalytic performance for oxidation of alkenes using O_2 and H_2O_2 as oxidant[199] Materials turned out to be stable under mild operation conditions and could be reused many times without significant loss of activity. Big effort have been made to incorporate metalloporphyrins into MOFs structure due to its unique electronic structures, chemical and physical properties. Apart of example where functional porphyrin molecules were used as organic linker[200,201], there are also many examples demonstrated that cationic porphyrins can be encapsulated into structures of HKUST-1 using "one-pot" self-assembly approach[202].

For NMPs introduction into MOFs different procedures have been developed, such as impregnation[203], incipient wetness method[204], deposition by solid grinding[205] and immobilization of core-shell hetero-metallic NPs[206]. For instance, core-shell Pd@IRMOF-3 nanostructures, with single Pd nanoparticle core surrounded by amino-functionalized IRMOF-3 shell was prepared by a mixed solvothermal method[207]. Catalytic activity and multifunctional properties of this material was evaluated in cascade reaction of Knoevenagel condensation of 4-nitrobenzaldehyde and malononitrile followed by selective hydrogenation of $-NO_2$ group of intermediate product by the Pd NP core. Both experimental and DFT calculation showed high catalytic performance of Pd@IRMOF-3 having its origin in their unique core-shell structures.

1.1.5. Defects in MOFs

Defects are now recognized as an important property in metal-organic frameworks. Thus, its tailoring gain more and more attention of research groups in the last few years, which is reflected in many reviews[208–213]. Followed by definition given by Fang et al. defects can be referred as "*sites that locally break the regular periodic arrangement of atoms or ions of the crystalline parent framework because of missing or dislocated atoms or ions*."[209]. Inside this wide definition, different subclasses of defects can be classified by their dimensions:

- *Point defects* – linker, node vacancies or their modifications
- *Line defects* – (e.g. dislocation)
- *Planar defects* – (e.g. boundaries and stacking faults)
- *Micro- and Macroscale volume defects* – (e.g. inclusions and voids)

More commonly, defects can be assigned as *external/surface defects*[214] (grooves, growth spirals, cracks) or *internal defects* (Schottky or Frenkel defects) according to their location in crystal structure[215].

1.1.5.1 Defects formation

Defects can occur normally during crystal growth, without intentional manipulations of synthetic procedure (regular conditions), then are called *inherent defects.* CNCs (coordination network compounds) like MOFs are prone to generate this type of misconnection and dislocation[216] or post-crystallization cleavage[217]. Inherent defects present on the surface of HKUST-1[216,218] and MOF-5[219] have been described by Attfield and coworkers, using atomic force microscopy (AFM). This method helped to reveal single- and multiple-growth spirals associated with screw dislocation on the surface of both materials (Figure 1.6).

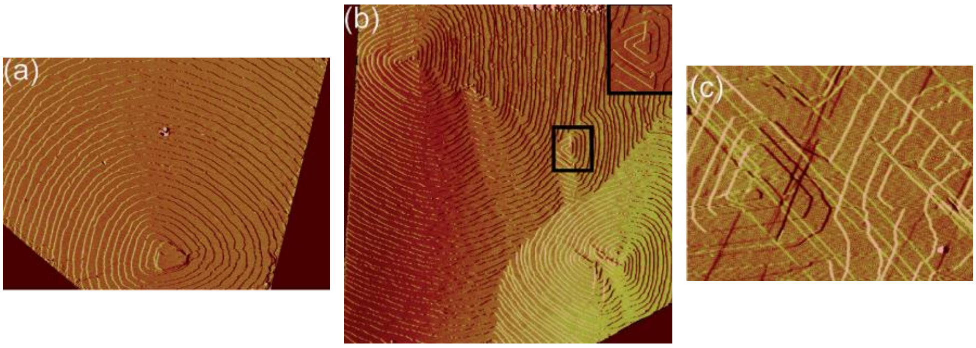

Figure 1.6 Ex-situ AFM amplitude images of {111} facets of HKUST-1, showing (a) a double-growth spiral, (b) merging single- and multiple- growth spirals (c) growth spirals overlaid with factures primarily in the <110> directions. The inset in (b) shows the emergence of a factures in a <110> direction at a relatively early stage of growth. The image sizes in (a), (b) and (c) are 10x6.85 μm^2, 15.0x15.0 μm^2, 2.5x1.58μm^2, respectively[216] Reproduced from Shöâeè, M.; Agger, J. R.; Anderson, M. W.; Attfield, M. P *CrystEngComm* 2008, *10* (6), 646 with permission from the The Royal Society of Chemistry

Formation of inherent internal defects, strongly depends on synthesis conditions. Fast growth or precipitation, affected by temperature or metal/ligand ratio can disrupt the molecules arrangement in the lattice leading to metal or linker vacancy, observed in IRMOF-3, MOF-5[214], HKUST-1[220,221] and UiO-66[222].

Methods to intentionally introduce defects, called defect engineering, allows to control the defects concentration in the material and thus alter its physical and chemical properties. Thanks to the flexibility and modularity of MOFs, various kinds of defects can be incorporate without compromising the overall integrity of the material. In general, defects can be introduced in two ways, firstly by *De Novo Synthesis*, which take place directly during the synthesis and secondly by *Post-Synthetic Treatment*, where defects are introduce after synthesis of pristine MOF. Among those two groups, different approaches/treatments are defined. (Figure 1.7).

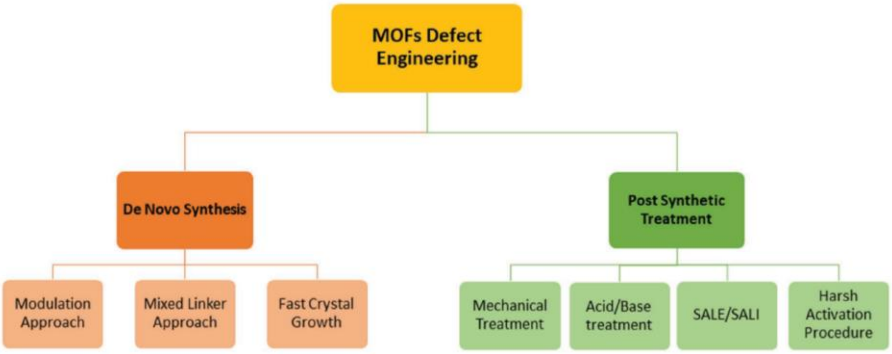

Figure 1.7 Main procedures to introduce defects in MOFs[208] Reprinted from Dissegna, S.; Epp, K.; Heinz, W. R.; Kieslich, G.; Fischer, R. A. *Adv. Mater.* 2018**, *1704501*, 1–23 with premission of WILEY-VCH Verlag GmbH & Co. KGaA, Weinheim**

In *De Novo* Synthesis, modification of reaction conditions is used to induce defects in the materials. *Modulation approach* is used to reduce crystallization speed of MOFs, by addition of monocarboxylic acids (modulators) during synthesis, to obtain higher degree of crystallinity. Varying modulator concentration during synthesis, can lead to introducing vacancy defects in controlled manner[215,223,224]. *Mixed linker approach* (known also as solid-solution) consist of partial substitution of parent framework by other linker or linkers with different coordinating group[179,178]. This approach can be extended by mixed metal-containing secondary building units (SBUs) or more complex, combining of both mix- SBUs and organic linkers within the same framework. As mentioned earlier *fast crystal growth approach*, might involve changing reaction procedure (e.g. high concentration of the precursor or use of microwave-assisted synthesis).

On the other hand defects can be introduced by *Post-synthesis treatment* of as prepared material via *mechanical treatment* like ball milling[225], *acid/base treatment*[226], *solvent-assisted ligand exchange* (SALE)[227], *solvent-assisted ligand incorporation* (SALI)[228] or *harsh activation procedure*[229,230].

1.1.5.2 Use of defective MOFs in catalysis

Defects formation inside the MOFs network as mentioned before can lead to tuning their porosity, accessibility of active catalytic sites and even charge transport. All these parameters can play a very important role in catalytic activity of the materials and exhibit properties which are not present in parent defect-free MOFs[208]. In one such example, Hupp and co-workers connected the catalytic activity of Zr/Hf-based MOFs series (UiO-66, UiO-67, PCN-57, NU-1000 and MOF-808)[231] to their defective sites and/or the connectivity of the Zr_6/Hf_6-clusters. Surprisingly, defect-free Zr-UiO-67 showed no conversion for acid catalysed epoxide ring opening of styrene oxide. On the other hand, defect-induced Zr-UiO-67 (HCl as modulator) (see Figure 1.8) showed catalytic conversion of 40% after 24h. NU-1000 and MOF-808 were found to be more active due to their more exposed Zr_6-nodes bearing additional –OH/-H_2O groups.

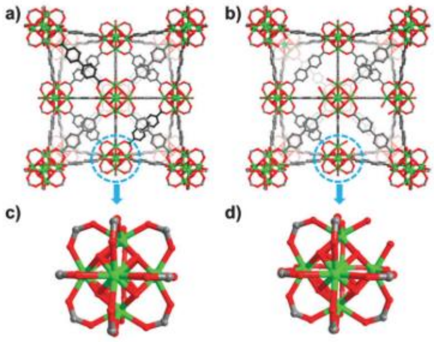

Figure 1.8 Crystal structure of (a) defect-free UiO-67 and (b) defective UiO-67 due to missing linkers, (c) Zr_6 cluster in defect-free UiO-67 and (d) defective Zr_6 cluster with terminal –OH and OH_2 groups[231] Reproduced from *Chem. Commun.* 2016, *52* (50), 7806–7809 with permission from the Centre National de la Recherche Scientifique (CNRS) and The Royal Society of Chemistry

Moreover, Dissegna et al. used water adsorption measurements to study the defects in acetic acid (AA) and trifluoroacetic acid (TFA) modulated UiO-66 samples[232]. It was shown that increasing the amount of modulator lead to increase of specific surface area and hydrophilicity properties of the material. Catalytic properties of the modulated and pristine materials were tested on cyanosilylation of benzaldehyde. The results indicated that increasing amount of TFA has beneficial effect on the material activity correlated to defect formation.

Apart from well-known modulator approach to induce defects in MOFs and thus enhanced their catalytic activity, other methods like ligand-fragmented mix-ligand MOFs and creation of mesoporosity was found to be very effective. However, this topic will be developed in more detail in Chapter 6.

1.2. Objectives

The general objective of this Thesis is ***to contribute to the development of novel divalent metal organic frameworks as heterogeneous catalysts for oxidation reactions, with special emphasis in the study of mixed-metal and mixed-ligand compounds***.

In more detail, specific objectives of each chapter are as follows:

Chapter 3:

- To facilitate the production of MOFs under industrial-friendly conditions by developing a green synthesis method in aqueous medium, working at room temperature and ambient pressure, easily scalable and with short synthesis time.

- To apply the above method to the synthesis of a wide range a compounds, including mono- and bimetallic divalent MOFs, as well as single and mixed-ligand compounds.

Chapter 4:

- To evaluate the application of mono- and bimetallic divalent MOFs, as well as single and mixed-ligand compounds prepared with the above method, as heterogeneous oxidation catalysts for an industrial relevant reaction: aerobic oxidation of cumene.

- To analyse in detail the effects of composition of the MOFs on the activity and selectivity of the reaction.

Chapter 5:

- To study the tag-dependent selectivity for the aerobic oxidation of cumene of cobalt bispyrazolate compounds bearing different functionalities in the organic struts.

Chapter 6:

- To modulate the concentration of defects introduced in the well-known copper trimesate HKUST-1 by preparing mixed-ligand compounds using a defect inducing linker, with the aim of obtaining hierarchical mesoporous-microporous compounds.

- To evaluate the impact of the defect inducing linker on the textural properties of the resulting hierarchical porous materials.

- To analyse the application of hierarchical porous HKUST-1 as oxidation catalysts for the oxidative coupling synthesis of a bulky substrate as quinazoline.

1.3. References

(1) Kinoshita, Y.; Matsubara, I.; Higuchi, T.; Saito, Y. The Crystal Structure of Bis(Adiponitrilo)Copper(I) Nitrate. *Bull. Chem. Soc. Jpn.* **1959**, *32* (11), 1221–1226.

(2) Knobloch, F. W.; Rauscher, W. H. Coordination Polymers of Copper(II) Prepared at Liquid-Liquid Interfaces. *J. Polym. Sci.* **1959**, *38* (133), 261–262.

(3) Bailar, J. C. *Preparative Inorganic Reactions*; 1964.

(4) Kubo, M.; Kishita, M.; Kuroda, Y. Polymer Molecules Involving Coordination Links in the Crystals of Cupric Oxalate and Related Compounds. *J. Polym. Sci.* **1960**, *48* (150), 467–471.

(5) Block, B. P.; Rose, S. H.; Schaumann, C. W.; Roth, E. S.; Simkin, J. Coordination Polymers with Inorganic Backbones Formed by Double-Bridging of Tetrahedral Elements. *J. Am. Chem. Soc.* **1962**, *84* (16), 3200–3201.

(6) Berlin, A. A.; Matveeva, N. G. Polymeric Chelate Compounds. *Russ. Chem. Rev.* **1960**, *29*, 119–128.

(7) Tomic, E. A. Thermal Stability of Coordination Polymers. *J. Appl. Polym. Sci.* **1965**, *9* (11), 3745–3752.

(8) Hoskins, B. F.; Robson, R. Design and Construction of a New Class of Scaffolding-like Materials Comprising Infinite Polymeric Frameworks of 3D-Linked Molecular Rods. A Reappraisal of the Zn(CN)2 and Cd(CN)2 Structures and the Synthesis and Structure of the Diamond-Related Framework. *J. Am. Chem. Soc.* **1990**, *112* (4), 1546–1554.

(9) Batten, S. R.; Hoskins, B. F.; Robson, R. Two Interpenetrating 3D Networks Which Generate Spacious Sealed-Off Compartments Enclosing of the Order of 20 Solvent Molecules in the Structures of Zn(CN)(NO3)(Tpt)2/3.Cntdot.Solv (Tpt = 2,4,6-Tri(4-Pyridyl)-1,3,5-Triazine, Solv = .Apprx.3/4C2H2Cl4.Cntdo. *J. Am. Chem. Soc.* **1995**, *117* (19), 5385–5386.

(10) Kitagawa, S.; Kawata, S.; Nozaka, Y.; Munakata, M. Synthesis and Crystal Structures of Novel Copper(I) Co-Ordination Polymers and a Hexacopper(I) Cluster of Quinoline-2-Thione. *J. Chem. Soc. Dalt. Trans.* **1993**, No. 9, 1399–1404.

(11) Yaghi, O. M.; Li, H. Hydrothermal Synthesis of a Metal-Organic Framework Containing Large Rectangular Channels. *J. Am. Chem. Soc.* **1995**, *117* (41), 10401–10402.

(12) Riou, D.; Ferey, G. Hybrid Open Frameworks (MIL-N). *J. Mater. Chem* **1998**, *8*, 2733–2735.

(13) Groen, J. C.; Peffer, L. A. A.; Pérez-Ramírez, J. Pore Size Determination in Modified Micro- and Mesoporous Materials. Pitfalls and Limitations in Gas Adsorption Data Analysis. *Microporous Mesoporous Mater.* **2003**, *60* (1–3), 1–17.

(14) Zecchina, A.; Bordiga, S.; Vitillo, J. G.; Ricchiardi, G.; Lamberti, C.; Spoto, G.; Bjørgen, M.; Lillerud, K. P. Liquid Hydrogen in Protonic Chabazite. *J. Am. Chem. Soc.* **2005**, *127* (17), 6361–6366.

(15) C. McKinlay, A.; Xiao, B.; S. Wragg, D.; S. Wheatley, P.; L. Megson, I.; E. Morris, R.; McKinlay, A. C.; Xiao, B.; Wragg, D. S.; Wheatley, P. S.; et al. Exceptional Behavior over the Whole Adsorption-Storage-Delivery Cycle for NO in Porous Metal Organic Frameworks. *J. Am. Chem. Soc.* **2008**, *130* (31), 10440–10444.

(16) Liu, J.; Chen, L.; Cui, H.; Zhang, J.; Zhang, L.; Su, C.-Y. Applications of Metal–Organic

Frameworks in Heterogeneous Supramolecular Catalysis. *Chem. Soc. Rev.* **2014**, *43* (16), 6011–6061.

(17) Huang, Y.-B.; Liang, J.; Wang, X.-S.; Cao, R. Multifunctional Metal–Organic Framework Catalysts: Synergistic Catalysis and Tandem Reactions. *Chem. Soc. Rev.* **2017**, *46* (1), 126–157.

(18) Gascon, J.; Corma, A.; Kapteijn, F.; Xamena, F. X. L. i. Metal Organic Framework Catalysis: Quo Vadis? **2013**.

(19) Alvaro, M.; Carbonell, E.; Ferrer, B.; Llabrés I Xamena, F. X.; Garcia, H. Semiconductor Behavior of a Metal-Organic Framework (MOF). *Chem. - A Eur. J.* **2007**, *13* (18), 5106–5112.

(20) Silva, C. G.; Luz, I.; Llabrés I Xamena, F. X.; Corma, A.; García, H. Water Stable Zr-Benzenedicarboxylate Metal-Organic Frameworks as Photocatalysts for Hydrogen Generation. *Chem. - A Eur. J.* **2010**, *16* (36), 11133–11138.

(21) Butova, V. V; Soldatov, M. A.; Guda, A. A.; Lomachenko, K. A.; Lamberti, C. Metal-Organic Frameworks: Structure, Properties, Methods of Synthesis and Characterization. *Russ. Chem. Rev.* **2015**, *85* (3), 280–307.

(22) Gangu, K. K.; Maddila, S.; Mukkamala, S. B.; Jonnalagadda, S. B. A Review on Contemporary Metal-Organic Framework Materials. *Inorganica Chim. Acta* **2016**, *446*, 61–74.

(23) Férey, G. Microporous Solids: From Organically Templated Inorganic Skeletons to Hybrid Frameworks...Ecumenism in Chemistry. *Chem. Mater.* **2001**, *13* (10), 3084–3098.

(24) Rowsell, J. L. C.; Yaghi, O. M. Metal-Organic Frameworks: A New Class of Porous Materials. *Microporous Mesoporous Mater.* **2004**, *73* (1–2), 3–14.

(25) Batten, S. R.; Champness, N. R.; Chen, X.; Garcia-Martinez, J.; Kitagawa, S.; Öhrström, L.; O'Keeffe, M.; Paik Suh, M.; Reedijk, J. Terminology of Metal–Organic Frameworks and Coordination Polymers (IUPAC Recommendations 2013). *Pure Appl. Chem.* **2013**, *85* (8), 1715–1724.

(26) Chizallet, C.; Lazare, S.; Bazer-Bachi, D.; Bonnier, F.; Lecocq, V.; Soyer, E.; Quoineaud, A.; Bats, N. Catalysis of Transesterification by a Nonfunctionalized Metal−Organic Framework: Acido-Basicity at the External Surface of ZIF-8 Probed by FTIR and Ab Initio Calculations. *J. Am. Chem. Soc.* **2010**, *132* (35), 12365–12377.

(27) Stock, N.; Biswas, S. Synthesis of Metal-Organic Frameworks (MOFs): Routes to Various MOF Topologies, Morphologies, and Composites. *Chem. Rev.* **2012**, *112* (2), 933–969.

(28) Cheong, V. F.; Moh, P. Y. Recent Advancement in Metal–Organic Framework: Synthesis, Activation, Functionalisation, and Bulk Production. *Mater. Sci. Technol. (United Kingdom)* **2018**, *34* (9), 1025–1045.

(29) Férey, G. Hybrid Porous Solids: Past, Present, Future. *Chem. Soc. Rev.* **2008**, *37* (1), 191–214.

(30) Banerjee, R.; Phan, A.; Wang, B.; Knobler, C.; Furukawa, H.; O'Keeffe, M.; Yaghi, O. M. High-Throughput Synthesis of Zeolitic Imidazolate Frameworks and Application to CO2 Capture. *Science* **2008**, *319* (5865), 939–943.

(31) Biemmi, E.; Christian, S.; Stock, N.; Bein, T. High-Throughput Screening of Synthesis Parameters in the Formation of the Metal-Organic Frameworks MOF-5 and HKUST-1.

Microporous Mesoporous Mater. **2009**, *117* (1–2), 111–117.

(32) Howarth, A. J.; Peters, A. W.; Vermeulen, N. A.; Wang, T. C.; Hupp, J. T.; Farha, O. K. Best Practices for the Synthesis, Activation, and Characterization of Metal–Organic Frameworks. *Chem. Mater.* **2017**, *29* (1), 26–39.

(33) Wasserscheid, P.; Keim, W. Ionic Liquids—New “Solutions” for Transition Metal Catalysis. *Angew. Chemie* **2000**, *39* (21), 3772–3789.

(34) Xu, L.; Choi, E.; Kwon, Y. Ionothermal Synthesis of a 3D Zn–BTC Metal-Organic Framework with Distorted Tetranuclear [Zn4(M4-O)] Subunits. *Inorg. Chem. Commun.* **2008**, *11* (10), 1190–1193.

(35) Liu, J.; Zou, X.; Liu, C.; Cai, K.; Zhao, N.; Zheng, W.; Zhu, G. Ionothermal Synthesis and Proton-Conductive Properties of NH 2 -MIL-53 MOF Nanomaterials. *CrystEngComm* **2016**, *18* (4), 525–528.

(36) Varma, R. S. Microwave Technology - Applications in Chemical Synthesis. In *Kirk-Othmer Encyclopedia of Chemical Technology, Copyright John Wiley*; 2013.

(37) Galema, S. A. Microwave Chemistry. *Chem. Soc. Rev.* **1997**, *26* (3), 233.

(38) Kappe, C. O. Controlled Microwave Heating in Modern Organic Synthesis. *Angew. Chemie Int. Ed.* **2004**, *43* (46), 6250–6284.

(39) Jhung, S. H.; Lee, J. H.; Forster, P. M.; Férey, G.; Cheetham, A. K.; Chang, J. S. Microwave Synthesis of Hybrid Inorganic - Organic Porous Materials: Phase-Selective and Rapid Crystallization. *Chem. - A Eur. J.* **2006**, *12* (30), 7899–7905.

(40) Khan, N. A.; Jhung, S. H. Synthesis of Metal-Organic Frameworks (MOFs) with Microwave or Ultrasound: Rapid Reaction, Phase-Selectivity, and Size Reduction. *Coord. Chem. Rev.* **2015**, *285*, 11–23.

(41) Li, Z.; Qiu, L.; Xu, T.; Wu, Y.; Wang, W.; Wu, Z.; Jiang, X. Ultrasonic Synthesis of the Microporous Metal–Organic Framework Cu3(BTC)2 at Ambient Temperature and Pressure: An Efficient and Environmentally Friendly Method. *Mater. Lett.* **2009**, *63* (1), 78–80.

(42) Chalati, T.; Horcajada, P.; Gref, R.; Couvreur, P.; Serre, C. Optimisation of the Synthesis of MOF Nanoparticles Made of Flexible Porous Iron Fumarate MIL-88A. *J. Mater. Chem.* **2011**, *21* (7), 2220–2227.

(43) Khan, N. A.; Jhung, S. H. Phase-Transition and Phase-Selective Synthesis of Porous Chromium-Benzenedicarboxylates. *Cryst. Growth Des.* **2010**, *10* (4), 1860–1865.

(44) Jhung, S. H.; Lee, J.; Chang, J. Microwave Synthesis of a Nanoporous Hybrid Material, MIL-100(Cr). *Bull. Korean Chem. Soc.* **2005**, *26* (6), 880–881.

(45) Jhung, S. H.; Lee, J.-H.; Yoon, J. W.; Serre, C.; Férey, G.; Chang, J.-S. Microwave Synthesis of Chromium Terephthalate MIL-101 and Its Benzene Sorption Ability. *Adv. Mater.* **2007**, *19* (1), 121–124.

(46) Ni, Z.; Masel, R. I. Rapid Production of Metal−Organic Frameworks via Microwave-Assisted Solvothermal Synthesis. *J. Am. Chem. Soc.* **2006**, *128* (38), 12394–12395.

(47) Khan, N. A.; Jhung, S.-H. Facile Syntheses of Metal-Organic Framework Cu3(BTC)2(H2O)3 under Ultrasound. *Bull. Korean Chem. Soc.* **2009**, *30* (12), 2921–2926.

(48) Haque, E.; Khan, N. A.; Park, J. H.; Jhung, S. H. Synthesis of a Metal-Organic Framework Material, Iron Terephthalate, by Ultrasound, Microwave, and Conventional Electric Heating: A Kinetic Study. *Chem. - A Eur. J.* **2010**, *16* (3), 1046–1052.

(49) Son, W.; Kim, J.; Kim, J.; Ahn, W. Sonochemical Synthesis of MOF-5. *Chem. Commun.* **2008**, No. 47, 6336.

(50) Mueller, U.; Puetter, H.; Hesse, M.; Wessel, H. Method for Electrochemical Production of a Crystalline Porous Metal Organic Skeleton Material. WO2005/049892, 2004.

(51) Richter, I.; Schubert, M.; Muller, U. Porous Metal Organic Framework Based on Pyrroles and Pyridinones. WO/2007/131955, 2007.

(52) Friščić, T. Metal-Organic Frameworks: Mechanochemical Synthesis Strategies. In *Encyclopedia of Inorganic and Bioinorganic Chemistry*; John Wiley & Sons, Ltd: Chichester, UK, 2014; pp 1–19.

(53) Klimakow, M.; Klobes, P.; Thünemann, A. F.; Rademann, K.; Emmerling, F. Mechanochemical Synthesis of Metal−Organic Frameworks: A Fast and Facile Approach toward Quantitative Yields and High Specific Surface Areas. *Chem. Mater.* **2010**, *22* (18), 5216–5221.

(54) James, S. L.; Adams, C. J.; Bolm, C.; Braga, D.; Collier, P.; Friščić, T.; Grepioni, F.; Harris, K. D. M.; Hyett, G.; Jones, W.; et al. Mechanochemistry: Opportunities for New and Cleaner Synthesis. *Chem. Soc. Rev.* **2012**, *41* (1), 413–447.

(55) Tranchemontagne, D. J.; Hunt, J. R.; Yaghi, O. M. Room Temperature Synthesis of Metal-Organic Frameworks: MOF-5, MOF-74, MOF-177, MOF-199, and IRMOF-0. *Tetrahedron* **2008**, *64* (36), 8553–8557.

(56) Gross, A. F.; Sherman, E.; Vajo, J. J. Aqueous Room Temperature Synthesis of Cobalt and Zinc Sodalite Zeolitic Imidizolate Frameworks. *Dalt. Trans.* **2012**, *41* (18), 5458–5460.

(57) Sánchez-Sánchez, M.; Getachew, N.; Díaz, K.; Díaz-García, M.; Chebude, Y.; Díaz, I. Synthesis of Metal–Organic Frameworks in Water at Room Temperature: Salts as Linker Sources. *Green Chem.* **2015**, *17* (3), 1500–1509.

(58) Zhang, W.; Yang, Y.; Zai, S.; Weng Ng, S.; Chen, X. Syntheses, Structures and Magnetic Properties of Dinuclear Copper(II)–Lanthanide(III) Complexes Bridged by 2-Hydroxymethyl-1-Methylimidazole. *Eur. J. Inorg. Chem.* **2008**, *2008* (5), 679–685.

(59) Farha, O. K.; Hupp, J. T. Rational Design, Synthesis, Purification, and Activation of Metal−Organic Framework Materials. *Acc. Chem. Res.* **2010**, *43* (8), 1166–1175.

(60) Farha, O. K.; Mulfort, K. L.; Thorsness, A. M.; Hupp, J. T. Separating Solids: Purification of Metal-Organic Framework Materials. *J. Am. Chem. Soc.* **2008**, *130* (27), 8598–8599.

(61) Eddaoudi, M.; Kim, J.; Rosi, N.; Vodak, D.; Wachter, J.; O'Keeffe, M.; Yaghi, O. M. Systematic Design of Pore Size and Functionality in Isoreticular MOFs and Their Application in Methane Storage. *Science (80-.).* **2002**, *295* (5554), 469–472.

(62) Zhang, J. J.; Wojtas, L.; Larsen, R. W.; Eddaoudi, M.; Zaworotko, M. J. Temperature and Concentration Control over Interpenetration in a Metal-Organic Material. *J. Am. Chem. Soc.* **2009**, *131* (47), 17040–17041.

(63) Ma, L.; Lin, W. Chirality-Controlled and Solvent-Templated Catenation Isomerism in Metal-

Organic Frameworks. *J. Am. Chem. Soc.* **2008**, *130* (42), 13834–13835.

(64) Ma, S.; Sun, D.; Ambrogio, M.; Fillinger, J. A.; Parkin, S.; Zhou, H. C. Framework-Catenation Isomerism in Metal-Organic Frameworks and Its Impact on Hydrogen Uptake. *J. Am. Chem. Soc.* **2007**, *129* (7), 1858–1859.

(65) Serre, C.; Millange, F.; Thouvenot, C.; Noguès, M.; Marsolier, G.; Louër, D.; Férey, G. Very Large Breathing Effect in the First Nanoporous Chromium(III)-Based Solids: MIL-53 or CrIII(OH)·{O2C-C6H4- CO2}·{HO2C-C6H4 -CO2H}x·H2Oy. *J. Am. Chem. Soc.* **2002**, *124* (45), 13519–13526.

(66) Loiseau, T.; Serre, C.; Huguenard, C.; Fink, G.; Taulelle, F.; Henry, M.; Bataille, T.; Férey, G. A Rationale for the Large Breathing of the Porous Aluminum Terephthalate (MIL-53) Upon Hydration. *Chem. - A Eur. J.* **2004**, *10* (6), 1373–1382.

(67) Dauth, A.; Love, J. A. Synthesis and Reactivity of M3(BTC)2 M=Cr,Cu,Mo,Zn,Fe,Ru. *Dalt. Trans.* **2012**, *41* (26), 7782.

(68) Kirchon, A.; Feng, L.; Drake, H. F.; Joseph, E. A.; Zhou, H. From Fundamentals to Applications: A Toolbox for Robust and Multifunctional MOF Materials. *Chem. Soc. Rev.* **2018**, *47* (23), 8611–8638.

(69) Kumar, P.; Vellingiri, K.; Kim, K. H.; Brown, R. J. C.; Manos, M. J. Modern Progress in Metal-Organic Frameworks and Their Composites for Diverse Applications. *Microporous Mesoporous Mater.* **2017**, *253* (January 2016), 251–265.

(70) Silva, P.; Vilela, S. M. F.; Tome, J. P. C.; Almeida Paz, F. A. Multifunctional Metal-Organic Frameworks: From Academia to Industrial Applications. *Chem. Soc. Rev.* **2015**, *44* (19), 6774–6803.

(71) Decoste, J. B.; Peterson, G. W. Metal − Organic Frameworks for Air Purification of Toxic Chemicals. *Chem. Rev.* **2014**, No. 114, 5695−5727.

(72) Kreno, L. E.; Leong, K.; Farha, O. K.; Allendorf, M.; Van Richard P., D.; Hupp, J. T. Metal-Organic Framework Materials as Chemical Sensors. *Chem. Rev. (Washington, DC, United States)* **2012**, *112*, 1105–1125.

(73) Wang, B.; Xie, L. H.; Wang, X.; Liu, X. M.; Li, J.; Li, J. R. Applications of Metal–Organic Frameworks for Green Energy and Environment: New Advances in Adsorptive Gas Separation, Storage and Removal. *Green Energy Environ.* **2018**, *3* (3), 191–228.

(74) Barea, E.; Montoro, C.; Navarro, J. A. R. Toxic Gas Removal – Metal–Organic Frameworks for the Capture and Degradation of Toxic Gases and Vapours. *Chem. Soc. Rev.* **2014**, *43* (16), 5419–5430.

(75) Li, H.; Wang, K.; Sun, Y.; Lollar, C. T.; Li, J.; Zhou, H. C. Recent Advances in Gas Storage and Separation Using Metal–Organic Frameworks. *Mater. Today* **2018**, *21* (2), 108–121.

(76) Wales, D. J.; Grand, J.; Ting, V. P.; Burke, R. D.; Edler, K. J.; Bowen, C. R.; Mintova, S.; Burrows, A. D. Gas Sensing Using Porous Materials for Automotive Applications. *Chem. Soc. Rev.* **2015**, *44* (13), 4290–4321.

(77) Keskin, S.; Kizilel, S. Biomedical Applications of Metal Organic Frameworks. *Ind. Eng. Chem. Res.* **2011**, *50* (4), 1799–1812.

(78) McKinlay, A. C.; Morris, R. E.; Horcajada, P.; Férey, G.; Gref, R.; Couvreur, P.; Serre, C.

BioMOFs: Metal-Organic Frameworks for Biological and Medical Applications. *Angew. Chemie Int. Ed.* **2010**, *49* (36), 6260–6266.

(79) Keskin, S.; Seda, K.; Kızılel, S. Biomedical Applications of Metal Organic Frameworks. *Science (80-.).* **2010**, *50*, 1799–1812.

(80) Naturwissenschaften, D. Der. Preparation and Characterization of Metal-Organic Frameworks for Biological Applications. **2011**, No. November.

(81) Cai, W.; Chu, C.; Liu, G.; Wáng, Y. J. Metal-Organic Framework-Based Nanomedicine Platforms for Drug Delivery and Molecular Imaging. *Small* **2015**, *11* (37), 4806–4822.

(82) Mínguez Espallargas, G.; Coronado, E. Magnetic Functionalities in MOFs: From the Framework to the Pore. *Chem. Soc. Rev.* **2018**, *47* (2), 533–557.

(83) Nadar, S. S.; Rathod, V. K. Magnetic-Metal Organic Framework (Magnetic-MOF): A Novel Platform for Enzyme Immobilization and Nanozyme Applications. *Int. J. Biol. Macromol.* **2018**, *120*, 2293–2302.

(84) Stavila, V.; Talin, A. A.; Allendorf, M. D. MOF-Based Electronic and Opto-Electronic Devices. *Chem. Soc. Rev.* **2014**, *43* (16), 5994–6010.

(85) Chopra, S.; Dhumal, S.; Abeli, P.; Beaudry, R.; Almenar, E. Metal-Organic Frameworks Have Utility in Adsorption and Release of Ethylene and 1-Methylcyclopropene in Fresh Produce Packaging. *Postharvest Biol. Technol.* **2017**, *130* (January), 48–55.

(86) Qiu, S.; Xue, M.; Zhu, G. Metal-Organic Framework Membranes: From Synthesis to Separation Application. *Chem. Soc. Rev.* **2014**, *43* (16), 6116–6140.

(87) Farrusseng, D.; Aguado, S.; Pinel, C. Metal-Organic Frameworks: Opportunities for Catalysis. *Angew. Chemie - Int. Ed.* **2009**, *48* (41), 7502–7513.

(88) Chen, Y. Z.; Zhang, R.; Jiao, L.; Jiang, H. L. Metal–Organic Framework-Derived Porous Materials for Catalysis. *Coord. Chem. Rev.* **2018**, *362*, 1–23.

(89) Dhakshinamoorthy, A.; Li, Z.; Garcia, H. Catalysis and Photocatalysis by Metal Organic Frameworks. *Chem. Soc. Rev.* **2018**, *7*.

(90) Gascon, J.; Corma, A.; Kapteijn, F.; Llabrés i Xamena, F. X. Metal Organic Framework Catalysis: Quo Vadis ? *ACS Catal.* **2014**, *4* (2), 361–378.

(91) Corma, A.; García, H.; Llabrés i Xamena, F. X. Engineering Metal Organic Frameworks for Heterogeneous Catalysis. *Chem. Rev.* **2010**, *110* (8), 4606–4655.

(92) Kholdeeva, O. A. Liquid-Phase Selective Oxidation Catalysis with Metal-Organic Frameworks. *Catal. Today* **2016**, *278*, 22–29.

(93) Wen, Y.; Zhang, J.; Xu, Q.; Wu, X. T.; Zhu, Q. L. Pore Surface Engineering of Metal–Organic Frameworks for Heterogeneous Catalysis. *Coord. Chem. Rev.* **2018**, *376*, 248–276.

(94) Alaerts, L.; Séguin, E.; Poelman, H.; Thibault-Starzyk, F.; Jacobs, P. A.; De Vos, D. E. Probing the Lewis Acidity and Catalytic Activity of the Metal-Organic Framework [Cu3(Btc)2] (BTC = Benzene-1,3,5-Tricarboxylate). *Chem. - A Eur. J.* **2006**, *12* (28), 7353–7363.

(95) Vermoortele, F.; Ameloot, R.; Alaerts, L.; Matthessen, R.; Carlier, B.; Fernandez, E. V. R.; Gascon, J.; Kapteijn, F.; De Vos, D. E. Tuning the Catalytic Performance of Metal–Organic Frameworks in Fine Chemistry by Active Site Engineering. *J. Mater. Chem.* **2012**, *22* (20),

10313.

(96) Schlichte, K.; Kratzke, T.; Kaskel, S. Improved Synthesis, Thermal Stability and Catalytic Properties of the Metal-Organic Framework Compound Cu3(BTC)2. *Microporous Mesoporous Mater.* **2004**, *73* (1–2), 81–88.

(97) Hu, Z.; Peng, Y.; Tan, K. M.; Zhao, D. Enhanced Catalytic Activity of a Hierarchical Porous Metal-Organic Framework CuBTC. *CrystEngComm* **2015**, *17* (37), 7124–7129.

(98) Jrad, A.; Abu Tarboush, B. J.; Hmadeh, M.; Ahmad, M. Tuning Acidity in Zirconium-Based Metal Organic Frameworks Catalysts for Enhanced Production of Butyl Butyrate. *Appl. Catal. A Gen.* **2019**, *570*, 31–41.

(99) Opanasenko, M.; Dhakshinamoorthy, A.; Hwang, Y. K.; Chang, J. S.; Garcia, H.; Čejka, J. Superior Performance of Metal-Organic Frameworks over Zeolites as Solid Acid Catalysts in the Prins Reaction: Green Synthesis of Nopol. *ChemSusChem* **2013**, *6* (5), 865–871.

(100) Aguirre-Díaz, L. M.; Gándara, F.; Iglesias, M.; Snejko, N.; Gutiérrez-Puebla, E.; Monge, M. Á. Tunable Catalytic Activity of Solid Solution Metal-Organic Frameworks in One-Pot Multicomponent Reactions. *J. Am. Chem. Soc.* **2015**, *137* (19), 6132–6135.

(101) Reinares-Fisac, D.; Aguirre-Díaz, L. M.; Iglesias, M.; Snejko, N.; Gutiérrez-Puebla, E.; Monge, M. Á.; Gándara, F. A Mesoporous Indium Metal-Organic Framework: Remarkable Advances in Catalytic Activity for Strecker Reaction of Ketones. *J. Am. Chem. Soc.* **2016**, *138* (29), 9089–9092.

(102) Castro-Gómez, F.; Salassa, G.; Kleij, A. W.; Bo, C. A DFT Study on the Mechanism of the Cycloaddition Reaction of CO 2 to Epoxides Catalyzed by Zn(Salphen) Complexes. *Chem. - A Eur. J.* **2013**, *19* (20), 6289–6298.

(103) He, H.; Perman, J. A.; Zhu, G.; Ma, S. Metal-Organic Frameworks for CO2 Chemical Transformations. *Small* **2016**, *12* (46), 6309–6324.

(104) Beyzavi, M. H.; Stephenson, C. J.; Liu, Y.; Karagiaridi, O.; Hupp, J. T.; Farha, O. K. Metalâ€“Organic Framework-Based Catalysts: Chemical Fixation of CO2 with Epoxides Leading to Cyclic Organic Carbonates. *Front. Energy Res.* **2015**, *2* (January), 1–10.

(105) Gao, W. Y.; Chen, Y.; Niu, Y.; Williams, K.; Cash, L.; Perez, P. J.; Wojtas, L.; Cai, J.; Chen, Y. S.; Ma, S. Crystal Engineering of an Nbo Topology Metal-Organic Framework for Chemical Fixation of CO2 under Ambient Conditions. *Angew. Chemie - Int. Ed.* **2014**, *53* (10), 2615–2619.

(106) Shamzhy, M. V.; Opanasenko, M. V.; Garcia, H.; Čejka, J. Annulation of Phenols with Methylbutenol over MOFs: The Role of Catalyst Structure and Acid Strength in Producing 2,2-Dimethylbenzopyran Derivatives. *Microporous Mesoporous Mater.* **2015**, *202* (C), 297–302.

(107) Doan, T. L. H.; Dao, T. Q.; Tran, H. N.; Tran, P. H.; Le, T. N. An Efficient Combination of Zr-MOF and Microwave Irradiation in Catalytic Lewis Acid Friedel-Crafts Benzoylation. *Dalt. Trans.* **2016**, *45* (18), 7875–7880.

(108) Phan, N. T. S.; Le, K. K. A.; Phan, T. D. MOF-5 as an Efficient Heterogeneous Catalyst for Friedel-Crafts Alkylation Reactions. *Appl. Catal. A Gen.* **2010**, *382* (2), 246–253.

(109) Calleja, G.; Sanz, R.; Orcajo, G.; Briones, D.; Leo, P.; Martínez, F. Copper-Based MOF-74 Material as Effective Acid Catalyst in Friedel–Crafts Acylation of Anisole. *Catal. Today* **2014**,

227, 130–137.

(110) Gascon, J.; Aktay, U.; Hernandez-Alonso, M.; Vanklink, G.; Kapteijn, F. Amino-Based Metal-Organic Frameworks as Stable, Highly Active Basic Catalysts. *J. Catal.* **2009**, *261* (1), 75–87.

(111) Vermoortele, F.; Ameloot, R.; Vimont, A.; Serre, C.; De Vos, D. An Amino-Modified Zr-Terephthalate Metal-Organic Framework as an Acid-Base Catalyst for Cross-Aldol Condensation. *Chem. Commun. (Camb).* **2011**, *47* (5), 1521–1523.

(112) Dhakshinamoorthy, A.; Asiri, A. M.; Garcia, H. Metal-Organic Frameworks as Catalysts for Oxidation Reactions. *Chem. - A Eur. J.* **2016**, *22* (24), 8012–8024.

(113) Dhakshinamoorthy, A.; Alvaro, M.; Garcia, H. Metal–Organic Frameworks as Heterogeneous Catalysts for Oxidation Reactions. *Catal. Sci. Technol.* **2011**, *1* (6), 856.

(114) Zhang, J.; Biradar, A. V; Pramanik, S.; Emge, T. J.; Asefa, T.; Li, J. A New Layered Metal-Organic Framework as a Promising Heterogeneous Catalyst for Olefin Epoxidation Reactions. *Chem. Commun. (Camb).* **2012**, *48* (52), 6541–6543.

(115) Nicola, C. Di; Karabach, Y. Y.; Kirillov, A. M.; Monari, M.; Pandolfo, L.; Pettinari, C.; Pombeiro, A. J. L. Supramolecular Assemblies of Trinuclear Triangular Copper (II) Secondary Building Units through Hydrogen Bonds. Generation of Different Metal−Organic Frameworks, Valuable Catalysts for Peroxidative Oxidation of Alkanes. *Inorg. Chem.* **2007**, *46* (1), 221–230.

(116) Santiago-Portillo, A.; Navalón, S.; Cirujano, F. G.; Xamena, F. X. L. I.; Alvaro, M.; Garcia, H. MIL-101 as Reusable Solid Catalyst for Autoxidation of Benzylic Hydrocarbons in the Absence of Additional Oxidizing Reagents. *ACS Catal.* **2015**, *5* (6), 3216–3224.

(117) Llabrés i Xamena, F. X.; Casanova, O.; Galiasso Tailleur, R.; Garcia, H.; Corma, A. Metal Organic Frameworks (MOFs) as Catalysts: A Combination of Cu2+ and Co2+ MOFs as an Efficient Catalyst for Tetralin Oxidation. *J. Catal.* **2008**, *255* (2), 220–227.

(118) Luz, I.; León, A.; Boronat, M.; Llabrés i Xamena, F. X.; Corma, A. Selective Aerobic Oxidation of Activated Alkanes with MOFs and Their Use for Epoxidation of Olefins with Oxygen in a Tandem Reaction. *Catal. Sci. Technol.* **2013**, *3* (2), 371–379.

(119) Saudan, L. A. Hydrogenation Processes in the Synthesis of Perfumery Ingredients. *Acc. Chem. Res.* **2007**, *40* (12), 1309–1319.

(120) Chapuis, C.; Jacoby, D. Catalysis in the Preparation of Fragrances and Flavours. *Appl. Catal. A Gen.* **2001**, *221* (1–2), 93–117.

(121) Cherkaoui, H.; Soufiaoui, M.; Grée, R. From Allylic Alcohols to Saturated Carbonyls Using Fe(CO)5 as Catalyst: Scope and Limitation Studies and Preparation of Two Perfume Components. *Tetrahedron* **2001**, *57* (12), 2379–2383.

(122) Kurosu, M.; Marcin, L. R.; Grinsteiner, T. J.; Kishi, Y. Total Synthesis of (±)-Batrachotoxinin A. *J. Am. Chem. Soc.* **1998**, *120* (26), 6627–6628.

(123) Plessers, E.; De Vos, D. E.; Roeffaers, M. B. J. Chemoselective Reduction of α,β-Unsaturated Carbonyl Compounds with UiO-66 Materials. *J. Catal.* **2016**, *340*, 136–143.

(124) Plessers, E.; Fu, G.; Tan, C.; De Vos, D.; Roeffaers, M. Zr-Based MOF-808 as Meerwein–Ponndorf–Verley Reduction Catalyst for Challenging Carbonyl Compounds. *Catalysts* **2016**, *6* (7), 104.

(125) Cavka, J. H.; Jakobsen, S.; Olsbye, U.; Guillou, N.; Lamberti, C.; Bordiga, S.; Lillerud, K. P. A New Zirconium Inorganic Building Brick Forming Metal Organic Frameworks with Exceptional Stability. *J. Am. Chem. Soc.* **2008**, *130* (42), 13850–13851.

(126) Wißmann, G.; Schaate, A.; Lilienthal, S.; Bremer, I.; Schneider, A. M.; Behrens, P. Modulated Synthesis of Zr-Fumarate MOF. *Microporous Mesoporous Mater.* **2012**, *152*, 64–70.

(127) Schaate, A.; Roy, P.; Godt, A.; Lippke, J.; Waltz, F.; Wiebcke, M.; Behrens, P. Modulated Synthesis of Zr-Based Metal-Organic Frameworks: From Nano to Single Crystals. *Chem. - A Eur. J.* **2011**, *17* (24), 6643–6651.

(128) Schaate, A.; Roy, P.; Preuße, T.; Lohmeier, S. J.; Godt, A.; Behrens, P. Porous Interpenetrated Zirconium-Organic Frameworks (PIZOFs): A Chemically Versatile Family of Metal-Organic Frameworks. *Chem. - A Eur. J.* **2011**, *17* (34), 9320–9325.

(129) Kandiah, M.; Nilsen, M. H.; Usseglio, S.; Jakobsen, S.; Olsbye, U.; Tilset, M.; Larabi, C.; Quadrelli, E. A.; Bonino, F.; Lillerud, K. P. Synthesis and Stability of Tagged UiO-66 Zr-MOFs. *Chem. Mater.* **2010**, *22* (24), 6632–6640.

(130) Chavan, S.; Vitillo, J. G.; Uddin, M. J.; Bonino, F.; Lamberti, C.; Groppo, E.; Lillerud, K. P.; Bordiga, S. Functionalization of UiO-66 Metal-Organic Framework and Highly Cross-Linked Polystyrene with Cr(CO)3: In Situ Formation, Stability, and Photoreactivity. *Chem. Mater.* **2010**, *22* (16), 4602–4611.

(131) Mowat, J. P. S.; Seymour, V. R.; Griffin, J. M.; Thompson, S. P.; Slawin, A. M. Z.; Fairen-Jimenez, D.; Düren, T.; Ashbrook, S. E.; Wright, P. A. A Novel Structural Form of MIL-53 Observed for the Scandium Analogue and Its Response to Temperature Variation and CO2adsorption. *Dalt. Trans.* **2012**, *41* (14), 3937–3941.

(132) Devic, T.; Horcajada, P.; Serre, C.; Salles, F.; Maurin, G.; Heurtaux, D.; Clet, G.; Vimont, A.; Grene, J.; Ouay, B. Le; et al. Functionalization in Flexible Porous Solids : Effects on the Pore Opening and the Host - Guest Interactions. *J. Am. Chem. Soc.* **2008**, No. 132, 1127–1136.

(133) Anokhina, E. V.; Vougo-Zanda, M.; Wang, X.; Jacobson, A. J. In(OH)BDC·0.75BDCH 2 (BDC = Benzenedicarboxylate), a Hybrid Inorganic−Organic Vernier Structure. *J. Am. Chem. Soc.* **2005**, *127* (43), 15000–15001.

(134) Volkringer, C.; Loiseau, T.; Guillou, N.; Férey, G.; Elkaïm, E.; Vimont, A. XRD and IR Structural Investigations of a Particular Breathing Effect in the MOF-Type Gallium Terephthalate MIL-53(Ga). *J. Chem. Soc. Dalt. Trans.* **2009**, *53* (12), 2241–2249.

(135) Gaab, M.; Trukhan, N.; Maurer, S.; Gummaraju, R.; Müller, U. The Progression of Al-Based Metal-Organic Frameworks – From Academic Research to Industrial Production and Applications. *Microporous Mesoporous Mater.* **2012**, *157*, 131–136.

(136) Senkovska, I.; Hoffmann, F.; Fröba, M.; Getzschmann, J.; Böhlmann, W.; Kaskel, S. New Highly Porous Aluminium Based Metal-Organic Frameworks: Al(OH)(Ndc) (Ndc = 2,6-Naphthalene Dicarboxylate) and Al(OH)(Bpdc) (Bpdc = 4,4′-Biphenyl Dicarboxylate). *Microporous Mesoporous Mater.* **2009**, *122* (1–3), 93–98.

(137) Lescouet, T.; Kockrick, E.; Bergeret, G.; Pera-Titus, M.; Farrusseng, D. Engineering MIL-53(Al) Flexibility by Controlling Amino Tags. *Dalt. Trans.* **2011**, *40* (43), 11359–11361.

(138) Biswas, S.; Ahnfeldt, T.; Stock, N. New Functionalized Flexible Al-MIL-53-X (X = -Cl, -Br, -CH 3 , -NO 2 , -(OH) 2) Solids: Syntheses, Characterization, Sorption, and Breathing

Behavior. *Inorg. Chem.* **2011**, *50* (19), 9518–9526.

(139) Furukawa, H.; Go, Y. B.; Ko, N.; Park, Y. K.; Uribe-Romo, F. J.; Kim, J.; O'Keeffe, M.; Yaghi, O. M. Isoreticular Expansion of Metal-Organic Frameworks with Triangular and Square Building Units and the Lowest Calculated Density for Porous Crystals. *Inorg. Chem.* **2011**, *50* (18), 9147–9152.

(140) Ma, L.; Lee, J. Y.; Li, J.; Lin, W. Three-Dimensional Metal-Organic Frameworks Based on Elongated Tetracarboxylate Building Blocks for Hydrogen Storage. *Inorg. Chem.* **2008**, *47* (10), 3955–3957.

(141) Furukawa, H.; Ko, N.; Go, Y. B.; Aratani, N.; Choi, S. B.; Choi, E.; Yazaydin, A. O.; Snurr, R. Q.; O'Keeffe, M.; Kim, J.; et al. Ultrahigh Porosity in Metal-Organic Frameworks. *Science (80-.).* **2010**, *329* (5990), 424–428.

(142) Li, Q.; Zhang, W.; Miljanić, O. Š.; Sue, C. H.; Zhao, Y. L.; Liu, L.; Knobler, C. B.; Stoddart, J. F.; Yaghi, O. M. Docking in Metal-Organic Frameworks. *Science (80-.).* **2009**, *325* (5942), 855–859.

(143) Evans, O. R.; Lin, W. Rational Design of Nonlinear Optical Materials Based on 2D Coordination Networks. *Chem. Mater.* **2001**, *13* (9), 3009–3017.

(144) Nguyen, T. T. M.; Le, H. M.; Kawazoe, Y.; Nguyen, H. L. Reticular Control of Interpenetration in a Complex Metal–Organic Framework. *Mater. Chem. Front.* **2018**.

(145) Venkataramanan, N. S.; Sahara, R.; Mizuseki, H.; Kawazoe, Y. Probing the Structure, Stability and Hydrogen Adsorption of Lithium Functionalized Isoreticular MOF-5 (Fe, Cu, Co, Ni and Zn) by Density Functional Theory. *Int. J. Mol. Sci.* **2009**, *10* (4), 1601–1608.

(146) Lin, X.; Telepeni, I.; Blake, A. J.; Dailly, A.; Brown, C. M.; Simmons, J. M.; Zoppi, M.; Walker, G. S.; Thomas, K. M.; Mays, T. J.; et al. High Capacity Hydrogen Adsorption in Cu(II) Tetracarboxylate Framework Materials: The Role of Pore Size, Ligand Functionalization, and Exposed Metal Sites. *J. Am. Chem. Soc.* **2009**, *131* (6), 2159–2171.

(147) Wu, S.; Ma, L.; Long, L.; Zheng, L.; Lin, W. 3D Metal-Organic Frameworks Based on Functionalized Tetracarboxylate Linkers : Synthesis , Structures , and Gas Sorption Studies. *North* **2009**, *48* (6), 1–10.

(148) Li, J.; Ren, Y.; Qi, C.; Jiang, H. Fully Meta -Substituted 4,4′-Biphenyldicarboxylate-Based Metal-Organic Frameworks: Synthesis, Structures, and Catalytic Activities. *Eur. J. Inorg. Chem.* **2017**, *2017* (11), 1478–1487.

(149) Cepeda, J.; Pérez-Mendoza, M.; Calahorro, A. J.; Casati, N.; Seco, J. M.; Aragones-Anglada, M.; Moghadam, P. Z.; Fairen-Jimenez, D.; Rodríguez-Diéguez, A. Modulation of Pore Shape and Adsorption Selectivity by Ligand Functionalization in a Series of "Rob"-like Flexible Metal–Organic Frameworks. *J. Mater. Chem. A* **2018**, *6* (36), 17409–17416.

(150) Song, F.; Zhang, T.; Wang, C.; Lin, W. Chiral Porous Metal-Organic Frameworks with Dual Active Sites for Sequential Asymmetric Catalysis. *Proc. R. Soc. A Math. Phys. Eng. Sci.* **2012**, *468* (2143), 2035–2052.

(151) Wade, C. R.; Dinca, M. Investigation of the Synthesis, Activation, and Isosteric Heats of CO2 Adsorption of the Isostructural Series of MOFs M3(BTC)2 (M=Cr,Fe,Ni,Cu,Mo,Ru). *Dalt. Trans.* **2012**, *41* (26), 7931.

(152) Vaidhyanathan, R.; Iremonger, S. S.; Dawson, K. W.; Shimizu, G. K. H. An Amine-

Functionalized Metal Organic Framework for Preferential CO 2 Adsorption at Low Pressures. *Chem. Commun.* **2009**, No. 35, 5230–5232.

(153) Stavitski, E.; Pidko, E. A.; Couck, S.; Remy, T.; Hensen, E. J. M.; Weckhuysen, B. M.; Denayer, J.; Gascon, J.; Kapteijn, F. Complexity behind CO2 Capture on NH2-MIL-53(Al). *Langmuir* **2011**, *27* (7), 3970–3976.

(154) Stylianou, K. C.; Warren, J. E.; Chong, S. Y.; Rabone, J.; Bacsa, J.; Bradshaw, D.; Rosseinsky, M. J. CO2 Selectivity of a 1D Microporous Adenine-Based Metal-Organic Framework Synthesised in Water. *Chem. Commun.* **2011**, *47* (12), 3389–3391.

(155) Song, F.; Wang, C.; Falkowski, J. M.; Ma, L.; Lin, W. Isoreticular Chiral Metal−Organic Frameworks for Asymmetric Alkene Epoxidation: Tuning Catalytic Activity by Controlling Framework Catenation and Varying Open Channel Sizes. *J. Am. Chem. Soc.* **2010**, *132* (43), 15390–15398.

(156) Bigdeli, F.; Abedi, S.; Hosseini-Monfared, H.; Morsali, A. An Investigation of the Catalytic Activity in a Series of Isoreticular Zn(II)-Based Metal-Organic Frameworks. *Inorg. Chem. Commun.* **2016**, *72*, 122–127.

(157) Ma, L.; Falkowski, J. M.; Abney, C.; Lin, W. A Series of Isoreticular Chiral Metal–Organic Frameworks as a Tunable Platform for Asymmetric Catalysis. *Nat. Chem.* **2010**, *2* (10), 838–846.

(158) Schneemann, A.; Bon, V.; Schwedler, I.; Senkovska, I.; Kaskel, S.; Fischer, R. A. Flexible Metal–Organic Frameworks. *Chem. Soc. Rev.* **2014**, *43* (16), 6062–6096.

(159) Deria, P.; Mondloch, J. E.; Karagiaridi, O.; Bury, W.; Hupp, J. T.; Farha, O. K. Beyond Post-Synthesis Modification: Evolution of Metal–Organic Frameworks via Building Block Replacement. *Chem. Soc. Rev.* **2014**, *43* (16), 5896–5912.

(160) Song, X.; Kim, T. K.; Kim, H.; Kim, D.; Jeong, S.; Moon, H. R.; Lah, M. S. Post-Synthetic Modifications of Framework Metal Ions in Isostructural Metal-Organic Frameworks: Core-Shell Heterostructures via Selective Transmetalations. *Chem. Mater.* **2012**, *24* (15), 3065–3073.

(161) Smith, S. J. D.; Ladewig, B. P.; Hill, A. J.; Lau, C. H.; Hill, M. R. Post-Synthetic Ti Exchanged UiO-66 Metal-Organic Frameworks That Deliver Exceptional Gas Permeability in Mixed Matrix Membranes. *Sci. Rep.* **2015**, *5*, 15–18.

(162) Liu, X.; Akerboom, S.; De Jong, M.; Mutikainen, I.; Tanase, S.; Meijerink, A.; Bouwman, E. Mixed-Lanthanoid Metal-Organic Framework for Ratiometric Cryogenic Temperature Sensing. *Inorg. Chem.* **2015**, *54* (23), 11323–11329.

(163) Wang, L. J.; Deng, H.; Furukawa, H.; Gándara, F.; Cordova, K. E.; Peri, D.; Yaghi, O. M. Synthesis and Characterization of Metal-Organic Framework-74 Containing 2, 4, 6, 8, and 10 Different Metals. *Inorg. Chem.* **2014**, *53* (12), 5881–5883.

(164) Yao, H. F.; Yang, Y.; Liu, H.; Xi, F. G.; Gao, E. Q. CPO-27-M as Heterogeneous Catalysts for Aldehyde Cyanosilylation and Styrene Oxidation. *J. Mol. Catal. A Chem.* **2014**, *394*, 57–65.

(165) Sun, Q.; Liu, M.; Li, K.; Han, Y.; Zuo, Y.; Wang, J.; Song, C.; Zhang, G.; Guo, X. Controlled Synthesis of Mixed-Valent Fe-Containing Metal Organic Frameworks for the Degradation of Phenol under Mild Conditions. *Dalt. Trans.* **2016**, *45* (19), 7952–7959.

(166) Cancino, P.; Vega, A.; Santiago-Portillo, A.; Navalon, S.; Alvaro, M.; Aguirre, P.; Spodine, E.; García, H. A Novel Copper(II)-Lanthanum(IIi) Metal Organic Framework as a Selective Catalyst for the Aerobic Oxidation of Benzylic Hydrocarbons and Cycloalkenes. *Catal. Sci. Technol.* **2016**, *6* (11), 3727–3736.

(167) Dhakshinamoorthy, A.; Garcia, H. Cascade Reactions Catalyzed by Metal Organic Frameworks. *ChemSusChem* **2014**, 2392–2410.

(168) Climent, M. J.; Corma, A.; Iborra, S.; Sabater, M. J. Heterogeneous Catalysis for Tandem Reactions. *ACS Catal.* **2014**, *4* (3), 870–891.

(169) Mitchell, L.; Williamson, P.; Ehrlichov, B.; Anderson, A. E.; Seymour, V. R.; Ashbrook, S. E.; Acerbi, N.; Daniels, L. M.; Walton, R. I.; Clarke, M. L.; et al. Mixed-Metal MIL-100(Sc,M) (M=Al, Cr, Fe) for Lewis Acid Catalysis and Tandem C-C Bond Formation and Alcohol Oxidation. *Chem. - A Eur. J.* **2014**, *20* (51), 17185–17197.

(170) Cirujano, F. G.; Llabrés i Xamena, F. X.; Corma, A. MOFs as Multifunctional Catalysts: One-Pot Synthesis of Menthol from Citronellal over a Bifunctional MIL-101 Catalyst. *Dalt. Trans.* **2012**, *41* (14), 4249.

(171) Jagadeesan, D. Multifunctional Nanocatalysts for Tandem Reactions: A Leap toward Sustainability. *Appl. Catal. A Gen.* **2016**, *511*, 59–77.

(172) Yin, Z.; Zhou, Y. L.; Zeng, M. H.; Kurmoo, M. The Concept of Mixed Organic Ligands in Metal-Organic Frameworks: Design, Tuning and Functions. *Dalt. Trans.* **2015**, *44* (12), 5258–5275.

(173) Kleist, W.; Jutz, F.; Maciejewski, M.; Baiker, A. Mixed-Linker Metal-Organic Frameworks as Catalysts for the Synthesis of Propylene Carbonate from Propylene Oxide and CO2. *Eur. J. Inorg. Chem.* **2009**, No. 24, 3552–3561.

(174) Goh, T. W.; Xiao, C.; Maligal-Ganesh, R. V.; Li, X.; Huang, W. Utilizing Mixed-Linker Zirconium Based Metal-Organic Frameworks to Enhance the Visible Light Photocatalytic Oxidation of Alcohol. *Chem. Eng. Sci.* **2015**, *124*, 45–51.

(175) Xu, X.; Van Bokhoven, J. A.; Ranocchiari, M. Tuning Regioisomer Reactivity in Catalysis Using Bifunctional Metal-Organic Frameworks with Mixed Linkers. *ChemCatChem* **2014**, *6* (7), 1887–1891.

(176) Krajnc, A.; Kos, T.; Zabukovec Logar, N.; Mali, G. A Simple NMR-Based Method for Studying the Spatial Distribution of Linkers within Mixed-Linker Metal-Organic Frameworks. *Angew. Chemie - Int. Ed.* **2015**, *54* (36), 10535–10538.

(177) Li, B.; Zhang, Y.; Ma, D.; Li, L.; Li, G.; Li, G.; Shi, Z.; Feng, S. A Strategy toward Constructing a Bifunctionalized MOF Catalyst: Post-Synthetic Modification of MOFs on Organic Ligands and Coordinatively Unsaturated Metal Sites. *Chem. Commun.* **2012**, *48* (49), 6151–6153.

(178) Marx, S.; Kleist, W.; Baiker, A. Synthesis, Structural Properties, and Catalytic Behavior of Cu-BTC and Mixed-Linker Cu-BTC-PyDC in the Oxidation of Benzene Derivatives. *J. Catal.* **2011**, *281* (1), 76–87.

(179) Kozachuk, O.; Luz, I.; Llabrés I Xamena, F. X.; Noei, H.; Kauer, M.; Albada, H. B.; Bloch, E. D.; Marler, B.; Wang, Y.; Muhler, M.; et al. Multifunctional, Defect-Engineered Metal-Organic Frameworks with Ruthenium Centers: Sorption and Catalytic Properties. *Angew.*

Chemie - Int. Ed. **2014**, *53* (27), 7058–7062.

(180) Mautschke, H. H.; Drache, F.; Senkovska, I.; Kaskel, S.; Llabrés Xamena, F. X. I. Catalytic Properties of Pristine and Defect-Engineered Zr-MOF-808 Metal Organic Frameworks. *Catal. Sci. Technol.* **2018**, *8* (14), 3610–3616.

(181) Masoomi, M. Y.; Bagheri, M.; Morsali, A. Application of Two Cobalt-Based Metal-Organic Frameworks as Oxidative Desulfurization Catalysts. *Inorg. Chem.* **2015**, *54* (23), 11269–11275.

(182) Haldar, R.; Reddy, S. K.; Suresh, V. M.; Mohapatra, S.; Balasubramanian, S.; Maji, T. K. Flexible and Rigid Amine-Functionalized Microporous Frameworks Based on Different Secondary Building Units: Supramolecular Isomerism, Selective CO 2 Capture, and Catalysis. *Chem. - A Eur. J.* **2014**, *20* (15), 4347–4356.

(183) Rasero-Almansa, A. M.; Corma, A.; Iglesias, M.; Sánchez, F. Zirconium Materials from Mixed Dicarboxylate Linkers: Enhancing the Stability for Catalytic Applications. *ChemCatChem* **2014**, *6* (12), 3426–3433.

(184) Siu, P. W.; Brown, Z. J.; Farha, O. K.; Hupp, J. T.; Scheidt, K. A. A Mixed Dicarboxylate Strut Approach to Enhancing Catalytic Activity of a de Novo Urea Derivative of Metal–Organic Framework UiO-67. *Chem. Commun.* **2013**, *49* (93), 10920–10922.

(185) Lili, L.; Xin, Z.; Shumin, R.; Ying, Y.; Xiaoping, D.; Jinsen, G.; Chunming, X.; Jing, H. Catalysis by Metal-Organic Frameworks: Proline and Gold Functionalized MOFs for the Aldol and Three-Component Coupling Reactions. *RSC Adv.* **2014**, *4* (25), 13093–13107.

(186) Le, H. T. N.; Tran, T. V.; Phan, N. T. S.; Truong, T. Efficient and Recyclable Cu2(BDC)2(BPY)-Catalyzed Oxidative Amidation of Terminal Alkynes: Role of Bipyridine Ligand. *Catal. Sci. Technol.* **2015**, *5* (2), 851–859.

(187) Wang, X. X.; Yu, B.; Van Hecke, K.; Cui, G. H. Four Cobalt(II) Coordination Polymers with Diverse Topologies Derived from Flexible Bis(Benzimidazole) and Aromatic Dicarboxylic Acids: Syntheses, Crystal Structures and Catalytic Properties. *RSC Adv.* **2014**, *4* (106), 61281–61289.

(188) Lin, H.-Y.; Luan, J.; Le, M.; Wang, X.-L.; Liu, D.-N.; Liu, G.-C. Controllable Assembly of Three Copper(II/I) Metal–Organic Frameworks Based on N,N′-Bis(4-Pyridinecarboxamide)-1,2-Cyclohexane and 4,4′-Oxydibenzoic Acid: From Three-Dimensional Interpenetrating Framework to One-Dimensional Infinite Chain. *Inorganica Chim. Acta* **2014**, *426*, 39–44.

(189) Wang, Z.; Cohen, S. M. Postsynthetic Modification of Metal–Organic Frameworks. *Chem. Soc. Rev.* **2009**, *38* (5), 1315.

(190) Lin, Z. J.; Liu, T. F.; Xu, B.; Han, L. W.; Huang, Y. B.; Cao, R. Pore-Size Tuning in Double-Pillared Metal-Organic Frameworks Containing Cadmium Clusters. *CrystEngComm* **2011**, *13* (10), 3321–3324.

(191) Lin, Y. Y.; Zhang, Y. B.; Zhang, J. P.; Chen, X. M. Pillaring Zn-Triazolate Layers with Flexible Aliphatic Dicarboxylates into Three-Dimensional Metal-Organic Frameworks. *Cryst. Growth Des.* **2008**, *8* (10), 3673–3679.

(192) Meilikhov, M.; Furukawa, S.; Hirai, K.; Fischer, R. A.; Kitagawa, S. Binary Janus Porous Coordination Polymer Coatings for Sensor Devices with Tunable Analyte Affinity. *Angew. Chemie - Int. Ed.* **2013**, *52* (1), 341–345.

(193) Wang, Q.-X.; Long, L.-S.; Hu, S.; Zeng, M.-H.; Tan, Y.-X.; Kurmoo, M.; Zhao, H.-X. Rigid Pillars and Double Walls in a Porous Metal-Organic Framework: Single-Crystal to Single-Crystal, Controlled Uptake and Release of Iodine and Electrical Conductivity. *J. Am. Chem. Soc.* **2010**, *132* (8), 2561–2563.

(194) Zeng, M. H.; Yin, Z.; Tan, Y. X.; Zhang, W. X.; He, Y. P.; Kurmoo, M. Nanoporous Cobalt(II) MOF Exhibiting Four Magnetic Ground States and Changes in Gas Sorption upon Post-Synthetic Modification. *J. Am. Chem. Soc.* **2014**, *136* (12), 4680–4688.

(195) Sudik, A. C.; Côté, A. P.; Wong-Foy, A. G.; O'Keeffe, M.; Yaghi, O. M. A Metal-Organic Framework with a Hierarchical System of Pores and Tetrahedral Building Blocks. *Angew. Chemie - Int. Ed.* **2006**, *45* (16), 2528–2533.

(196) Chughtai, A. H.; Ahmad, N.; Younus, H. A.; Laypkov, A.; Verpoort, F. Metal-Organic Frameworks: Versatile Heterogeneous Catalysts for Efficient Catalytic Organic Transformations. *Chem. Soc. Rev.* **2015**, *44* (19), 6804–6849.

(197) Yang, H.; Li, J.; Zhang, H.; Lv, Y.; Gao, S. Facile Synthesis of POM@MOF Embedded in SBA-15 as a Steady Catalyst for the Hydroxylation of Benzene. *Microporous Mesoporous Mater.* **2014**, *195*, 87–91.

(198) Kockrick, E.; Lescouet, T.; Kudrik, E. V.; Sorokin, A. B.; Farrusseng, D. Synergistic Effects of Encapsulated Phthalocyanine Complexes in MIL-101 for the Selective Aerobic Oxidation of Tetralin. *Chem. Commun.* **2011**, *47* (5), 1562–1564.

(199) Maksimchuk, N. V.; Timofeeva, M. N.; Melgunov, M. S.; Shmakov, A. N.; Chesalov, Y. A.; Dybtsev, D. N.; Fedin, V. P.; Kholdeeva, O. A. Heterogeneous Selective Oxidation Catalysts Based on Coordination Polymer MIL-101 and Transition Metal-Substituted Polyoxometalates. *J. Catal.* **2008**, *257* (2), 315–323.

(200) Farha, O. K.; Shultz, A. M.; Sarjeant, A. A.; Nguyen, S. T.; Hupp, J. T. Active-Site-Accessible, Porphyrinic Metal-Organic Framework Materials. *J. Am. Chem. Soc.* **2011**, *133* (15), 5652–5655.

(201) Fateeva, A.; Chater, P. A.; Ireland, C. P.; Tahir, A. A.; Khimyak, Y. Z.; Wiper, P. V.; Darwent, J. R.; Rosseinsky, M. J. A Water-Stable Porphyrin-Based Metal-Organic Framework Active for Visible-Light Photocatalysis. *Angew. Chemie - Int. Ed.* **2012**, *51* (30), 7440–7444.

(202) Larsen, R. W.; Wojtas, L.; Perman, J.; Musselman, R. L.; Zaworotko, M. J.; Vetromile, C. M. Mimicking Heme Enzymes in the Solid State: Metal-Organic Materials with Selectively Encapsulated Heme. *J. Am. Chem. Soc.* **2011**, *133* (27), 10356–10359.

(203) Wu, F.; Qiu, L. G.; Ke, F.; Jiang, X. Copper Nanoparticles Embedded in Metal-Organic Framework MIL-101(Cr) as a High Performance Catalyst for Reduction of Aromatic Nitro Compounds. *Inorg. Chem. Commun.* **2013**, *32*, 5–8.

(204) Sabo, M.; Henschel, A.; Fröde, H.; Klemm, E.; Kaskel, S. Solution Infiltration of Palladium into MOF-5: Synthesis, Physisorption and Catalytic Properties. *J. Mater. Chem.* **2007**, *17* (36), 3827–3832.

(205) Ishida, T.; Nagaoka, M.; Akita, T.; Haruta, M. Deposition of Gold Clusters on Porous Coordination Polymers by Solid Grinding and Their Catalytic Activity in Aerobic Oxidation of Alcohols. *Chem. - A Eur. J.* **2008**, *14* (28), 8456–8460.

(206) Wu, T.; Zhang, P.; Ma, J.; Fan, H.; Wang, W.; Jiang, T.; Han, B. Catalytic Activity of

Immobilized Ru Nanoparticles in a Porous Metal-Organic Framework Using Supercritical Fluid. *Chinese J. Catal.* **2013**, *34* (1), 167–175.

(207) Zhao, M.; Deng, K.; He, L.; Liu, Y.; Li, G.; Zhao, H.; Tang, Z. Core-Shell Palladium Nanoparticle@metal-Organic Frameworks as Multifunctional Catalysts for Cascade Reactions. *J. Am. Chem. Soc.* **2014**, *136* (5), 1738–1741.

(208) Dissegna, S.; Epp, K.; Heinz, W. R.; Kieslich, G.; Fischer, R. A. Defective Metal-Organic Frameworks. *Adv. Mater.* **2018**, *1704501*, 1–23.

(209) Fang, Z.; Bueken, B.; De Vos, D. E.; Fischer, R. a. Defect-Engineered Metal-Organic Frameworks. *Angew. Chem Int. Ed.* **2015**, *54* (25), 7234–7254.

(210) Herm, Z. R.; Bloch, E. D.; Long, J. R. Hydrocarbon Separations in Metal−Organic Frameworks. *Chem. Mater.* **2014**, *26* (1), 323–338.

(211) Burrows, A. D. Mixed-Component Metal–Organic Frameworks (MC-MOFs): Enhancing Functionality through Solid Solution Formation and Surface Modifications. *CrystEngComm* **2011**, *13* (11), 3623.

(212) Cairns, A. B.; Goodwin, A. L. Structural Disorder in Molecular Framework Materials. *Chem Soc Rev* **2013**, No. 42, 4881–4893.

(213) Fang, Z.; Ju, Q. Role of Defects in Catalysis. *Met. Fram.* **2018**, 341–378.

(214) Choi, J. S.; Son, W. J.; Kim, J.; Ahn, W. S. Metal-Organic Framework MOF-5 Prepared by Microwave Heating: Factors to Be Considered. *Microporous Mesoporous Mater.* **2008**, *116* (1–3), 727–731.

(215) Wu, H.; Chua, Y. S.; Krungleviciute, V.; Tyagi, M.; Chen, P.; Yildirim, T.; Zhou, W. Unusual and Highly Tunable Missing-Linker Defects in Zirconium Metal-Organic Framework UiO-66 and Their Important Effects on Gas Adsorption. *J. Am. Chem. Soc.* **2013**, *135* (28), 10525–10532.

(216) Shöâeè, M.; Agger, J. R.; Anderson, M. W.; Attfield, M. P. Crystal Form, Defects and Growth of the Metal Organic Framework HKUST-1 Revealed by Atomic Force Microscopy. *CrystEngComm* **2008**, *10* (6), 646.

(217) Dumrul, S.; Bazzana, S.; Warzywoda, J.; Biederman, R. R.; Sacco, A. Imaging of Crystal Growth-Induced Fine Surface Features in Zeolite A by Atomic Force Microscopy. *Microporous Mesoporous Mater.* **2002**, *54* (1–2), 79–88.

(218) Shoaee, M.; Anderson, M. W.; Attfield, M. P. Crystal Growth of the Nanoporous Metal-Organic Framework HKUST-1 Revealed by in Situ Atomic Force Microscopy. *Angew. Chemie - Int. Ed.* **2008**, *47* (44), 8525–8528.

(219) Cubillas, P.; Anderson, M. W.; Attfield, M. P. Crystal Growth Mechanisms and Morphological Control of the Prototypical Metal-Organic Framework MOF-5 Revealed by Atomic Force Microscopy. *Chem. - A Eur. J.* **2012**, *18* (48), 15406–15415.

(220) Bordiga, S.; Regli, L.; Bonino, F.; Groppo, E.; Lamberti, C.; Xiao, B.; Wheatley, P. S.; Morris, R. E.; Zecchina, A. Adsorption Properties of HKUST-1 toward Hydrogen and Other Small Molecules Monitored by IR. *Phys. Chem. Chem. Phys.* **2007**, *9* (21), 2676–2685.

(221) St. Petkov, P.; Vayssilov, G. N.; Liu, J.; Shekhah, O.; Wang, Y.; Wöll, C.; Heine, T. Defects in MOFs: A Thorough Characterization. *ChemPhysChem* **2012**, *13* (8), 2025–2029.

(222) Valenzano, L.; Civalleri, B.; Chavan, S.; Bordiga, S.; Nilsen, M. H.; Jakobsen, S.; Lillerud, K. P.; Lamberti, C. Disclosing the Complex Structure of UiO-66 Metal Organic Framework: A Synergic Combination of Experiment and Theory. *Chem. Mater.* **2011**, *23* (7), 1700–1718.

(223) Vermoortele, F.; Bueken, B.; Le Bars, G.; Van De Voorde, B.; Vandichel, M.; Houthoofd, K.; Vimont, A.; Daturi, M.; Waroquier, M.; Van Speybroeck, V.; et al. Synthesis Modulation as a Tool to Increase the Catalytic Activity of Metal-Organic Frameworks: The Unique Case of UiO-66(Zr). *J. Am. Chem. Soc.* **2013**, *135* (31), 11465–11468.

(224) Cliffe, M. J.; Wan, W.; Zou, X.; Chater, P. A.; Kleppe, A. K.; Tucker, M. G.; Wilhelm, H.; Funnell, N. P.; Coudert, F.-X.; Goodwin, A. L. Correlated Defect Nanoregions in a Metal–Organic Framework. *Nat. Commun.* **2014**, *5* (1), 4176.

(225) Bennett, T. D.; Todorova, T. K.; Baxter, E. F.; Reid, D. G.; Gervais, C.; Bueken, B.; Van De Voorde, B.; De Vos, D.; Keen, D. A.; Mellot-Draznieks, C. Connecting Defects and Amorphization in UiO-66 and MIL-140 Metal-Organic Frameworks: A Combined Experimental and Computational Study. *Phys. Chem. Chem. Phys.* **2016**, *18* (3), 2192–2201.

(226) Vermoortele, F.; Ameloot, R.; Alaerts, L.; Matthessen, R.; Carlier, B.; Fernandez, E. V. R.; Gascon, J.; Kapteijn, F.; De Vos, D. E. Tuning the Catalytic Performance of Metal-Organic Frameworks in Fine Chemistry by Active Site Engineering. *J. Mater. Chem.* **2012**, *22* (20), 10313–10321.

(227) Karagiaridi, O.; Lalonde, M. B.; Bury, W.; Sarjeant, A. A.; Farha, O. K.; Hupp, J. T. Opening ZIF-8: A Catalytically Active Zeolitic Imidazolate Framework of Sodalite Topology with Unsubstituted Linkers. *J. Am. Chem. Soc.* **2012**, *134* (45), 18790–18796.

(228) Deria, P.; Mondloch, J. E.; Tylianakis, E.; Ghosh, P.; Bury, W.; Snurr, R. Q.; Hupp, J. T.; Farha, O. K. Perfluoroalkane Functionalization of NU-1000 via Solvent-Assisted Ligand Incorporation: Synthesis and CO2adsorption Studies. *J. Am. Chem. Soc.* **2013**, *135* (45), 16801–16804.

(229) Shearer, G. C.; Chavan, S.; Ethiraj, J.; Vitillo, J. G.; Svelle, S.; Olsbye, U.; Lamberti, C.; Bordiga, S.; Lillerud, K. P. Tuned to Perfection: Ironing out the Defects in Metal-Organic Framework UiO-66. *Chem. Mater.* **2014**, *26* (14), 4068–4071.

(230) Gadipelli, S.; Guo, Z. Postsynthesis Annealing of MOF-5 Remarkably Enhances the Framework Structural Stability and CO2 Uptake. *Chem. Mater.* **2014**, *26* (22), 6333–6338.

(231) Liu, Y.; Klet, R. C.; Hupp, J. T.; Farha, O. Probing the Correlations between the Defects in Metal-Organic Frameworks and Their Catalytic Activity by an Epoxide Ring-Opening Reaction. *Chem. Commun.* **2016**, *52* (50), 7806–7809.

(232) Dissegna, S.; Hardian, R.; Epp, K.; Kieslich, G.; Coulet, M. V.; Llewellyn, P.; Fischer, R. A. Using Water Adsorption Measurements to Access the Chemistry of Defects in the Metal-Organic Framework UiO-66. *CrystEngComm* **2017**, *19* (29), 4137–4141.

Chapter 2

Characterization techniques

2.1. X-ray Diffraction (XRD)

X-ray diffraction (XRD) is one the most frequently applied techniques for solid catalysts characterization. This non-destructive technique can be used to identify crystallographic structure (e.g. lattice and cell parameters), chemical composition, crystallite size and preferred orientation.

Braggs geometry

The phenomenon of diffraction is described by the Bragg's Law which relates the angle of incident radiation (ϴ) with the interplanar distance (d) presented in Equation 1:

$$2d_{hkl}sin\theta = n\lambda \qquad (1)$$

Where:

n is a positive integer,

λ is the wavelength of the incident wave

d is interplanar distance of Miller indices of the crystallographic planes

Structural and unit cell determination form Powder XRD data using Le Bail method

Diffraction pattern contains important information about the structure of crystalline materials. By analysing positions of diffraction maxima, which strongly depends on the periodicity of the crystalline network, we can determine dimensions of the unit cell. Meanwhile relative intensities of diffraction maxima, which depends on the distribution of scattering matter, provides information of atoms or molecules in the unit cell. Using this information, the first step for proper determination of crystal structure is to attribute (to index) individual Miller indices (*h*,*l*,*k*) to every peak observed in XRD pattern in order to obtain cell parameters of measured crystal. This data serve as an input for further procedure. In the second step peaks intensities are fitted to the parameters and atomic structure is defined. In general, the intensities of powder diffraction data are more complex due to overlapping diffraction peaks with similar d-spacings. For this purpose different WPPD[1] (Whole Powder Pattern Decomposition) like *Pawley*[2] or *Le Bail*[3] methods can be used. *Le Bail* method use diffraction peak intensities (I_{hkl}) as starting data, and by its decomposition and subsequent refinement of profile parameters, gives the best match to measured diffraction pattern. All process is based on the Rietveld decomposition formula[4] (Equation 2):

$$I_K(obs) = \sum_j \{w_{j,K} \cdot S_K^2(calc) \cdot y_i(obs)/y_j(calc)\} \qquad (2)$$

$I_K(obs)$ is a integrated intensity,

$w_{j,K}$ is a measure of the contribution of the Bragg peak at position $2\theta_K$,

y_j is a diffraction profile at position $2\theta_j$,

S_K^2 is a squared calculated $|S|$ for reflection K

Le Bail is a quick method to refine the unit cell, provides very accurate estimation of the allowed peak intensities for different symmetries of crystal. Moreover, can be useful in finding phase transition in high pressure and temperature experiments.

Specific details on X-ray diffraction characterization of the materials used in each chapter of the thesis are given below.

Chapter 3 and 4

Powder XRD characterization. Powder M-BTC materials synthetized by water solution were characterized by X-ray powder diffraction (XRPD) using a Bruker AXS D8 Advance diffractometer equipped with a primary Ge (111) Johansson monochromator (selecting Cu Kα1 radiation) and a mono-dimensional detector Lynxeye. In the case of Co-BTC, in order to reduce low signal to noise ratio induced by Co fluorescence, the electronic windows for photon acceptance has been reduced and counting time increased to obtain comparable patterns to the others materials.

Single crystal XRD characterization. Data collections were performed at low temperature (T = 100(2) K) using an APEXII Bruker-AXS diffractometer and Mo-Kα radiation (λ = 0.71073 Å). Several single crystals were tested in order to check their quality and that there was no allotropic phase. Each time, they were mounted on a cryoloop with the help of Paraton grease.

Chapter 5

PXRD qualitative analyses were carried out with a vertical-scan Bruker AXS D8 Advance θ:θ diffractometer equipped with a Lynxeye linear position-sensitive detector, an X-ray tube (CuKα, λ = 1.5418 Å), a filter of nickel in the diffracted beam, and the following optical components: primary beam Soller slits (2.5°), fixed divergence slit (0.5°), antiscatter slit (8 mm). The generator was set at 40 kV and 40 mA. PXRD data were acquired at room temperature in the 5.0–105.0° 2θ range, with steps of 0.02° and time per step of 10 s, and treated by means of whole powder pattern refinements, as implemented in TOPAS-Academic V6.

Chapter 6

Powder materials analysis were performed on PANalytical Cubix fast diffractometer, using CuKα1 radiation (λ= 1,5406Å) and an X'Celerator detector with Bragg-Brentano geometry. XRD patterns recorded in the 2θ range from 2 to 60 were analyzed using X'pert Highscore Plus software.

2.2. Thermogravimetric Analysis (TGA)

TGA technique is commonly used to study stability of the material, where desolvation or dehydration, decomposition, etc. can be distinguished. During the analysis mass changes of the sample are registered as a function of temperature by TG device. The TG is combined with differential thermal analysis (DTA), which records exothermic or endothermic events during the sample transformation compared with an inert reference material.

Thermogravimetric analyses (TGA) and differential scanning calorimetry (DSC) for the samples described in **Chapter 5** were carried out simultaneously using a NETZSCH STA 409 PC instrument on **Co(BPZNH$_2$)·DMF** and the activated counterpart. In the first case, ~10 mg of as-synthesised **Co(BPZNH$_2$)·DMF** were placed in an oven at 323 K for 24 hours; then, they were transferred in an alumina crucible dedicated to the thermogravimetric analysis. In the second case ~10 mg of as-synthesised **Co(BPZNH$_2$)·DMF** were activated at 413 K under vacuum (10^{-3} bar) for 24 h; then, they were transferred in an alumina crucible. The temperature was raised from 303 to 1173 K or 1073 K with a rate of 10 K min^{-1} under a flow of N_2 (40 mL min^{-1}). The raw data obtained were corrected based on a background curve

TGA for the samples presented in the rest of chapters of this thesis was performed using a Mettler Toledo TGA/SDATA851e thermos-balance under air in the range form 303 – 873 K with heating and cooling rates of 10 K/min.

2.3. Nuclear Magnetic Resonance (NMR)

Nuclear Magnetic Resonance spectroscopy is a very powerful analytical tool used for identification and analysis of organic compounds. The principle of this method is based on splitting of energy levels of a nucleus with spin different from zero by interaction of nuclear magnetic moments with a constant and uniform external magnetic field. This technique allows to identify the chemical environment of the atoms in prepared sample, by the variation of resonance frequency of the nucleus (chemical shift). Due to the shielding by surrounding electrons, chemical shift is characteristic feature of the chemical environment of the nucleus.

In this work NMR technique was used to determine the content of each organic ligand present in mixed-ligand MOFs (**Chapter 3** and **Chapter 6**). For this purpose, liquid phase ^{1}H-NMR spectra of the digested activated MOFs (473K for 4h) were measured and analysed on a Bruker Avance spectrometer of 300 MHz frequency using TMS as internal standards and normalizing the signals to the DMSO-d_6 signal. The samples were digested in 0.5 ml DMSO-d_6 and 0.1 ml D_2SO_4 (99%) in a NMR tube.

2.4. N_2 Adsorption-Desorption Experiment

N_2 adsorption-desorption method can be used to analyse the porosity of materials. The textural properties of the solid catalyst, such as specific surface area, pore volume, and pore size distribution, are determined using adsorption isotherm measurements. The different kinds of adsorption isotherms (type I to VI) have been classified by IUPAC according to the appearance of the isotherm[5].

A BET method was developed by Brunauer, Emmett, and Teller in 1938 and is commonly employed to calculate the specific surface area of a porous solid. The area value is usually determined from the physisorption nitrogen isotherms data collected at 77 K. Five assumptions have to be followed for proper BET area development:

1) The sample surface is homogeneous,
2) Uppermost layer is in equilibrium with vapour phase,
3) The heat of adsorption at all sites is constant and equal to the heat of condensation from the second layer on,
4) There are no lateral interactions between molecules,
5) At saturation pressure, the number of layers has infinite thickness

$$\frac{p}{n^a(p_0-p)} = \frac{1}{n_m^a C} + \frac{(C-1)p}{n_m^a p_0} \qquad (3)$$

Where,

n^a is the amount adsorbed

p is the pressure

p_0 is the saturation pressure of adsorbed gas at given temperature

n_m^a is monolayer capacity

C is related to the energetics of adsorption

Based on the obtained nitrogen isotherms, the left side of Equation 3 was plotted against relative pressure. In order to calculate the BET specific surface area from a BET plot, a linear region was selected from the plot so C and n_m^a could be extracted from linear regression after fulfilling four consistency criteria recommended by Rouquerol[6,7]:

1) Selected range of the pressure should monotonically increase with $n^a(1-\frac{p}{p_0})$ as a function of $\frac{p}{p_0}$
2) The parameter C resulting from the linear regression should be greater than zero
3) The monolayer loading n_m^a should correspond to a relative pressure $\frac{p}{p_0}$ within the selected linear range
4) The relative pressure corresponding to the calculated value for the monolayer formation $(1/(\sqrt{C}+1)$ should be equal to the pressure determined in criterion 3 (although a tolerance of 20% is acceptable)

Having those 4 criteria fulfilled specific surface area can be calculated from the following equation:

$$S_{BET} = \frac{n_m^a N_A a_m}{m}$$

N_A is the Avogadro constant

a_m is molecular cross-section area occupied by a single adsorbate molecule in the complete monolayer

m is a mass of adsorbent

Barrett-Joyner-Halenda (BJH) method is used for calculation of mesopore distribution form nitrogen adsorption data, which may be summarized in the formula:

$$v_{ads}(x_k) = \sum_{i-1}^{k} \Delta V_i\big(r_i \leq r_c(x_k)\big) + \sum_{i=k+1}^{n} \Delta S_i t_i(r_i > r_c(x_k))$$

Where,

$v_{ads}(x_k)$ is the volume of adsorbate (cm^3/g) at relative pressure x_k (calculated from the value of adsorption expressed in cm^3/g STP by $v_{ads}(x)$= 0.0015468 a(x)),

V_i is pore volume (cm^3/g)

S_i is a surface area (m^2/g)

t_i is a thickness of adsorbed layer

N_2 adsorption-desorption isotherms were collected on Micrometrics Gemini V gas adsorption analyser at 77 K, after degassing the sample at 393 K overnight in a Micrometrics Flow prep 060 system with nitrogen flux gas. The specific surface area (S_{BET}) was obtained using the BET method (*p/p₀* 0.01 to 0.1 range) after fulfilling Rouquerol criteria. The specific external surface area (S_{ext}) and the micropore volume (V_{micro}) were determined using *t*-plot analysis.

2.5. Scanning Electron Microscopy + EDX

Scanning electron microscopy allows for high resolution imaging of surface by using high-energy electrons (1.5-20 KeV) generated by a heated tungsten filament. An incident beam of electrons caused a secondary emission across the sample surface, which is collected to form an image of the surface. It is possible to obtain diverse constant images, i.e., backscattered electrons (BSE), auger electrons (AES) and energy dispersive x-ray spectroscopy (EDX). BSE causes different contrast subjected to the atomic number, Z, of the elements, so this technique can be used to characterize the elemental composition of the volume analysed. EDX is performed in conjunction with a SEM, but uses the X-rays that are emitted from the sample due to the electron beam. The combination of SEM with EDX allows the analysis of the sample morphology and the composition of the different phases that are present.

Morphology and element mapping of the single crystal samples, were analysed with a Field Emission Scanning Electron Microscope (FESEM) model JEOL 7001F, equipped with a spectrometer of energy dispersion of X-ray (EDX) form Oxford Instruments.

2.6. Gas Chromatography (GC)

Gas Chromatography (GC)

Gas Chromatography (GC) is an analytical technique that measures the content of different organic components in gas or liquid samples. The sample solution is injected into a column, where the products are separated and transfer to the detector by a carrier gas (pure and inert with the sample). The separation of the products is influenced by solubility in the gas phase of each compound, temperature of the column and affinity of each solute to the stationary phase. As a consequence, components with different chemical and physical properties will be detected in a different time called retention time (RT).

Taking into account that the ionization detectors give a signal proportional to the mass product analysed trough the chromatographic area, the use of corrected areas using response factors of each analyte, allows the concentration calculation of each component in the mixture.

$$n_i = \frac{A_i \cdot n_{Si}}{A_{Si} \cdot R_i}$$

Where, n_i is the mols of the i compound

A_i is the chromatographic area of the i compound

n_{Si} is the mols of the internal standard

A_{Si} is the chromatographic area of the internal standard

R_i is the response factor of the i compound

Having calculated the number of initial mols of your reagent ($n_{r,0}$) and the mols of this substrate at a determined time t ($n_{r,0}$), the conversion at certain time can be determined by following equation :

$$Conv_t(\%) = \frac{n_{r,0} - n_{r,t}}{n_{r,0}} \cdot 100$$

$Yield_{i,t}$ and selectivity $Selec_{i,t}$for a determined time is defined as:

$$Yield_{i,t}(\%) = \frac{n_{sit}}{n_{r,0}} \cdot 100$$

$$Selec_{i,t}(\%) = \frac{n_{sit}}{n_{r,0} - n_{r,t}} \cdot 100$$

Where n_{sit} is the number of moles a compound in a time t

GC analysis were carried out in an Agilent 7890A equipped with a Flame Ionization Detector (FID) and with a Biodiesel column with stationary phase made of 5% alternated phenylsilicone.

2.7. Inductively Coupled Plasma Optical Emission Spectroscopy (ICP-OES)

ICP-OES is technique used for detection of chemical elements. Inductively coupled plasma is used to produce excited atoms and ions that emit electromagnetic radiation at wavelengths characteristic of a particular element allowing the identification of atoms and their quantification.

The metal content and ratio of the synthesized MOF catalysts were confirmed and determined by ICP-OES on Varian 715-ES. The powder samples (30 mg) were placed in a 50 mL volumetric flask. Mixture of H_2O:H_2SO_4 (1:1) 4 mL was added primary to dissolve the MOFs and consequently, flask was filled to 50 mL with MiliQ water. Calibration curve was adjusted to the expected analyte concentration using standard solutions.

2.8. Elemental Analysis

Elemental analysis serves for determination of the total content of carbon, hydrogen, nitrogen and sulphur present in either solid or liquid samples through burning them in pure oxygen at high temperature (1297 K).

Chapter 3 and 6

The Elemental Analysis of the different catalyst was performed in EuroEA Elemental Analyzer (Eurovector) to determine the carbon content, using as reference sulphanilamide.

Chapter 5

Elemental analyses (C, H, N) were performed with a Fisons Instruments 1108 CHNS-O elemental analyser

2.9. Fourier Transform Infrared Spectroscopy (FTIR)

Infrared spectroscopy technique provides information about the structure, the surface and the acid.basic properties of solid materials through absorption of IR radiation (λ=750 – 10^5 nm). Thanks to energy transitions in certain vibrational levels of chemical bounds a FTIR spectrum shows specific bands, characteristic vibrations of tension or reflexion. Each group of atoms, are characterized by the intensity and frequency range in which are produced. FTIR technique combined with the use of probe molecules provides information about e.g. the acidity, the basicity and the nature of chemical elements present in the catalyst surface.

Chapter 3 and 6

The Fourier Transform Infrared (FTIR) spectra were recorded on Jasco FT/IR-6200 model spectrometer.

Chapter 5

Spectra were recorded as neat from 4000 to 600 cm^{-1} with a PerkinElmer Spectrum One System instrument

2.10. Heat of Immersion

The enthalpy of wetting or enthalpy of immersion, ΔH_{imm} (when referred to unit of mass of the solid) is defined as the difference (at constant temperature) between the enthalpy of a solid completely immersed in a wetting liquid, and that of the solid and liquid taken separately. It must be specified whether the solid in the initial state is in contact with vacuum or with the vapour of the liquid at a given partial pressure. Measurements of the enthalpy of wetting of a solid equilibrated with varying relative pressures of the vapour of a pure wetting liquid may be used to derive the differential enthalpy of adsorption of the vapour.

Heat of immersion experiment. The accurate mass of sample was placed in a glass bulb with a brittle end, and out-gassed under high vacuum for 24 h at 333 K. Then, the bulb was sealed and transfer to calorimeter (Setaram Calvet-type C80), equipped with mixing cell containing 4,00 g of wetting liquid (CM or CHP), and carefully closed by o-ring seal. The whole system was located into the calorimeter block and left for temperature equilibration (303 K) between the sample setup and the calorimeter. Once the thermal equilibrium has been achieved, the cell rod was gently pressed to break the brittle end of the bulb with the bottom of the calorimeter cell. The wetting liquid enters into the sample, and the heat is released. The evolution of the heat was monitored as a function of time. Integration of this signal gives the total experimental heat of immersion, which has to be corrected by terms such as energy of the bulb breaking (exothermic), and the heat of vaporization of the immersion liquid to fill the empty volume of the bulb with the vapour at the corresponding vapour pressure (endothermic). These corrections were made by measuring empty (reference) cells under the same conditions.

2.11. References

(1) Le Bail, A. Whole Powder Pattern Decomposition Methods and Applications: A Retrospection. *Powder Diffr.* **2005**, *20* (04), 316–326.

(2) Pawley, G. S. Unit-Cell Refinement from Powder Diffraction Scans. *J. Appl. Crystallogr.* **1981**, *14* (6), 357–361.

(3) Le Bail, A.; Duroy, H.; Fourquet, J. L. Ab-Initio Structure Determination of LiSbWO6 by X-Ray Powder Diffraction. *Mater. Res. Bull.* **1988**, *23* (3), 447–452.

(4) Rietveld, H. M. A Profile Refinement Method for Nuclear and Magnetic Structures. *J. Appl. Crystallogr.* **1969**, *2* (2), 65–71.

(5) Thommes, M.; Kaneko, K.; Neimark, A. V.; Olivier, J. P.; Rodriguez-Reinoso, F.; Rouquerol, J.; Sing, K. S. W. Physisorption of Gases, with Special Reference to the Evaluation of Surface Area and Pore Size Distribution (IUPAC Technical Report). *Pure Appl. Chem.* **2015**, *87* (9–10), 1051–1069.

(6) J. Rouquerol, F. Rouquerol, P. Llewellyn, G. Maurin, K. S. W. S. *Adsorption by Powders and Porous Solids: Principles, Methodology and Application*; Academic Press, 2013.

(7) Gómez-Gualdrón, D. A.; Moghadam, P. Z.; Hupp, J. T.; Farha, O. K.; Snurr, R. Q. Application of Consistency Criteria to Calculate BET Areas of Micro- and Mesoporous Metal-Organic Frameworks. *J. Am. Chem. Soc.* **2016**, *138* (1), 215–224.

Chapter 3

Facile “green” aqueous synthesis of MIX-MOFs

3.1. Introduction

Synthesis procedure is one of the main drawback for the industrial applications of MOFs. Thus, in order to make MOFs more attractive for industrial applications in general, alternative synthesis procedures need to be developed. Indeed, most MOF compounds are usually prepared in DMF[1–3] or other organic solvents[4,5], which can be toxic and/or dangerous to handle, and many of them require the use of non-commercial and/or expensive organic ligands, which introduce additional synthesis steps and rise up the final price of the catalyst, thus hampering the large-scale synthesis of these MOFs. It is thus evident that new, greener and easily scalable synthetic procedures of "cheap" MOFs are required to facilitate their transfer to the industrial scale production.

H. Reinsch[6] draw attention to green synthesis procedure requirements like: reduction of amounts of solvent and replacement them by a "greener" solvent, high-yield synthesis and by-product elimination, use of non-hazardous and renewable feed stocks, avoid if possible use of auxiliary substances, lower the energy consumption, by use of room temperature synthesis or employing alternative energy application like ultrasound or mechano-chemistry and synthesis of high stability materials to avoid leaching of toxic and hazardous building units out of the system.

Acknowledging above mentioned requirements, developed new water based synthesis of common MOFs are very important from environmental and economical point of view, as generated products do not require solvent exchange prior to activation in order to permit gas adsorption and storage[7].

Conventionally in MOFs synthesis, organic linkers are used in their protonated form (carboxylic acids or imidazoles), which can lead to production of mineral acid by-products like HNO_3, HCl or H_2SO_4 (depending on the metal anion source), upon solvothermal reaction conditions. Thus, recently use of linkers in the anionic form, as slats has been explored[8]. This method is a promising way to obtain industrially competitive materials due to associated energetic and environmental benefits as the reaction can be completed in few hours or even minutes at room temperature. Syntheis of MIL-53(Al),

NH_2-MIL-52(Al) and NO_2-MIL-52(Al)[9], was reported using organic linker salt approach. Moreover, compared with conventional method (Figure 3.1) obtained materials were nanocrystalline, have notable ordered inter-crystalline mesoporosity and contained a reduced or even a negligible amount of unreacted linker within the pores. This method was also extended for the preparation of MOF-74 and MOF-5.

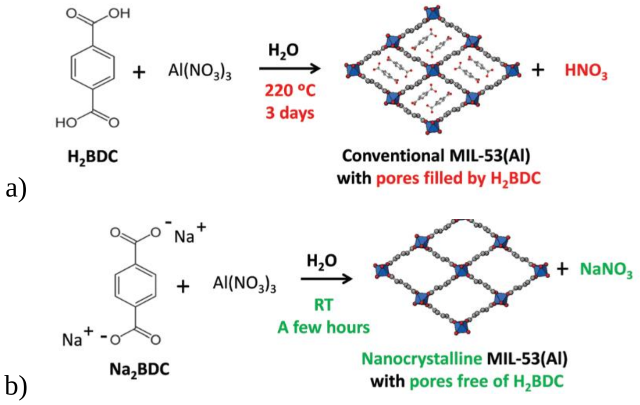

Figure 3.1 General schemes of a) conventional and b) room temperature conditions for MIL-53(Al) synthesis Reprinted from *Green Chem.* 2015, *17* (3), 1500–1509 with permission from the The Royal Society of Chemistry

Another interesting contribution towards sustainable sourcing of MOF linkers is the synthesis of a terephthalate MOFs with the linker sourced from poly(ethylene)terephthalate (PET) plastic bottle waste. This approach was used for the synthesis of MIL-53(Al)[10] MIL-47 and MIL-53(Cr, Al, Ga)[11]. Moreover, Ren and co-workers, demonstrated one-pot conversion of waste PET bottles to Cr-MOF materials with slightly improved textural properties, compared to those obtained from commercial BDC[12], promising MOF materials for hydrogen storage applications.

Recently, interesting progress has been done on solvent-free[13–15] and liquid-assisted mechanochemical MOF synthesis[16–18], as well as continuous flow synthesis at the gram and multigram scale[19], which represent significant steps in the future of "green" and industrial friendly synthesis of MOFs in a more sustainable way.

Many synthesis approaches offered for MOFs, can be extended for production of isoreticular compounds having the same topology and pore architecture but containing different ligands[20,21] and/or metals[22] ions in the structure called also solid solutions. For instance, replacing one metal ion by another in the inorganic building units provides a way to fine tune the chemical properties of these compounds, such as acid-base[23] and redox properties[24]. Additionally, bimetallic MOFs can also be prepared, either by direct synthesis or through post-synthesis modification, in which the second metal type can either modulate the properties of the other metal ions in the MOF, or it can introduce totally new functionalities not present in the pristine compound (for more detail description see Chapter 1). It is even possible to combine in just one compound different activities arising from the individual metal ions or functionalized linkers, so that multifunctional MOFs can readily be prepared to be used in multi-step one pot transformations.

Following the aforementioned indications, in the present work we have applied a "green" aqueous synthesis procedure to prepare a series of trimesate MOFs in high yields, at room temperature, ambient pressure and very short time (10 minutes). Herein, we will show that the method can be used to prepare various monometallic divalent compounds, as well as bimetallic and biligand compounds of different compositions. In the latter case, we will demonstrate that true solid solutions are formed, in which both metal ions distribute homogeneously throughout the whole crystal.

3.2. Results and discussion

3.2.1. General synthesis approach

The generic synthesis method used in this work is schematically shown in Figure 3.2. Briefly, an aqueous solution of sodium ligand salt (Na_3BTC in majority of the cases) was poured onto a suitable divalent metal salt solid precursor at room temperature under vigorous stirring. The amounts of ligand salt solution and metal precursor used were adjusted to have an optimal molar ratio, corresponding to the stoichiometric formula of expected compound. Optionally, a small volume of ethanol can also be added to the above mixture, which was shown to accelerate the precipitation of the MOF and to increase the final yield obtained, which is typically higher than 90% in all cases. Stirring of the mixture was continued for 10 minutes, and the solid obtained was separated by centrifugation and carefully washed with distilled water (three times) and ethanol (once). Finally, the powder so obtained was air-dried overnight at room temperature.

Figure 3.2 Aqueous synthesis of MOFs is carried out at room temperature and atmospheric pressure within 10 minutes

As it can be observed, the above method has a series of advantages that improve the green credentials, sustainability and industrial feasibility of the MOF preparation:

synthesis from non-toxic water solutions, room temperature and atmosphere pressure, very short synthesis time (~ 10 min.), high yield (>90%), easy separation and washing protocols, easily scalable method, and the use of a cheap and commercially available ligand precursors like H_3BTC (trimesic acid), H_2IP (isophthalic acid) or H_2NH_2IP (5-aminoisophthalic acid) presented in this *Chapter*. Also, the method tolerates a variety of metal salt precursors without producing appreciable changes in crystallinity of the final product, including nitrates, chlorides or sulfates, which are usually the preferred option for industry to minimize safety and corrosion issues[25].

3.2.2. Monometallic compounds

Various monometallic compounds were prepared following the method described above, and the solids were first characterized by powder diffraction (PXRD). MOFs containing Co^{2+}, Ni^{2+}, Cu^{2+} or Zn^{2+} were all found to be crystalline and isoreticular. In contrast, all our attempts to obtain an isoreticular Mn^{2+} compound were unsuccessful. The material obtained presented a clearly lower crystallinity and a different structure (see Figure A.3.1 in Annex A.3). Hereafter, we will refer to these metal trimesate compounds as M-BTC, where M indicates the metal used in each case, though a more representative formula should be $[\{\mu\text{-}M(H_2O)_4\}_2(BTC)\{M(H_2O)_4\}BTC]$.

By comparing the XRD peak positions of the M-BTC materials with the existing MOF collected in the Cambridge Structure Database[26], the solids prepared with the above method were found to correspond to a family of metal trimesate compounds of general formula $M_3BTC_2\cdot 12H_2O$, first synthetized by Yaghi and co-workers using a conventional solvothermal method[27]. This structural assignment was confirmed by Rietveld refinement of the synthetized M-BTC compounds, as shown in Figure 3.3.

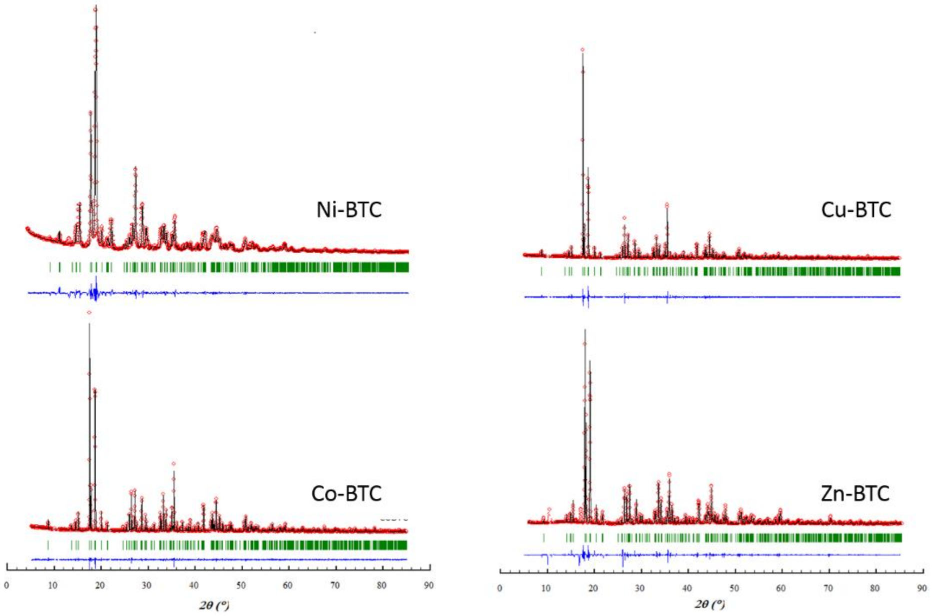

Figure 3.3 Rietveld refinement of XRD patterns: Observed (red dots), refined (black solid lines), and their difference (blue bottom line). Green vertical bars indicate the X-ray reflection positions

Thermogravimetric curves of the M-BTC compounds (see Figure A.3.2 in Annex A.3) typically showed two main steps at about 398-423 K and 693-753 K, corresponding to coordinated water and decomposition of the organic ligand, respectively. The observed weight losses were in agreement with the stoichiometry expected for a $M_3BTC_2{\cdot}12H_2O$ compound (see Table A.3.1 in Annex A.3). In all cases, this stoichiometry was also in agreement with the corresponding ICP and elemental analysis (see Table A.3.2 in Annex A.3).

$M_3BTC_2{\cdot}12H_2O$ compounds crystallize in the monoclinic *C*2 (5) space group with a layered structure whose cell metrics depends on the nature of the metal atom (see Table 3.1). The structure features infinite zigzag chains aligned along [101] direction that are formed by the alternation of BTC with M atoms. The repeating unit (black rectangle in Figure 3.4 a) contains two types of M atoms, hereafter denoted bridging

(Wyckoff position *4c*) and terminal (Wyckoff position *2b*), in a 2:1 ratio. Both BTC molecules in the repeating unit bind to bridging M atoms in an unidentate mode along the chain, and an additional M atom is coordinated in a bidentate fashion by one free carboxylate group on alternate BTC molecules. Individual zigzag chains stack along the *b* axis (Figure 3.4 b) to form layers in the (10-1) plane, while these layers are stacked along the *c* axis with an ABA arrangement (Figure 3.4 c and d). Interactions between chains are dominated by hydrogen bonds between water molecules of bridging and terminal M atoms, while interlayer interactions consist of hydrogen bonds between the carboxylate oxygens and the water molecule coordinated to both type of M atoms (see Figure A.3.3 in Annex A.3).

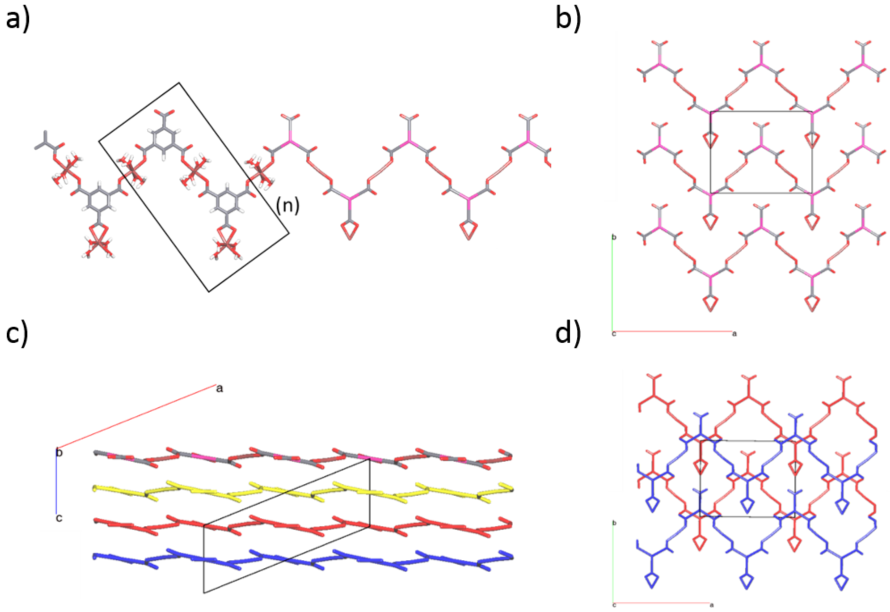

Figure 3.4 a) $M_3BTC_2 \cdot 12H_2O$ zigzag chains. The black rectangle single out the repeating unit. b) Single $M_3BTC_2 \cdot 12H_2O$ layer representation along (001) direction. Hydrogen atoms and water molecules have been removed for clarity. Cell borders are indicated by black lines. Layer packing representations along (001) and (010) directions are shown in parts c) and d) respectively. Chain are colored depending from the layer in which they lay.

Table 3.1 Cell metrics obtained by Le Bail refinement for monometallic trimesate MOFs

Compound	**Co-BTC**	**Ni-BTC**	**Cu-BTC**	**Zn-BTC**
Space group	*C*2	*C*2	*C*2	*C*2
***a* (Å)**	17.467(1)	17.440(7)	17.412(2)	17.475(6)
***b* (Å)**	12.947(1)	12.867(9)	12.913(3)	12.926(5)
***c* (Å)**	6.556(6)	6.539(6)	6.5669(2)	6.582(3)
β (°)	112.230(3)	112.603(4)	111.93(2)	112.443(4)
***V* (Å^3)**	1372.53(3)	1354.91(7)	1369.63(5)	1374.30(6)
χ^2	1.62	1.35	1.45	1.78

3.2.3. Bimetallic compounds

3.2.3.1 Co-Ni bimetallic compounds

The above synthesis method was adapted to prepare different series of bimetallic compounds, including Co-Ni and Co-Zn mixtures. Thus, Co-Ni bimetallic trimesates with Co:Ni ratios in all the range of compositions were first prepared by mixing appropriate amounts of the two metal precursors with an aqueous Na_3BTC solution, as described in the Experimental Section below. Hereafter, we will refer to these materials as CoxNi-BTC, in which x represents the (nominal) molar percentage of cobalt in the solid.

Powder XRD analysis confirmed that all the Co-Ni bimetallic materials were crystalline and isoreticular, as shown in Figure 3.5.

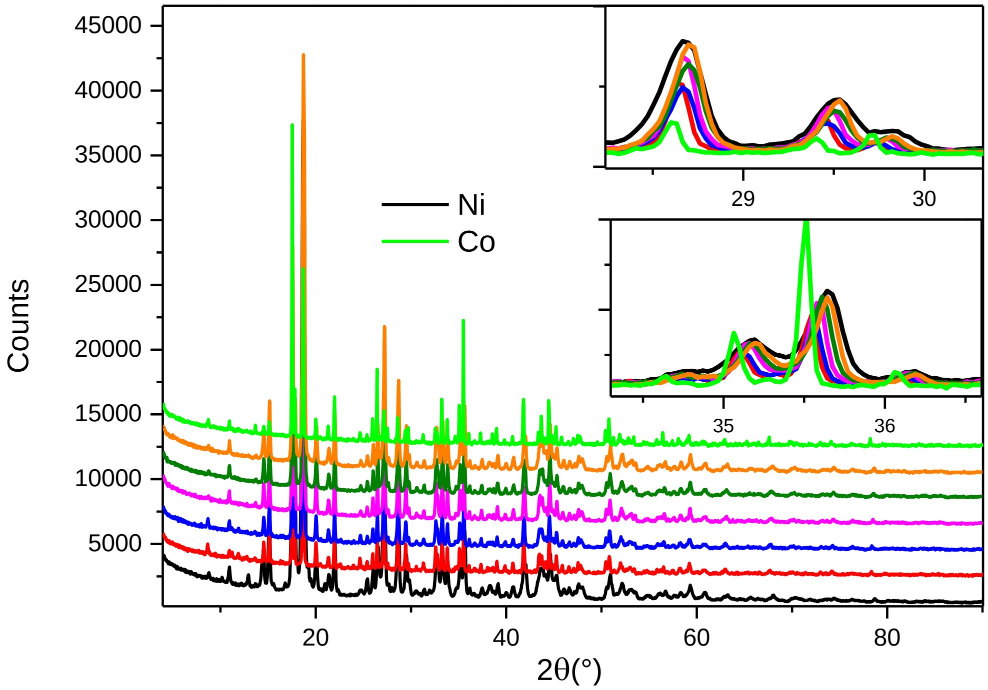

Figure 3.5 XRD diffraction patterns (Cu Kα radiation) of the CoxNi-BTC samples. The insets show expanded view of some selected peaks, in which peak discrimination is clearly observed

According to the ICP analysis (see Table A.3.2 in Annex A.3), incorporation of both metals in the final solid was found to be quantitative with respect to the initial concentration of precursors used. Accordingly, a progressive colour change of the samples with the composition was observed, passing from green (for the pure Ni-BTC) to pink (for pure Co-BTC), as shown in Figure 3.6.

Figure 3.6 Aspect of the CoxNiy-BTC samples: (from *left* to *right*) Ni-BTC, Co10Ni-BTC, Co20Ni-BTC, Co30Ni-BTC, Co50Ni-BTC, Co60Ni-BTC, Co70Ni-BTC, Co80Ni-BTC and Co-BTC

Since the pure monometallic compounds, Ni-BTC and Co-BTC, are both isoreticular with very similar cell parameters (see Table 3.1), one can expect that the isomorphous replacement of one metal by the other should be readily feasible without changing the framework structure of the MOF. However, due to the similar ionic radii and scattering factors of Ni^{2+} and Co^{2+}, it is not at all straightforward from the experimental point of view to discriminate whether a true solid solution or a simply physical mixture of the two monometallic MOFs is formed during the synthesis of the bimetallic samples. This is in general the case for the rest of bimetallic series prepared in the present work, which will be discussed later.

A first indication in favour of the formation of true solid solutions is that we did observe clear differences in the TGA curves of the bimetallic compounds and those corresponding to physical mixtures of the two pure Ni-BTC and Co-BTC, as shown in Figure 3.7.

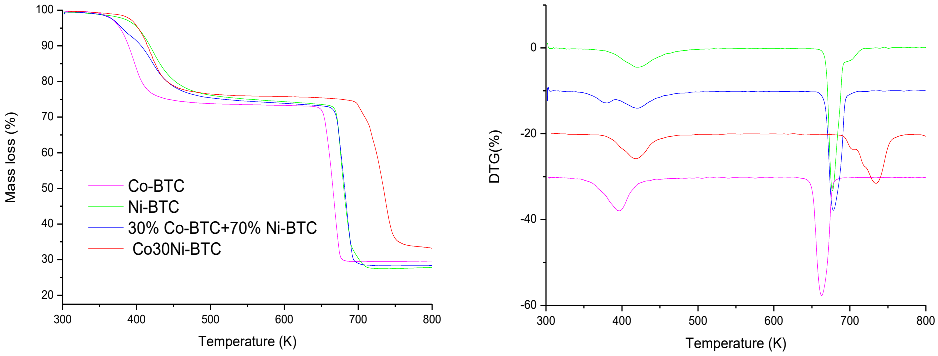

Figure 3.7 TGA (*left*) and derivative curves (*right*) of pure Co-BTC and Ni-BTC, a bimetallic Co30Ni-BTC sample, and a physical mixture of 30% Co-BTC and 70% Ni-BTC

In particular, we note that in the case of the physical mixture there are two distinct weight losses associated to water (below 473 K), corresponding to the two pure compounds, while only one water weight loss is seen in the Co30Ni-BTC solid solution. Likewise, the decomposition temperature of the solid solution and physical mixture are also clearly different, being around 70 K higher for the solid solution.

Formation of solid solution is further supported by powder XRD. Indeed, we did not observe any peak splitting or the presence of new shoulders in the XRD patterns of the CoxNi-BTC samples, as could be expected for a physical mixture of the two monometallic MOFs. Moreover, the peaks of the bimetallic compounds are narrower than those of the pure Ni-BTC material (see insets in Figure 3.5). We observed definite shifts of the signals with the composition on going from pure Co-BTC to pure Ni-BTC, which clearly speaks in favour of a solid solution and against a simple physical mixture. To address this point in more detail, we have used Le Bail methods to extract the cell parameters from the corresponding powder XRD patterns of the compounds. The results obtained are shown graphically in Figure 3.8.

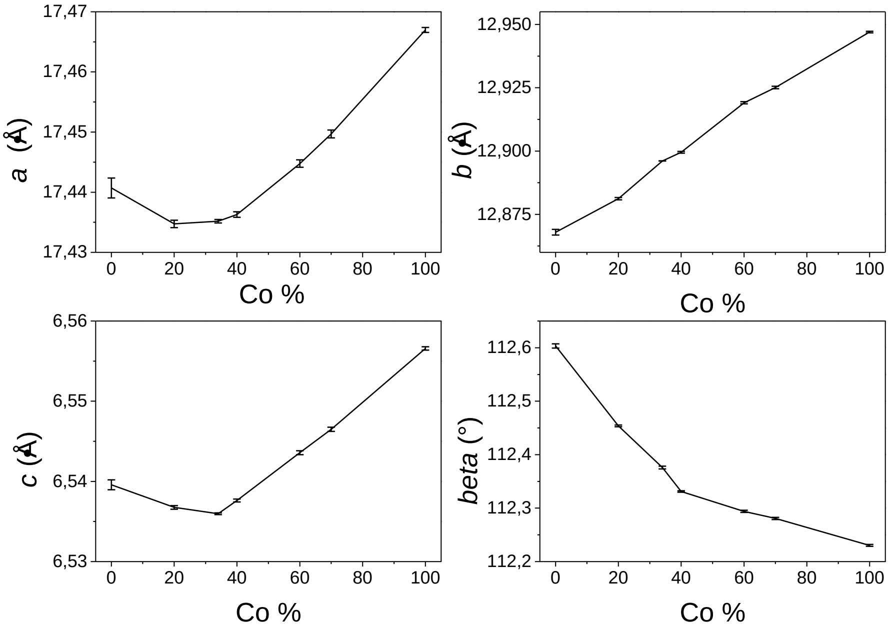

Figure 3.8 Variation of the cell parameters *a, b, c* and *β*, of bimetallic CoxNi-BTC compounds as a function of the molar composition

As it can be observed, although the differences are relatively small, there is a continuous evolution of the cell parameters of CoxNi-BTC as a function of the composition, which follow different trends for *a, b c* and *β*. The observed variations in cell parameters are a consequence of the different complex interactions (mainly hydrogen bonding) between the carboxylate groups of the ligand and the water molecules in the MOF, whose relative strength and bond distances may slightly change when either Ni or Co ions are present in the framework. The existence of such a continuous evolution (rather than a random variation) of cell parameters with the composition is a clear indication in favour of the formation of a true solid solution. In particular, the *b* parameter increases continuously with the amount of Co in the bimetallic compound, while *β* follows the opposite trend. In contrast, parameters *a* and *c* follow a more complex evolution, with clear minima at around 33 mol% of Co.

The lack of a strict linearity of the cell parameters with composition indicates that the CoxNi-BTC compounds do not obey the Vegard's law[28]. This fact indicates that the distribution of Co and Ni ions in the bimetallic compounds is not completely random. The presence of the minima in the curves of *a* and *c* at *ca*. 33 mol% Co strongly suggests a preferential occupation of the Co ions at the terminal positions, which are in a 1:2 multiplicity ratio with respect to bridging sites (see Figure 3.8). This is a relevant observation, since if we assume that the terminal sites are preferentially occupied by Co^{2+} ions, rather than a random distribution of both elements, this would lead to a precise and predictable array of metal ions in the framework, which can be finely tuned by changing the overall composition of the bimetallic MOF. Thus, it should be possible to predict, to a certain extent, what would be the average separation between two closest Co ions as a function of the Co:Ni molar ratio of the solid, or to determine the probability to have an isolated Co^{2+}, surrounded only by Ni^{2+} ions in the closest positions. This certainly has important implications in the design and catalytic properties of well-defined single-site catalysts[29,30], as we will illustrate in a forthcoming work.

It is worth mentioning that the addition of ethanol was found to be beneficial for the preparation of true solid solutions. Ethanol accelerates the overall precipitation process, which avoids the segregation of two pure phases of each individual monometallic MOF due to different rates of precipitation. Indeed, in the absence of ethanol, different precipitation rates were observed for pure Ni-BTC and Co-BTC monometallic compounds. Accordingly, when ethanol was not added to the synthesis mixture of bimetallic materials, incorporation of the two metals in the final compound was less quantitative (important deviations with respect to the ratio of precursors used) and varied from batch to batch, indicating that the crystallization process without ethanol is less homogeneous than when ethanol is added to the synthesis mixture.

To lend further support to the formation of solid solutions, we have slightly modified the synthesis conditions to obtain crystals suitable for single crystal diffraction (see Table A.1.1 in Annex A.1). Such large crystals (> 10 μm) were big enough for a complementary single crystal diffraction and SEM/EDX analysis. On one hand, single crystal diffraction confirmed the formation of the bimetallic compound with the same crystalline structure as the one obtained above[31]. On the other hand, EDX element mapping allowed us to conclude that both Ni and Co were simultaneously incorporated in a single particle and that they distribute homogeneously throughout the whole crystal; i.e., we did not detect Ni- or Co-enriched regions (such as tips or rims) in any of the single crystals analysed Figure 3.9 shows typical SEM/EDX measurements obtained for samples containing 33% and 50% of cobalt, as representative examples of the whole CoxNi-BTC series.

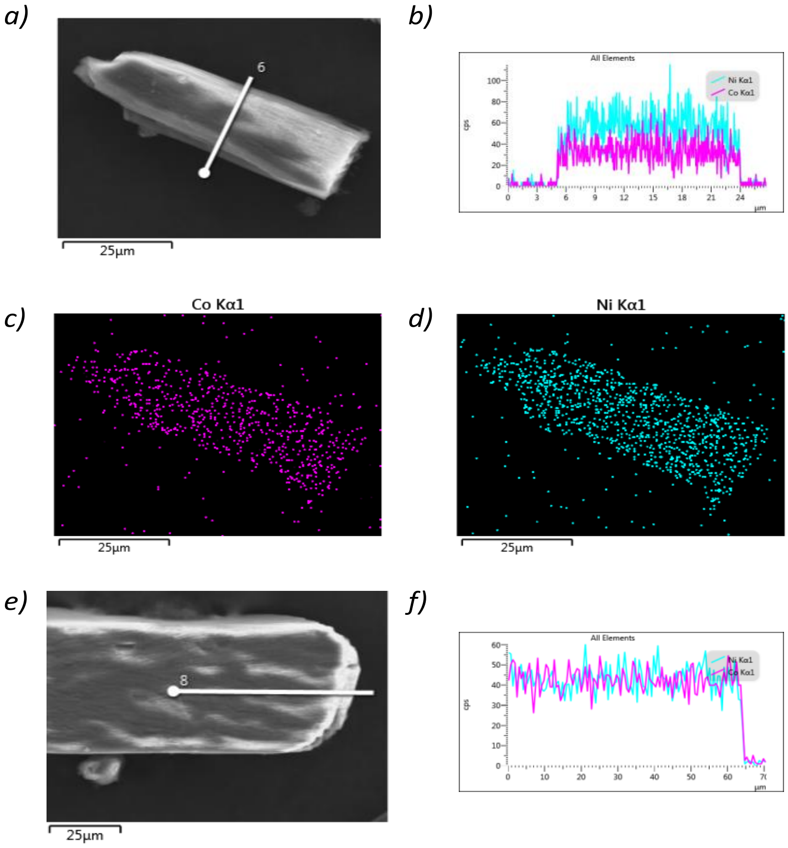

Figure 3.9 SEM/EDX analysis of samples Co33Ni-BTC (*a*-*d*) and Co50Ni-BTC (*e*,*f*) single crystal samples. *a*) and *e*): SEM images of the solids; *c*) and *d*): Co and Ni element mappings of the crystal shown in *a*); *b*) and *f*): Evolution of the Co (pink line) and Ni (cyan line) compositions along the white lines indicated in *a*) and *e*), respectively.

3.2.3.2 Co-Zn bimetallic compounds

The versatility and scope of the room temperature aqueous synthesis method described above was further investigated by preparing an additional series of Co-Zn bimetallic materials. The compounds were all found to be isoreticular in the complete range of compositions, as shown in Figure 3.10.

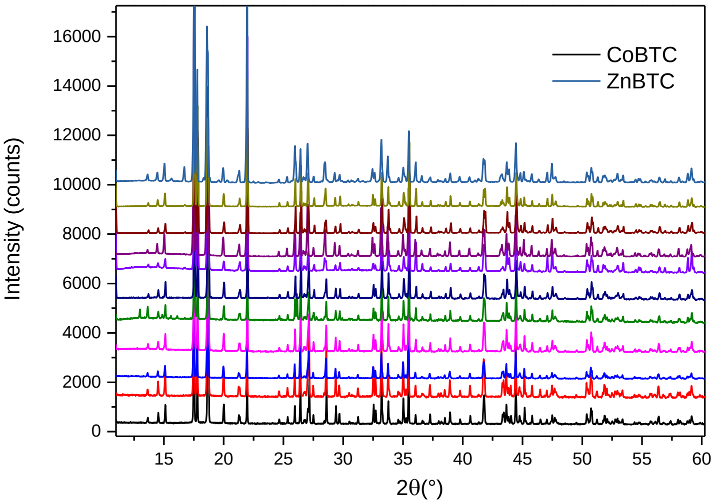

Figure 3.10 XRD diffraction patterns (Cu Kα radiation) of the CoxZn-BTC samples

Also in this case, a continuous evolution of the cell parameters with the composition was clearly observed, but parameters *a* and *c* showed an opposite trend with respect to that observed for the Co-Ni series (Figure 3.8), with relative maxima (instead of minima) at *ca*. 30% Co, as shown in Figure 3.11. In our opinion, the presence of these maxima in the evolution of *a* and *c* parameters reinforce the hypothesis that a preferred occupancy of the terminal positions by Co^{2+} ions occurs also in Co-Zn bimetallic mixtures. Meanwhile, parameters *b* and β followed a similar evolution with composition as that observed for Co-Ni mixtures: *i.e.*, *b* increases and β decreases with the Co content of the mixture.

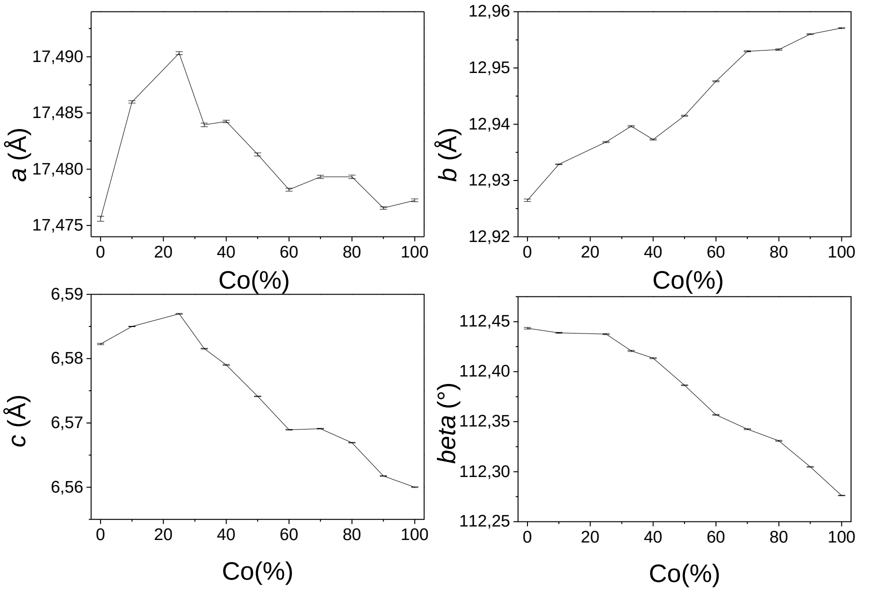

Figure 3.11 Variation of the cell parameters *a, b, c* and *β*, of bimetallic CoxZn-BTC compounds as a function of the molar composition

3.2.3.3 Mn-Ni bimetallic compounds

In the course of an ongoing catalytic study of the M-BTC compounds (the results will be presented elsewhere), we were also interested in preparing Mn^{2+}-containing compounds having the same structure as the Co-BTC prepared herein. Unfortunately, as commented above, we have not been able to prepare a pure monometallic Mn-BTC isoreticular compound using the same aqueous synthesis. Nevertheless, we succeeded in preparing a series of bimetallic compounds with the right structure containing Mn^{2+} ions in a Ni-BTC matrix up to a maximum concentration of 50% Mn, as shown in Figure 3.12. Above this concentration of Mn^{2+} ions, bimetallic compounds showed a considerably lower crystallinity and the same (unknown) structure observed for the pure Mn-BTC compound.

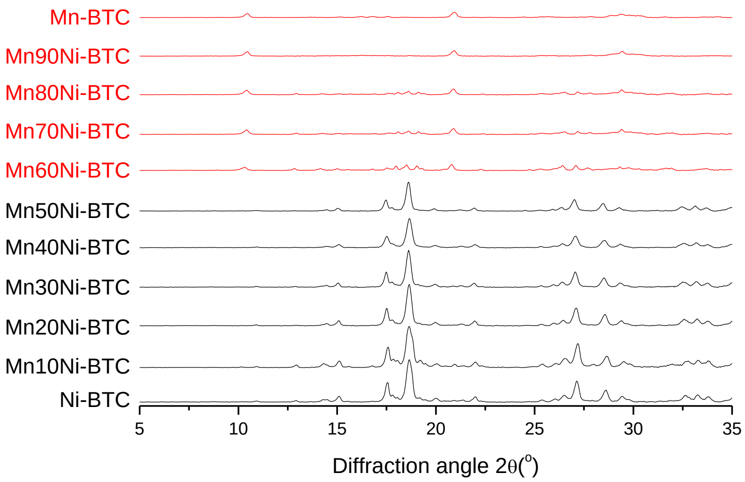

Figure 3.12 XRD diffraction patterns (Cu Kα radiation) of the MnxZn-BTC samples

The evolution of the cell parameters with the composition for the isoreticular MnxNi-BTC compounds, up to a maximum Mn content of 50%, is shown in Figure 3.13. While parameters *b* and β follow the same general evolution already discussed for Co-Ni and Co-Zn compounds (*b* increases and β decreases with the Mn content), the continuous trends of the cell parameters *a* and *c* do not present any evident maxima or minima, but only a discontinuity in the trend of the *a* axis is observed at *ca*. 30-40% Mn. Unfortunately, our data in this case is not conclusive on whether a preferential site occupation or a random distribution of Mn^{2+} ions takes place.

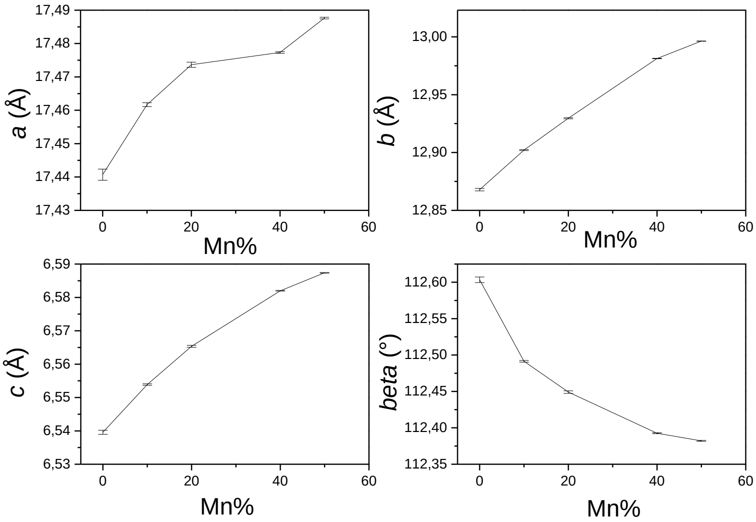

Figure 3.13 Variation of the cell parameters *a, b, c* and *β*, of bimetallic MnxNi-BTC compounds as a function of the molar composition

3.2.4. Mixed ligand compounds

In order to further explore the versatility of this room-temperature synthesis of isoreticular MOFs, we adapted the above method to prepare two mixed-ligand series, in which BTC is partially substituted by either isophthalic acid (IP) or 5-aminoisophthalic acid (NH_2IP) ligand. Both linkers are called defective (DL), since they both possess only two carboxylate groups instead of three. This can cause distortion in the crystal structure and lead to the formation of defects. Both CoBTC-x%IP and CoBTC-x%NH_2IP series were prepared with nominal initial synthesis loading of the defective linker of x=10, 20, 30%.

As shown in Figure 3.14, the PXRD patterns of as prepared mixed-ligand samples from both CoBTC-IP and CoBTC-NH_2IP series match the pure CoBTC compound, indicating the isoreticular character. No additional peaks visible on the diffractograms indicate phase purity, which may suggest formation of true solid solution instead of two distinct materials. Note that the use of pure ditopic ligand in the synthesis could never lead to an isoreticular compound, due to the lack of the third carboxylate group. Therefore, in case of a mixture of two different materials (one with only BTC ligands and another material with only IP or NH$_2$IP ligands), the resulting diffractogram should clearly show additional lines associated to the second phase.

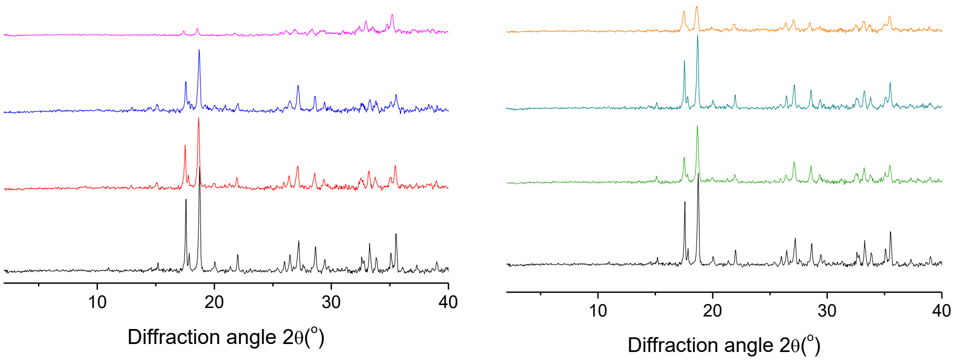

Figure 3.14 PXRD of mixed-ligand MOFs. CoBTC-NH$_2$IP series (*left*) and CoBTC-IP (*right*). The diffractograms correspond to (from *bottom* to *top*) pure Co-BTC, and 10%, 20% and 30% nominal amount of ditopic ligand.

It can be seen that low level of defective linker loading in synthesis mixture (up to 20% nominal amount), does not affect the crystal integrity of mixed-ligand materials. However, upon further increase of defective linker (DL) content in the synthesis mixture up to 30%, there was a significant loss in material yield (<50%) and obtained MOFs showed poor crystallinity (Figure 3.14 pink and orange) compared to pristine CoBTC.

The incorporation and quantification of DL have been testified by NMR spectroscopy of the digested samples (in D_2SO_4 and DMSO-$_{d6}$), after activation at 473K for 4h. Figure 3.15 shows the corresponding ^{1}H NMR spectra of the different mixed-ligand compounds, evidencing the simultaneous presence of BTC and IP or NH$_2$IP ligands in the solids, as indicated in Figure 3.15. The percentage of linker substitution was evaluated from the integrated intensities of the characteristic peaks of each ligand. Hereafter, the samples will be referred to as CoBTC-x%IP and CoBTC-x%NH$_2$IP, in which *x%* indicates the real concentration of IP or NH$_2$IP in the material. It was found that the real framework incorporation amounts of IP and NH$_2$IP increase upon the concentration of DL in the reactant solutions and closely follow the nominal values, as shown in Table 3.2. The only relevant exception to this is sample CoBTC-18%IP (30% defective ligand loading).

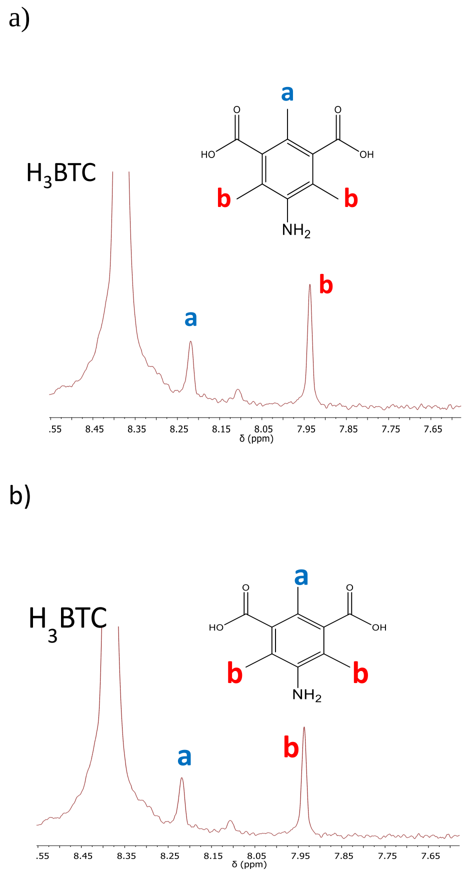

Substitution level :

6% of NH$_2$-isophthalic

CoBTC-6%NH$_2$IP

Substitution level :

15% of NH$_2$-isophthalic

CoBTC-15%NH$_2$IP

Figure 3.15 (Part I) NMR spectra of mixed-ligand MOFs a) CoBTC-6%NH$_2$IP b) *CoBTC-7%IP* c) CoBTC-15%NH$_2$IP d) *CoBTC-14%IP* e) CoBTC-32%NH$_2$IP and f) *CoBTC-18%IP*

c)

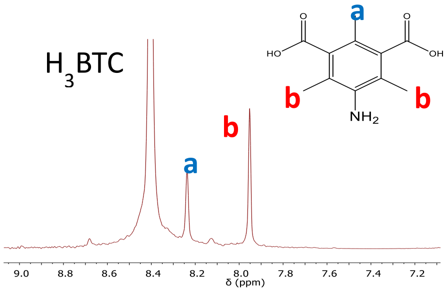

Substitution level :

32% of NH_2-isophthalic

CoBTC-32%NH_2IP

d)

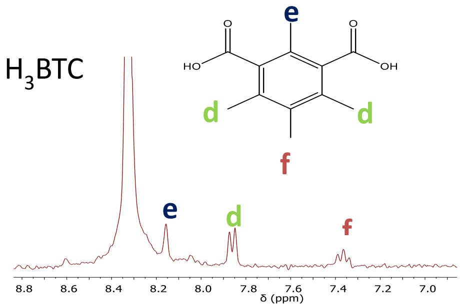

Substitution level :

7% of Isophthalic

CoBTC-7%IP

e)

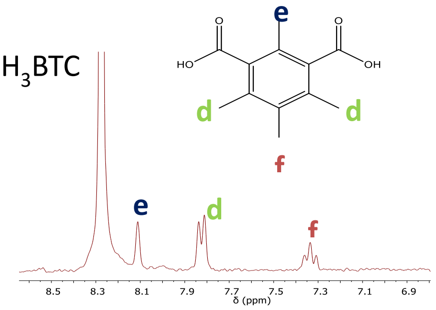

Substitution level :

14% of Isophthalic

CoBTC-14%IP

Figure 3.15 (Part II) NMR spectra of mixed-ligand MOFs a) CoBTC-6%NH_2IP b) *CoBTC-7%IP* c) CoBTC-15%NH_2IP d) *CoBTC-14%IP* e) CoBTC-32%NH_2IP and f) *CoBTC-18%IP*

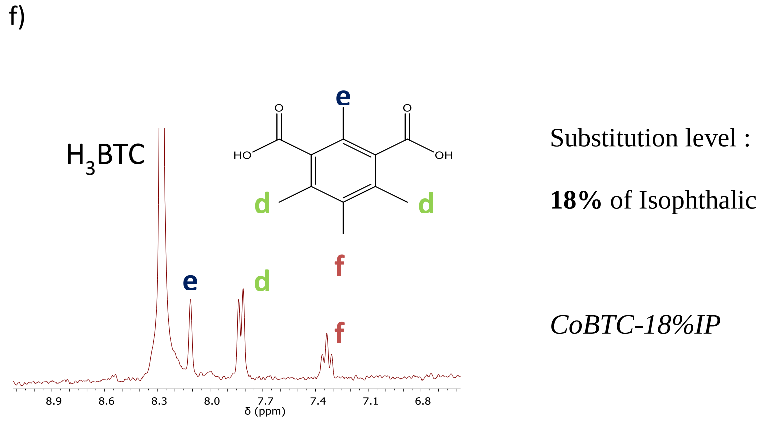

Figure 3.15 (Part III) NMR spectra of mixed-ligand MOFs a) CoBTC-6%NH_2IP b) *CoBTC-7%IP* c) CoBTC-15%NH_2IP d) *CoBTC-14%IP* e) CoBTC-32%NH_2IP and f) *CoBTC-18%IP*

Table 3.2 Amount of defective linker in the CoBTC-x%IP and CoBTC-x%NH_2IP

Sample	**Nominal amount of DL**	**Ligand incorporation**[a]
CoBTC-6%NH_2IP	10% of NH_2IP	6% of NH_2IP
CoBTC-15%NH_2IP	20% of NH_2IP	15% of NH_2IP
CoBTC-32%NH_2IP	30% of NH_2IP	32% of NH_2IP
CoBTC-7%IP	10% of IP	7% of IP
CoBTC-14%IP	20% of IP	14% of IP
CoBTC-18%IP	30% of IP	18% of IP

[a] Determined from the ^{1}H NMR spectra shown in Figure 3.15.

To examine the thermal stability if these mixed-ligand series, thermogravimetric analysis (TGA) was carried out (Figure 3.16 and Figure 3.17). All the mixed-ligand materials exhibit the same two-stage mass loss attributed to water removal and ligand decomposition as it has been discussed earlier for Co-BTC. The relative weight losses were used to calculate the molecular formula of each compound, as shown in Table 3.3.

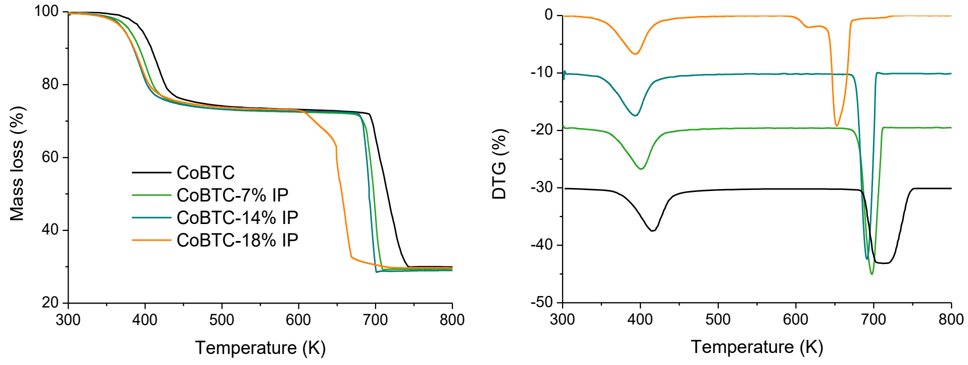

Figure 3.16 TGA (*left*) and derivative curves (*right*) of pure CoBTC and CoBTC-7%IP, CoBTC-14%IP and CoBTC-18%IP

Incorporation of defective IP and NH_2IP, causes a gradual loss in thermal stability, as compared to the parent CoBTC. The biggest difference can be seen for the samples with the highest loading, CoBTC-18%IP and CoBTC-32%NH_2IP, which may be connected with a poor crystallinity of the material.

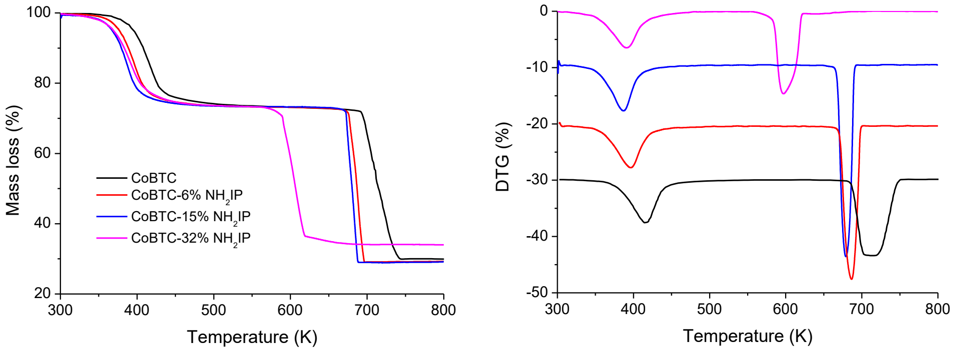

Figure 3.17 TGA (*left*) and derivative curves (*right*) of pure CoBTC and CoBTC-6%NH_2IP, CoBTC-15%NH_2IP and CoBTC-32%NH_2IP

Table 3.3 Measured weight losses for each step in the TGA curves in Figure 3.16 and 3.17, and calculated molecular formula of the MOF (assuming that the solid residue corresponds to the respective metal oxide)

MOF	**Weight loss (%)**				**FORMULA**
		STEP I	STEP II	RESIDUE	
CoBTC	Theoretical	26.7	45.5	27.8	$Co_3BTC_{1,8}\cdot 11,3H_2O$
	Experimental	26.9	43.0	30.1	
CoBTC-6%NH$_2$IP	Experimental	25,2	45,3	29,5	$Co_3(BTC+NH_2IP)_{1,7}\cdot 10,7H_2O$
CoBTC – 15%NH$_2$IP	Experimental	25,0	45,4	29,6	$Co_3(BTC+NH_2IP)_{1,7}\cdot 10,6H_2O$
CoBTC-32%NH$_2$IP	Experimental	25,6	41,0	33,4	$Co_3(BTC+NH_2IP)_{1,4}\cdot 9,7H_2O$
CoBTC-7%IP	Experimental	25,9	44,4	29,7	$Co_3(BTC+IP)_{1,6}\cdot 10,8H_2O$
CoBTC-14%IP	Experimental	25,1	45,7	29,2	$Co_3(BTC+IP)_{1,7}\cdot 10,9H_2O$
CoBTC-18%IP	Experimental	24,5	45,4	30,1	$Co_3(BTC+IP)_{1,7}\cdot 10,2H_2O$

Figures 3.18-20 show field emission scanning electron microscopy (FESEM) images of the CoBTC, CoBTC-x%IP and CoBTC-x%NH$_2$IP MOFs series respectively. As it can be seen from comparison of FESEM images of CoBTC and CoBTC-7%IP, incorporation of IP defective linker significantly increases the crystal size (approximately 10 times) with respect to the pristine CoBTC. For materials CoBTC-7%IP and CoBTC-14%IP, increase of DL content in the structure provokes an increase of surface deformation, which becomes more rough, without affecting the overall shape or size of the crystals (Figure 3.18 *a* and *b*). However, further increased of the DL content up to 18% (30% of initial synthesis loading) resulted in non-homogeneous crystal size (Figure 3.18 *c*), in which small crystals are deposited on top of the bigger ones. It is worth to notice,

that increase of DL initial content in the synthesis mixture visibly slows down the crystallization rate. Also, the yield of the obtained materials drop progressively to 60%, 48% and to 25% for CoBTC-7%IP, CoBTC-14%IP and CoBTC-18%IP MOF, respectively.

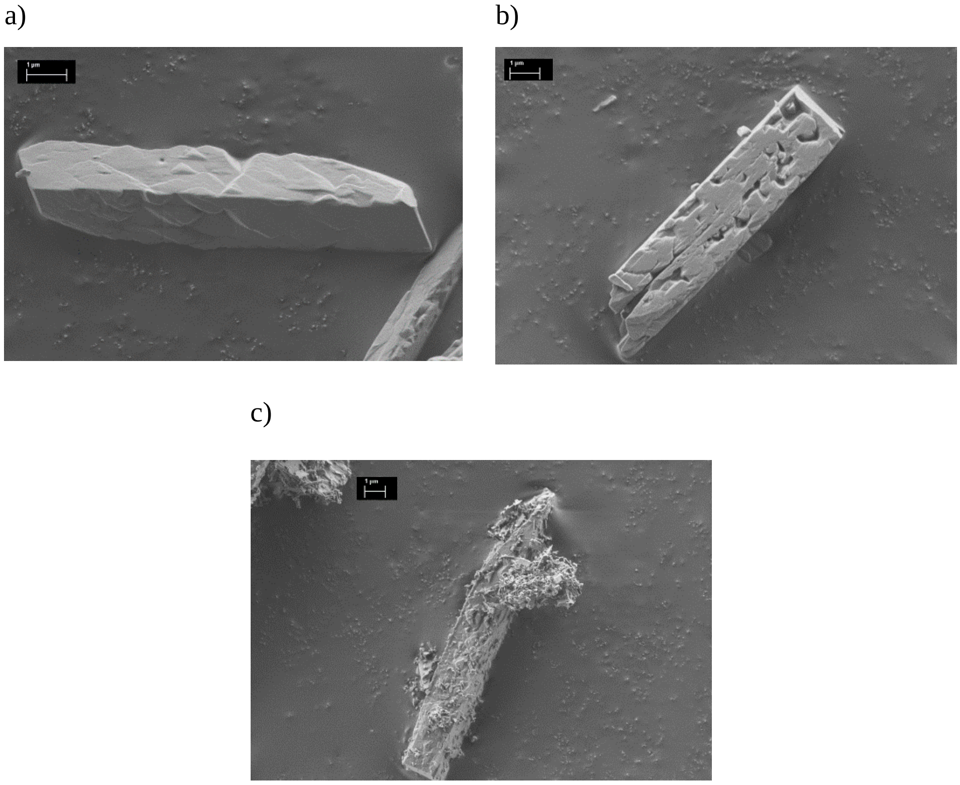

Figure 3.18 FESEM images of a) CoBTC-7%IP b) CoBTC-14%IP c) CoBTC-18%IP

In case of CoBTC-xNH_2IP series, showed in Figure 3.19, the size of the crystal also increased with respect to CoBTC, however the surface stays flat. Upon increasing the amount of NH_2IP ligand in the MOF structure crystal size decreased as well as the aspect ratio. Rods become shorter and the aspect changes to plates for the most concentrated sample.

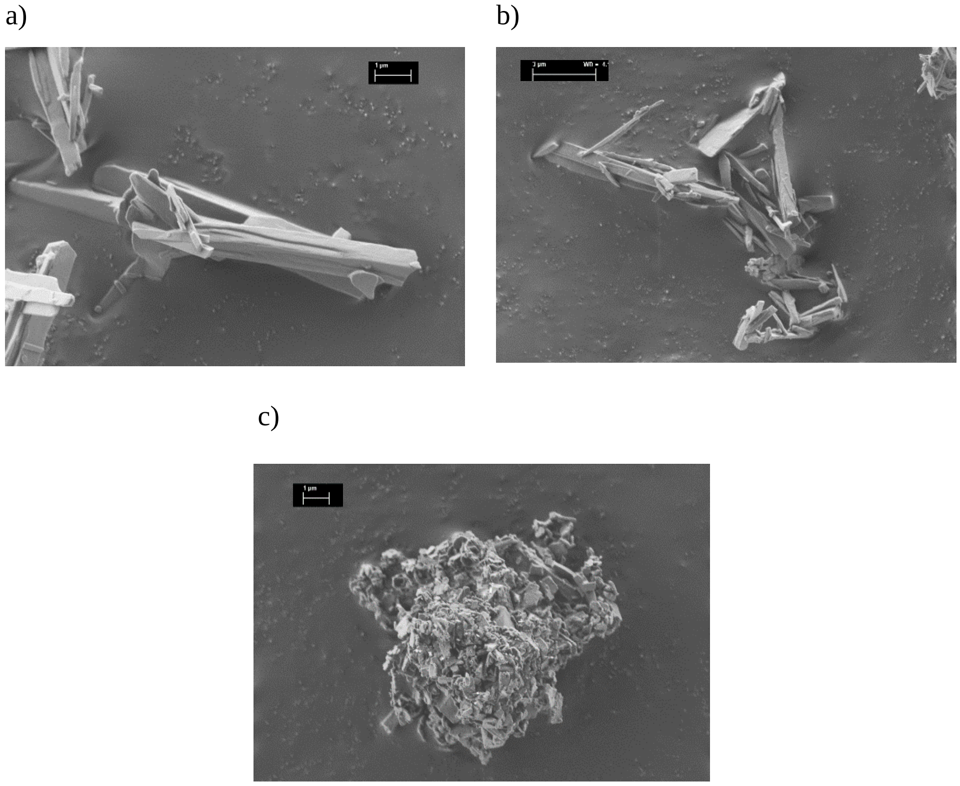

Figure 3.19 FESEM images of a) CoBTC-6%NH_2IP b) CoBTC-15%NH_2IP c) CoBTC-32%NH_2IP

Similar like in the case of CoBTC-IP series, increasing NH_2IP initial synthesis content slows down crystallization rate and decrease the final yield of the product - 63%, 40% and 20% for CoBTC-6%NH_2IP, CoBTC-15%NH_2IP and CoBTC-32%NH_2IP respectively.

3.3. Conclusions

Herein we have applied a fast, sustainable and industrially friendly procedure for the synthesis of a series of isoreticular monometallic and bimetallic M-BTC compounds from aqueous solutions. These materials feature zigzag chains containing two positions for the metal ions; an unidentate bridging position (along the chain) and a bidentate terminal position (on alternate BTC molecules), in a 2:1 ratio. Packing of these chains into layers, and layer stacking lead to the three dimensional structure of the MOFs.

Following the synthesis method described here, we have been able to prepare isoreticular Co-Ni and Co-Zn binary mixtures in all range of compositions, as well as Mn-Ni compounds up to a maximum Mn concentration of 50%. By combining powder and single-crystal diffraction and SEM/EDX analysis of the solids, we have unambiguously demonstrated that true solid solutions are formed rather than physical mixtures, in which the two metal ions distribute homogeneously throughout the whole crystal (enrichment of one of the two metals at tips, rims or other regions of the crystal has never been observed in any of the analyzed samples). Moreover, a careful analysis of the evolution of the cell parameters with the composition of Co-Ni and Co-Zn bimetallic compounds strongly suggests that a preferential occupation of the terminal positions by Co^{2+} ions takes place. If this is so, then the synthesis method used herein would lead to the formation of well-defined and predictable environments for the metal ions in the framework, which would basically depend upon the overall chemical composition of the binary materials. This would determine relevant parameters for the material properties, such as average distance between neighbor metal active sites or the statistical probability to have site isolation. As far as Mn-Ni mixtures is concerned, although preferential site occupation of terminal positions by Mn^{2+} ions is also feasible, our data are not conclusive enough to state it with certainty.

This synthesis method can be extended to prepare mixed-ligand MOFs containing DL in their structure (IP or NH_2IP). Single phase formation during the synthesis was confirmed by powder XRD, while the DL content was quantified by NMR of the digested solid. Both techniques suggest true incorporation of the second ligand into MOF structure. Moreover, SEM analysis of the mixed-ligand solids was used to track morphological changes that occurs for all material series. It was found that maximum incorporation of DL (by this synthesis method) differs for IP and NH_2IP (18% and 32% respectively) and lead to great loss of crystallinity in both cases.

3.4. References

(1) Gascon, J.; Aktay, U.; Hernandez-Alonso, M.; Vanklink, G.; Kapteijn, F. Amino-Based Metal-Organic Frameworks as Stable, Highly Active Basic Catalysts. *J. Catal.* **2009**, *261* (1), 75–87.

(2) Israr, F.; Chun, D.; Kim, Y.; Kim, D. K. High Yield Synthesis of Ni-BTC Metal-Organic Framework with Ultrasonic Irradiation: Role of Polar Aprotic DMF Solvent. *Ultrason. Sonochem.* **2016**, *31*, 93–101.

(3) Dalapati, R.; Sakthivel, B.; Dhakshinamoorthy, A.; Buragohain, A.; Bhunia, A.; Janiak, C.; Biswas, S. A Highly Stable Dimethyl-Functionalized Ce(Iv)-Based UiO-66 Metal-Organic Framework Material for Gas Sorption and Redox Catalysis. *CrystEngComm* **2016**, *18* (40), 7855–7864.

(4) Xie, L.; Liu, S.; Gao, C.; Cao, R.; Cao, J.; Sun, C.; Su, Z. Mixed-Valence Iron(II, III) Trimesates with Open Frameworks Modulated by Solvents. *Inorg. Chem.* **2007**, *46* (19), 7782–7788.

(5) Hao, X.-R.; Wang, X.-L.; Shao, K.-Z.; Yang, G.-S.; Su, Z.-M.; Yuan, G. Remarkable Solvent-Size Effects in Constructing Novel Porous 1,3,5-Benzenetricarboxylate Metal–organic Frameworks. *CrystEngComm* **2012**, *14* (17), 5596.

(6) Reinsch, H. “Green” Synthesis of Metal-Organic Frameworks. *Eur. J. Inorg. Chem.* **2016**, *2016* (27), 4290–4299.

(7) Cattaneo, D.; Warrender, S. J.; Duncan, M. J.; Castledine, R.; Parkinson, N.; Haley, I.; Morris, R. E. Water Based Scale-up of CPO-27 Synthesis for Nitric Oxide Delivery. *Dalt. Trans.* **2016**, *45* (2), 618–629.

(8) Loera-Serna, S.; Núñez, L. L.; Flores, J.; López-Simeon, R.; Beltrán, H. I. An Alkaline One-Pot Metathesis Reaction to Give a [Cu 3 (BTC) 2] MOF at r.t., with Free Cu Coordination Sites and Enhanced Hydrogen Uptake Properties. *RSC Adv.* **2013**, *3* (27), 10962–10972.

(9) Sánchez-Sánchez, M.; Getachew, N.; Díaz, K.; Díaz-García, M.; Chebude, Y.; Díaz, I. Synthesis of Metal–organic Frameworks in Water at Room Temperature: Salts as Linker Sources. *Green Chem.* **2015**, *17* (3), 1500–1509.

(10) Deleu, W. P. R.; Stassen, I.; Jonckheere, D.; Ameloot, R.; De Vos, D. E.; Yoshida, M. I.; Araujo, M. H.; Lago, R. M.; David, O.; Magnier, E.; et al. Waste PET (Bottles) as a Resource or Substrate for MOF Synthesis. *J. Mater. Chem. A* **2016**, *4* (24), 9519–9525.

(11) Lo, S. H.; Senthil Raja, D.; Chen, C. W.; Kang, Y. H.; Chen, J. J.; Lin, C. H. Waste Polyethylene Terephthalate (PET) Materials as Sustainable Precursors for the Synthesis of Nanoporous MOFs, MIL-47, MIL-53(Cr, Al, Ga) and MIL-101(Cr). *Dalt. Trans.* **2016**, *45* (23), 9565–9573.

(12) Ren, J.; Dyosiba, X.; Musyoka, N. M.; Langmi, H. W.; North, B. C.; Mathe, M.; Onyango, M. S. Green Synthesis of Chromium-Based Metal-Organic Framework (Cr-MOF) from Waste Polyethylene Terephthalate (PET) Bottles for Hydrogen Storage Applications. *Int. J. Hydrogen Energy* **2016**, *41* (40), 18141–18146.

(13) Chui, S. S.-Y. A Chemically Functionalizable Nanoporous Material [Cu3(TMA)2(H2O)3]N. *Science (80-.).* **1999**, *283* (5405), 1148–1150.

(14) Yuan, W.; Garay, A. L.; Pichon, A.; Clowes, R.; Wood, C. D.; Cooper, A. I.; James, S. L. Study of the Mechanochemical Formation and Resulting Properties of an Archetypal MOF: Cu3(BTC)2 (BTC = 1,3,5-Benzenetricarboxylate). *CrystEngComm* **2010**, *12* (12), 4063.

(15) Pichon, A.; Lazuen-Garay, A.; James, S. L. Solvent-Free Synthesis of a Microporous Metal–organic Framework. *CrystEngComm* **2006**, *8* (3), 211.

(16) Klimakow, M.; Klobes, P.; Thünemann, A. F.; Rademann, K.; Emmerling, F. Mechanochemical Synthesis of Metal−Organic Frameworks: A Fast and Facile Approach toward Quantitative Yields and High Specific Surface Areas. *Chem. Mater.* **2010**, *22* (18), 5216–5221.

(17) Stolar, T.; Batzdorf, L.; Lukin, S.; Žilić, D.; Motillo, C.; Friščić, T.; Emmerling, F.; Halasz, I.; Užarević, K. In Situ Monitoring of the Mechanosynthesis of the Archetypal Metal–Organic Framework HKUST-1: Effect of Liquid Additives on the Milling Reactivity. *Inorg. Chem.* **2017**, *56* (11), 6599–6608.

(18) Friščić, T.; Jones, W. Recent Advances in Understanding the Mechanism of Cocrystal Formation via Grinding. *Cryst. Growth Des.* **2009**, *9* (3), 1621–1637.

(19) Reinsch, H.; Waitschat, S.; Chavan, S. M.; Lillerud, K. P.; Stock, N. A Facile "Green" Route for Scalable Batch Production and Continuous Synthesis of Zirconium MOFs. *Eur. J. Inorg. Chem.* **2016**, *2016* (27), 4490–4498.

(20) Cavka, J. H.; Jakobsen, S.; Olsbye, U.; Guillou, N.; Lamberti, C.; Bordiga, S.; Lillerud, K. P. A New Zirconium Inorganic Building Brick Forming Metal Organic Frameworks with Exceptional Stability. *J. Am. Chem. Soc.* **2008**, *130* (42), 13850–13851.

(21) Eddaoudi, M.; Kim, J.; Rosi, N.; Vodak, D.; Wachter, J.; O'Keeffe, M.; Yaghi, O. M. Systematic Design of Pore Size and Functionality in Isoreticular MOFs and Their Application in Methane Storage. *Science (80-.).* **2002**, *295* (5554), 469–472.

(22) Wade, C. R.; Dinca, M. Investigation of the Synthesis, Activation, and Isosteric Heats of CO2 Adsorption of the Isostructural Series of MOFs M3(BTC)2 (M=Cr,Fe,Ni,Cu,Mo,Ru). *Dalt. Trans.* **2012**, *41* (26), 7931.

(23) Zou, R.; Li, P.-Z.; Zeng, Y.-F.; Liu, J.; Zhao, R.; Duan, H.; Luo, Z.; Wang, J.-G.; Zou, R.; Zhao, Y. Bimetallic Metal-Organic Frameworks: Probing the Lewis Acid Site for CO 2 Conversion. *Small* **2016**, *12* (17), 2334–2343.

(24) Sun, D.; Sun, F.; Deng, X.; Li, Z. Mixed-Metal Strategy on Metal-Organic Frameworks (MOFs) for Functionalities Expansion: Co Substitution Induces Aerobic Oxidation of Cyclohexene over Inactive Ni-MOF-74. *Inorg. Chem.* **2015**, *54* (17), 8639–8643.

(25) Gaab, M.; Trukhan, N.; Maurer, S.; Gummaraju, R.; Müller, U. The Progression of Al-Based Metal-Organic Frameworks – From Academic Research to Industrial Production and Applications. *Microporous Mesoporous Mater.* **2012**, *157*, 131–136.

(26) Groom, C. R.; Bruno, I. J.; Lightfoot, M. P.; Ward, S. C. The Cambridge Structural Database. *Acta Crystallogr. Sect. B Struct. Sci. Cryst. Eng. Mater.* **2016**, *72* (2), 171–179.

(27) Yaghi, O. M.; Li, H.; Groy, T. L. Construction of Porous Solids from Hydrogen-Bonded Metal Complexes of 1,3,5-Benzenetricarboxylic Acid. *J. Am. Chem. Soc.* **1996**, *118* (38), 9096–9101.

(28) Denton, A. R.; Ashcroft, N. W. Vegard's Law. *Phys. Rev. A* **1991**, *43* (6), 3161–3164.

(29) Rogge, S. M. J.; Bavykina, A.; Hajek, J.; Garcia, H.; Olivos-Suarez, A. I.; Sepúlveda-Escribano, A.; Vimont, A.; Clet, G.; Bazin, P.; Kapteijn, F.; et al. Metal–organic and Covalent Organic Frameworks as Single-Site Catalysts. *Chem. Soc. Rev.* **2017**, *46* (11), 3134–3184.

(30) Osadchii, D. Y.; Olivos-Suarez, A. I.; Szécsényi, Á.; Li, G.; Nasalevich, M. A.; Dugulan, I. A.; Crespo, P. S.; Hensen, E. J. M.; Veber, S. L.; Fedin, M. V.; et al. Isolated Fe Sites in Metal Organic Frameworks Catalyze the Direct Conversion of Methane to Methanol. *ACS Catal.* **2018**, *8* (6), 5542–5548.

(31) *Unfortunately, Single Crystal Diffraction Analysis Is Not Conclusive on an Eventual Preferential Occupation of the Terminal Sites by Co*.

(32) Braude, E. A.; Nachod, F. C.; Editors. *Determination of Organic Structures by Physical Methods*; Academic Press, 1955.

(33) Petříček, V.; Dušek, M.; Palatinus, L. Crystallographic Computing System JANA2006: General Features. *Zeitschrift für Krist. - Cryst. Mater.* **2014**, *229* (5), 345–352.

(34) Le Bail, A. Whole Powder Pattern Decomposition Methods and Applications: A Retrospection. *Powder Diffr.* **2005**, *20* (04), 316–326.

(35) Rodríguez-Carvajal, J. Recent Advances in Magnetic Structure Determination by Neutron Powder Diffraction. *Phys. B Condens. Matter* **1993**, *192* (1–2), 55–69.

(36) Bérar, J. F.; Lelann, P. E.s.d.'s and Estimated Probable Error Obtained in Rietveld Refinements with Local Correlations. *J. Appl. Crystallogr.* **1991**, *24* (1), 1–5.

(37) Sheldrick, G. M. SHELXT – Integrated Space-Group and Crystal-Structure Determination. *Acta Crystallogr. Sect. A Found. Adv.* **2015**, *71* (1), 3–8.

(38) Sheldrick, G. M. Crystal Structure Refinement with SHELXL. *Acta Crystallogr. Sect. C Struct. Chem.* **2015**, *71* (1), 3–8.

(39) Dolomanov, O. V.; Bourhis, L. J.; Gildea, R. J.; Howard, J. A. K.; Puschmann, H. OLEX2 : A Complete Structure Solution, Refinement and Analysis Program. *J. Appl. Crystallogr.* **2009**, *42* (2), 339–341.

Chapter 4

Selective aerobic oxidation of cumene over MIX-MOFs

4.1. Introduction

Selective liquid-phase aerobic oxidation of cumene (CM) to cumene hydroperoxide (CHP) (Scheme 4.1, Eq. 1), is a relevant reaction in chemical industry, since CHP is an important intermediate in the production of phenol, which can then be further converted into phenolic resins and polycarbonates via bisphenol A[1,2]. CHP can also be used as an initiator of polymerization reaction[3]. Nearly 90% of phenol world production goes through the cumene route.

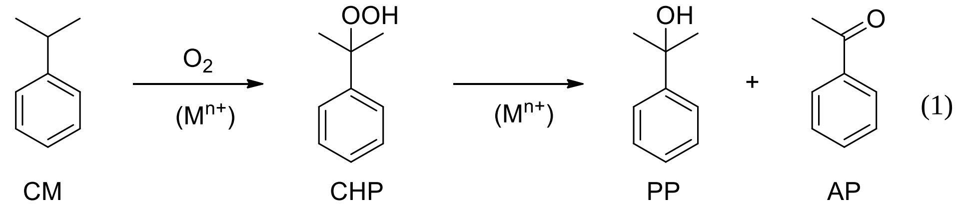

Scheme 4.1 Aerobic oxidation of cumene (CM) to cumene hydroperoxide (CHP) followed by decomposition CHP to two main side products 2-phenyl-2propanol (PP) and acetophenone (AP)

Typically, CM oxidation to CHP is carried out thermally in the temperature range between 353 K and 393 K and from atmospheric pressure up to 7 bars, in the absence of any catalyst (autooxidation process) and using small amounts of self-initiator CHP[4] or NHPI[5–7]. CHP as all organic peroxides is sensitive to heat, presence of acids, metal ions etc. For this reason, alkaline agents like NaOH[8], Na_2CO_3[9] or NH_4NaCO_3[10] are added to neutralize by-product organic acids and prevent phenol formation, which can have negative effect on selectivity and productivity of cumene hydroperoxide[11]. The selectivity attained under these conditions is typically above 90-92%. However, the productivity of such autooxidation processes (expressed in terms of grams of CHP produced per liter of CM and per hour; g L^{-1} h^{-1}) is usually below the desired values.

In order to understand better this reaction and drive catalyst design to maximize the selectivity towards desired product, it is necessary to gain a deep knowledge on the reaction mechanism. Hereafter, a detailed description of the well-established cumene autooxidation mechanism[12] is provided.

The autooxidation of CM proceeds through a radical chain reaction pathway, which involves three main steps: initiation, propagation and termination. Initiation of the reaction involves generation of the cumyl free radicals, by the thermal decomposition of CHP (Scheme 4.2, Eq. 2) and subsequent reaction of the intermediate radicals (Cumylhydroxy radical) with Cumene (Scheme 4.2, Eq. 3). Cumyl radicals can also be formed in alternative reaction of hydroxyl radical with cumene (Scheme 4.2, Eq. 4). In the typical cumene autooxidation reaction, some percent of initiator (CHP) is added (4-5%) in order to improve the velocity of this reaction step, by favoring formation of the radicals.

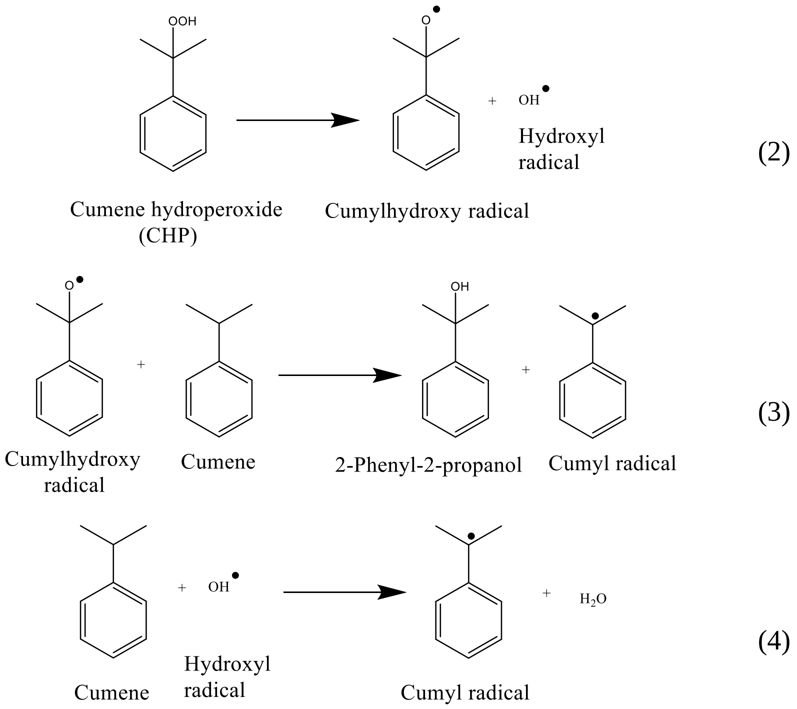

Scheme 4.2 Initiation steps in CM oxidation reaction

The second step – propagation, is the rate determining step. Here, formed cumyl radical (Scheme 4.2, Eq. 3 and 4) reacts with oxygen to form cumene hydroperoxide radical (Scheme 4.3, Eq. 5) which in turn reacts with another CM molecule yielding CHP and regenerating the cumyl radical (Scheme 4.3, Eq. 6).

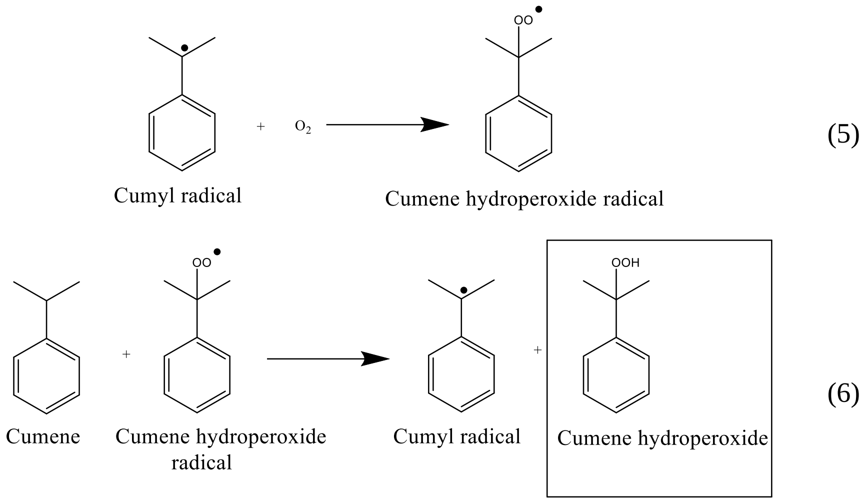

Scheme 4.3 Propagation steps in CM oxidation process

The last step – termination, stops the reaction chain by the disappearance of radicals. Here, the two major side products are formed: 2-Phenyl-2-propanol (PP) is produced from decomposition of CHP (Scheme 4.4, Eq. 7) and acetophenone (AP) produced from Cumylhydroxy radical (Scheme 4.4, Eq. 8)

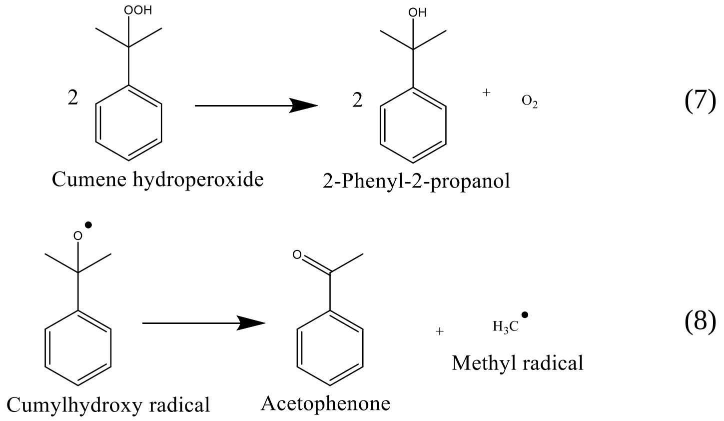

Scheme 4.4 Termination steps in CM process

In order to increase the CHP productivity, attained in the autooxidation, while maintaining the excellent selectivity to CHP, the use of different catalysts have been considered[13-16]. Some selected examples are summarized in Table 4.1. In the following, we will briefly describe a few relevant reports directly related to our current work.

Table 4.1 Comparison of chosen catalyst for CM oxidation

Catalyst	Reaction conditions	Conv. /Selec. to CHP	Reference
Cr$_2$O$_3$, **MnO$_2$,** **Fe$_2$O$_3$**	353 K; cumene 1 mL, 45 min, 0.01 g cat. 1 bar O$_2$	S:62.56% S:70.00% S:65.12% *initial amout of hydroperoxide included	17
Fe-O/ZrO$_2$ **Fe-O/TiO$_2$** **Fe-O/Al$_2$O$_3$**	363 K, 6 mL cumene Fe=5 wt.%, 1 bar O$_2$	C: 10-12% S:10% C:10-12% S:4% C: 10-12% S:5%	18
Cu(OAc)$_2$-BR-0.6	cumene 10 mL, catalyst 0.20 g at 363 K; pO2: 103 kPa	C: 6.4% S:97.6%	19
Cr(NO3)$_3$ -BR-0.6	cumene 10 mL, catalyst 0.20 g at 363 K; pO2: 103 kPa	C: 8.02% S:97%	20
TRIP-Cu(II)SO4	363 K; 0.1MPa; initial CHP concentration, 20 wt.%; air feed, 120 mL/min; 3 h; cat. 20 ppm	Formation CHP: 3.7wt% S: 91.1%	21
CuO nanoparticles	0.25 g, 0.1 mol Cumene 358 K, O$_2$	C: 44.2% S: 93.2%	22
Metalloporphyrins (p-Cl)TPPMnCl	(7.2 × 10–5 mol/L), 393 K, air: 600 mL/min, 1 atm.	C:22.9% S:94.4%	23
Silver-activated carbon nanotubes	333 K, atm pressure, cumene (5 mL), 5 mg cat. (0.12wt%), O$_2$	C: 28% S: 76%	24
Ionic Liquids: **[C$_4$dmim]OH** **[C$_4$mim]OH**	Cumene:0.35mol ILs:0.0015 mol, air flow=160 mL/min, CHP initiator: 0.8g, 363 K, time:11 h	C:57.1% S:63.2% C:53.7% S:67.1%	25
Carbon nanotubes (CNTs) Nitrogen-doped NCNT-3 **N/(N+C) = 3.44**	Cumene: 10mL, catalyst 0.1g, 353 K, 8 h, O$_2$ flow 10mL/min	C: 16.1% S: 90% C:74.7% S: 3.1%	26
MOFs			
CuO@Cu$_3$(BTC)$_2$ **CuO** **Cu2(BTC)$_2$**	Cumene (100 mL) + 1% CHP, 30 mg cat, 383 K, air flow (600 mL/min) 12 h	Max yield CHP: Y: 18.1% Y: 13.6% Y: 8.7%	27
MIL-101 (Cr)	7.5 mg catalyst, 20 mmol substrate, O$_2$ atmosphere, 393 K. 70 h	C:100% S:18%	28
Cu(pymo)$_2$ **Cu(im)$_2$**	Cumene/metal= 200 Air, 363 K bubbling rate (0.5mL/s)	C: 64% (23 h) S: 24% CHP (8 h) C:74% (23h) S: 2% CHP (1.5 h)	29

Most of the presented catalysts (see Table 4.1) contains in the structure transition metals, which are well known for its activity in a wide range of catalytic oxidation reactions[30-33]. In these types of processes salts of transition metal ions can be involved in two main mechanisms: homolytic or heterolytic[34,35]. The homolitic oxidation, is setting the role of the catalyst as generator of organic radicals that react with molecular oxygen by an "auto-oxidation" mechanism. Here, the metal ion is oxidized outside the coordination sphere via radical chain by one-electron redox step, as it is shown in Scheme 4.5, Eq. 9. In the heterolitic oxidation, the metal ion site is acting as a Lewis acid site, where by coordinating with the substrate or oxidizing reagent resulted in an increase in the polarization of reactive bonds (Scheme 4.5, Eq. 10).

$$M^{n+} + O_2 \longrightarrow M^{(n+1)+} + O_2^{\bullet -} \qquad (9)$$

$$M^{(n+1)+} \xrightarrow{ROOH} {}^{n+}M\text{-}O\text{-}O\text{-}R + H^+ \qquad (10)$$

Scheme 4.5 Homolitic and heterolitic oxidation with transition metals

Considering CM oxidation, metal active site is strongly involved in the initiation step, leading to faster decomposition of CHP (Scheme 4.6, Eq. 11 and 12) and increasing concentration of free radicals in reaction mixture. This important action influence both velocity and selectivity of the CM process.

$$ROOH + M^{n+} \longrightarrow RO^{\bullet} + M^{(n+1)+} + OH^{-} \qquad (11)$$

$$M^{(n+1)+} + ROOH \longrightarrow M^{n+} + ROO^{\bullet} + H^{+} \qquad (12)$$

Scheme 4.6 Transition metal role in CHP decomposition (initiation step of CM oxidation)

Coming back to the selected precedents on CM oxidation shown in Table 4.1, an interesting example was reported by Zhang et. al., who used supported CuO nanoparticles and O_2 as an oxidant at 358K[22]. The results showed very good selectivity to CHP (93.2%) at a relatively high conversion level (44.2%). Additionally, the used catalyst could be recycled up to 6 times without loss of activity. Complex investigation of the transition metal compounds, supported on polymer as heterogeneous catalyst for CM oxidation process (353 K in O_2 atmosphere), was done by Hsu and Cheng et al.[19,20,36]. Among all tested materials superior results were obtained for $Cu(OAc)_2$-BR-0.6 (BR=Bio-Rex 70), which showed 99% selectivity towards CHP at 6.8% conversion. This result turned out to be 84% faster than blank sample (auto-initiated with CHP) under similar conditions.

We and others have shown that several Metal-Organic Frameworks (MOFs) can also be used as solid promoters for the aerobic oxidation (i.e., using only air or oxygen as the oxidant) of activated alkanes, such as tetralin[37], indane[28], and various alkylbenzenes[38], including cumene[29]. Wu and co-workers used $CuO@Cu_3(BTC)_2$ composite in cumene oxidation reaction in air flow, with addition of CHP as initiator. Maximum yields % of CHP obtained using the $CuO@Cu_3(BTC)_2$, CuO or $Cu_3(BTC)_2$ as catalyst were 18%, 13.6% and 8.7% respectively[27]. Unfortunately, the authors did not provide data on conversion level or selectivity obtained. According to the reported results, it seems that encapsulation of the CuO nanoparticles inside the MOF framework has a beneficial effect on the final CHP obtained.

Besides production of CHP as an intermediate for phenol production as commented above, CM oxidation has also other applications. Thus, many examples of highly active catalyst, reported in cumene oxidation, results also in high ability to decompose cumene hydroperoxide (CHP) formed as the primary product into the two main side products of this reaction – 2-phenyl-2-propanol (PP) and acetophenone (AP) – as commented above (Scheme 4.4). These are also highly valuable intermediates in the manufacture of perfumes, pharmaceutical and resins[39]. Nevertheless, this raises the question, how we can tune properties of our catalyst, either to promote formation of CHP and minimizing its decomposition, or otherwise, to successfully promote CHP decomposition into the target product (PP and/or AP), while avoiding unwanted accumulation of CHP in the reaction mixture, which may raise safety concerns.

In previous reports from our group, various MOFs (MIL-101, Cu(im)$_2$ and Cu(pymo)$_2$) were tested in oxidation reactions of different aromatic benzylic hydrocarbons[28,29]. In the case of cumene, 100% of conversion was reached using Cr^{3+}containing MIL-101 as a catalyst, with only 18% of selectivity towards CHP and 78% to AP. For both tested copper MOFs, high activity towards cumene conversion was attained (Figure 4.1a). Despite the similarity in coordination environment of Cu^{2+} in both materials (Cu^{2+} ions coordinated to diazaheteorcyclic compounds (imidazole and pyrimidine), leading to CuN$_4$ centers), Cu(im)$_2$ was better in terms of CHP decomposition and PP selectivity, which reached 74% (Figure 4.1b). On the other hand, Cu(pymo)$_2$ showed CHP accumulation period (Figure 4.1c), and smaller final selectivity towards PP (64%).

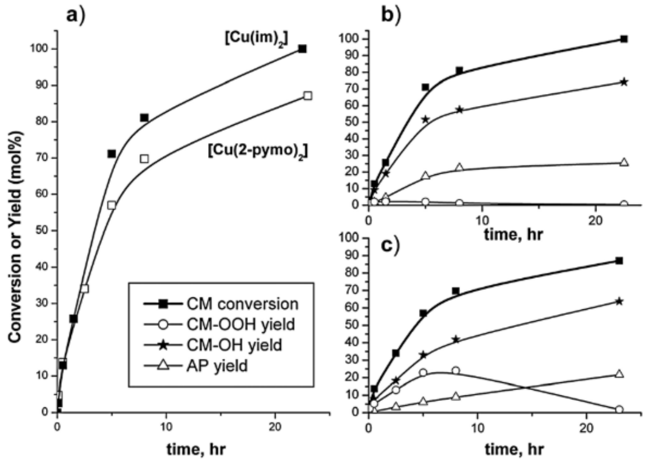

Figure 4.1 Conversion of CM over [Cu(im)$_2$] and [Cu(2-pymo)$_2$] (part a). Time conversion of CM and time evolution of products over [Cu(im)$_2$] and [Cu(2-pymo)$_2$] is also shown in parts (b) and (c), respectively. Reproduced from Catal. Sci. Technol., 2013,3, 371-379 with permission from The Royal Society of Chemistry.

DFT calculations were used to explain these differences in reactivity. It was shown that Cu(im)$_2$ possess a more adaptable framework, able to expand copper coordination sphere from 4 to 5 upon interaction with •OH radicals, while Cu(pymo)$_2$, produce the displacement of one of the 2-pymo ligands from Cu central site, which is obviously a more demanding process resulting in an overall slower rate of CHP decomposition.

An interesting study to illustrate the interplay between CM oxidation and CHP decomposition in order to obtain good selectivity of overall catalytic process to either CHP or PP/AP, was recently reported by Liao and co-workers, which studied carbon nanotubes (CNTs) and nitrogen-doped carbon nanotubes (NCNTs)[40]. As it was showed, NCNTs not only increased activity in aerobic oxidation of cumene (from 16% conversion obtain by CNTs to 74% for NCNTs) but also provided very high selectivity towards PP and AP (96.7%), whereas CNTs showed high selectivity to CHP (90%). DFT calculation revealed that the difference in catalytic performance and product distribution of NCNTs is caused by strong interaction with cumene hydroperoxide (Figure 4.2e,f), which once adsorbed on the catalyst surface is less probably to be substituted by other cumene molecule, unlike on the CNTs surface (Figure 4.2 a,d), where the affiliation to CHP is lower than CM.

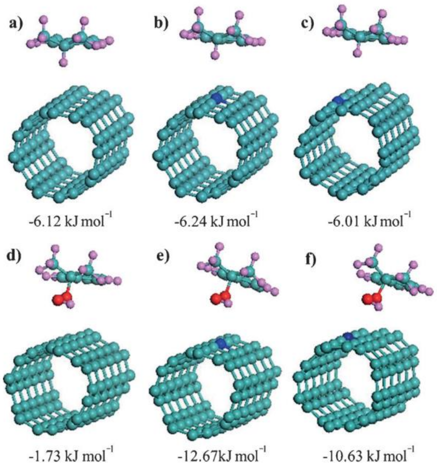

Figure 4.2 Optimized structures and adsorption energies of a–c) cumene and d–f) CHP on the surface of a, d) CNT; b, e) N site of NCNT; and c, f) adjacent C site of NCNT (C-green, O-red, N-blue, H-pink) Reproduced from ChemCatChem 2014, 6, 555-560 with permission from John Wiley and Sons.

This research was extended by kinetic study[41], proving that N doping of the CNTs can accelerate all the elementary reactions (Schemes 4.2-4.4), in particular the CHP decomposition to form active radicals (RO• and •OH), which was pointed as the rate-determining step (slowest rate constant).

In this chapter we described the catalytic properties of various isoreticular mono- (Co^{2+}, Ni^{2+}, Cu^{2+} and Zn^{2+}) and bimetallic (Co-Ni, Mn-Ni) trimesate MOFs, prepared by a facile and "green" synthesis method (see Chapter 3) as selective catalysts for the aerobic liquid phase oxidation of cumene. Additionally, the influence of active metal sites isolation in solid solution materials on activity and CHP selectivity will be evaluated. Moreover, by introducing defective linkers with strongly activating functional groups like aminoisophthalic (NH_2-IP) into the MOF structure, we will describe the effect on CHP decomposition and as a consequence, raising the selectivity towards PP and AP products.

4.2. Results and discussion

4.2.1. Catalytic studies of aerobic oxidation of cumene to cumene hydroperoxide: Mono- and bimetallic trimesate MOFs

As discussed above, the room temperature aqueous synthesis method[42] presented in Chapter 3 allowed us to produce crystalline, isoreticular monometallic MOFs of general formula $M_3BTC_2 \cdot 12H_2O$ (M= Co, Ni, Cu, Zn). Consequently, by adapting the above method, a second metal with desired metal ratio was introduced during synthesis procedure, resulting in bimetallic Co-Ni and Mn-Ni MOF series called CoXNi-BTC and MnXNi-BTC (where X represents (nominal) molar percentage of metal ions M substitution in bimetallic compound). Combining powder and single-crystal X-ray diffraction with SEM/EDX analysis of prepared catalysts, we demonstrated that bimetallic compounds form true solid solutions, where metal ions are distributed homogeneously in the crystal lattice. No appreciable enrichment of any metal at any crystal region such as tips or rims was observed. As previously described in Chapter 3, analysis of the evolution of the cell parameters with the composition of Co-Ni bimetallic compounds showed that Co^{2+} ions may preferentially occupy terminal framework positions, leading to well-defined and predictable environments for the metal ions in the framework as a function of the chemical composition of the binary materials. Unfortunately, Mn-Ni data analysis were not conclusive enough to provide similar statement of preferential siting of Mn^{2+} ions on terminal positions.

Nevertheless, the above findings can have clear implications on the catalytic behavior of the materials, since this should influence, e.g., the average distance between neighbor metal active sites as a function of the chemical composition of the solid solution, or the probability to have metal site isolation. In the following, we will show the effect of these parameters on the aerobic oxidation of cumene.

The scope of our preparative method was further extended to a series of mixed-ligand Co-BTC, in which the native trimesate ligands were combined with either isophthalic (IP) or 5-aminoisophthalic (NH_2IP) using mixture of both ligand salts in desired ratio (10, 20, 30% of defective linker).

Full characterization of catalysts used in this chapter, both mixed-metal and mixed-ligand is provided in Chapter 3.

4.2.1.1 Cumene oxidation over monometallic trimesate MOFs

Evaluation of catalytic activity for the aerobic oxidation of cumene was firstly performed on isoreticular monometallic compounds, Co-BTC, Ni-BTC, Cu-BTC and Zn-BTC (Table 4.2). Obtained results were compared together with blank (auto-catalyzed) reaction measured under the same conditions. While both Ni-BTC and Zn-BTC (Entries 2 and 4, Table 4.2,) were inactive for this reaction, Cu-BTC showed only slightly better CM conversion as compared to blank experiment (Entry 3, Table 4.3).

Table 4.2 Summary of catalytic results over monometallic MOFs [a]

Entry	**MOF**	**Conversion[b] (%)**	**Selectvity to CHP (%)**	**Productivity of CHP ($g·L^{-1}·h^{-1}$)**	**E-factor[c]**
1	Co-BTC	49	69	53	0.453
2	Ni-BTC	6	91	8	0.102
3	Cu-BTC	12	94	18	0.057
4	Zn-BTC	3	95	4	0.048
5	Blank	5	94	8	0.070

[a] Reaction conditions: 1 mL of cumene (7.17 mmol), catalyst (cumene-to-metal molar ratio = 150), $p(O_2)$= 4 bar, 363 K, 7 h of reaction. [b] Conversion (mol%), determined by GC. [c] Environmental factor, calculated as the mass ratio of waste to desired product

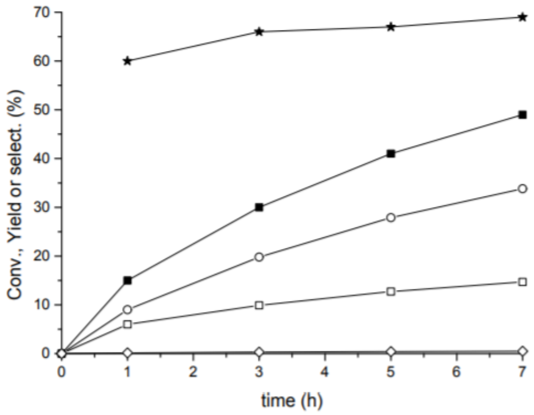

Figure 4.3 Cumene conversion (-■ -), yields of CHP (-○-), PP (-□ -), AP (-◇-), and selectivity to CHP (-*-) obtained over Co-BTC. Reaction conditions: 1mL of cumene (7.17 mmol), catalyst (cumene-to-Co molar ratio = 150) *p*(O_2)= 4 bar, 90°C.

On the contrary, Co-BTC afforded 49% conversion of CM after 7 h of reaction time, which represents an almost 10-fold increase with respect to blank sample, which produced only 5% CM conversion at the same reaction time (Entries 1 and 5 in Table 4.3). At the view of the catalytic performance of the monometallic MOFs considered here, we selected Co-BTC for further studies.

Additionally, to prove the dominant role of radical species in our system, 2,6-ditertbutyl-4-methylphenol (BHT) as a radical scavenger was used in cumene oxidation over Co-BTC. Results are shown in Table A.2.1 in Annex A.2. After addition of BHT, the reaction was totally prevented, which indicates that cumene oxidation catalyzed by Co-BTC is a radical-involved reaction.

Despite the high activity of the Co-BTC, selectivity towards CHP was only moderate, 69%, being 2-phenyl-2-propanol (PP) the main side product formed (30% selectivity), along with a small amount (*ca*. 1%) of acetophenone (AP) coming from non-selective decomposition side reactions (Scheme 4.4, Eq. 8). Time evolution of products and selectivity to CHP obtained over Co-BTC is shown in Figure 4.3. These results are in sharp contrast with the excellent CHP selectivity obtained in the blank experiment

(94%). The reason for the big CHP selectivity difference between both values is that Co^{2+} is also contributing in other reactions presented in Scheme 4.6 Eq. 11 and Eq.12, where decomposition of CHP takes place. Intensity of both mentioned reaction, and high concentration of free radicals can lead to faster termination step and production of PP and AP side products, which decreases the final CHP yield.

The activity of CoBTC calculated as turnover frequency (TOF) at short reaction time was 22.5 h^{-1} i.e., 22.5 mmol of CM were converted per mmol of metal and per hour. However, productivity of the reaction can also be expressed in terms of grams of CHP produced per liter of cumene and per hour (g L^{-1} h^{-1}). Note that this quantity takes into account the CM conversion over time and CHP selectivity, but it is independent of the amount of metal catalyst used. This makes the comparison between catalyzed and auto-catalyzed experiments straightforward. We have chosen calculated CHP formation rate, as the main value, in order to facilitate the comparison between catalyzed and non-catalyzed experiments. All productivities calculated in this way have been included in Table 4.2. Thus, in spite of the lower selectivity to CHP, the use of Co-BTC still produces an almost 7-fold increase of the productivity with respect to the blank experiment: from 8 to 53 g L^{-1} h^{-1} during 7 h of reaction, respectively (Entries 1 and 5, Table 4.2). However, considering the low CHP selectivity and the generation of relatively large amount of byproducts (PP and AP), the corresponding E-factor[43] of the metal-catalysed process was relatively high: 0.453, as compared to the auto-catalysed process with E-factor of 0.070. Overall, results obtained using Co-BTC as catalyst are still far from the optimum. We therefore started an optimization of the reaction conditions to improve these results.

4.2.1.2 Optimization of the reaction temperature

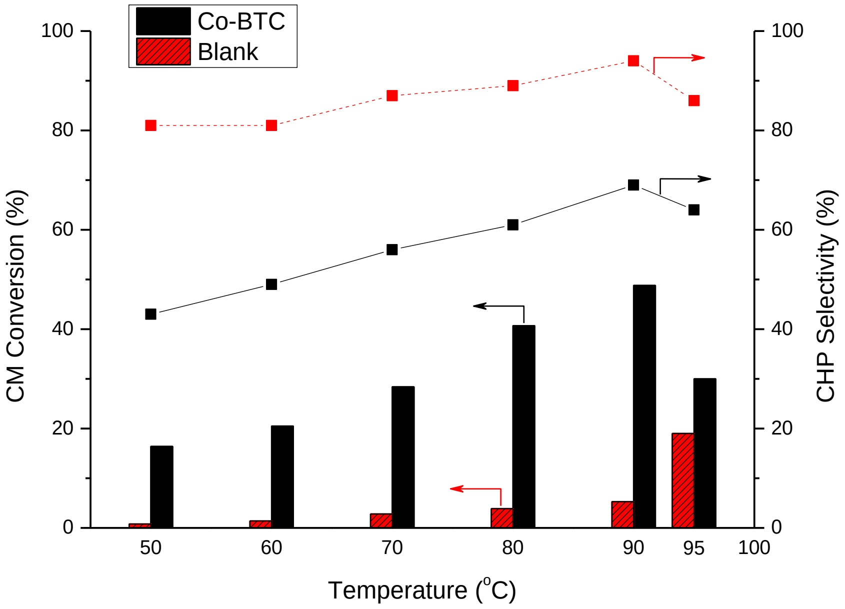

In order to determine the influence of various reaction parameters on the performance of trimesate MOFs and to improve the catalytic performance, our initial studies addressed the effect of temperature on the conversion and selectivity towards CHP. Figure 4.4 summarizes the catalytic results obtained for Co-BTC and auto-catalysed experiments at reaction temperatures ranging from 323 K – 368 K (50° to 95°C).

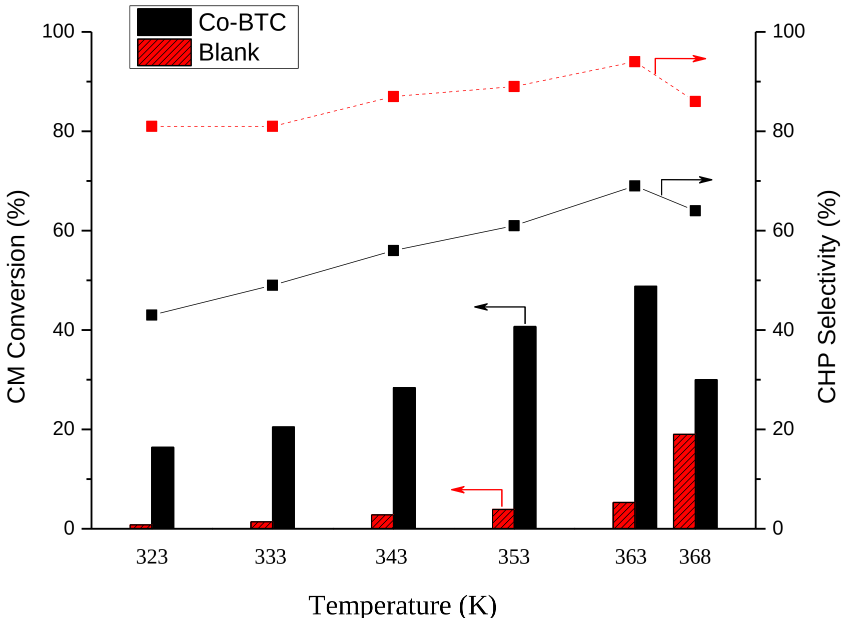

Figure 4.4 Effect of temperature on conversion (left) and selectivity to CHP (right) attained over Co-BTC and auto-catalyzed reactions. Conversions and selectivities reported in this figure correspond to 7 h of reaction

As it is shown, the increase of the temperature produces a concomitant increase of both cumene conversion and selectivity to CHP for both catalysed and non-catalysed reactions in the temperature range from 323 K – 368 K. Unfortunately, increasing further the reaction temperature above 363 K produced a gradual dehydration of the Co-BTC ($Co_3BTC_2 \cdot 12H_2O$), which is associated with an evident color change (from pink to purple) and a severe loss of the crystallinity of the MOF (see Figure A.3.4 in Annex A.3). Note that water molecules directly coordinated to the metal ions engage in a hydrogen bonding network that holds the MOF structure, so their removal causes the collapse of the framework. This crystallinity loss causes also a decrease of the catalytic activity of the material (from 49% conversion at 363 K to 30% at 368 K) and a slight decrease of selectivity to CHP (from 69% to 64%). Therefore, 363 K can be considered as the optimum reaction temperature for this type of materials, and this was the temperature selected for all the experiments presented below.

4.2.1.3 Optimization of catalyst's chemical composition for CHP production: bimetallic MOFs

As a next step, we evaluated the catalytic activity of various bimetallic MOFs having different Co/Ni ratios, hoping for beneficial effect of Cobalt active site separation, inside the Ni inactive matrix. Results obtained at 363 K are presented in Entries 3-6, Table 4.3. Detail kinetic data for bimetallic materials are shown in Experimental Section at the end of this Chapter (Figure A.3.5 in Annex A.3).

Table 4.3 Summary of results of CM oxidation over mono- and bimetallic Co-Ni MOFs of various compositions.[a]

Entry	**MOF**	**CM:Co^{2+} ratio**	**Conv.[b] (%)**	**Select. CHP (%)**	**Productivity CHP (g·L^{-1}·h^{-1})**	**E-factor[c]**
1	Blank	-	5	94	8	0.070
2	Co-BTC	150	49	69	53	0.453
3	Co33Ni-BTC	450	35	76	41	0.323
4	Co5Ni-BTC	3000	30	91	43	0.098
5	Co2Ni-BTC	7500	19	91	27	0.100
6	Co1Ni-BTC	15000	14	92	20	0.089
7	Ni-BTC	-	6	91	8	0.102

[a] Reaction conditions: 1 mL of cumene (7.17 mmol), catalyst (14 mg of MOF, the resulting cumene to Co^{2+} molar ratio is indicated), *p*(O_2)= 4 bar, 363 K, 7 h of reaction. [b] Conversion (mol%), determined by GC. [c] Environmental factor, calculated as the mass ratio of waste to desired product

As it can be seen, there is a progressive and gradual increase of cumene conversion with the Co content of the MOF, passing from the pure Ni-BTC (6%) to pure Co-BTC (49%). Meanwhile, the selectivity to CHP is maintained above 90% for a Co content below 5%, and then starts to decrease rapidly as the Co content increases further. Therefore, the Co5Ni-BTC bimetallic compound (containing 5 mol% of Co) was considered the best compromise between cumene conversion and CHP productivity and selectivity. With respect to the blank experiment, Co5Ni-BTC provides a much higher productivity (43 vs 8 g L^{-1} h^{-1}), while still maintaining an excellent selectivity to CHP (91% vs 94% attained by the non-catalysed reaction). Accordingly, the E-factor obtained with this bimetallic catalyst is low (0.098) and not far from that of the auto-catalysed process (0.070).

The gradual slowdown of the oxidation reaction moving form Co-BTC to Ni-BTC and all the bimetallic materials in between, can be attributed to a dilution effect, resulting in reduced amount of Co^{2+} ions available for this transformation (from a CM:Co^{2+} ratio of 150 in pure Co-BTC down to 15000 in Co1Ni-BTC). Meanwhile, the diminution of CHP selectivity upon increasing the amount of Co^{2+} ions can be explained by considering that Co^{2+} ions also catalyse side reactions leading to CHP decomposition, while Ni^{2+} ions are inactive for CHP decomposition. To address the influence of the presence of transition metal in the catalyst structure on CHP decomposition we conducted additional experiment. Here, CHP decomposition was tested over Co-BTC and Ni-BTC at 90°C under nitrogen atmosphere. Results showed that indeed Co-BTC is able to convert the CHP 9-fold faster (Table 4.4) than inactive Ni-BTC, which here served as a blank sample. Thus, these findings also explain the observed progressive decrease of CHP selectivity as the cobalt content of the solid increases.

Table 4.4 CHP decomposition over monometallic Co-BTC and Ni-BTC[a]

Catalyst	**Conversion[b] of CHP (%)**
Co-BTC	36
Ni-BTC	4

[a] Reaction conditions: 1 mL of acetonitrile, 14mg catalyst, 110 µL of CHP, and diphenylether as internal standard (50 µL) N_2 atmosphere, 363 K, 7 h of reaction. [b] Conversion (mol%), determined by GC

However, it is important to point out that dilution might not be the only factor responsible for the higher CHP selectivity of Co5Ni-BTC with respect to pure CoBTC. In our opinion, Co^{2+} site isolation (i.e., isolation of the active Co^{2+} ions in a matrix of inert Ni^{2+} sites) may play as well an important role, as we will discuss below. In order to investigate the superior effect of true active site isolation as compared with a simple dilution effect, we conduct the same reaction over physical mixture of monometallic materials (Co-BTC and Ni-BTC) in the appropriated ratio to obtain a Co:Ni molar ratio of 5:95; i.e., the same Co:Ni ratio found in bimetallic Co5Ni-BTC, and keeping a CM:Co^{2+} ratio of 3000. Table 4.5 summarize the catalytic data obtained for this experiment.

Table 4.5 Catalytic results obtained for the CM oxidation over bimetallic Co5Ni-BTC and a physical mixture of pure Co-BTC and Ni-BTC in a 5:95 ratio. The results obtained with pure Co-BTC are also included for comparison ^{a}

Entry	**MOF**	**Conversion** ^{c}**(%)**	**Selectivity to CHP(%)**	**Productivity of CHP (g·L-1·h-1)**
1	Co-BTC^b	49	69	53
2	CoBTC:NiBTC (5:95)	28	85	38
3	Co5%NiBTC	30	91	43

***a* Reaction conditions: 1 mL of cumene (7.17 mmol), catalyst (Co:Ni = 5:95 and CM to Co^{2+} molar ratio = 3000), *p*(O2)= 4 bar, 363 K, 7 h of reaction. *b* Same conditions as in Table 1 and 2; i.e., CM to Co^{2+} = 150). *c* Conversion (mol%), determined by GC**

Results showed that physical mixture produced a similar level of CM conversion (28%) as bimetallic MOF (30%) after the same reaction time, with a CHP selectivity of 85%. Although, this CHP selectivity was much higher than that of pure Co-MOF (i.e., 69%), it was still significantly below the selectivity obtained for the Co5Ni-BTC bimetallic compounds at the same level of conversion (85% vs. 91%). This difference of selectivity between the solid solution and the physical mixture might seem at first small, but it was significantly higher at lower levels of CM conversion, as shown in Figure 4.5.

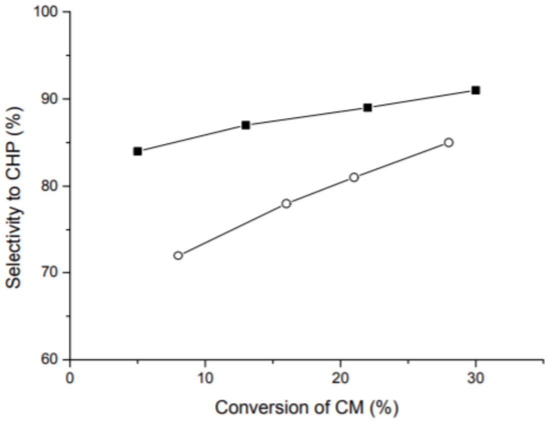

Figure 4.5 Comparison of CM conversion and CHP selectivity obtained over Co5Ni-BTC (-■-) and a physical mixture of pure Ni-BTC and Co-BTC monometallic compounds in a 5:95 ratio (-□-)

Therefore, although the physical dilution effect probably plays an important role, it is probably not the only effect determining the excellent CHP selectively attained over Co5Ni-BTC.

As it was concluded in previous Chapter, Co^{2+} ions are distributed homogeneously throughout the whole crystalline framework, with a high tendency to occupy terminal positions in the first place (up to a 33% concentration). It is then reasonable to assume that at such a low concentration (5% total cobalt content), most of the Co^{2+} ions will occupy terminal positions.

In the M-BTC crystalline framework, each ion in a terminal site is surrounded by 8 closest neighbors: 6 bridging atoms at distances $d_{term\text{-}bridg}$ = 5.89 Å (two sites), 5.63 Å (two sites) and 5.60 Å (two sites), and 2 terminal atoms at distances $d_{term\text{-}term}$ = 6.53 Å. Beyond these 8 closest neighbors, other metal-metal contacts are too distant (e.g., $d_{term\text{-}term}$ = 16.11 Å, $d_{term\text{-}bridg}$ = 10.40 Å and $d_{bridg\text{-}bridg}$ = 8.32 Å), so that they can be neglected. Figure 4.5 represents the possible structural arrangement of Co^{2+} ions considering spatial distribution of metal sites and the preferred site occupation of terminal sites.

Based on this estimation, the statistical probability of each configuration can be calculated as a function of the total cobalt content of the bimetallic compound (further details on the calculation procedure are given in the Experimental Section of this chapter).

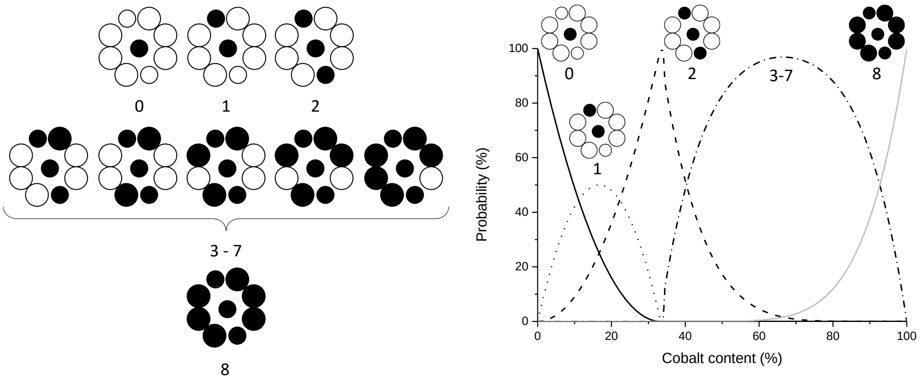

Figure 4.6 (*Left*) Possible arrangement of Co^{2+} ions in CoxNi-BTC bimetallic compounds. In these schematic drawings, a central Co^{2+} ion (black) in a terminal position is surrounded by 8 closest neighbors (less than 7 Å apart): 6 bridging sites (large circles) and 2 terminal sites (small circles), that can be occupied either by another Co^{2+} ion (black) or a Ni^{2+} ion (white). The number of Co^{2+} closest neighbors in each arrangement is indicated below each picture. (*Right*) Statistical probability of having each of the Co^{2+} arrangements as a function of the total cobalt content in the bimetallic compound, calculated as detailed in the Experimental Section of this Chapter.

Note that, according to the simple model considered above, the probability of having an isolated Co^{2+} site (i.e., a Co^{2+} ion surrounded by 8 Ni^{2+} ions) falls sharply at relatively low cobalt concentration. Thus, the probability of having site isolation would be of around 73% in Co5Ni-BTC, while this probability would fall down to 15% for Co20Ni-BTC, and to zero for Co33Ni-BTC, in which all Co^{2+} would be surrounded by two other Co^{2+} ions. This means that statistically 73% of the total Co^{2+} sites in Co5Ni-BTC will have no other Co^{2+} atom in any of the 8 closest neighbor positions. Or, in other words, that two neighbor Co^{2+} ions will be at least 8-9 Å apart.

Site isolation can be an important factor in determining catalytic properties of a material[44–46], which we also observed in the case of CM oxidation. Once a CHP molecule is formed in the main reaction, it can either desorb into the liquid phase, or it can undergo secondary oxidation or decomposition events at the surface of the catalyst that will consume CHP (decreasing the final CHP selectivity of the overall catalytic process). When the average separation between two neighbor Co^{2+} sites in the bimetallic material increases, the active sites become isolated, so that CHP decomposition and other secondary oxidation events are less likely to take place. This will result in an overall higher CHP selectivity of the catalytic process, as show schematically in Figure 4.7.

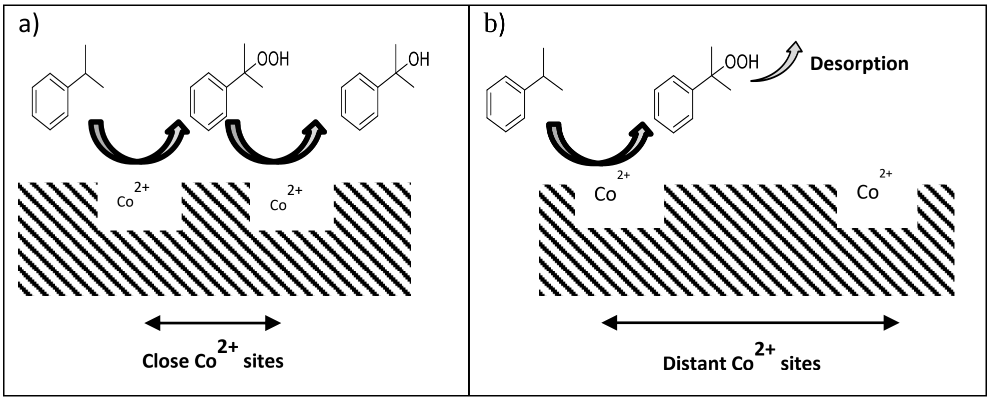

Figure 4.7 CHP decomposition is more likely to occur on close Co^{2+} sites (*Left*) than on distant, site isolated Co^{2+} sites (*Right*).

To lend further support to this "site isolation effect" as the responsible for the high CHP selectivities observed, we have extended our results to analogous series of bimetallic Mn-Ni BTC MOFs in which the catalytically active sites Mn^{2+} are diluted in an inert Ni^{2+} matrix. As it was mentioned in the previous chapter we were not able to prepare pure Mn-BTC with the same crystalline structure as the Co- and Ni- BTC compounds. Nevertheless, we were able to prepare isoreticular Mn-Ni bimetallic MOFs up to a maximum Mn concentration of 50%. We thus prepared Mn-Ni bimetallic trimesates having 1%, 2% and 5% Mn and used them as catalysts for the aerobic oxidation of CM. The catalytic results obtained are summarized in Table 4.6.

As compared with the Co-Ni compounds, the Mn-Ni MOFs are slightly more active for the cumene conversion, but less selective to CHP (see entries 1-3 in Table 4.6). Nevertheless, the same general trends are also observed: an increase of the Mn/Ni ratio in the solid solution produces an increase in the cumene conversion and a decrease of the selectivity to CHP.

Table 4.6 Catalytic results of CM oxidation over bimetallic Mn-Ni MOFs of various compositions[a]

Entry	MOF	CM:M^{2+} ratio	Conversion [b] (%)	Selectivity to CHP (%)	Productivity of CHP ($g \cdot L^{-1} \cdot h^{-1}$)	E-factor[c]
1	Mn1Ni-BTC	15000	25	90	36	0.112
2	Mn2Ni-BTC	7500	30	87	41	0.156
3	Mn5Ni-BTC	3000	43	77	51	0.307
[a] Reaction conditions: 1 mL of cumene (7.17 mmol), catalyst (14 mg of MOF, the resulting cumene to Co^{2+} or Mn^{2+} molar ratio is indicated), *p*(O_2)= 4 bar, 363 K, 7 h of reaction. [b] Conversion (mol%), determined by GC. [c] Environmental factor, calculated as the mass ratio of waste to desired product						

The best performance for Mn-Ni series was observed for Mn2Ni-BTC (Entry 2, Table 4.6), which gives 30% conversion with 87% selectivity to CHP. Using the same Mn^{2+} content, we performed physical mixture experiment using monometallic materials, to further support previous results on matrix isolation. Again, the solid solution compounds provide a higher CHP selectivity than simple physical mixtures: 87% vs. 82% (Table 4.7). In our opinion, these finding support the hypothesis of the site isolation effect as one of the reasons behind the elevated CHP selectivities obtained with bimetallic trimesate MOFs.

Table 4.7 Catalytic results of CM oxidation over Mn-BTC and Ni-BTC physical mixture[a] (2:98 molat ratio)

Entry	MOF	Conversion [b] (%)	Selectivity to CHP(%)	Productivity of CHP ($g \cdot L^{-1} \cdot h^{-1}$)	E-factor [c]
1	MnBTC:NiBTC(2:98)	32	82	42	0.222
2	Mn2%NiBTC	30	87	41	0.156
[a] Reaction conditions: 1 mL of cumene (7.17 mmol), catalyst (Co:Ni = 5:95 and CM to Co^{2+} molar ratio = 3000), *p*(O_2)= 4 bar, 363 K, 7 h of reaction. [b] Conversion (mol%), determined by GC. [c] Environmental factor, calculated as the mass ratio of waste to desired product					

4.2.1.4 Stability tests

Both Co5Ni-BTC and Mn2Ni-BTC catalysts were tested in terms of its stability. The materials were found to maintain the catalytic activity and CHP selectivity practically unchanged for at least 5 consecutive catalytic cycles (see Figure 4.8 for the Co5Ni-

BTC sample, and Figure. 4.9 for sample Mn2Ni-BTC). According to the XRD of the materials recovered after the reactions, both bimetallic compounds were found to maintain their crystallinity (see Figure 4.10).

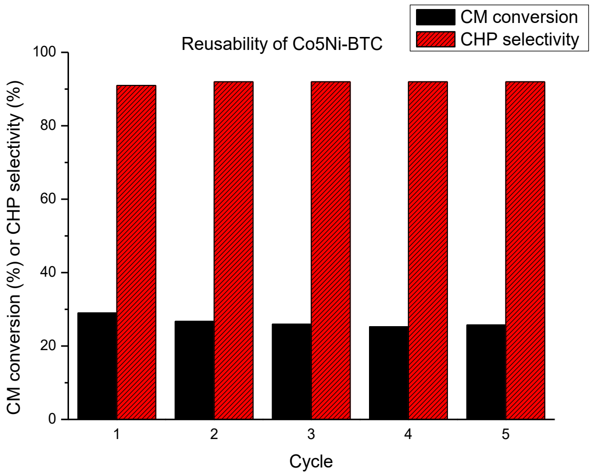

Figure 4.8 Reusability of Co5Ni-BTC bimetallic MOF in five consecutive catalytic cycles.

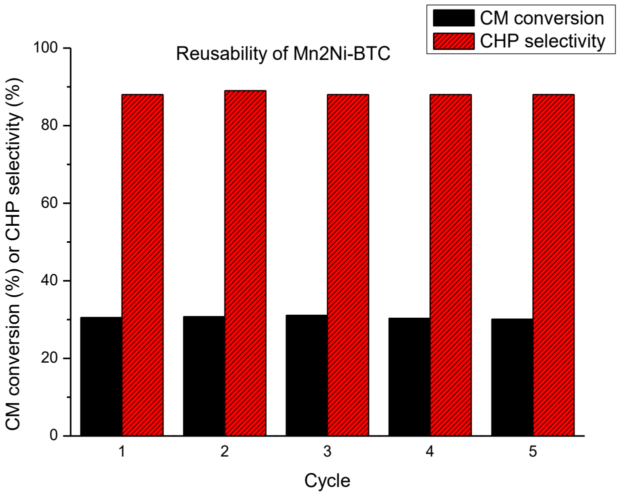

Figure 4.9 Reusability of Mn2Ni-BTC bimetallic MOF in five consecutive catalytic cycles

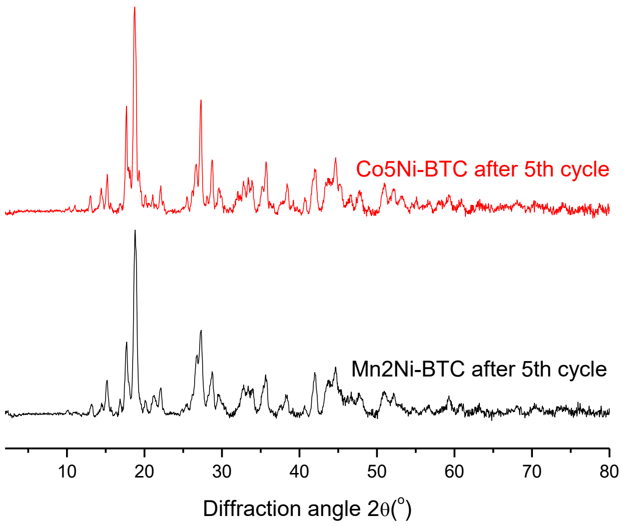

Figure 4.10 XRD of bimetallic MOFs after 5th cycle

4.2.2. Optimization of catalyst's chemical composition for PP production: mixed-linker MOFs

Cumene hydroperoxide as all organic peroxide, is very reactive and sensitive to temperature, acids, metals or to the presence of other compounds that provoke strong interaction with cumene hydroperoxide. In this part of the Chapter, we have evaluated the performance of various mixed-linker MOFs for the aerobic oxidation of cumene, with special emphasis on eventual changes in product distribution and CHP decomposition. In this way, we have considered isoreticular mixed-linker CoBTC compounds in which the parent trimesate ligands have been partially replaced by dicarboxylate ligands isophthalic acid (IP) or 5-aminoisophthalic acid (NH_2-IP). The synthesis and characterization of these mixed linker MOFs have been described in detail in Chapter 3.

In the first step, materials containing different amounts of isophthalic acid (7%, 14% and 18%) were tested in cumene oxidation reaction (see Table 4.8). Comparing with previous CoBTC results (conv. 49% and CHP selec. 69%), increasing substitution of IP up to 18% in the MOF, leads to a slight increase of CM conversion to 56% and a decrease of selectivity towards CHP (60%). Overall, the final selectivity and productivity of PP obtained over the sample Co-BTC 18%IP are 33% and 26 $g \cdot L^{-1} \cdot h^{-1}$, respectively.

In our opinion, the trend observed can be explained by an increasing concentration of point defects created in the structure as the amount of ditopic IP ligands incorporated in the material increases. As a consequence of these point defects, more Co^{2+} sites become progressively available to catalyse CHP decomposition, leading to the formation of PP (and a minor extend, also AP). Details of kinetic data and products distribution are presented in Figure A.3.6 in Annex A.3 In all tested mixed-ligand CoBTC-xIP MOFs the highest selectivity towards PP is obtained at the beginning of the reaction, and slightly decrease with time. On the other hand, selectivity to CHP slightly increase with reaction time evolution and seems to be stable even after prolonging reaction time.

Table 4.8 Cumene oxidation over CoBTC-IP materials[a]

Entry	**MOF**	**Conversion[b] (%)**	**Selectivity to PP (%)**	**Selectvity to CHP (%)**	**Productivity of PP ($g \cdot L^{-1} \cdot h^{-1}$)**
1	CoBTC	49	30	69	21
2	CoBTC - 7%IP	52	26	70	19
3	CoBTC - 14%IP	52	30	66	21
4	CoBTC - 18%IP	56	33	60	26

[a] Reaction conditions: 1 mL of cumene (7.17 mmol), 14mg of MOF catalyst, CM to Co^{2+} molar ratio = 150), $p(O_2)$= 4 bar, 363 K, 7 h of reaction. [b] Conversion (mol%), determined by GC

Additionally, to support our hypothesis, CHP decomposition experiments were performed using the procedure described above. Results are showed in Table 4.9. The obtained levels of CHP decomposition follow the same trend as in cumene oxidation, being the CoBTC-18%IP catalyst the most active in decomposition of CHP.

Table 4.9 CHP decomposition over CoBTC-IP MOFs[a]

Entry	**MOF**	**Conversion of CHP[b]**
1	Co-BTC	36
2	Co-BTC7%IP	40
3	Co-BTC14%IP	49
4	Co-BTC18%IP	55

[a] Reaction conditions: 1 mL of acetonitrile, 14mg catalyst, 110 µL of CHP, and diphenylether as internal standard (50 µL) N_2 atmosphere, 363 K, 7 h of reaction. [b] Conversion (mol%), determined by GC

Subsequently, mixed-ligand materials CoBTC-NH_2IP (6%, 15%, 32%), were tested in both reactions (CM oxidation and CHP decomposition). Results obtained for cumene oxidation are summarized in Table 4.10.

Table 4.10 CM oxidation over CoBTC-NH_2IP MOFs[a]

Entry	**MOF**	**Conversion[b] (%)**	**Selectivity to PP (%)**	**Selectvity to CHP (%)**	**Productivity of PP ($g·L^{-1}·h^{-1}$)**
1	CoBTC	49	30	69	21
2	CoBTC- 6%NH_2IP	66	32	63	29
3	CoBTC- 15%NH_2IP	68	36	58	35
4	CoBTC- 32%NH_2IP	71	48	43	47

[a] Reaction conditions: 1 mL of cumene (7.17 mmol), 14mg of MOF catalyst, CM to Co^{2+} molar ratio = 150), *p*(O_2)= 4 bar, 363 K, 7 h of reaction. [b] Conversion (mol%), determined by GC

In this case, more visible effect on ligand substitution can be seen. Increasing second ligand content have improving influence on both CM conversion and CHP decomposition. The conversion in CoBTC-32%NH_2IP material increased to 71% and selectivity towards CHP drop to 43%. Consequently, the final selectivity and productivity of PP obtained over the sample CoBTC-32%NH_2IP are 48% and 47 $g·L^{-1}·h^{-1}$, respectively. Details of kinetic data and products distribution are presented in Figure A.3.7 in Annex A.3. Similar trend of PP and CHP selectivity, described for CoBTC-xIP material was observed. CHP content stayed stable even after prolonging the reaction up to 24 h.

When CHP decomposition experiment was conducted over CoBTC-xNH_2 materials (see Table 4.11), increased activity towards CHP decomposition was observed, upon raising 5-aminoisophthalic (NH_2IP) ligand content inside the network, being Co-BTC32%NH_2IP the most active catalyst.

Table 4.11 CHP decomposition over CoBTC-NH_2IP MOF[a]

Entry	MOF	Conversion of CHP[b] (%)
1	Co-BTC	36
2	Co-BTC 6%NH_2IP	55
3	Co-BTC 15%NH_2IP	68
4	Co-BTC 32%NH_2IP	79

[a] Reaction conditions: 1 mL of acetonitrile, 14mg catalyst, 110 µL of CHP, and diphenylether as internal standard (50 µL) N_2 atmosphere, 363 K, 7 h of reaction. [b] Conversion (mol%), determined by GC

In spite of the significant increase of CHP decomposition rate observed upon ditopic linker incorporation (especially in the case of NH_2IP), the final selectivity to PP attained over our best mixed-linker compounds is only moderate (48% after 7h in the case of CoBTC-32%NH_2IP under the same conditions used. Such a low value is due to the persistence of CHP in the reaction medium, even after maintaining the reaction for 24 h.

However, the change in activity in cumene oxidation reaction and selectivity to CHP in CoBTC-32%NH_2IP MOF (71% and 43% respectively) comparing to Co-BTC (49% and 69%) can be attributed to the presence of structure defects formation introduced by the defective linker. Moreover, it has been previously shown that cumene conversion increases with CHP decomposition rate.[40] These findings were in agreement our previous reports[29], where catalyst activity in alkanes oxidation was directly connected to its ability of hydroperoxide decomposition.

As we already mentioned for our bimetallic catalyst with the best selectivity towards CHP production - Co5Ni-BTC, the low activity in CHP decomposition indicates that the formed CHP is more probable to desorb from the surface of the catalyst and only a minor fraction of it is decomposed for the new cycle. On the other site, a high concentration of transition metal together with incorporation of -NH_2 group on the benzene ring of the linkers can increase charge density of the surface, which can facilitate the CHP adsorption on the surface, resulting in a faster decomposition reaction of CHP. Therefore, more cumylhydroxy and cumyl free radicals are generated, leading to a higher reaction rate and PP concentration. Also small amount of AP is produced through β-scission (Scheme 4.4 Eq.8). The concentration of CHP remains quite high for CoBTC-32%NH_2IP probably because the decomposition rate of CHP is still too low. However, these results give us more insights to understand the differences in catalytic activity and product distribution between Co-BTC and CoBTC-32%NH_2 and may help to design better catalysts for cumene oxidation in the future.

4.3. Conclusions

In this Chapter we have shown that bimetallic Co-Ni and Mn-Ni trimesate MOFs prepared by a fast aqueous synthesis are excellent and reusable catalysts for the selective oxidation of cumene to cumene hydroperoxide. Isolation of Co^{2+} (or Mn^{2+}) in an inert Ni-BTC framework by progressively decreasing the total cobalt content of the binary solid solution is a good strategy to optimize CHP selectivity above 90%, and to minimize production of side products (mainly PP). This beneficial effect is probably due in part to a dilution effect: since Co^{2+} are the only sites that can catalyze CHP decomposition, we can expect a drop of the CHP selectivity as the cobalt content increases.

Meanwhile, the homogeneous distribution of Co^{2+} ions throughout the Ni-BTC framework and their preferential occupation of terminal sites allowed us to construct a simple model to calculate the statistical probability of having isolated Co^{2+} sites, surrounded only by (inactive) Ni^{2+} sites in the closest positions, as a function of the total cobalt content of the bimetallic compound. In this way, the excellent CHP selectivity (91%) obtained over our best compound, Co5Ni-BTC, can be explained in terms of a "site isolation" or "matrix isolation" effect. Indeed, according to our model, this sample statistically contains 73% of the total Co^{2+} ions as isolated sites, so that CHP decomposition/over-oxidation processes at the surface of the catalyst are not likely to occur before CHP desorption takes place. This "site isolation" effect was further supported by similar findings on Mn-Ni bimetallic compounds.

Moreover, introduction of defective linker with strongly activated group like 5-aminoisophthalic acid into Co-BTC structure, resulted in higher conversion level of CM and increases the selectivity towards PP. The significant drop in CHP selectivity over Co-BTC32%NH_2IP could be assigned to the creation of point defects and a concomitant increased charge density on the MOF surface, which have a direct impact in increasing CHP decomposition rate. Although the final PP selectivity obtained is still not satisfactory (up to 48%), the results obtained allow us to understand better the catalytic process, which may help to design better catalysts for cumene oxidation in the future.

4.4. References

(1) Zakoshansky, V. M. The Cumene Process for Phenol—Acetone Production. *Pet. Chem.* **2007**, *47* (4), 307–307.

(2) Reddy, P. V. L.; Kim, K.-H.; Kavitha, B.; Kumar, V.; Raza, N.; Kalagara, S. Photocatalytic Degradation of Bisphenol A in Aqueous Media: A Review. *J. Environ. Manage.* **2018**, *213*, 189–205.

(3) Leverne, H. The Curnene Hydroperoxide-Iron(I1) Reaction i n the Absence of Oxygen1. **1950**, *943* (2), 1634–1637.

(4) Costa, C.; Ribeiro, F.; Lazaro, J. Cumene Oxidation to Cumene Hydroperoxide Instituto Superior Técnico Abstract This Thesis of Master in Chemical Engineering Is Based on the Study of Cumene Oxidation to CHP , the Key Reaction of a Phenol Production Industrial Process . The Main Objective I. **2009**, 1–10.

(5) Sapunov, V. N.; Kurganova, E. A.; Koshel, G. N. Kinetics and Mechanism of Cumene Oxidation Initiated by N -Hydroxyphthalimide. *Int. J. Chem. Kinet.* **2018**, *50* (1), 3–14.

(6) Kasperczyk, K.; Zawadiak, J. Aerobic Oxidation of Cumene Catalysed by 4-Alkyloxycarbonyl-N-Hydroxyphthalimide. **2014**, *12* (11).

(7) Melone, L.; Prosperini, S.; Ercole, G.; Pastori, N.; Punta, C. Is It Possible to Implement N-Hydroxyphthalimide Homogeneous Catalysis for Industrial Applications? A Case Study of Cumene Aerobic Oxidation. *J. Chem. Technol. Biotechnol.* **2014**, *89* (9), 1370–1378.

(8) Hou, H. Y.; Shu, C. M.; Tsai, T. L. Reactions of Cumene Hydroperoxide Mixed with Sodium Hydroxide. *J. Hazard. Mater.* **2008**, *152* (3), 1214–1219.

(9) Amstrong, G. P.; Hall, R. H.; Quin, D. C.; Turck, K. H. W. Manufacture of Peroxidic Compounds. *United States Pat.* **1965**.

(10) Zakoshansky, V. M.; Griaznov, A. K.; Vasilieva, I. I.; Flumer, J. W.; Kight, W. D. Cumene Oxidation Process. *United States Pat.* **1998**, No. 19.

(11) Feder, R. L.; Fuhrmann, R.; Pisanchyn, J.; Elishewitz, S.; Insinger, T. H.; Chempolil; Mathew, T. Continuous Process for Preparing Cumene Hydroperoxide. *United States Pat.* **1975**.

(12) Folgado, C.; Gordicho, S. Cumene Oxidation to Cumene Hydroperoxide. *Master Thesis, Inst. Super. Tec. Univ. Tec. Lisboa* **2009**.

(13) Shannon, S. S. (Editor); Paul, L. A. (Editor). *Liquid Phase Aerobic Oxidation Catalysis: Industrial Applications and Academic Perspectives*; John Wiley & Sons, 2016.

(14) Opeida, I. A.; Kytsya, A. R.; Bazylyak, L. I.; Pobigun, O. I. Silver Nanoparticle Catalysis of the Liquid-Phase Radical Chain Oxidation of Cumene by Molecular Oxygen. *Theor. Exp. Chem.* **2017**, *52* (6), 369–374.

(15) Ismail, S. M. Liquid Phase Oxidation of Cumene over Heretogeneous Catalysts. J.Chem.Soc.Pak, Vol. 8, No.1 1984.

(16) Maksimov, M. V. T. Y. K. V. S. N. B. V. Selectivity and Mechanism of Cumene Liquid-Phase Oxidation in the Presence of Powdered Mixed Iron-Aluminum Oxides\rprepared by Alkoxy Method. *Appl. Catal.* **2000**, *193*, 237–242.

(17) Srivastava, R. K.; Srivastava, R. D. Kinetics of Liquid Phase Oxidation of Cumene with Cr ,

O ,, MnOz and Fe , O , Catalysts. **1975**, *323*, 317–323.

(18) Maksimov, Y.; Suzdalev, I. Study of Cumene Oxidation over Zirconia-, Titania- and Alumina-Based Complex Oxides Obtained by Sol-Gel Methods: Activity-Structure Relationships. *J. Mol. Catal. A Chem.* **1996**, *1169* (95), 167–173.

(19) Hsu, Y. F.; Cheng, C. P. Polymer Supported Catalyst for the Effective Autoxidation of Cumene to Cumene Hydroperoxide. *J. Mol. Catal. A Chem.* **1997**, *120* (1–3), 109–116.

(20) Hsu, Y. F.; Cheng, C. P. Mechanistic Investigation of the Autooxidation of Cumene Catalyzed by Transition Metal Salts Supported on Polymer. *J. Mol. Catal. A Chem.* **1998**, *136* (1), 1–11.

(21) Matsui, S.; Fujita, T. New Cumene-Oxidation Systems - O2 Activator Effects and Radical Stabilizer Effects. *Catal. Today* **2001**, *71* (1–2), 145–152.

(22) Zhang, M.; Wang, L.; Ji, H.; Wu, B.; Zeng, X. Cumene Liquid Oxidation to Cumene Hydroperoxide over CuO Nanoparticle with Molecular Oxygen under Mild Condition. *J. Nat. Gas Chem.* **2007**, *16* (4), 393–398.

(23) Yang, W.-J.; Guo, C.-C.; Tao, N.-Y.; Cao, J. Aerobic Oxidation of Cumene to Cumene Hydroperoxide Catalyzed by Metalloporphyrins. *Kinet. Catal.* **2010**, *51* (2), 194–199.

(24) Kobotaeva, N. S.; Skorokhodova, T. S.; Ryabova, N. V. Catalytic Systems of Cumene Oxidation Based on Multiwalled Carbon Nanotubes. *Russ. J. Phys. Chem. A* **2015**, *89* (3), 462–468.

(25) Xu, S.; Zhang, J.; Chen, B.; Lei, Z. Process Intensification on the Selective Catalytic Oxidation of Cumene with Ionic Liquids. *Chem. Eng. Process. - Process Intensif.* **2018**, *130* (December 2017), 88–92.

(26) Liao, S.; Chi, Y.; Yu, H.; Wang, H.; Peng, F. Tuning the Selectivity in the Aerobic Oxidation of Cumene Catalyzed by Nitrogen-Doped Carbon Nanotubes. *ChemCatChem* **2014**, *6* (2), 555–560.

(27) Wang, F.; Jia, S.; Li, D.; Yu, B.; Zhang, L.; Liu, Y.; Han, X.; Zhang, R.; Wu, S. Self-Template Synthesis of CuO@Cu3(BTC)2 Composite and Its Application in Cumene Oxidation. *Mater. Lett.* **2016**, *164*, 72–75.

(28) Santiago-Portillo, A.; Navalón, S.; Cirujano, F. G.; Xamena, F. X. L. I.; Alvaro, M.; Garcia, H. MIL-101 as Reusable Solid Catalyst for Autoxidation of Benzylic Hydrocarbons in the Absence of Additional Oxidizing Reagents. *ACS Catal.* **2015**, *5* (6), 3216–3224.

(29) Luz, I.; León, A.; Boronat, M.; Llabrés i Xamena, F. X.; Corma, A. Selective Aerobic Oxidation of Activated Alkanes with MOFs and Their Use for Epoxidation of Olefins with Oxygen in a Tandem Reaction. *Catal. Sci. Technol.* **2013**, *3* (2), 371–379.

(30) Albero, J.; García, H. Metal Organic Frameworks as Catalysts for Organic Reactions. In *New Materials for Catalytic Applications*; Elsevier, 2016; pp 13–40.

(31) Dhakshinamoorthy, A.; Alvaro, M.; Garcia, H. Metal–organic Frameworks as Heterogeneous Catalysts for Oxidation Reactions. *Catal. Sci. Technol.* **2011**, *1* (6), 856.

(32) Kholdeeva, O. A. Liquid-Phase Selective Oxidation Catalysis with Metal-Organic Frameworks. *Catal. Today* **2016**, *278*, 22–29.

(33) Zhang, J.; Biradar, A. V; Pramanik, S.; Emge, T. J.; Asefa, T.; Li, J. A New Layered Metal-Organic Framework as a Promising Heterogeneous Catalyst for Olefin Epoxidation Reactions.

Chem. Commun. (Camb). **2012**, *48* (52), 6541–6543.

(34) Sheldon, R. A.; Kochi, J. K. Introduction to Metal-Catalyzed Oxidations. *Met. Oxidations Org. Compd.* **1981**, 1–14.

(35) Cirujano, F. G.; Nowacka, A. *Zeolites and MOFs as Catalysts in Fine Chemical Reactions (Book Chapter)*; Amsterdam University Press, 2018.

(36) Hsu, Y. F.; Yen, M. H.; Cheng, C. P. Autooxidation of Cumene Catalyzed by Transition Metal Compounds on Polymeric Supports. *J. Mol. Catal. A Chem.* **1996**.

(37) Llabrés i Xamena, F. X.; Casanova, O.; Galiasso Tailleur, R.; Garcia, H.; Corma, A. Metal Organic Frameworks (MOFs) as Catalysts: A Combination of Cu2+ and Co2+ MOFs as an Efficient Catalyst for Tetralin Oxidation. *J. Catal.* **2008**, *255* (2), 220–227.

(38) Dhakshinamoorthy, A.; Asiri, A. M.; Herance, J. R.; Garcia, H. Metal Organic Frameworks as Solid Promoters for Aerobic Autoxidations. *Catal. Today* **2017**, 1–7.

(39) Scognamiglio, J.; Jones, L.; Letizia, C. S.; Api, A. M. Fragrance Material Review on 2-Phenyl-2-Propanol. *Food Chem. Toxicol.* **2012**, *50* (SUPPL. 2), S130–S133.

(40) Liao, S.; Chi, Y.; Yu, H.; Wang, H.; Peng, F. Tuning the Selectivity in the Aerobic Oxidation of Cumene Catalyzed by Nitrogen-Doped Carbon Nanotubes. *ChemCatChem* **2014**, *6* (2), 555–560.

(41) Mu, C.; Cao, Y.; Wang, H.; Yu, H.; Peng, F. A Kinetics Study on Cumene Oxidation Catalyzed by Carbon Nanotubes: Effect of N-Doping. *Chem. Eng. Sci.* **2018**, *177*, 391–398.

(42) Jin, L.; Liu, Q.; Sun, W. Room Temperature Solution-Phase Synthesis of Flower-like Nanostructures of [Ni3(BTC)2 12H2O] and Their Conversion to Porous NiO. *Chinese Chem. Lett.* **2013**, *24* (8), 663–667.

(43) Sheldon, R. A. The E Factor: Fifteen Years On. *Green Chem.* **2007**, *9* (12), 1273.

(44) Grasselli, R. K. Site Isolation and Phase Cooperation: Two Important Concepts in Selective Oxidation Catalysis: A Retrospective. *Catal. Today* **2014**, *238*, 10–27.

(45) Rogge, S. M. J.; Bavykina, A.; Hajek, J.; Garcia, H.; Olivos-Suarez, A. I.; Sepúlveda-Escribano, A.; Vimont, A.; Clet, G.; Bazin, P.; Kapteijn, F.; et al. Metal–organic and Covalent Organic Frameworks as Single-Site Catalysts. *Chem. Soc. Rev.* **2017**, *46* (11), 3134–3184.

(46) Osadchii, D. Y.; Olivos-Suarez, A. I.; Szécsényi, Á.; Li, G.; Nasalevich, M. A.; Dugulan, I. A.; Crespo, P. S.; Hensen, E. J. M.; Veber, S. L.; Fedin, M. V.; et al. Isolated Fe Sites in Metal Organic Frameworks Catalyze the Direct Conversion of Methane to Methanol. *ACS Catal.* **2018**, *8* (6), 5542–5548.

Chapter 5

Cobalt(II) bis(pyrazolate) MOFs as catalyst in cumene oxidation: a tag dependent selectivity

5.1. Introduction

In the last two decades, MOFs have been in-depth investigated in terms of their properties and functionality. Apart of well-known metal-organic frameworks families, based on oxygen-donor ligands, mostly carboxylates coupled to different metal ions, another big group are azolate-based MOFs[1,2]. Here, five-membered heterocycle organic ligand, can possess two or more nitrogen atoms like: pyrazolate (pz-), imidazolate (im-), 1,2,4-triazolate (tz-), 1,2,3-triazolate (vtz-) and tetrazolate (ttz-), where each nitrogen atom have donor function to bridge metal ions into polymeric structures[2]. Azolate ligands have several advantages, which can differentiate them from O-donors in carboxylate groups. In general, coordination behavior of azolate groups is easier to predict, the resulting materials often exhibit better thermal and chemical stability than the carboxylate-based counterparts and additionally, triazolates and tetrazolates- based MOF possess uncoordinated N atoms, which can serve as additional active sites.

In order to construct higher dimensional networks, polypyrazolate ligand can be used instead of monopyrazolates,. One of the example is 4,4'-bipyrazolate (BPZ) spacer, which coordination chemistry have been recently investigated. Pettinati et al.[3] were able to obtain Zn(BPZ) and Co(BPZ) isomorphous materials, with 3D porous networks, containing 1D square shape channels. Both materials crystallize in the tetragonal space group $P4_2$/mmc. Zn(II)/Co(II) ions are coordinated, within tetrahedral stereo- chemistry, by four N atoms of four-tetradentate BPZ ligands (Figure 5.1)

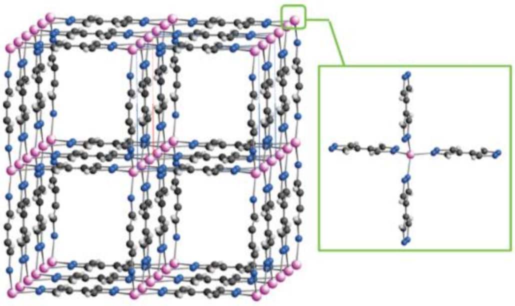

Figure 5.1 Zn(BPZ) crystal packing psecies. Zn, purple; N, blue; C, gray; H, light gray. Adapted with permission from Inorganic Chemistry 2012,9,5235-5245. Copyright 2012 American Chemical Society.

The same group extended they research to new functionalized linker 3,3'-Dimethyl-1H,1'-4,4'-bipyrazole - M(Me_2BPZ), with Co^{2+} and Zn^{2+} as metal ion. The obtain materials Co-Me_2BPZ·S and Zn-Me_2BPZ·S (Me-methyl group; S-solvent)[4], were isoreticular to the two couples of MOFs M-BPZ (M = Co, Zn; H_2BPZ = 1H,1′H-4,4′-bipyrazole)[3]. To investigate their textural properties all materials were compared in terms of N_2 and CO_2 adsorption at 77 K and 273 K, respectively. As could be expected, the empty volume and channel size decrease passing from M-BPZ > M-Me_2BPZ. A slight increase of E_{ads} of CO_2 in M-Me_2BPZ compare to M-BPZ, was explained by DFT calculation on CH_3-functionalized benzene, done by others[5]. The results lead to CH_3- positive effect, that improve the interaction between CO_2 and the aromatic ring by increasing electron density in aromatic system and in this way its interaction with CO_2 molecule.

A series of BPZ MOF isoreticular compounds containing NO_2 functionalized BPZ ligand, was also tested as CO_2 adsorbent[6]. These materials showed good thermal stability combined with permanent porosity. The Zn-BPZNO_2 and Co-BPZNO_2 samples, can be classified among best-performing, NO_2 containing MOFs for CO_2 uptake. Additional HR-PXRD analysis of materials under CO_2-loaded treatment and GC-MC calculation proved an interaction of CO_2 with the C(3)-NO_2 moiety.

Many other isoreticular BPZ family materials like M(BDP) [M=Co[7],Zn[8] ; H_2BDP=1,4-bis(pyrazolyl)benzene] were also studied, however most of the research was dedicated to examined their sorption properties. Due to relatively high thermal and chemical stability, provided by strong Metal-N bond, BPZ materials can also be very promising candidate in catalysis. In this chapter we attempted to investigate the catalytic performance of isoreticular series of BPZ materials with functionalized organic linker containing -NH_2 and -NO_2 groups. We have thus evaluated the applicability of Co-containing functionalized BPZ compounds for the aerobic oxidation of cumene (CM).

5.2. Results and discussion

5.2.1. Synthesis and characterization

Synthesis and characterization of bis(pyrazolate) materials described in this chapter was carried out in collaboration with the groups of Simona Galli (University of Insubria), Corrado di Nicola (University of Camerino) and Andrea Rossin (University of Florence).

Three metal-organic frameworks (MOFs) of general formula **Co(BPZ)** and **Co(BPZX)** (BPZ^{2-} = 4,4'-bis(pyrazolate); $BPZX^{2-}$ = 3-X-4,4'-bis(pyrazolate), X = NH_2, NO_2 (see Figure 5.2) built up with ligands bearing different functional groups on the same 4,4'-bis(pyrazolate) skeleton, was synthesized under solvothermal conditions in DMF solution (detail synthesis procedure can be find in Annex A.1.). All of the materials were obtained in high yields in the form of air-stable powders insoluble in the most common organic solvents, which suggests their polymeric nature. Consequently, MOFs were characterized by several analytical methods.

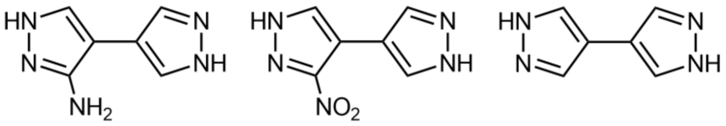

Figure 5.2 Molecular structure of the ligands used in the materials synthesis: 3-amino-4,4'-bipyrazole (H_2BPZ-NH_2, left), 3-nitro-4,4'-bipyrazole (H_2BPZ-NO_2, centre) and 4,4'-bipyrazole (H_2BPZ, right)

All prepared samples (activated) were characterized by Powder X-ray diffraction (Figure 5.3-5.5). Materials were deposited in the hollow of a silicon zero-background plate 0.2 mm deep (Assing Srl, Monterotondo, Italy). PXRD data acquisition was performed with the diffractometer described in the Chapter 2 in the 2θ range 5.0-105.0°, with steps of 0.02° and an overall scan time of approximately 12 hours.

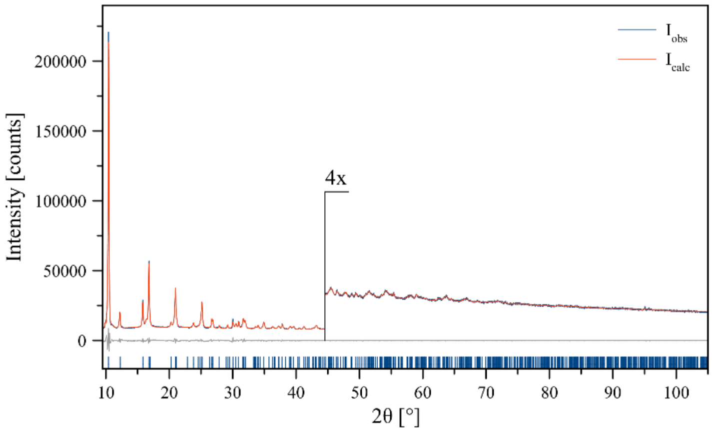

Figure 5.3 Graphical result of the Le Bail refinement performed on the X-ray diffraction pattern of Co(bpz). R_{wp}: 2.59%. Blue line: observed pattern; red line: calculated pattern; grey line: difference between observed and calculated patterns; blue ticks: peak maximum positions

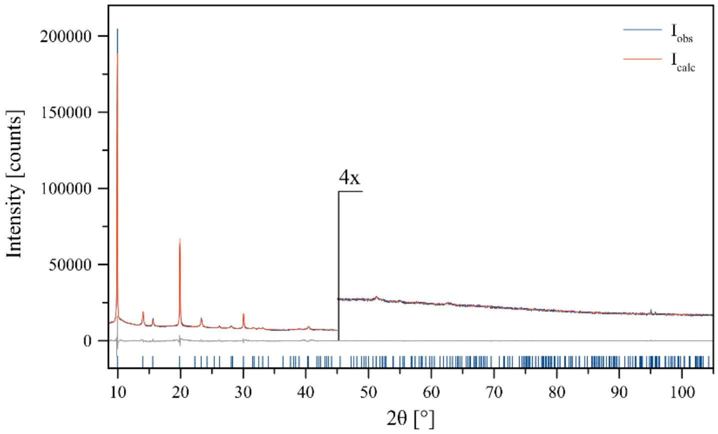

Figure 5.4 Graphical result of the Le Bail refinement performed on the X-ray diffraction pattern of Co(bpzNO$_2$). R_{wp}: 2.57%. Blue line: observed pattern; red line: calculated pattern; grey line: difference between observed and calculated patterns; blue ticks: peak maximum positions

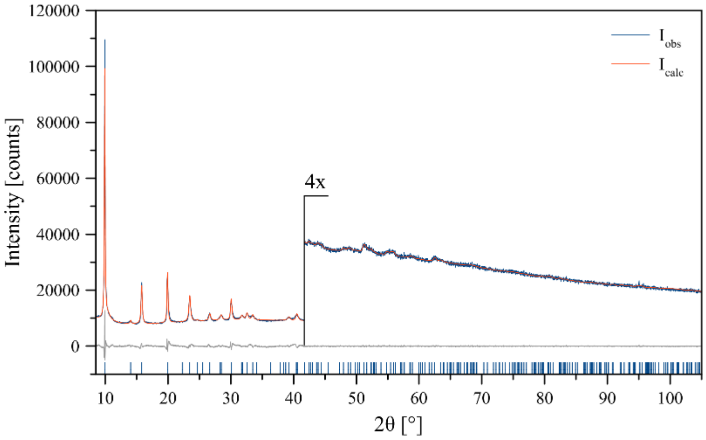

Figure 5.5 Graphical result of the Le Bail refinement performed on the X-ray diffraction pattern of Co(bpzNH$_2$). R$_{wp}$: 2.53%. Blue line: observed pattern; red line: calculated pattern; grey line: difference between observed and calculated patterns; blue ticks: peak maximum positions

Table 5.1 Crystalographic data of prepared Co(BPZX) materials

Catalyst	**Co(BPZ)=Zn(BPZ)**	**Co(BPZNO$_2$)** **·0.7 DMF**	**Co(BPZNH$_2$)** **Phase 1** **$C_6H_5CoN_5·2H_2O$**	**Co(BPZNH$_2$)** **Phase 2** **$C_6H_5CoN_5·0.7H_2O$**
Fw, g/mol	191.1	287.23	242.1	218.7
Cryst sys	tetragonal	tetragonal	Orthohombic	Orthohombic
Space group, Z	P4$_2$/mmc, 2	P4$_2$/mmc, 2	Cccm, 4	Cccm, 4
***a*, Å**	8.831(2)	8.9093(6)	12.350(7)	12.530(12)
***b*, Å**	8.831(2)	8.9093(6)	12.815(8)	12.758(13)
***c*, Å**	7.301(2)	7.362(2)	7.2225(14)	7.2400(11)
α, deg	90	90	90	90
β, deg	90	90	90	90

γ, deg	90	90	90	90
V, Å^3	569.4(3)	584.4(2)	1143.1(10)	1157.4(16)
ρ_{calcd} g cm^{-3}	1.153	1.632	1.407	1.255
Refinement 2Θ range, deg	8.5-105.0	8.5-105.0	8.5-105.0	8.5-105.0
N_{data}	4851	4826	4826	4826
R_p, R_{wp} [a]	0.081, 0.114	0.019, 0.025	0.014, 0.018	0.014, 0.018
R_{Bragg} [a]	0.052	0.006	0.006	0.007

[a] $R_p = \sum_i |y_{i,o} - y_{i,c}|/\sum_i |y_{i,o}|$; $R_{wp} = [\sum_i w_i(y_{i,o} - y_{i,c})^2/\sum_i w_i(y_{i,o})2]^{1/2}$; $R_{Bragg} = \sum_n |I_{n,o} - I_{n,c}|/\sum_n I_{n,o}$, where $y_{i,o}$ and $y_{i,c}$ are the observed and calculated profile intensities, respectively, while $I_{n,o}$ and $I_{n,c}$ are the observed and calculated intensities. The summations run over i data points or n independent reflections. Statistical weights wi are normally taken as $1/y_{i,o}$.

MOFs Co(BPZ) and Co(BPZNO$_2$) crystallize in tetragonal space group P4$_2$/mmc and their crystalline structures were reported previously[3,6] (see Table 5.1). They are isoreticular to number of other known MOFs, such as M(BDP) [M=Co[7], Zn[8] H$_2$BDP=1,4-bis(pyrazolyl)benzene]. Co(BPZNH$_2$) is retraceable to those MOFs with orthorhombic *Cccm* crystallographic symmetry. In all the batches examined there are two phases with slightly different unit cell parameters and ligand conformation. The intrinsic ligand asymmetry may generate a locally different conditioned order of the NH$_2$ substituents (Figure 5.6).

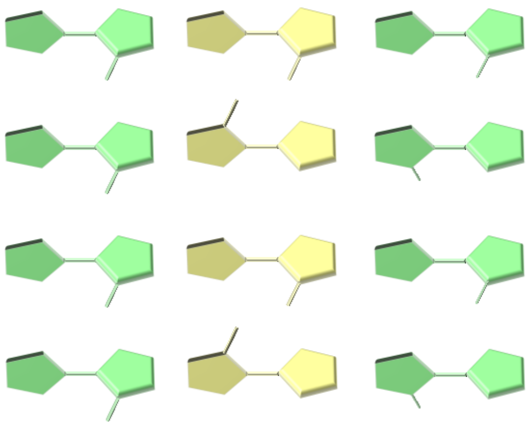

Figure 5.6 Conditioned order in Co(BPZNH$_2$): possible reciprocal dispositions of the amino groups along the *a*- and *b*-axis, in the hypothesis that the 3-amino-4,4'-bipyrazolate ligand is not planar

On one hand, in **Co(BPZNH$_2$) Phase 1** a torsion angle of ~20° was found between the two pyrazolate rings; on the other hand, **Co(BPZNH$_2$) Phase 2** shows a planar ligand (Figure 5.7a). Tetrahedral CoN$_4$ nodes (Figure 5.7b) and *exo*-tetradentate spacers build up a 3-D (4,4)-connected open framework (Figure 5.7c), featuring 1-D rhombic channels parallel to the crystallographic direction [001]. The aperture of the channels, and consequently the accessible volume, are strictly related to the ligand orientation and the torsion angle between its pyrazolate rings. At room temperature and pressure conditions, the empty volume[9] of the two different phases ranges between 44 and 46%, which translates into a pore volume of ~0.37-0.39 cm^3 g^{-1}. The ($3^{12} \cdot 4^{24} \cdot 5^9$) network topology belonging to the **10-c** net is confirmed by the topological analysis performed with TOPOS 4.0[10] considering both the Co(II) ions and the ligands as tetra-connected nodes.

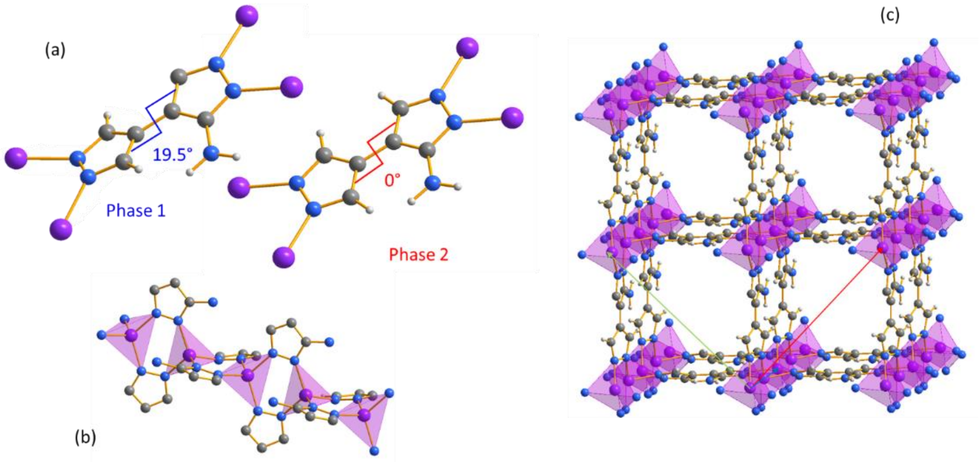

Figure 5.7 Representation of the crystal structure of Co(BPZNH$_2$)**: (a) the different ligand torsion angles in** Phase 1 **and** Phase 2**. (b) the μ-pyrazolate coordination mode through the 1-D chains along the [001] crystallographic direction. (c) Portion of the crystal packing of** Co(BPZNH$_2$) Phase 1 **viewed in perspective along the [001] crystallographic direction. Carbon, grey; hydrogen, light grey; cobalt, violet; nitrogen, blue. The solvent molecules have been omitted for clarity. Main bond distances and angles: Phase 1: Co-N, 2.062(2), 2.081(2) Å; Co···Co, 3.611(2), 8.899(6) Å; N-Co-N, 109.6(6)-110.8(6)°; Phase 2: Co-N, 2.051(5) Å; Co···Co, 3.620(4), 8.941(6) Å; N-Co-N, 108(2)-112.7(14)°**

Thermal Behaviour. Before carrying out the simultaneous thermal analysis (STA), a sample of as-synthesized **Co(BPZNH$_2$)·DMF** was kept in an oven at 323 K for 4 hours, to eliminate traces of humidity on the material outer surface. As shown by the TGA trace (Figure A.3.15a in Annex A.3), the MOF is stable under N_2 up to ~673 K (decomposition temperature onset), showing a higher thermal stability than **Co(BPZ)** (T_{dec} = 593 K)[3] and **Co(BPZNO$_2$)** (T_{dec} = 623 K)[6]. Before decomposition, the MOF undergoes two weight losses (~2.9% in the temperature range 303-351 K; ~19.0% in the temperature range 370-583 K). The first weight loss can be confidently ascribed to water vapour adsorbed by the sample during the transfer from the oven to the STA instrument. The second weight loss can be reasonably interpreted as the loss of 0.7 mol of DMF per mol of **Co(BPZNH$_2$)** (calculated weight loss 19.6%). The residual mass (30.2%) can be interpreted in terms of cobalt(II) oxide (CoO; calculated value 28.4%). *In situ* variable-temperature PXRD carried out in air on a sample of as-synthesized

Co(BPZNH$_2$)·DMF shows that the MOF does not lose its porosity upon solvent loss (Figure A.3.15 in Annex 3). The two orthorhombic phases are clearly visible (in terms of peak doubling) up to 423 K (blue traces in Figure A.3.15b in Annex 3); starting from 443 K, their PXRD patterns coalesce and right-side anisotropic broadening of specific Miller indexes classes appears. At 623 K, decomposition is complete.

N$_2$ Adsorption. The porous nature of **Co(BPZNH$_2$)** was investigated through N_2 adsorption at 77 K after thermal activation (403 K, 10^{-6} Torr, 24 h). As shown in Figure 5.8, **Co(BPZNH$_2$)** shows a type IV isotherm with an extended hysteresis loop typical of a micro-mesoporous material with slit-like pore shape; the BET specific surface area equals 317 m^2/g. This value is comparable to that found for Zn(BPZNH$_2$) (395 m^2/g)[11] but lower than that of the untagged analogue **Co(BPZ)** (926 m^2/g)[3] and of the nitro-tagged **Co(BPZNO$_2$)** (645 m^2/g)[6]. The total pore volume evaluated at $p/p^0 = 0.98$ equals 0.21 cm^3/g. The limiting micropore volume (0.14 cm^3/g) estimated through the application of the Dubinin-Astakhov model to the N_2 adsorption isotherm is much lower than the pore volume calculated from the crystal structure (0.38 cm^3/g, *vide supra*), which suggest that the real sample porosity is different from the crystallographic one obtained through purely geometrical considerations. In fact, the orthorhombic/tetragonal phase transition that is commonly observed in bipyrazolate MOFs[3,6,11] reveals a high framework structural flexibility that may reduce the pore size. The Dubinin-Astakhov analysis also revealed that the micropore volume represents the main contribution to the total pore volume (67%). In **Co(BPZNH$_2$)** there are two different micropore sizes (retrieved from the DFT analysis – slit pore shape of carbon-based materials) of 1.4 and 1.6 nm. The mesopore size (estimated through the BJH model applied to the desorption branch of the isotherm) is of 3.9 nm.

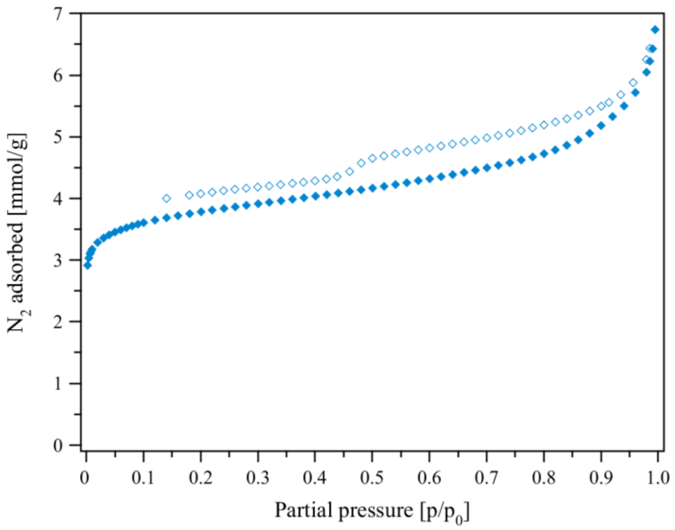

Figure 5.8 N_2 adsorption isotherm measured at 77 K on Co(BPZNH$_2$). The desorption branch is drawn with empty symbols

O_2 Adsorption. Co(BPZ) and **Co(BPZX)** MOFs were tested as a O_2 adsorbents at T = 195 and 273 K and p_{O2} up to 1 bar (Figure 5.9 and Figure A.3.16 in Annex A.3, respectively). Table 5.2 collects the BET areas and the main O_2 adsorption data. The nitro-tagged MOF is a better adsorbent at higher temperatures, while the untagged **Co(BPZ)** is the best O_2 adsorbent at low temperatures. In terms of weight percentage, the amount of O_2 adsorbed at 195 K is proportional to the respective BET areas.

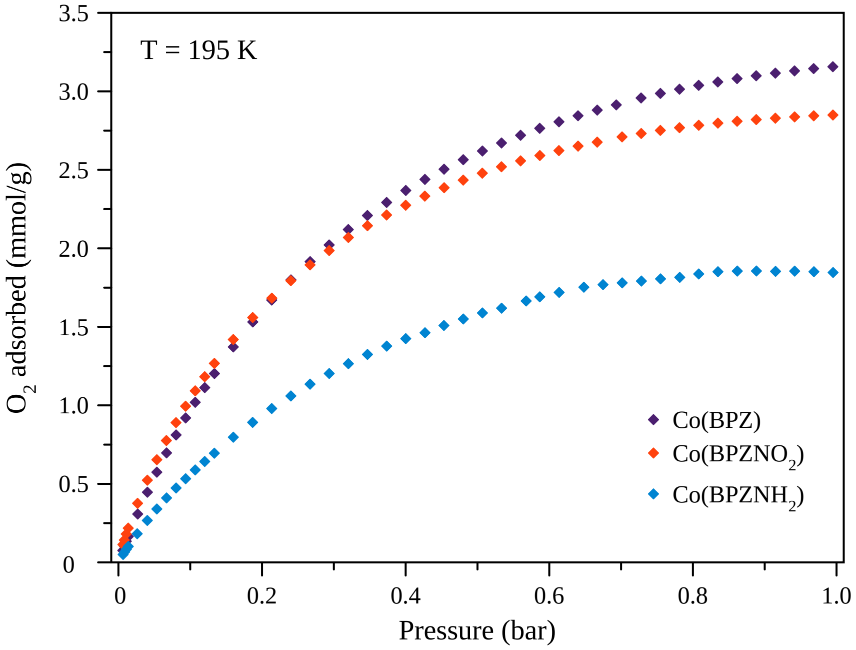

Figure 5.9 O_2 adsorption isotherms measured at 195 K on Co(BPZ)**,** Co(BPZNO$_2$) and Co(BPZNH$_2$)

Table 5.2 Collective data on BET areas, O_2 uptake (at 1 bar and T = 273 K and 195 K) and oxygen isosteric heat of adsorption (Q_{st}) of the Co(BPZ) and Co(BPZX) MOFs presented in this work

	BET area (m^2/g)	**Q_{st} (kJ/mol)**	**O_2 adsorbed (mmol/g)**	
			273 K	**195 K**
Co(BPZ)	926[3]	17.7	0.6 (2.0 wt.%)	3.2 (10.1 wt.%)
Co(BPZNO$_2$)	645[6]	13.7	1.1 (3.5 wt.%)	2.8 (9.1 wt.%)
Co(BPZNH$_2$)	317	15.9	0.5 (1.6 wt.%)	1.8 (5.9 wt.%)

To quantify the strength of the O_2-MOF interactions, the isosteric heat of adsorption (Q_{st}) of O_2 was evaluated (Table 5.2) with a variant of the Clausius-

Clapeyron equation, through the comparison of the O_2 adsorption isotherms recorded at 273 and 195 K. The isosteric heat of adsorption reflects the interaction strength between O_2 and the inner pore walls of the MOFs. The highest value of 17.7 kJ/mol calculated at zero coverage is that estimated for **Co(BPZ)**. The Q_{st} trend follows the order **Co(BPZ)** > **Co(BPZNH$_2$)** > **Co(BPZNO$_2$)**. In general, the Q_{st} values found for these MOFs are higher than those found for the Co(II) MOFs MFU-1 (11.1 kJ/mol) and MFU-2 (8.5 kJ/mol) built with the 1,4-bis[(3,5-dimethyl)pyrazol-4-yl]benzene ligand and featured by much higher BET areas (1525 and 1474 m^2/g, respectively)[12]. The thermodynamic affinity for O_2 of **Co(BPZ)** is comparable to that of PCN-9 (17.8 kJ/mol), a Co(II) MOF containing the triazine-2,4,6-triyltribenzoate spacer and with a BET area of 1064 m^2/g[13].

5.2.2. Cumene oxidation catalysis with Co(BPZX).

In the following step, the effect of different tags on catalytic cumene oxidation reaction and product distribution was evaluated. Firstly, we tested Co(BPZ) without any functional groups. The catalytic results are showed in Table 5.3

The results showed good activity of the material towards CM oxidation (34% conversion attained after 7 h of reaction), as compared with the blank (auto-catalysed) process, which afforded 5% CM conversion under the same reaction conditions. Meanwhile, the selectivity towards CHP obtained over CoBPZ was very high (maximum CHP selectivity of ~90% at 8% CM conversion attained after 1 h), and only slightly lower than the autocatalytic process (94%). This selectivity slightly decreases as the reaction is continued (down to 84% at 34% CM conversion after 7h), which lead to formation of side products like PP and AP. Presence of these side products, however in this case it is minority, is a consequence of CHP decomposition, which is catalysed by the same metal active sites that catalyse CM oxidation.

Table 5.3 Aerobic oxidation of cumene [*a*]

				Selectivity %)			
Entry	Catalyst	time (h)	Conv.(%)[b]	CHP	PP	AP	CMD
1	Blank	7	5	94	6	0	0
2	Co(BPZ)	1 7	8 34	90 84	10 15	0 1	0 0
3	Co(BPZNO$_2$)	1 7	10 32	74 74	22 22	3 3	1 1
4	Co(BPZNH$_2$)	7 24	72 84	16 7	69 73	11 14	4 6
5	CoBTC	7	49	69	30	1	0

[a] Reaction conditions: 1 mL of cumene (7.17 mmol), catalyst (cumene-to-metal molar ratio = 150), *p*(O_2)= 4 bar, 363 K, 7 h of reaction. [*b*] Conversion (mol%), determined by GC.

In Chapter 4 we have described the catalytic activity for the aerobic oxidation of CM of mono- and bimetallic trimesate compounds prepared from aqueous solution. As compared with monometallic CoBTC, the CM conversion obtained with the present CoBPZ material was found to be slightly lower under the same experimental conditions (34 vs 49% CM conversion after 7 h), but the selectivity to CHP was significantly higher: 84 vs 69%, for CoBPZ and CoBTC, respectively (compare entries 2 and 5 in Table 5.3). These differences in catalytic activity and CHP selectivity reflect the different chemical and coordination properties of Co^{2+} sites imposed by the nature of the ligand. The general trend is observed again here, so that the higher CM conversion is accompanied by a lower CHP selectivity.

Introduction of –NO_2 groups on the pyrazolate ring, [Co(BPZ-NO_2)], did not have a significant influence on the catalytic activity: at short reaction times, CoBPZ-NO_2

was only slightly more active than CoBPZ (10% vs. 8% CM conversion after 1 h for CoBPZ-NO_2 and Co(BPZ), respectively), while at longer reaction times, the activity was practically the same (32% vs 34% CM conversion after 7 h). However, small changes were observed in product distribution for the CM oxidation process, decreasing the CHP selectivity to 74% and slightly favouring the formation of PP and AP. In the case of CoBPZ-NO2, formation of small traces (ca. 1% selectivity) of an additional, heavier product, was also observed, that has been identified as a cumene dimer[14] (CMD). Formation of this dimer comes from the direct coupling of two cumyl radicals, which is an additional termination of the radical chain reaction alternative to those leading to PP and AP formation (see Chapter 4).

More significant changes were observed when –NH_2 were introduced into the pyrazolate ring, Co(BPZ-NH2). In this case, catalyst activity and distribution of the cumene oxidation products change dramatically (see Figure A.3.17 in Annex A.3), as compared with both Co(BPZ) and CoBPZ-NO_2. Conversion of CM after only 1 h of reaction time was already 39%, which increased to 72% after 7 h, while the selectivity to CHP dropped to 16%. Interestingly, the resulting selectivity to PP formation obtained over CoBPZ-NH_2 was increased up to 69%. Extending further the reaction time only produced a slight increase of conversion and selectivity to PP (up to 84% CM conversion and 73% PP selectivity after 24 h), but the amount of cumene dimer formed increased significantly, accounting for up to 6% of all converted CM.

As was described in previous Chapter, CHP is the primary product of the aerobic oxidation of CM, while PP and AP are side products coming from CHP decomposition. Therefore, PP and AP formation do depend on the ability of the Co^{2+} sites to decompose the CHP formed in the main reaction. In this sense, we have observed that a similar dependency exists between CM conversion and CHP decomposition for other MOFs[15] (see Chapter 4). According to the catalytic data shown in Table 5.3, the differences in product distribution between Co(BPZX) compounds should then be related with the ability of the catalyst to oxidize CM and, at the same time, to decompose CHP. We thus carried out additional experiments of CHP decomposition over the different Co(BPZX) compounds. The results obtained are summarized in Table 5.4.

Table 5.4 Decomposition of CHP over MOFs[a]

		CHP decomposition (%)	
Entry	Catalyst	7 h	24 h
1	Blank	2.8	4.4
2	Co(BPZ)	4.4	7.1
3	Co($BPZNO_2$)	11.5	17.2
4	Co($BPZNH_2$)	26.6	55.3

[a] Reaction conditions: 1 mL of cumene, 14mg catalyst, 110 μL of CHP, and diphenylether as internal standard (50 μL) N_2 atmosphere, 363 K, [b] CHP decomposition (%), determined by GC

By comparing the data shown in Tables 5.3 and 5.4, it is evident that the higher the ability of the catalyst to decompose CHP, the lower is the final CHP selectivity attained in the aerobic oxidation of CM. Thus, decomposition of CHP over Co(BPZ) is only slightly faster than in the blank experiment (thermal CHP decomposition): 7.1 versus 4.4% of CHP decomposed after 24 h, respectively. In sharp contrast, decomposition of CHP is much faster over CoBPZ-NH_2, reaching a 55.3% decomposition under the same conditions after 24 h. Meanwhile, the activity of CoBPZ-NO_2 for CHP decomposition is intermediate between the above to compounds (but closer to CoBPZ), as so is the final CHP selectivity attained in the aerobic CM oxidation experiments. Moreover, CoBPZ-NO2 is slightly more active than CoBPZ at short reaction times (< 1h), but it deactivates faster, which is probably due to the formation of bulky CM dimers.

It has been pointed out[16] that the presence of O_2 during CM oxidation can minimize CHP decomposition. In this sense, the higher affinity of CoBPZ for O_2

as compared with CoBPZ-NO_2 and CoBPZ-NH_2 in terms of isosteric heat of adsorption (see Table 5.2) might also contribute to some extent to the higher selectivity to CHP obtained over CoBPZ.

To summarize the catalytic results presented above, the activity of the CoBPZ-X compounds for CM conversion and CHP decomposition follows the trend: Co(BPZNH_2) >> Co(BPZNO_2) > Co(BPZ), which is the opposite for the CHP selectivity. Therefore, we think that the presence of –NH_2 groups (and to a minor extend, -NO_2 groups) in the MOF linkers play a crucial role in determining the catalytic properties of the compounds, so there is a clear tag-dependent selectivity.

In our opinion, introduction of –NH_2 groups in the BPZ ligands can have two different effects: On the one hand, they might change the local charge density on Co^{2+} due to electronic induction effects. On the other hand, amino groups can also introduce additional adsorption sites for CHP (by establishing hydrogen bonds between CHP and the solid catalyst), which can facilitate ensuing decomposition of CHP. Although we cannot rule out the first effect, we believe that the latter role may have a higher impact on the catalytic properties of CoBPZ-X compounds.

In line with the above hypothesis, Liao et al. have recently studied the use of carbon nanotubes (CNTs) and nitrogen-doped carbon nanotubes (NCNTs) as catalysts for the aerobic oxidation of CM[17]. NCNTs were found to be substantially more active than CNT for this reaction (74% vs 16% CM conversion), producing mainly PP (96.7% selectivity), whereas CNT was highly selective towards CHP (90%). According to their DFT calculations, those authors concluded that the high catalytic performance and PP selectivity of NCNTs is caused by a strong interaction with CHP. Therefore, once CHP is formed, it remains strongly adsorbed to the catalyst surface, where it can readily undergo over-oxidation and decomposition to PP. On the contrary, the calculated interaction energy between CHP and non-doped CNT was considerably lower, so desorption of CHP is more likely to occur, which minimizes decomposition events.

To understand whether the role of the $–NH_2$ on determining the catalytic properties of our Co(BPZX) compounds had a similar origin, we wanted to evaluate the strength of the interaction between CM and CHP and the solid catalyst. In order to do this, we thus measured the heat of immersion. Use of this technique can give us information related not only to the surface area available to the liquid, but also to the specific interaction between the solid surface and immersion liquid[18]. The enthalpy of immersion, ΔH_{imm}, is defined as the enthalpy change at constant temperature, that takes place when solid is immersed into a wetting liquid in which it does not dissolve nor react[19]. Moreover, immersion in the pure liquid solution can closely mimic catalytic conditions used in this experiment. The results of the heat of immersion experiment are summarized in Table 5.5.

Table 5.5 Heat of adsorption for selected MOFs in CM and CHP

MOF	**Heat in CM**	**Heat in CHP**
Co(BPZ)	-81 J/g	-137 J/g
Co(BPZNH$_2$)	-219 J/g	-283 J/g

If we compare the heat of immersion of CHP in both compounds, it is clearly much higher for CoBPZ-NH_2 than for CoBPZ: 283 vs 137 J/g, respectively. This probably reflects the presence in the former material of the $–NH_2$ groups, which introduce additional (stronger) adsorption sites for CHP, probably by allowing new hydrogen bonds between CHP and the $–NH_2$ of the linkers. Moreover, the heat of immersion of CHP is higher than for CM for both CoBPZ and CoBPZ-NH2. This indicates that both compounds has a certain tendency to decompose CHP, even in the case of CoBPZ, as already shown in the CHP decomposition experiments summarized in Table 5.4. Note that if the heat of immersion of CM were higher than CHP, one would expect that as soon as CHP is formed, fresh CM would push it away from the surface of the catalyst, thus avoiding its decomposition.

Thus, the data presented in Table 5.5 present a feasible explanation to understand the different behaviour of CoBPZX materials and the observed tag-dependent selectivity for the aerobic oxidation of cumene.

5.3. Conclusions

In this Chapter, and in collaboration with the groups of Galli, di Nicola and Rossin, we have carried out the synthesis of various CoBPZX compounds (X = H, NO_2 and NH_2). While the preparation of the first two compounds is already known from the literature, the amino-functionalized materials has never been prepared before. Therefore, a more detailed characterization of this latter compound is discussed herein.

These Co-containing materials have been evaluated for the aerobic oxidation of CM. A clear tag-dependency of both catalytic activity (rate of CM conversion) and selectivity (towards CHP or PP) has been observed. Thus, while CoBPZ afforded a low activity but a high CHP selectivity, CoBPZ-NH_2 showed the opposite characteristics: a very high catalytic activity along with a high selectivity to PP; while CoBPZ-NO_2 has a somewhat intermediate behaviour. These catalytic results can be correlated with the ability of the material to catalyse CHP decomposition. Thus, as CHP decomposition activity of the material increases, the rate of CM conversion is also seen to increase, while the final selectivity of CHP decreases concomitantly.

In order to understand these finding, we have measured the strength of C; and CHP interaction with CoBPZ and CoBPZ-NH_2 by measuring the corresponding heats of immersion of the pure liquids in pre-activated solids. The results obtained indicate that: i) the heat of immersion of CHP is higher for CoBPZ-NH_2 than for CoBPZ. This probably reflects the creation of new hydrogen bond interactions between CHP and the amino groups in CoBPZ-NH_2, which increases the adsorption strength; and ii) the heat of immersion of CHP onto each solid is lower than in the case of CM, which indicates that both compounds has a certain tendency to decompose CHP, even in the case of CoBPZ.

In summary, the results presented here represent a clear example of the potential of ligand functionalization as a strategy for fine-tuning the catalytic properties of MOFs.

5.4. References

(1) Zhang, J. P.; Zhang, Y. B.; Lin, J. Bin; Chen, X. M. Metal Azolate Frameworks: From Crystal Engineering to Functional Materials. *Chem. Rev.* **2012**, *112* (2), 1001–1033.

(2) Liao, P.-Q.; He, C.-T.; Zhou, D.-D.; Zhang, J.-P.; Chen, X.-M. Porous Metal Azolate Frameworks. *Chem. Met. Fram. Sythesis, Charact. Appl.* **2016**, 309–343.

(3) Pettinari, C.; Tăbăcaru, A.; Boldog, I.; Domasevitch, K. V.; Galli, S.; Masciocchi, N. Novel Coordination Frameworks Incorporating the 4,4′-Bipyrazolyl Ditopic Ligand. *Inorg. Chem.* **2012**, *51* (9), 5235–5245.

(4) Mosca, N.; Vismara, R.; Fernandes, J. A.; Casassa, S.; Domasevitch, K. V.; Bailón-García, E.; Maldonado-Hódar, F. J.; Pettinari, C.; Galli, S. CH3-Tagged Bis(Pyrazolato)-Based Coordination Polymers and Metal-Organic Frameworks: An Experimental and Theoretical Insight. *Cryst. Growth Des.* **2017**, *17* (7), 3854–3867.

(5) Torrisi, A.; Mellot-Draznieks, C.; Bell, R. G. Impact of Ligands on CO2 Adsorption in Metal-Organic Frameworks: First Principles Study of the Interaction of CO2 with Functionalized Benzenes. II. Effect of Polar and Acidic Substituents. *J. Chem. Phys.* **2010**, *132* (4).

(6) Mosca, N.; Vismara, R.; Fernandes, J. A.; Tuci, G.; Di Nicola, C.; Domasevitch, K. V.; Giacobbe, C.; Giambastiani, G.; Pettinari, C.; Aragones-Anglada, M.; et al. Nitro-Functionalized Bis(Pyrazolate) Metal-Organic Frameworks as Carbon Dioxide Capture Materials under Ambient Conditions. *Chem. - A Eur. J.* **2018**, *24* (50), 13170–13180.

(7) Choi, H. J.; Dincă, M.; Long, J. R. Broadly Hysteretic H 2 Adsorption in the Microporous Metal−Organic Framework Co(1,4-Benzenedipyrazolate). *J. Am. Chem. Soc.* **2008**, *130* (25), 7848–7850.

(8) Galli, S.; Masciocchi, N.; Colombo, V.; Maspero, A.; Palmisano, G.; López-Garzón, F. J.; Domingo-Garcia, M.; Fernández-Morales, I.; Barea, E.; Navarro, J. A. R. Adsorption of Harmful Organic Vapors by Flexible Hydrophobic Bis-Pyrazolate Based MOFs. *Chem. Mater.* **2010**, *22* (5), 1664–1672.

(9) Spek, A. L. Structure Validation in Chemical Crystallography. *Acta Crystallogr. Sect. D Biol. Crystallogr.* **2009**, *65* (2), 148–155.

(10) Blatov, V. A.; Shevchenko, A. P.; Proserpio, D. M. Applied Topological Analysis of Crystal Structures with the Program Package Topospro. *Cryst. Growth Des.* **2014**, *14* (7), 3576–3586.

(11) Vismara, R.; Tuci, G.; Mosca, N.; Domasevitch, K. V.; Di Nicola, C.; Pettinari, C.; Giambastiani, G.; Galli, S.; Rossin, A. Amino-Decorated Bis(Pyrazolate) Metal-Organic Frameworks for Carbon Dioxide Capture and Green Conversion into Cyclic Carbonates. *Inorg. Chem. Front.* **2019**, *6* (2), 533–545.

(12) Tonigold, M.; Lu, Y.; Mavrandonakis, A.; Puls, A.; Staudt, R.; Möllmer, J.; Sauer, J.; Volkmer, D. Pyrazolate-Based Cobalt(II)-Containing Metal-Organic Frameworks in Heterogeneous Catalytic Oxidation Reactions: Elucidating the Role of Entatic States for Biomimetic Oxidation Processes. *Chem. - A Eur. J.* **2011**, *17* (31), 8671–8695.

(13) Ma, S.; Zhou, H. C. A Metal-Organic Framework with Entatic Metal Centers Exhibiting High Gas Adsorption Affinity. *J. Am. Chem. Soc.* **2006**, *128* (36), 11734–11735.

(14) Wang, Z. J.; Lv, J. J.; Yi, R. N.; Xiao, M.; Feng, J. J.; Liang, Z. W.; Wang, A. J.; Xu, X.

Nondirecting Group Sp 3 C−H Activation for Synthesis of Bibenzyls via Homo-Coupling as Catalyzed by Reduced Graphene Oxide Supported PtPd@Pt Porous Nanospheres. *Adv. Synth. Catal.* **2018**, *360* (5), 932–941.

(15) Luz, I.; León, A.; Boronat, M.; Llabrés i Xamena, F. X.; Corma, A. Selective Aerobic Oxidation of Activated Alkanes with MOFs and Their Use for Epoxidation of Olefins with Oxygen in a Tandem Reaction. *Catal. Sci. Technol.* **2013**, *3* (2), 371–379.

(16) Casemier, J.; Nieuwenhuys, B. E.; Sachtler, W. M. H. The Oxidation of Cumene and the Decomposition of Cumene Hydroperoxide on Silver, Copper, and Platinum. *J. Catal.* **1973**, *29* (3), 367–373.

(17) Liao, S.; Chi, Y.; Yu, H.; Wang, H.; Peng, F. Tuning the Selectivity in the Aerobic Oxidation of Cumene Catalyzed by Nitrogen-Doped Carbon Nanotubes. *ChemCatChem* **2014**, *6* (2), 555–560.

(18) Go, C.; Salazar, D.; Sepu, A. Characterization of Microporous Solids by Immersion Calorimetry. *Physicochem. Eng. Asp.* **2001**, *188*, 151–165.

(19) Everett, D. H. Manual of Symbols and Terminology for Physicochemical Quantities and Units. *Int. Union Pure Appl. Chem.* **1971**.

Chapter 6

Hierarchically structured mixed-ligand HKUST-1

6.1. Introduction

6.1.1. HKUST-1 MOF

The HKUST-1 (copper-based MOF, known also as Cu-BTC or MOF-199), with structural formula $Cu_3(BTC)_2$ (BTC = 1,3,5- benzenetricalboxylate) is one of the most studied MOF compound[1], reported for the first time by Chui et al.[2] in 1999. Its crystalline structure consists of a copper paddle wheel units, with a Cu–Cu distance of 0.263 nm, where each copper atom is octahedrally coordinated by four oxygen atoms of the BTC linkers and by one water molecule form solvent (see Figure 6.1).

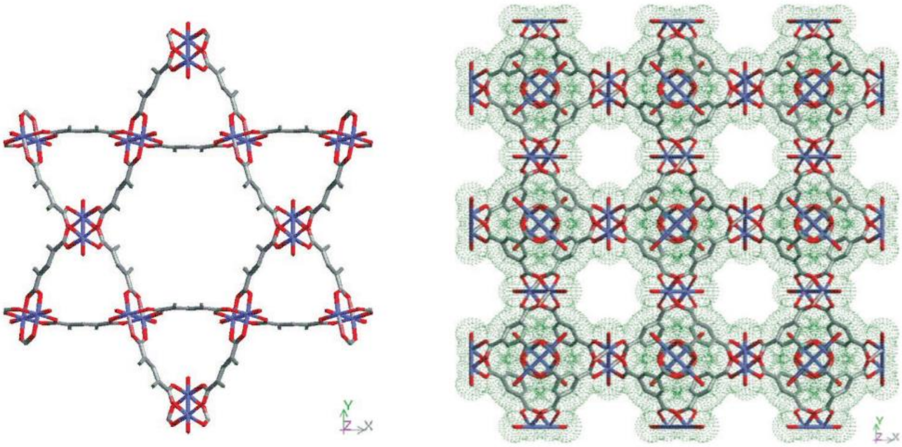

Figure 6.1 (*Left*) $Cu_3(BTC)_2(H_2O)_3$, viewed along the cell body diagonal [111], showing a hexagonal shaped 18Å window at the intersection of the nanopores. (*Right*) $Cu_3(BTC)_2(H_2O)_3$ framework viewed down the [100] direction, showing nanochannels with four-fold symmetry[2]. Reproduced from *Science* 1999, *283* (5405), 1148–1150 with permission Copyright © 1999, The American Association for the Advancement of Science

The material can be easily activated under a vacuum leaving unsaturated Cu sites available for adsorption and catalytic transformations. HKUST-1 possesses relatively good thermal stability, chemical resistance and accessible catalytic sites. Thus, it is a perfect candidate for heterogeneous Lewis acid catalysis like cyanosilylation of carbonyl compounds[3], the isomerization of α-pinene oxide, the cyclization of citronellal[4], and oxidation or epoxidation[5,6].

6.1.2. Hierarchically structured MOFs and its use in catalysis

Despite of good catalytic performance of MOFs as heterogeneous catalyst[7], most of them are microporous (pore size < 2 nm). This, in many cases can be a drawback, as small pore size provokes diffusion limitation and limits the access of large molecules to the metal active sites of MOF and discards their applications involving bulky molecules[8,9]. Thus, considerable efforts have been made to expand the pore size of MOFs to the mesoporous regime.

Currently, many *de Novo* Methods like ligand extension, bulky building block method, template method[10], template-free method, modulator-induced, metal-ligand-fragment co-assembly, gelation, supercritical fluid and Post-Synthetic methods like hydrolytic post-synthetic strategy, stepwise ligand exchange and encapsulation, have been proved to generate large-scale defects, resulting in hierarchically structured MOFs[11] as presented in Figure 6.2.

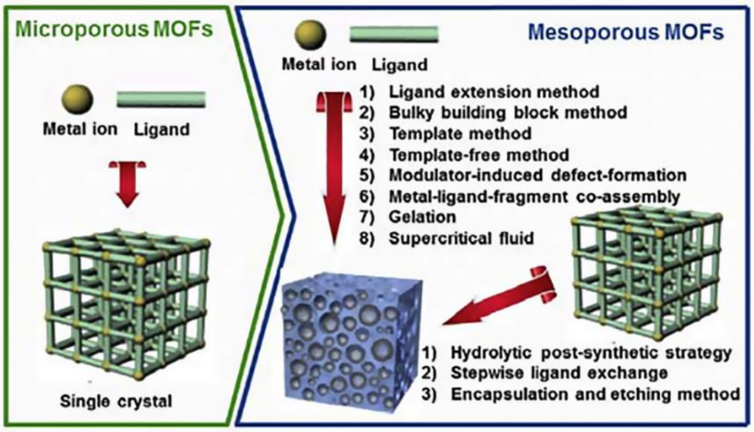

Figure 6.2 Conceptual illustration for mesopore fabrication in MOFs[11] Reprinted form *Coord. Chem. Rev.* 2018**, *369*, 76–90 with permission of Copyright © 2019 Elsevier B.V**

Among the listed methods metal-ligand-fragment co-assembly (called also defective linker (DL) approach), has gained a lot of attention not only thanks to its simplicity to expand interior cavities, or decorate them with functional groups, but also to remain material isostructural to the parent MOF avoiding to some extent structural interpenetration. In this method, the primitive ligand of parent MOF is mixed with its fragmented part (defective linker, usually with one or more missing carboxylate groups). Induced large-scale of such a defects (e.g. clustering of point defects) related with missing linker or node, can lead to generation of mesopores in the crystal structure. Such materials are called hierarchically structured MOFs, where micro- and mesopores coexist without compromising crystal structure of the material. Presence of mesopores can greatly influence mass-transport pathways, rigidity and density of the network, electronic and magnetic properties and also by rearrangement of CUSs benefits in catalytic reactions[12–14].

In one such example, a series of defect-engineered metal-organic frameworks based on parent HKUST-1 was prepared by doping with different defective linkers. Introduction of different ligand with different ratio, led to simultaneous and controllable modification of coordinatively unsaturated metal sites (CUS) and introduction of functionalized mesopores in case of 5-hydroxyisophthalic and pyridine-3,5-dicarboxylate linkers[15]. Higher implementation level of those fragmented linkers significantly influenced electronic properties and increased the functionalized mesopores in the lattice. Another hierarchically structured HKUST-1 was prepared by partially replacing of benzene-1,3,5-tricarboxylic acid by benzoic acid, which resulted in micro-mesoporous system with an improved external surface area compared to conventional HKUST-1[16]. Zhou group used this strategy to introduce functionalized mesopores in MOF structure by mixing primitive ligand (TPTC) and its ligand fragment R-isoprhthalic (R= -H, $-CH_3$, $-NH_2$, $-CH_2NH_2$, $-NO_2$, $-SO_3H$, $-SO_3Na$), without reduction of accessible pore volume[17]. In other example, Dai and co-workers used mesoporous HKUST-1 with hierarchical-structure-encaplulated phosphotungstic acid (HPW) (HPWs@ Meso-HKUST-1) in selective oxidation of cyclopentene (CPE) to glutaraldehyde (GA) using tert-butyl hydroperoxide and acetonitrile (MeCN) as the oxidant and solvent, respectively[18]. High catalytic activity and stability of the material was assigned to the unique textural properties of Meso-HKUST-1 and the good dispersion of HPWs inside the mesoporous cages, which in proper loading provides additional Lewis acid sites for the reaction.

In this Chapter we intended to prepare HKUST-1 type MOFs having micro-meso hierarchical porosity using the defective linker method approach. Subsequently, we will try to investigate the influence of the created defects and hierarchical porosity of synthesised MOFs in catalytic reaction with bulky product compared to pristine HKUST-1. As model reaction we have considered the one-pot oxidative synthesis of quinazoline (with approximate dimensions of 12 x 8 x 3 Å^3, very close to the pore windows present on HKUST-1 (with diameter of ca 9 Å).

6.1.3. Quinazoline synthesis

N-heterocycles are present in many natural products and are well known biologically active molecules. These compounds are very crucial in drug design, mostly because presence of nitrogen heterocycles in the drug structure increase its solubility and allow formation of salts, which influence their absorption and bioavailability. Among high structural diversity of *N*-heterocycles, quinazolines and quinazolinones skeletons are recurrently encountered heterocyclic compounds in medicinal chemistry literature. Conventionally quinazolines can be prepared by the Bischler cyclization between dicarbonyls and diamines. However, many scientists put an effort to develop new synthetic routes. Thus, Fu et al.demonstrated a simple and efficient, ligand-free CuI-catalyzed condensation between substituted (2-bromophenyl)methylamines and amides to achieve quinazoline derivatives[19]. In another example, CuCl/DABCO/4-HO-TEMPO was employed as catalyst for the aerobic oxidative synthesis of 2- substituted quinazolines from the one-pot reaction of aldehydes with 2-aminobenzylamines[20]. Despite of good results obtained by homogeneous systems, developing an efficient heterogeneous catalyst for the quinazoline synthesis is still of huge need. Heterogeneous systems including iron oxide (g-Fe_2O_3) nanoparticles[21] and polymer-supported bi-metallic platinum/iridium (Pt/Ir) alloyed nanoclusters[22] has been reported. Also MOFs were used for synthesizing quinazoline. ZIF-67[23] has shown high activity for the cyclization reaction of 2-aminobenzoketones and benzylamines forming 2-arylquinazolines. Moreover, the material could be reused several times without losing activity.

6.2. Results and discussion

6.2.1. Synthesis and characterization

The concept of mixed-ligand solid solution was applied to obtain two hierarchically structured, copper containing MOFs. HKUST-1 analogues **HM-1** and **HM-2** were synthesized by slightly modified, previously reported method[15] using mixtures of trimesic acid (BTC) and 5-hydroxyisophthalic acid (OH-isophthalic) with different ligands ratio. The detailed procedure is described in the *Annexes A.1*. Powder XRD patterns of the mixed-ligand materials prepared and parent HKUST-1 (**M-1**) are shown in Figure 6.3. The X-ray powder patterns are in good agreement with simulated pattern of HKUST-1, indicating that all materials are isoreticular and correspond to phase pure materials, even after incorporation of the second ligand. Formation of a mixture of two phases can be ruled out, since the XRD patterns show no evidences of peak splitting or any significant peak broadening. Moreover, an eventual phase pure OH-isophthalic copper MOF would necessary have a different crystalline structure. This would result in the appearance of additional diffraction peaks not corresponding to the HKUST-1 structure, which are not observed in any case.

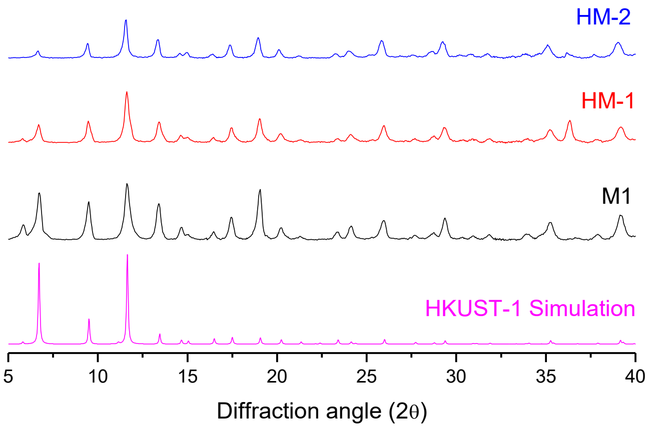

Figure 6.3 XRD patterns of prepared materials

The ratios of linkers incorporated in the final MOF were quantified by ^{1}H NMR spectroscopy upon digestion of the MOFs with d_2-H_2SO_4 in d_6-DMSO. HM-1 and HM-2 MOFs were found to contained 10% and 15% of the OH-isophthalic linker, respectively (Figure 6.4).

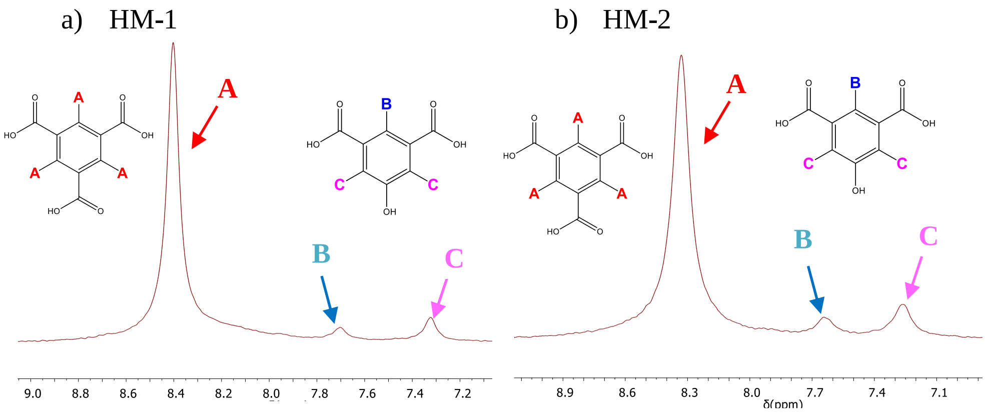

Substitution level : **10%** of OH-isophthalic Substitution level : **15%** of OH-isophthalic

Figure 6.4 a) ^{1}H NMR spectrum of HM-1; b) ^{1}H NMR spectrum of HM-2.

The presence of OH-isophthalic in the digested solid does not necessarily imply that this ligand is incorporated into the framework and partially replacing the original BTC linkers. It might also be simply adsorbed inside the pores or bound to the external surface of a phase-pure HKUST-1. In order to rule out this possibility, we performed a soaking experiment in which pristine HKUST-1 was contacted with a solution containing OH-isophthalic, as described in *Annexes 2*. However, the corresponding ^{1}H NMR of the digested solids after soaking for 24 h only showed a signal due to BTC ligands and no traces of OH-isophthalic.

In order to examine the thermal stability of these materials, thermogravimetric analysis (TGA) was carried out. TGA of all measured samples displays a two-stage mass loss in the temperature range 300-700 K (Figure 6.5). First loss corresponds to coordinated water loss around 350 K with mass loss around ~30% and the second, between

550-600 K to organic linker decomposition. The obtained curves indicate that with increasing amount of OH-isophthalic linker incorporated in the MOF structure, the thermal stability of resulting materials is decreasing (Figure 6.5a). This can be clearly seen by the shift of the DTG temperature peak of organic linkers decomposition (Figure 6.5b), where for pure M-1 decomposition starts at ca. 583 K, for the HM-1 with 10% of defective linker at ca. 563 K and for the HM-2 with the highest defective linker content (15%) at ca. 553 K.

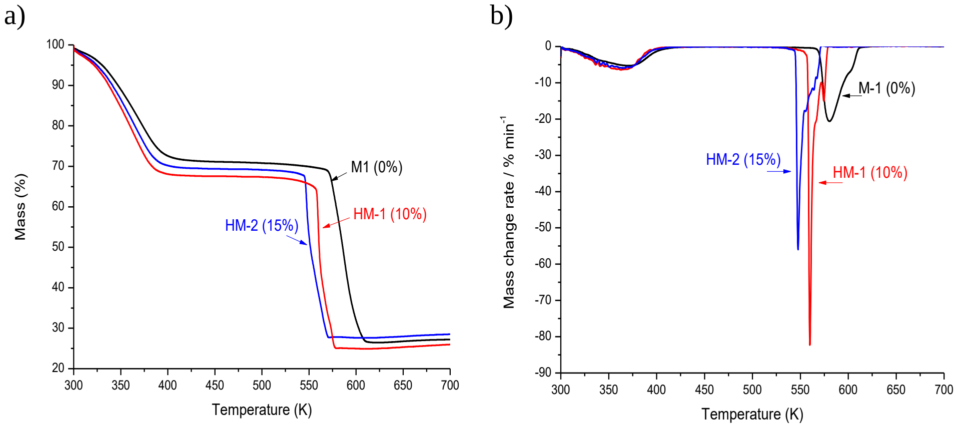

Figure 6.5 (a)TGA of prepared MOFs, (b) DTG of prepared MOFs

N_2 adsorption-desorption isoptherms are presented in Figure 6.6. As it can be seen, pristine M-1 (HKUST-1) exhibits a type-I isotherm[24], with a sharp increase in the N_2 uptake (at low nitrogen relative pressure) followed by a plateau, typical for microporous materials[25]. A very small hysteresis loop (akin to H3 or H4 type according to the IUPAC classification (ref 44), can be observed at high relative pressures, which is indicative of the presence of interparticle porosity. On the other side, materials with defective linker HM-1 and HM-2, shows a type IV isotherm[24], with well-defined H2-type hysteresis loop at a relatively high pressure ($P/P_0 > 0.4$) that indicates capillary condensation of N_2 in mesopores. This results proves the co-existence of micropores and mesopores[15–17] in the HM-1 and HM-2 samples.

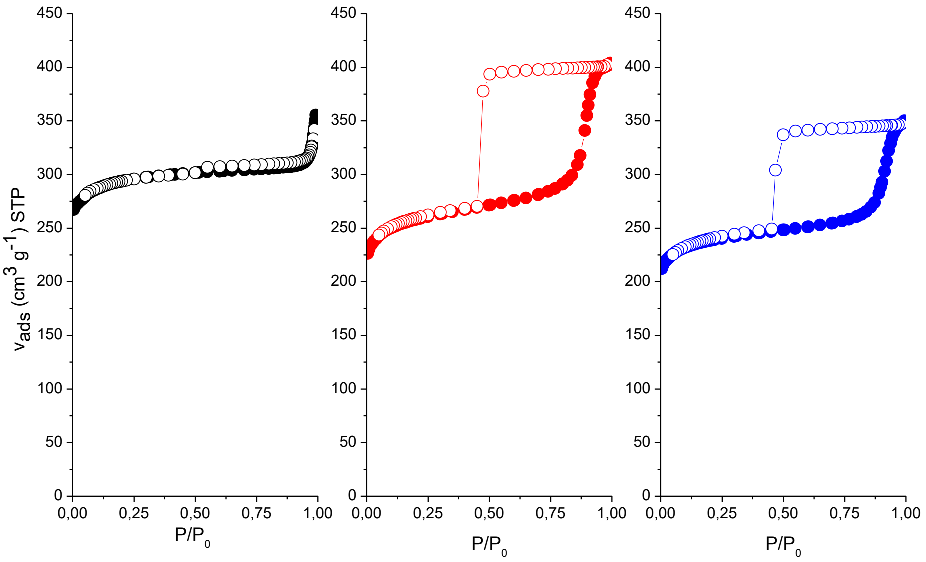

Figure 6.6 N_2 adsorption-desorption isotherms

Summary of textural properties of all prepared materials is shown in Table 6.1. For the calculation of Brunauer−Emmett−Teller (BET) specific surface area, the 0.01-0.1 p/p_0 pressure range of the isotherm was used to fit the data. Within this range, all the Rouquerol consistency criteria are satisfied. Pore size distribution was determined through the BJH method[26] applied to the adsorption branch of the isotherm. The corresponding curves obtained for HM-1 and HM-2 are shown in Figure 6.7.

Table 6.1 Textural properties of prepared materials

Sample	**S_{BET} (m^2/g)[a]**	**Pore volumes (cm^3/g)**			**Pore diameter (nm)[e]**
		V_{total}[b]	V_{micro}[c]	V_{meso}[d]	
M-1	1166	0.5499	0.4489	0.0358	No mesopores
HM-1	1008	0.6248	0.3714	0.2397	19.0
HM-2	939	0.5417	0.3511	0.1487	24.8

[a] S_{BET}: Brunnauer-Emmett-Teller surface area. Only data points satisfying the Rouquerol consistency criterion [27] have been considered (see Annexes A.3); [b] V_{total}: total pore volume, calculated from the nitrogen adsorption data at P/P_0=0.995; [c] V_{micro}: micropore volume obtained by the t-plot method (see Annexes A.3); [d] V_{meso}: mesopore volume calculated by the Barrett-Joyner-Halenda (BJH) method.

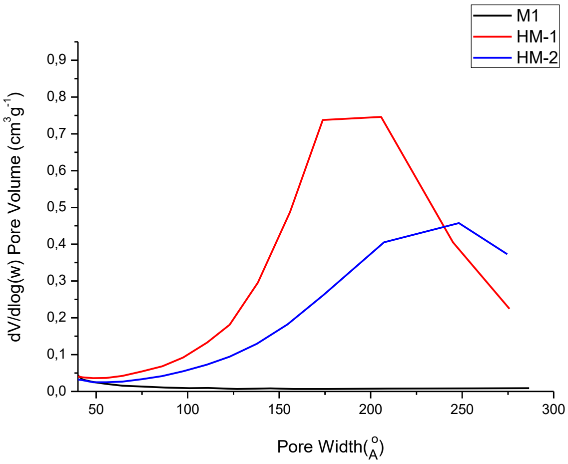

Figure 6.7 Pore volume of prepared MOFs

An increase of OH-isophthalic substitution affects specific surface area (BET), which slightly decreased for HM-1 and HM-2, compared to pristine M-1 material. This can be attributed to an increase of the pore size[17] in hierarchical MOFs, where HM-1 and HM-2 possess mesopores with 19,0 and 24,8 nm diameter respectively. Moreover, BET values can be affected by a decrease in the crystallinity degree in overall material due to formation of structural defects[16]. Presence of mesopores accompanied by certain loss of surface area values was reported before by many researchers[16,17,28–33]. While M-1 is basically microporous, both HM-1 and HM-2 presents an important volume of mesopores, representing up to 40% of the total pore volume in the case of sample HM-1, and somewhat lower (ca. 30%) in the case of HM-2.

The presence of mesoporosity for the mixed-ligand HKUST-1 with OH-isophthalic has been previously reported also by Fisher and co-workers[28]. Incorporation of OH-isophthalic into the HKUST-1 network lead to the appearance of uncompensated charges, arising from the difference charge on $[BTC]^{3-}$ and $[OH\text{-isophthalic}]^{2-}$ ligands. According to the authors, the excess charge can be compensated either by partial reduction of Cu^{2+} to Cu^{+} sites at the SBUs, or by missing linkers and/or by missing copper SBUs, leading in both cases to the creation of local defects. Clustering of these defects would eventually lead to the creation of mesopores in the solid, as shown schematically in Figure 6.8.

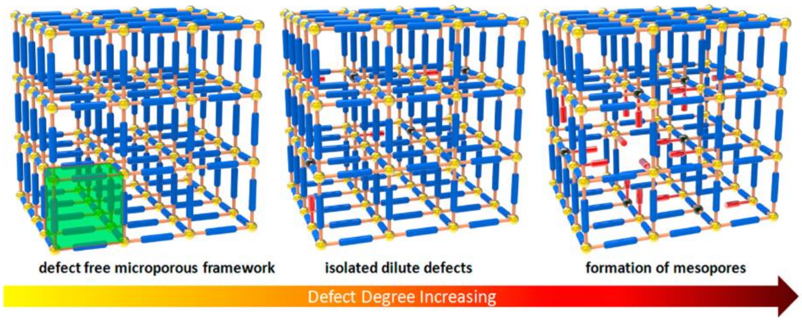

Figure 6.8 Defect-engineered MOFs (DEMOFs). The modulation of the defect structure on the micro- and mesoscales by defective linker doping of the framework is shown. The blue and short red sticks represent perfect and defective linkers. The yellow and black balls represent perfect and defective metal sites, respectively. The green highlighted unit indicates parent micropores.[28] Reprinted from J. Am. Chem. Soc. 2014, 136 (27), 9627–9636 with premisson of American Chemical Society

However, in their original work those authors did not analyzed whether or not the introduction of OH-isophthalic defective linkers in HKUST-1, and the corresponding creation of mesopores, were also accompanied by any morphological changes of the solid particles.

Figure 6.9-11 shows field emission scanning electron microscopy (FESEM) images of the M-1, HM-1 and HM-2 samples. As shown in Figure 6.9, conventional M-1 exhibits crystals with octahedral morphology typical of HKUST-1, with sharp edges and some inherent defects over the surface, formed during crystallization[34]. The same overall morphology is also observed for the materials prepared by mixed-linker approach HM-1 (Figure 6.10) and HM-2 (Figure 6.11). However, surface defects become more visible and ordered upon OH-isophthalic incorporation, and the edges of the octahedral crystals become more rounded.

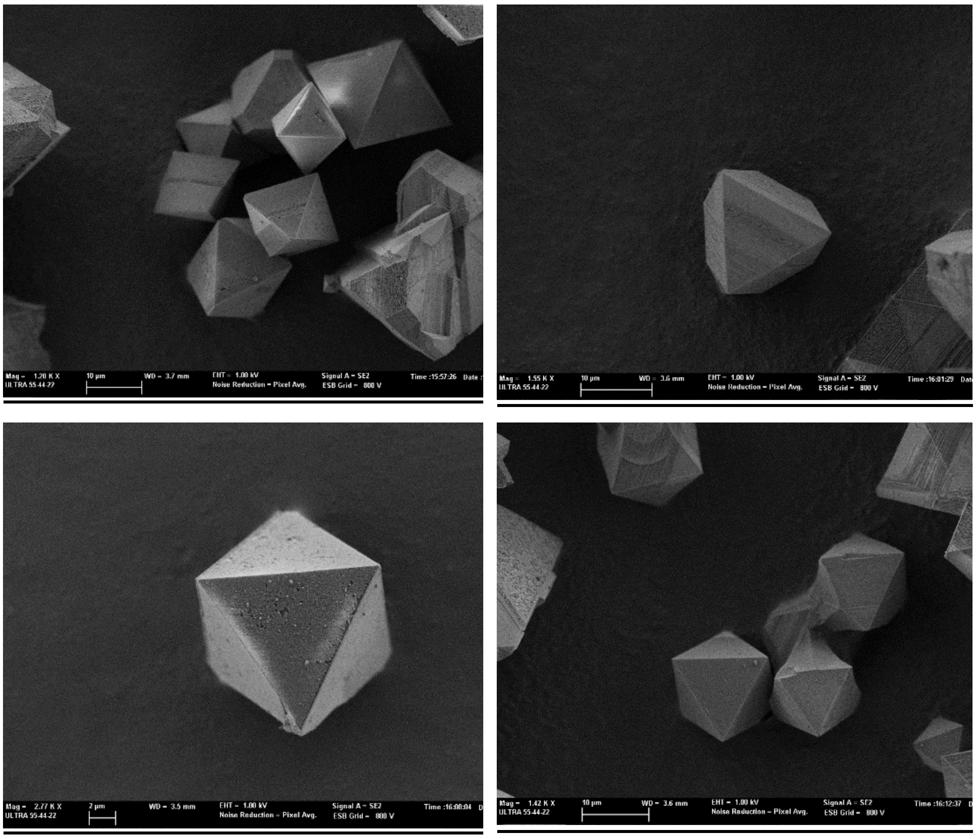

Figure 6.9 FESEM images of M-1

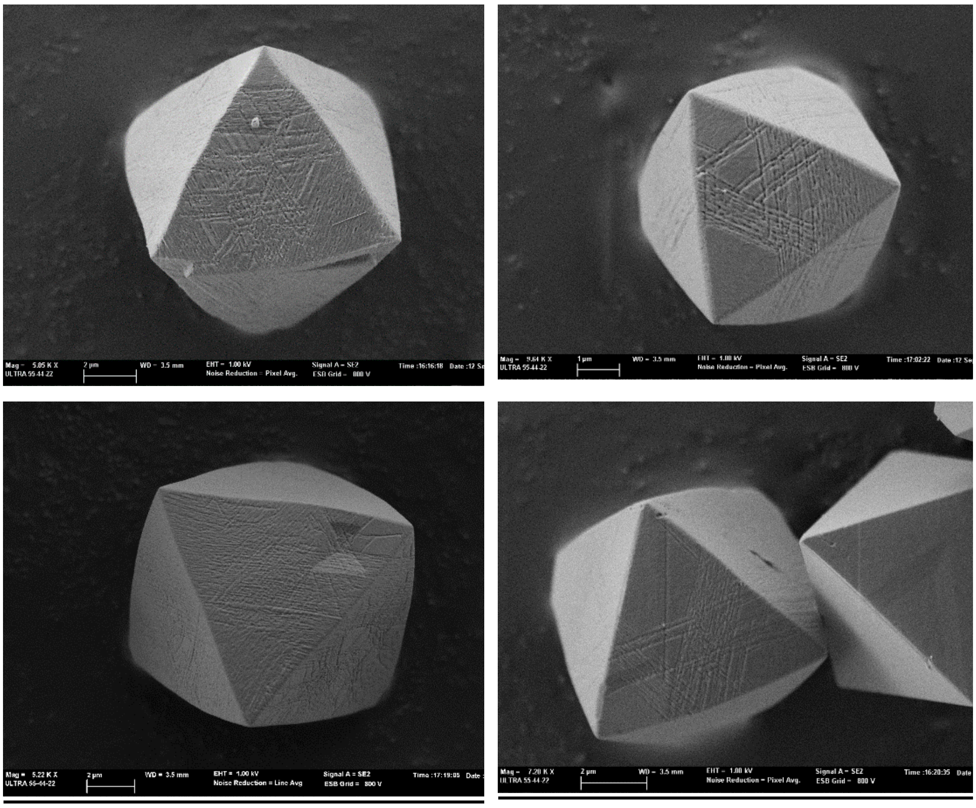

Figure 6.10 FESEM images of HM-1 sample

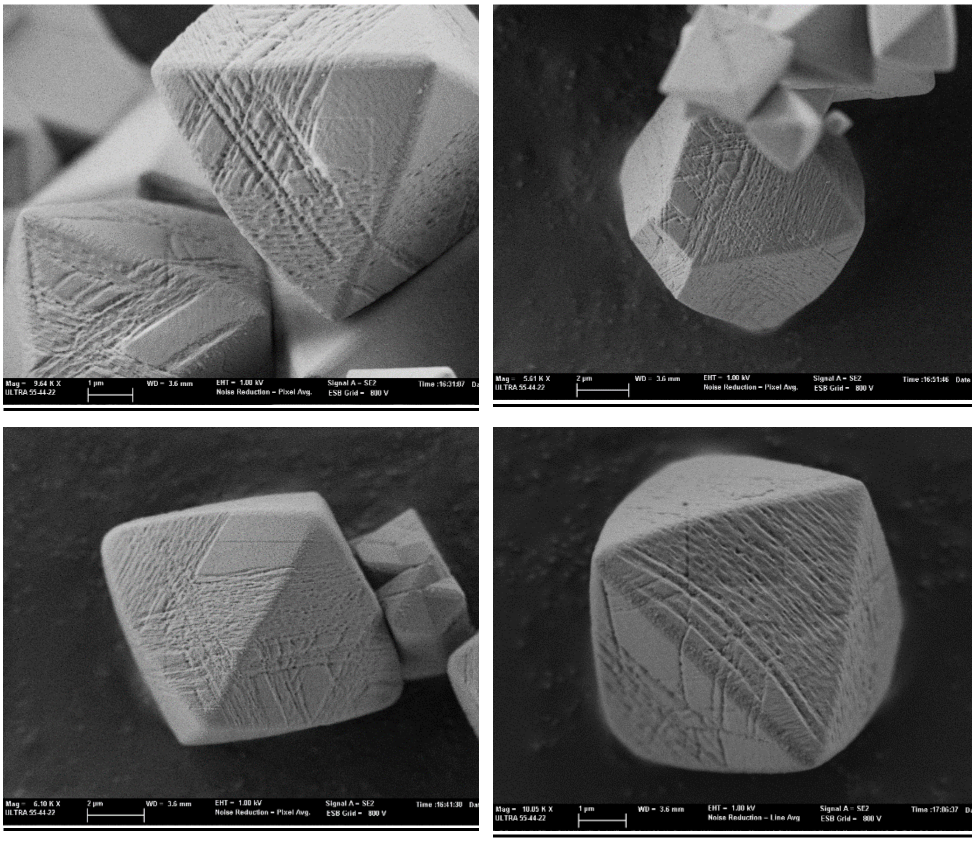

Figure 6.11 FESEM images of HM-2 sample

Formation of a hierarchical microporous-mesoporous system has been previously described on different mixed-linker HKUST-1 materials[16,35], in which BTC ligands were mixed with either benzoic acid or ascorbic acid. In both studies, the authors described the formation of mesopores, having a large impact on crystal morphology. The mesopores induced by the addition of either benzoic acid or citric acid tend to aggregate in both cases to form relatively big holes randomly distributed on the surface of the octahedral crystals.

Interestingly, the defects created in HM-1 and HM-2 do not seem to be randomly distributed along the crystal, in sharp contrast with the mesopore holes created by addition of benzoic or ascorbic acids. Rather, they tend to form long range trenches running parallel to the edges of the octahedral crystal. The observed ordered defect lines may be the result of the formation of BTC-rich domains mixed with OH-isophthalic-rich domains throughout the crystal, in which the two ligands cannot be thoroughly mixed[17]. The trenches formed in HM-1 and HM-2 are reminiscent of similar defect lines running also parallel to the edges of the octahedra described by Shoaee et al. [34,36], and by Ameloot et al. [37], using AFM and confocal fluorescence microscopy *in operando* conditions, respectively. Those authors attributed the presence of such line defects to the creation of dislocations of the crystalline network along the <110> direction. Projection of the HKUST-1 structure down the <110> direction evidences that there are two possible surface terminations for the {111} planes (corresponding to the faces of the octahedron) that involve no breaking of intramolecular bonds in the trimesate moieties. Of these two possible surface terminations, the most feasible is the one indicated in Figure 6.12, in which only one carboxylate group per trimesate ligand is not integrated into the bulk crystal structure. It is reasonable to hypothesize that OH-isophthalic, having only two carboxylate groups instead of the three present in trimesate, may tend to occupy preferentially these positions at the {111} surface terminations, so that the OH group would be dangling (indicated as a large green sphere in the figure), but the linker would still connected to the crystal through the two remaining strong carboxylate groups. Thus, as the amount of OH-isophthalic incorporated in the solid increases (on passing from HM-1 to HM-2), a higher concentration of the defective linker at these surface termination positions is expected. This could explain the formation of extended line defects running parallel to the edges of the octahedral crystals, leading eventually to the formation of broad and deep trenches evidenced in the FESEM images shown above.

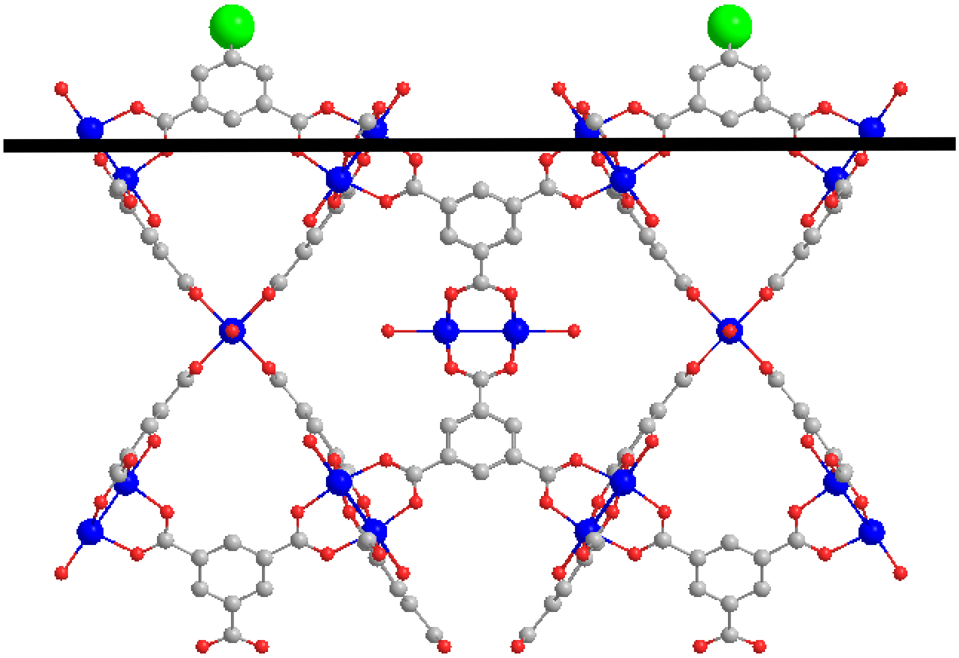

Figure 6.12 Structure of HKUST-1 viewed along <110> direction, showing the most likely surface termination at the {111} faces

6.2.2. Catalytic test

As mentioned above, a bulky compound such as quinazoline was chosen as a model reaction to evaluate the beneficial effect of defective ligand incorporation and creation of hierarchical porosity inside the crystals. Thus, M-1, HM-1 and HM-2 materials were evaluated in terms of their catalytic activities in oxidative quinazoline synthesis from 2-aminoacetophenone and benzylamine with tert-butyl hydroperoxide (TBHP) as oxidant and DMSO as solvent at 353 K (Scheme 6.1).

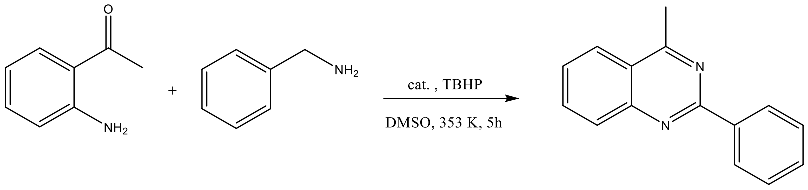

Scheme 6.1 Typical reaction condition for cyclization of 2-aminoacetophenone and benzylamine

Figure 6.13 summarizes the catalytic results obtained during 5 h of reaction time. A blank experiment (without any catalyst) was also performed under the same conditions for comparison, however no quinazoline yield was observed even after continuing the reaction for 8 h.

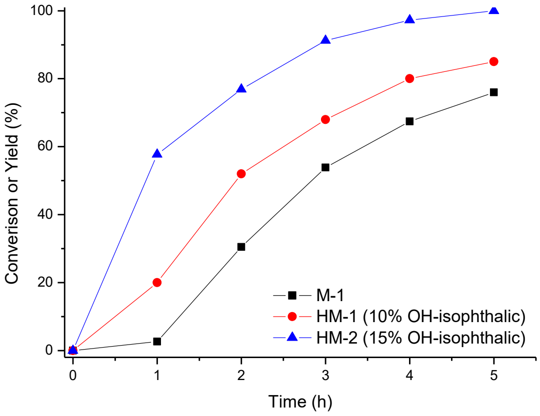

Figure 6.13 Catalytic results of quinazoline synthesis over M-1, HM-1 and HM-2 MOFs. Reaction conditions: 2-aminoacetophenone (1 mmol), benzylamine (1.5 mmol), tert-butyl hydroperoxide 70% in water (5 mmol), and diphenyl ether (100 µL) as internal standard in DMSO (2 mL) stirred at 353 K for 5 h.

All materials showed good activity and selectivity (as no other products were detected). Reaction rate and conversion significantly increased upon increasing concentration of defective linker inside the MOF structure, in the order M-1, HM-1 and HM-2 MOF: from 54%, 68% to 91% conversion after 3 h of reaction time, respectively. A progressive suppression of the induction period for hierarchically structured materials can be also observed. The material with the highest OH-isophthalic concentration (15%), HM-2, showed the best catalytic performance among tested materials, reaching 100% conversion after 5h of reaction time and thus, was chosen for further stability examination.

The heterogeneous character of the reaction was tested by hot filtration experiment, during the course of the reaction. The quinazoline synthesis was carried out under typical reaction condition for 0.5 h, using HM-2 as a catalyst. At this point, whit a 24% conversion, the catalyst was separated from the reaction mixture and reaction was continued for an additional 4.5 h, while withdrawing aliquots at different reaction time. Results showed that almost no further conversion was observed after catalyst separation

(Figure 6.14). Furthermore, ICP analysis of the filtrate indicate that no significant leaching of copper took place. These results suggest that the cyclization reaction between 2-aminoacetophenone and benzylamine is truly heterogeneous.

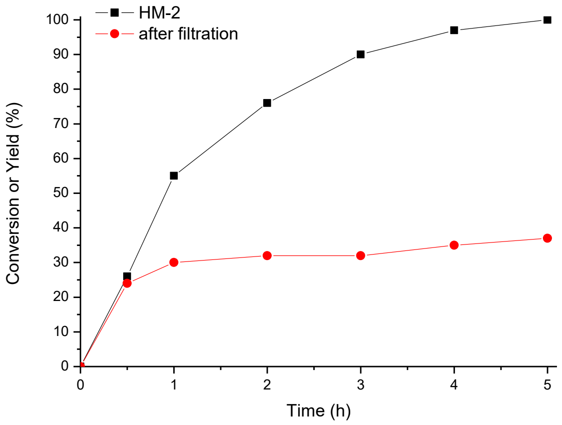

Figure 6.14 Hot filtration test over HM-2 catalyst. Reaction conditions: 2-aminoacetophenone (1 mmol), benzylamine (1.5 mmol), tert-butyl hydroperoxide 70% in water (5 mmol), and diphenyl ether (100 µL) as internal standard in DMSO (2 mL) stirred at 353 K.

Additionally, the stability test was preformed over HM-2 catalyst (Figure 6.15). To this end, the as prepared HM-2 catalyst was reused in consecutive catalytic cycles performed under identical reaction conditions. After every run (5 h), the catalyst was recovered by centrifugation, washed with fresh DMSO and acetone, dried under vacuum at room temperature overnight and reused in the subsequent reaction cycle. The HM-2 demonstrated good reusability for at least 4 cycles, with only slight loss of activity. PXRD after 4th reaction cycle (Figure 6.16) reveals some decrease of the intensity of the diffraction lines of the used material, which may originate from the adsorption of products on the catalyst surface or to some actual loss of crystallinity (due to the mechanical attrition between particles during the reaction). Nevertheless, the structure integrity of the material is overall maintained.

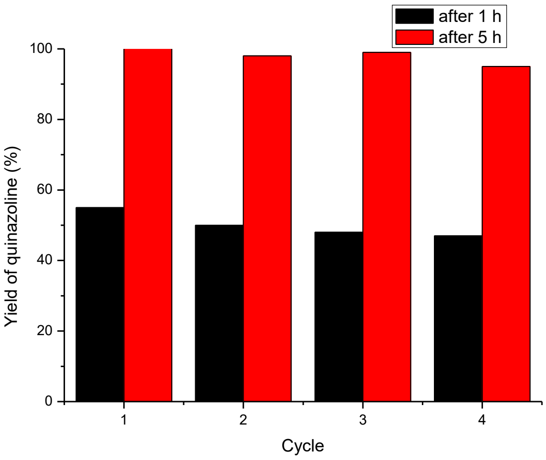

Figure 6.15 Reusability test of HM-2 after 1 h and 5 h of reaction time. Reaction conditions: 2-aminoacetophenone (1 mmol), benzylamine (1.5 mmol), tert-butyl hydroperoxide 70% in water (5 mmol), and diphenyl ether (100 µL) as internal standard in DMSO (2 mL) stirred at 353 K for 5 h.

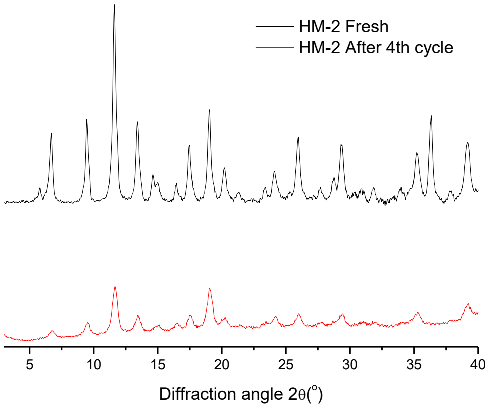

Figure 6.16 Powder XRD of fresh and used HM-2 catalyst

The proposed mechanism for this reaction is shown in Scheme 6.2. First, the intermediate imine product (3) is generated by condensation of 2-aminoacetophenone and benzylamine. Subsequently (3) is oxidized and undergoes intramolecular cyclization under the reaction conditions to form semiproduct (4). After this, (4) is further oxidized to the final product (5). The first step of the reaction (formation of intermediate imine (3) is almost immediate and it can take place even under catalyst free conditions.

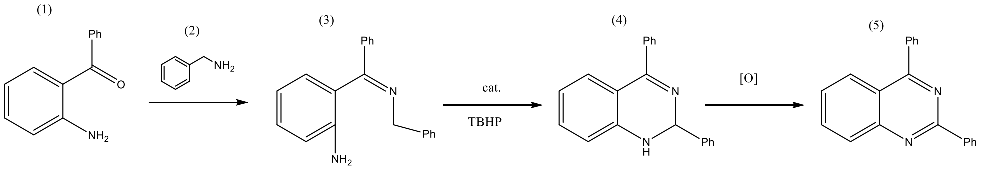

Scheme 6.2 Possible reaction mechanism

There are a number of publications reporting the use of defective linkers as a strategy to improve the catalytic properties of the material, or even to introduce new properties totally absent in the unmodified material. Usually, the improvement of the catalytic activity is attributed to the creation of point defects leading to the creation of more accessible and/or more reactive catalytic centres. For instance, creation of mixed-valence Cu- or Ru-HKUST-1 sites upon defective linker incorporation was deemed responsible for a higher reactivity in the oxidation of benzene derivatives[6], olefin hydrogenation and CO_2 reduction[38] or Paal-Knorr pyrrole synthesis[39], to name a few examples. Therefore, a similar effect may also be responsible for the increased catalytic activity observed here for the quinazoline synthesis: replacement of BTC by OH-isophthalic linkers can create defective sites similar to those present in other mixed-ligand MOFs. However, FTIR spectroscopy of adsorbed CO at 77 K onto M-1 and HM-2 (see Annexes 3) surprisingly revealed that no significant differences exist in the type, concentration and/or accessibility of the active centres present in these two materials. In particular, we noticed that introduction of OH-isophthalic defective linkers did not produce a sensibly higher amount of reduced Cu^+ sites (as reported in related precedents), since this should necessarily lead to appreciable changes in the relative intensities of certain absorption bands over the others in the FTIR spectra. Therefore, even if the creation of a small fraction of defective sites with a higher reactivity cannot be totally excluded, the higher catalytic of HM-1 and HM-2 with respect to M-1 for quinazoline synthesis may have another origin.

Therefore, a possible explanation to understand the catalytic results presented in Figure 6.15 is the presence, in HM-1and HM-2 of a hierarchical microporous-mesoporous system. Note that the reaction substrates used in quinazoline synthesis, 2-aminoacetophenone and benzylamine, are small enough to penetrate and freely diffuse inside the pores of HKUST-1 (with diameter of ca 9 Å). However, this is not the case for quinazoline, with approximate dimensions of 12 x 8 x 3 $Å^3$, very close to the pore windows present on HKUST-1. Therefore, once quinazoline is formed inside the MOF pores, strong diffusion limitations are expected for quinazoline desorption, increasing its residence time inside the pores and partially blocking the access of fresh reactants to the active sites. Creation of an additional mesopore system in the microporous MOF by the mixed-ligand approach can thus provide alternative diffusion pathways for quinazoline desorption, passing through these mesopores. This would minimize pore-blocking phenomena, which will translate into a higher reaction rate. This is schematically depicted in Scheme 6.3.

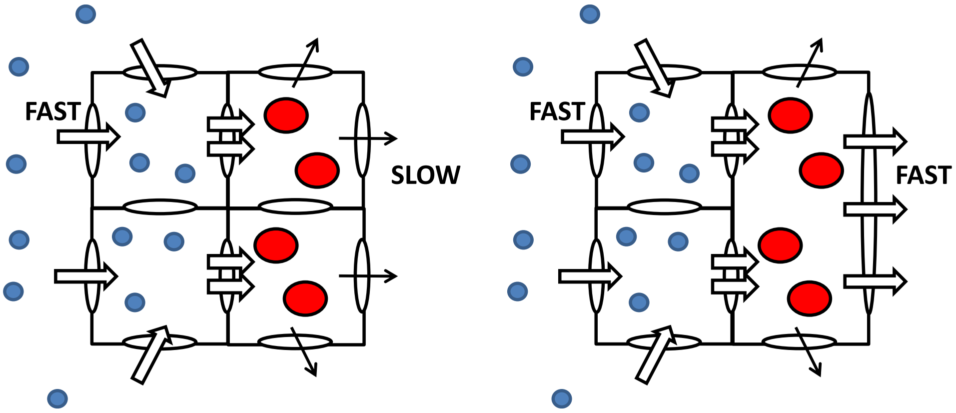

Scheme 6.3. Diffusion of small reactants (blue spheres) and bulky products (red spheres) in: (*left*) normal microrporous M-1; and (*right*) hierarchical mesoporous-mesoporous material.

Besides the above mentioned benefits of creating a hierarchical pore system in mixed-ligand MOFs, in principle other factors might as well contribute to the different catalytic properties of M-1 and HM-1/HM-2. One such factor could be particle size. A smaller particle size would indeed reduce the diffusion path length, thus minimizing mass transport limitations. However, we note from the FESEM images shown in Figure 6.9-11 that there is a certain dispersion of the particle size in all the samples prepared, but most of the crystals present an average particle size close to 10-12 μm, for both M-1 and HM-1/HM-2 mixed-ligand compounds. Furthermore, the relatively large size of the crystals implies that most of the Cu^{2+} active sites will be located at the internal surface of the catalyst, so the contribution from the external Cu^{2+} sites to the observed catalytic activity is expected to be low.

6.3. Conclusions

In this Chapter, we have described the preparation of isoreticular mixed-ligand HKUST-1 materials in which BTC linkers have been partially replaced (up to 15%) by OH-isophthalic. Characterization of the samples indicate that isomorphous substitution of one ligand for the other takes place. Introduction of this defective linker results in the creation of a hierarchical microporous-mesoporous system, in which mesopores account for up to 40% of the total pore volume of the solid, as evaluated from N_2 adsorption isotherms. This increased mesoporosity is accompanied by a slight decrease of specific surface area (S_{BET}), from 1166 to 939 $m^2 g^{-1}$. Morphological analysis of the samples by FESEM showed that there are no significant changes in average size of the octahedral crystals (of about 10-12 μm). However, the mesopores present in the mixed-ligand compounds are clearly observed in the form of wide and deep trenches running parallel to the edges of the octahedron. These line defects are compatible with dislocations occurring in the <110> direction, which would lead to preferential surface terminations at the {111} faces in which the linker is integrated into the bulk crystal through 2 carboxylate groups. Reasonably, these surface terminations are preferentially occupied by ditopic OH-isophthalic linkers, so as the amount of defective linker incorporated increases, the concentration of line defects in the solid is expected to increase.

Both pristine (M-1) and mixed-ligand (HM-1 and HM-2) MOFs have been tested as oxidation catalysts for the synthesis of quinazoline, a bulky molecule with dimensions very close to the pore opening of the MOFs. A progressive increase of the reaction rate is observed, which has been attributed to the presence of mesopores in the mixed-linker MOFs, that are able to alleviate diffusion limitations for the desorption of quinazoline formed inside the MOF pores.

6.4. References

(1) Prestipino, C.; Regli, L.; Vitillo, J. G.; Bonino, F.; Damin, A.; Lamberti, C.; Zecchina, A.; Solari, P. L.; Kongshaug, K. O.; Bordiga, S. Local Structure of Framework Cu(II) in HKUST-1 Metallorganic Framework: Spectroscopic Characterization upon Activation and Interaction with Adsorbates. *Chem. Mater.* **2006**, *18* (5), 1337–1346.

(2) Chui, S. S. A Chemically Functionalizable Nanoporous Material [Cu3(TMA)2(H2O)3]N. *Science (80-.).* **1999**, *283* (5405), 1148–1150.

(3) Schlichte, K.; Kratzke, T.; Kaskel, S. Improved Synthesis, Thermal Stability and Catalytic Properties of the Metal-Organic Framework Compound Cu3(BTC)2. *Microporous Mesoporous Mater.* **2004**, *73* (1–2), 81–88.

(4) Alaerts, L.; Séguin, E.; Poelman, H.; Thibault-Starzyk, F.; Jacobs, P. A.; De Vos, D. E. Probing the Lewis Acidity and Catalytic Activity of the Metal-Organic Framework [Cu3(Btc)2] (BTC = Benzene-1,3,5-Tricarboxylate). *Chem. - A Eur. J.* **2006**, *12* (28), 7353–7363.

(5) Wu, Y.; Qiu, L.-G.; Wang, W.; Li, Z.-Q.; Xu, T.; Wu, Z.-Y.; Jiang, X. Kinetics of Oxidation of Hydroquinone to P-Benzoquinone Catalyzed by Microporous Metal-Organic Frameworks M3(BTC)2 [M = Copper(II), Cobalt(II), or Nickel(II); BTC = Benzene-1,3,5-Tricarboxylate] Using Molecular Oxygen. *Transit. Met. Chem.* **2009**, *34* (3), 263–268.

(6) Marx, S.; Kleist, W.; Baiker, A. Synthesis, Structural Properties, and Catalytic Behavior of Cu-BTC and Mixed-Linker Cu-BTC-PyDC in the Oxidation of Benzene Derivatives. *J. Catal.* **2011**, *281* (1), 76–87.

(7) Corma, A.; García, H.; Llabrés i Xamena, F. X. Engineering Metal Organic Frameworks for Heterogeneous Catalysis. *Chem. Rev.* **2010**, *110* (8), 4606–4655.

(8) Lan, Y.; Jiang, H.; Li, S.; Xu, Q. Mesoporous Metal-Organic Frameworks with Size-Tunable Cages : Selective CO 2 Uptake , Encapsulation of Ln 3 + Cations for Luminescence , and Column-Chromatographic Dye Separation. **2011**, 5015–5020.

(9) Jiang, H.; Tatsu, Y.; Lu, Z.; Xu, Q. Non- , Micro- , and Mesoporous Metal - Organic Framework Isomers : Reversible Transformation , Fluorescence Sensing , and Large Molecule Separation. **2010**, 5586–5587.

(10) Huang, X. X.; Qiu, L. G.; Zhang, W.; Yuan, Y. P.; Jiang, X.; Xie, A. J.; Shen, Y. H.; Zhu, J. F. Hierarchically Mesostructured MIL-101 Metal-Organic Frameworks: Supramolecular Template-Directed Synthesis and Accelerated Adsorption Kinetics for Dye Removal. *CrystEngComm* **2012**, *14* (5), 1613–1617.

(11) Guan, H.; Leblanc, R. J.; Xie, S.; Yue, Y. Recent Progress in the Syntheses of Mesoporous Metal – Organic Framework Materials. *Coord. Chem. Rev.* **2018**, *369*, 76–90.

(12) He, S.; Chen, Y.; Zhang, Z.; Ni, B.; He, W.; Wang, X. Competitive Coordination Strategy for the Synthesis of Hierarchical-Pore Metal-Organic Framework Nanostructures. *Chem. Sci.* **2016**, *7* (12), 7101–7105.

(13) Choi, K. M.; Jeon, H. J.; Kang, J. K.; Yaghi, O. M. Heterogeneity within Order in Crystals of a Porous Metal-Organic Framework. *J. Am. Chem. Soc.* **2011**, *133* (31), 11920–11923.

(14) Xin, Z.; Bai, J.; Pan, Y.; Zaworotko, M. J. Synthesis and Enhanced H2adsorption Properties of a Mesoporous Nanocrystal of MOF-5: Controlling Nano-/Mesostructures of MOFs to

Improve Their H2heat of Adsorption. *Chem. - A Eur. J.* **2010**, *16* (44), 13049–13052.

(15) Fang, Z.; Dürholt, J. P.; Kauer, M.; Zhang, W.; Lochenie, C.; Jee, B.; Albada, B.; Metzler-Nolte, N.; Pöppl, A.; Weber, B.; et al. Structural Complexity in Metal-Organic Frameworks: Simultaneous Modification of Open Metal Sites and Hierarchical Porosity by Systematic Doping with Defective Linkers. *J. Am. Chem. Soc.* **2014**, *136* (27), 9627–9636.

(16) Liu, B.; Li, Y.; Oh, S. C.; Fang, Y.; Xi, H. Fabrication of a Hierarchically Structured HKUST-1 by a Mixed-Ligand Approach. *RSC Adv.* **2016**, *6* (66), 61006–61012.

(17) Park, J.; Wang, Z. U.; Sun, L. B.; Chen, Y. P.; Zhou, H. C. Introduction of Functionalized Mesopores to Metal-Organic Frameworks via Metal-Ligand-Fragment Coassembly. *J. Am. Chem. Soc.* **2012**, *134* (49), 20110–20116.

(18) Yang, X.; Qiao, L.; Dai, W. One-Pot Synthesis of a Hierarchical Microporous-Mesoporous Phosphotungstic Acid-HKUST-1 Catalyst and Its Application in the Selective Oxidation of Cyclopentene to Glutaraldehyde. *Cuihua Xuebao/Chinese J. Catal.* **2015**, *36* (11), 1875–1885.

(19) Wang, C.; Li, S.; Liu, H.; Jiang, Y.; Fu, H. Copper-Catalyzed Synthesis of Quinazoline Derivatives via Ullmann-Type Coupling and Aerobic Oxidation. *J. Org. Chem.* **2010**, *75* (22), 7936–7938.

(20) Han, B.; Yang, X. L.; Wang, C.; Bai, Y. W.; Pan, T. C.; Chen, X.; Yu, W. CuCl/DABCO/4-HO-TEMPO-Catalyzed Aerobic Oxidative Synthesis of 2-Substituted Quinazolines and 4 H -3,1-Benzoxazines. *J. Org. Chem.* **2012**, *77* (2), 1136–1142.

(21) Anand, N.; Reddy, K. H. P.; Satyanarayana, T.; Rao, K. S. R.; Burri, D. R. A Magnetically Recoverable γ-Fe 2 O 3 Nanocatalyst for the Synthesis of 2-Phenylquinazolines under Solvent-Free Conditions. *Catal. Sci. Technol.* **2012**, *2* (3), 570–574.

(22) Yuan, H.; Yoo, W. J.; Miyamura, H.; Kobayashi, S. A Cooperative Catalytic System of Platinum/Iridium Alloyed Nanoclusters and a Dimeric Catechol Derivative: An Efficient Synthesis of Quinazolines through a Sequential Aerobic Oxidative Process. *Adv. Synth. Catal.* **2012**, *354* (16), 2899–2904.

(23) Truong, T.; Hoang, T. M.; Nguyen, C. K.; Huynh, Q. T. N.; Phan, N. T. S. Expanding Applications of Zeolite Imidazolate Frameworks in Catalysis: Synthesis of Quinazolines Using ZIF-67 as an Efficient Heterogeneous Catalyst. *RSC Adv.* **2015**, *5* (31), 24769–24776.

(24) Sing, K.S.W., Everet, D. H., Haul, R. A. W. Reporting Physisorption Data For Gas/Solid Systems. *Pure Appl. Chem.* **1985**, *57* (11), 603–619.

(25) Xian, S.; Xia, Q.; Xu, F.; Li, Y.; Li, Z. Effect of Textural Properties on the Adsorption and Desorption of Toluene on the Metal-Organic Frameworks HKUST-1 and MIL-101. *Adsorpt. Sci. Technol.* **2013**, *31* (4), 325–339.

(26) Joyner, L. G.; Barrett, E. P.; Skold, R. The Determination of Pore Volume and Area Distributions in Porous Substances. II. Comparison between Nitrogen Isotherm and Mercury Porosimeter Methods. *J. Am. Chem. Soc.* **1951**, *73* (7), 3155–3158.

(27) J. Rouquerol, F. Rouquerol, P. Llewellyn, G. Maurin, K. S. W. S. *Adsorption by Powders and Porous Solids: Principles, Methodology and Application*; Academic Press, 2013.

(28) Fang, Z.; Dürholt, J. P.; Kauer, M.; Zhang, W.; Lochenie, C.; Jee, B.; Albada, B.; Metzler-Nolte, N.; Pöppl, A.; Weber, B.; et al. Structural Complexity in Metal-Organic Frameworks: Simultaneous Modification of Open Metal Sites and Hierarchical Porosity by Systematic

Doping with Defective Linkers. *J. Am. Chem. Soc.* **2014**, *136* (27), 9627–9636.

(29) Diring, S.; Furukawa, S.; Takashima, Y.; Tsuruoka, T.; Kitagawa, S. Controlled Multiscale Synthesis of Porous Coordination Polymer in Nano/Micro Regimes. *Chem. Mater.* **2010**, *22* (16), 4531–4538.

(30) Du, H.; Bai, J.; Zuo, C.; Xin, Z.; Hu, J. A Hierarchical Supra-Nanostructure of HKUST-1 Featuring Enhanced H 2 Adsorption Enthalpy and Higher Mesoporosity. *CrystEngComm* **2011**, *13* (10), 3314–3316.

(31) Klimakow, M.; Klobes, P.; Rademann, K.; Emmerling, F. Characterization of Mechanochemically Synthesized MOFs. *Microporous Mesoporous Mater.* **2012**, *154*, 113–118.

(32) Sun, L. B.; Li, J. R.; Park, J.; Zhou, H. C. Cooperative Template-Directed Assembly of Mesoporous Metal-Organic Frameworks. *J. Am. Chem. Soc.* **2012**, *134* (1), 126–129.

(33) Tian, X.-Y.; Wu, Y.; Jiang, X.; Qiu, L.-G.; Li, Z.-Q.; Xu, T.; Zhang, L.-D.; Wang, W. Hierarchically Micro- and Mesoporous Metal-Organic Frameworks with Tunable Porosity. *Angew. Chemie Int. Ed.* **2008**, *47* (49), 9487–9491.

(34) Shoaee, M.; Anderson, M. W.; Attfield, M. P. Crystal Growth of the Nanoporous Metal-Organic Framework HKUST-1 Revealed by in Situ Atomic Force Microscopy. *Angew. Chemie - Int. Ed.* **2008**, *47* (44), 8525–8528.

(35) Liu, T.; Liu, Y.; Yao, L.; Yang, W.; Tian, L.; Liu, H.; Liu, D.; Wang, C. Controllable Formation of Meso- and Macropores within Metal-Organic Framework Crystals via Citric Acid Modulator. *Nanoscale* **2018**.

(36) Shöâeè, M.; Agger, J. R.; Anderson, M. W.; Attfield, M. P. Crystal Form, Defects and Growth of the Metal Organic Framework HKUST-1 Revealed by Atomic Force Microscopy. *CrystEngComm* **2008**, *10* (6), 646.

(37) Ameloot, R.; Vermoortele, F.; Hofkens, J.; De Schryver, F. C.; De Vos, D. E.; Roeffaers, M. B. J. Three-Dimensional Visualization of Defects Formed during the Synthesis of Metal-Organic Frameworks: A Fluorescence Microscopy Study. *Angew. Chemie - Int. Ed.* **2013**, *52* (1), 401–405.

(38) Kozachuk, O.; Luz, I.; Llabrés I Xamena, F. X.; Noei, H.; Kauer, M.; Albada, H. B.; Bloch, E. D.; Marler, B.; Wang, Y.; Muhler, M.; et al. Multifunctional, Defect-Engineered Metal-Organic Frameworks with Ruthenium Centers: Sorption and Catalytic Properties. *Angew. Chemie - Int. Ed.* **2014**, *53* (27), 7058–7062.

(39) Zhang, W.; Kauer, M.; Halbherr, O.; Epp, K.; Guo, P.; Gonzalez, M. I.; Xiao, D. J.; Wiktor, C.; LIabrés i Xamena, F. X.; Wöll, C.; et al. Ruthenium Metal-Organic Frameworks with Different Defect Types: Influence on Porosity, Sorption, and Catalytic Properties. *Chem. - A Eur. J.* **2016**, 1–12.

Chapter 7

Conclusions

Conclusions

The main conclusions extracted from the results presented and discussed in previous chapter are the following:

1) It is possible to prepare isoreticular mono- and bimetallic MOFs, as well as single and mixed-ligand compound, by applying a green synthesis method in aqueous medium, working at room temperature and ambient pressure, easily scalable and with short synthesis time. These conditions are highly desirable for the production of this type of compounds to allow their application at the industrial scale.

2) Mixed-metal compounds based on Co-Ni, Co-Zn (and probably also Mn-Ni) prepared with the above method show a highly desirable preferential occupation of Co^{2+} (and Mn^{2+}) ions of specific sites of the framework. This affords a means for controlling site isolation of these Co^{2+} centers by simple variations in the chemical composition of the compound.

3) Mono- and bimetallic cobalt based compounds prepared with the above method show interesting catalytic properties for the aerobic oxidation of cumene. By controlling site isolation (through chemical composition) and minimizing unwanted side reactions, it is possible to develop highly selective catalysts for the production of cumene hydroperoxide, with selectivities over 90%.

4) Preparation of related mixed-linker cobalt compounds is found to be a way to determine also the final selectivity of the catalytic material, by turning the selectivity of the process from the production of cumene hydroperoxide (CHP) to 2-phenyl-2-propanol (PP) depending on the amount of the secondary linker incorporated.

5) Cobalt based bipyrazolate compounds are also active for the aerobic oxidation of cumene. Depending on the functionalization of the bispyrazolate linkers of the MOF, a clear tag-dependent selectivity towards the final product of the reaction is observed. Non-functionalized CoBPZ has a low activity but it is highly selective for CHP production.

Meanwhile, the amino-functionalized CoBPZ-NH_2 is much more active, but the selectivity is turned towards the preferential production of PP. These results can be rationalized by a stronger adsorption of CHP on CoBPZ-NH_2, which facilitates the decomposition of the CHP formed during the reaction to PP.

6) Mixed-ligand HKUST-1 materials prepared with OH-isophthalic defective linkers show a hierarchical microporous-mesoporous system consisting of deep trenches running parallel to the edges of the octahedral crystals. Formation of these trenches is attributed to dislocations in the <110> directions of the crystal, and clustering of defects induced by the introduction of OH-isophthalic at the termination of the {111} faces.

7) The benefits of this hierarchical micro-mesopore system is evidenced when the mixed-ligand HKUST-1 materials are used as catalysts for the oxidative coupling of 2-amino-acetophenone and benzylamine to form the corresponding bulky quinazoline.

Chapter 8

Annexes

A.1. Synthesis Procedures

All reagents were of analytical grade and used as received without further purification.

Chapter 3

Powder material preparation. All materials were prepared by “green”, water based synthesis procedure at room temperature and ambient pressure. First, a 0.1M ligand salt (Na_3BTC, Na_2IP or Na_2NH_2IP) solutions were prepared by dissolving appropriate amount of NaOH (30 or 20 mmol according to molar ratio) and 10 mmol of desired linker (1,3,5-benzenetricarboxylic acid, isophthalic acid or 5-aminoisophthalic acid) in 100 mL of distilled water under vigorous stirring. Consequently, the MOFs were obtained by mixing together under rapid stirring 3 mmol of metal salt precursor (Co, Ni, Zn, Cu, or its mixture in appropriate ratio) and 20 mL of the ligand salt (or its mixture) 0.1M(aq) solution (2 mmol). Optionally, 10 mL of ethanol absolute was also added to the above solution. Stirring was continuing at room temperature and ambient pressure for the next 10 min. The solid obtained was separated by centrifugation and carefully washed with distilled water (3x) and ethanol (1x). The resulting powder materials where let to dry in air at room temperature.

Single crystal materials preparation. Starting from the above stock 0.1M Na_3BTC aqueous solution, a 1:8 dilutions was obtained, resulting in a Na_3BTC 0.0125M solution. For the preparation of monometallic compounds, a 0.1M aqueous solution of the corresponding metal precursor was prepared and placed inside a test tube. In the second step, Na_3BTC 0.0125M solution was added carefully to the solution in the tube using a syringe (sliding down the walls of the tube). As prepared solutions were left overnight for crystallization. Obtain single crystals were carefully washed with water and dried in air at room temperature. For the preparation of bimetallic compounds, the Ni 0.1M and Co

0.1M solutions were mixed with water in proper ratio, giving “Ni/Co solution” (see Table A.1.1 and placed inside the test tube, and treated likewise.

Table A.1.1 Solutions mixture ratio used in the synthesis of Co-Ni bimetallic trimesate single crystals

Ni/Co-BTC	Preparation of Ni/Co solution			Ni/Co solution	Na_3BTC solution (0.0125 M)
	Ni 0,1M solution	Co 0,1M solution	H_2O		
Ni-BTC	1.9 mL	0 mL	8.1 mL	6 mL	6 mL
Co10Ni-BTC	1.71 mL	0.19 mL	8.1 mL	6 mL	6 mL
Co20Ni-BTC	1.52 mL	0.38 mL	8.1 mL	6 mL	6 mL
Co30Ni-BTC	1.33 mL	0.57 mL	8.1 mL	6 mL	6 mL
Co40Ni-BTC	1.14 mL	0.76 mL	8.1 mL	6 mL	6 mL
Co50Ni-BTC	0.95 mL	0.95 mL	8.1 mL	6 mL	6 mL
Co60Ni-BTC	0.76 mL	1.14 mL	8.1 mL	6 mL	6 mL
Co70Ni-BTC	0.57 mL	1.33 mL	8.1 mL	6 mL	6 mL
Co80Ni-BTC	0.38 mL	1.52 mL	8.1 mL	6 mL	6 mL
Co90Ni-BTC	0.19 mL	1.71 mL	8.1 mL	6 mL	6 mL
Co-BTC	0 mL	1.9 mL	8.1 mL	6 mL	6 mL

Structure determination of powder materials. The crystal structure for monometallic materials has been confirmed by Rietveld refinement of the diagrams so obtained, applying rigid body constrain to the carbon atoms of BTC molecule, using the software Jana[1]. During minimization, atomic positions and thermal parameters with isotropic profile parameters describing instrumental broadening, size and strain effect were refined. Thermic parameters were considered isotropic for all atoms, and constrained to be the same for each chemical species. It is worth to note that although the quality of fit is sufficient to clarify the structure, few negative thermal parameters are present in the final refinement probably due to the difficulty to discriminate between close elements in X-ray diffraction and the relatively higher error associated with the scattering of light elements (C,O). For bi-metallic material series, in order to obtain the most precise cell parameters determinations the diagrams were analyzed by Le Bail refinement[2] as implemented in the Fullprof code[3]. Such approach allows to fully de-correlate atomic parameters from cell metrics and to avoid possible systematic errors induced by an approximate estimation of reflection intensity. Errors on the fitting parameters have been corrected by Berar factors[4]

Structure determination of single crystal materials. The structure was solved by dual-space algorithm using the SHELXT program[5], and then refined with full-matrix least-square methods (SHELXL)[6] with the aid of the Olex2 interface[7]. All non-hydrogen atoms were refined with anisotropic atomic displacement parameters. H atoms were finally included in their calculated positions. Further details of refinement are available in the CIF files.

Chapter 5

Synthesis of Co(BPZ)·DMF

Co(BPZ) was prepared according to the already published procedure[8].

Elem. Anal. Calc. for $C_9H_{13}CoN_5O$ (MW = 266.2 g mol^{-1}): C, 40.61; H, 4.92; N, 26.31%. Found: C, 40.91; H, 4.98; N, 25.88%.

IR (neat, cm^{-1}): 3093 (w) [ν(C–H$_{aromatic}$), 2927 (w) (C–H$_{aliphatic}$)], 1664 (vs) , [ν(C=O)], 1503 (s) [ν(C=C+C=N)], 1434 (w), 1385 (s), 1257 (m), 1162 (m), 1089 (w), 1051 (s), 915 (m), 854 (m), 636 (s).

Synthesis of Co(BPZNO$_2$)·DMF

Co(BPZ-NO$_2$) was prepared according to the already published procedure[9].

Elem. Anal. Calc. for $C_9H_{12}CoN_6O_3$ (MW = 311.2 g mol^{-1}): C, 40.61; H, 4.92; N, 26.31%. Found: C, 40.91; H, 4.98; N, 25.88%.

IR (neat, cm^{-1}): 3323 (m,br) [ν(N–H)], 3125 (w,br) [ν(C–H$_{aromatic}$), 2932 (w,br) (C–H$_{aliphatic}$)], 1643 (vs), [ν(C=O)], 1493 (m) [ν(C=C+C=N)], 1349 (s,br), 1181 (w), 1098 (m), 1049 (w), 947 (w), 820 (s), 762 (s).

Synthesis of Co(BPZNH$_2$)·DMF

H_2BPZ(NH$_2$)[10] (0.149 g, 1.00 mmol) was dissolved in DMF (15 mL). Then, $Co(NO_3)_2\cdot 6H_2O$ (0.291 g, 1. 00 mmol) was added. The mixture was left under stirring at 393 K for 24h, and after slow cooling to room temperature a dark violet precipitate was formed. The precipitate was filtered off, washed with hot DMF (2 x 10 mL) and dried under vacuum. Yield: 73%. Co(BPZ(NH$_2$)·DMF is insoluble in dimethyl sulfoxide, alcohols, acetone, acetonitrile, chlorinated solvents and water.

Elem. Anal. Calc. for $C_9H_{14}CoN_6O$ (MW = 281.2 g mol^{-1}): C, 38.44; H, 5.02; N, 29.89%. Found: C, 37.92; H, 4.94; N, 29.78%.

IR (neat, cm^{-1}): 3323 (m,br) [ν(N–H)], 3112 (w) [ν(C–H$_{aromatic}$), 2934 (w) (C–H$_{aliphatic}$)], 1658 (vs) , [ν(C=O)], 1508 (s) [ν(C=C+C=N)], 1436 (m), 1385 (s), 1282 (m), 1255 (w), 1209 (w), 1133 (s), 1092 (m), 1014 (m), 976 (vs), 830 (s).

Chapter 6

M-1 synthesis procedure. HKUST-1 (M-1) was prepared by slightly modifying previously reported procedure. Firstly, metal precursor $Cu(NO_3)_2·2.5\ H_2O$ (5 mmol) was dissolved in 25 mL H_2O. Secondly, trimesic acid (BTC, 2.5 mmol) was dissolved in 25 mL of DMF. Both solutions were mixed under rapid stirring, transfer to the autoclave and placed in the preheated oven at 373 K for 4 h. The blue precipitate was then filtered off, washed with fresh DMF, soaked 3 times in methanol (methanol was replaced for fresh one each 6 h) subsequently prepared material was dried at 573 K overnight under the vacuum.

Mixed-ligand HM-1 and HM-2 synthesis procedure. Mixed-ligand materials with different ligand ration, were prepared by modifying previous procedure, using mixture of trimesic acid (BTC) and 5-hydroxyisophthalic acid (OH-isophthalic) in desired ratio. To obtain HM-1 and HM-2 materials, 70:30 and 50:50 ratio of BTC : OH-isophthalic was used respectively. The blue precipitate was then filtered off, washed with fresh DMF, soaked 3 times in methanol (methanol was replaced for fresh one each 6 h) subsequently prepared material was dried at 573 K overnight under the vacuum.

A.2. Catalytic and Experimental Procedures

Chapter 4 and 5

Catalytic studies of cumene oxidation. CAUTION!! The following reaction conditions have been carefully selected to avoid flammable mixtures. Any deviation from these conditions must be carefully evaluated. In a typical catalytic experiment, 1 mL (7.14 mmol) of cumene (CM, 99% Sigma-aldrich) and the desired amount of solid catalyst were placed inside a home-made glass microreactor (volume = 6 mL) equipped with magnetic stirring, a manometer, a gas inlet and a liquid sampling valve. The reactor was connected with a cannula to an O_2 supply system, fixed at a total pressure of 4 bars. This reservoir system provides a continuous supply to restock the O_2 consumed during the oxidation reaction, so that the concentration of O_2 was constant throughout the reaction. The reactors were placed in iron hot-plate at the desired temperature. Time-evolution of products was carried out by GC analysis (Agilent Technologies 7890A, capillary column 10 m x 320 µm x 0.1µm) on sample aliquots taken at fixed time intervals. The samples were injected directly on-column to minimize the possible decomposition of the hydroperoxide at the injector.

CHP decomposition experiment. Decomposition of CHP, was conducted in tube reactor contained: 1mL of acetonitrile or cumene (as indicated in the chapter), 14 mg of catalyst and diphenylether as internal standard (50 µL). After flushed reactor with N_2, CHP was added (110 µL) and reaction was placed in iron bath at 363 K. The conversion of CHP was determined by GC (Agilent Technologies 7890A, capillary column 10 m x 320 µm x 0.1µm) using on-column injection with relation to internal standard.

Radical test. Quenching radical test was performed to prove true racidal mechanism of cumene oxidation. Typical cumene oxidation reaction was done over Co-BTC MOF. At 5 h of reaction, radical quencher - 2,6-ditertbutyl-4-methylphenol, BHT (79mg) was added, and reaction was continued for another 20 h. After that time, certain aliquot was taken from the reaction mixture and analysed by GC. Results for this test are summarized in Table A.2.1.

Table A.2.1 Quenching radical test results over Co-BTC

Entry	**Time (h)**	**Conversion[b] (%)**	**Selectivity to CHP (%)**
1	5	44	65
2	25	45	60

[a] Reaction conditions: 1 mL of cumene (7.17 mmol), 14 mg of catalyst, $p(O_2)$= 4 bar, 363 K, [b] Conversion (mol%), determined by GC

As it can be seen, reaction stopped completely after addition of radical quencher, which is direct prove of radical character of this process. Only a small change in CHP content was observed due to its decomposition.

Chapter 6

Soaking experiment. Pristine HKUST-1 (1 mmol) was contacted with a DMF solution containing OH-isophthalic (1 mmol). Mixture was let to rest for 24 h and subsequently material was then filtered off, washed with fresh DMF, soaked 3 times in methanol (methanol was replaced for fresh one each 6 h) subsequently prepared material was dried at 573 K overnight under the vacuum. Obtained solid was analysed by H^1NMR for organic ligand content.

Quinazoline synthesis. In a typical experiment, 20 mg of as prepared catalyst was added to the reaction tube containing a mixture of 2-aminoacetophenone (122 µL, 1 mmol), benzylamine (164 µL, 1.5 mmol), tert-butyl hydroperoxide 70% in water (685 µL, 5 mmol), and diphenyl ether (100 µL) as internal standard in DMSO (2 mL). The reaction mixture was stirred at 353 K (80°C) for 5 h. The reaction conversion was monitored by withdrawing aliquots from the reaction mixture at different time intervals, quenching with an aqueous KOH solution (5%, 1 mL), drying over anhydrous Na_2SO_4, analyzing by GC with reference to diphenyl ether.

A.3. Additional Experimental Data

Chapter 3

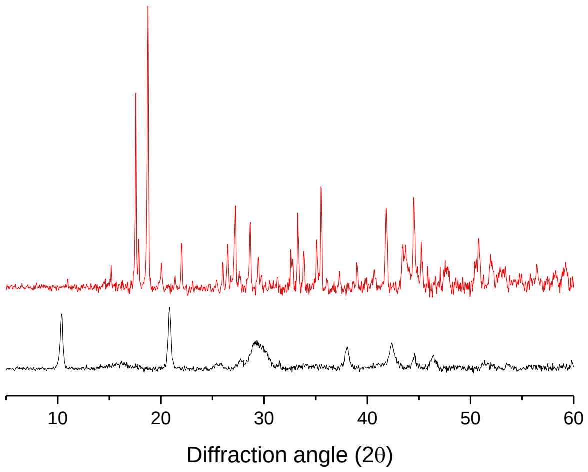

Figure A.3.1 XRD diffraction pattern (Cu Kα radiation) of Co-BTC (top) and Mn-BTC (bottom).

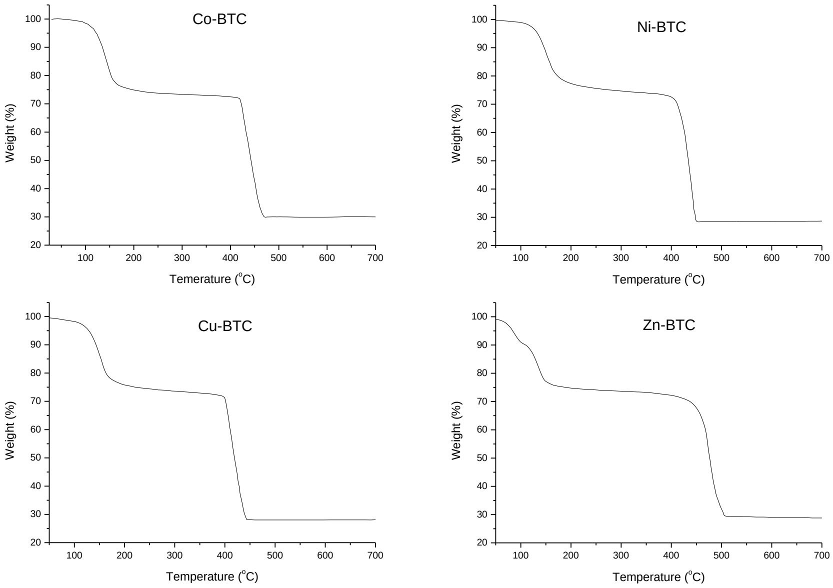

Figure A.3.2 TGA curves of monometallic M-BTC materials (M = Co, Ni, Cu, Zn)

Table A.3.1 Measured weight losses for each step in the TGA curves in Figure 3.21, and calculated molecular formula of the MOF (assuming that the solid residue corresponds to the respective metal oxide)

MOF	Weight loss (%)				FORMULA
		STEP I	STEP II	RESIDUE	
Co-BTC	Theoretical	26.7	45.5	27.8	$Co_3BTC_{1,8}\cdot 11,3H_2O$
	Experimental	26.9	43.0	30.1	
Ni-BTC	Theoretical	26.7	45.5	27.8	$Ni_3BTC_{1,9}\cdot 11,2H_2O$
	Experimental	25.6	45.7	28.7	
Cu-BTC	Theoretical	26.3	44.6	29.1	$Cu_3BTC_{2,1}\cdot 12H_2O$
	Experimental	25.9	45.5	28.6	
Zn-BTC	Theoretical	26.1	44.3	29.6	$Zn_3BTC_2\cdot 12,2H_2O$
	Experimental	25.6	44.7	29.7	

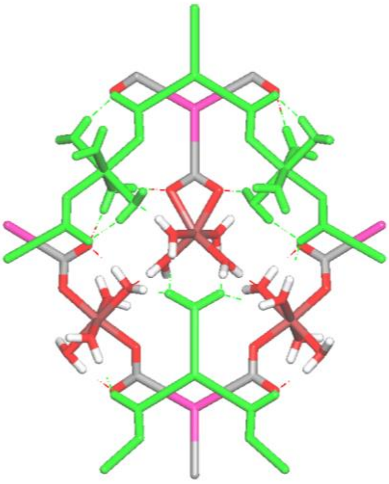

Figure A.3.3 Detailed view of $M_3(BTC)_2 \cdot 12\ H_2O$ showing hydrogen bonds. Atoms in the lower layer are colored as a function of atomic type while the atoms in the upper layer are all colored green

Table A.3.2 Total metal content and percentage of Ni and Co of the various CoxNi-BTC samples, as determined by ICP analysis

MOF	Co molar %	Ni molar%	Total metal content %
NiBTC	0	100	23.6
Co10Ni-BTC	10.6	89.4	24.4
Co20Ni-BTC	19.6	80.4	24.4
Co30Ni-BTC	30.9	69.1	24.7
Co40Ni-BTC	41.3	58.7	24.4
Co50Ni-BTC	50.9	49.1	24.1
Co60Ni-BTC	60.6	39.4	24.6
Co70Ni-BTC	71.0	29.0	25.3
Co80Ni-BTC	80.1	19.9	25.4
Co90Ni-BTC	89.9	10.1	24.5
CoBTC	100	0	24.4

Chapter 4

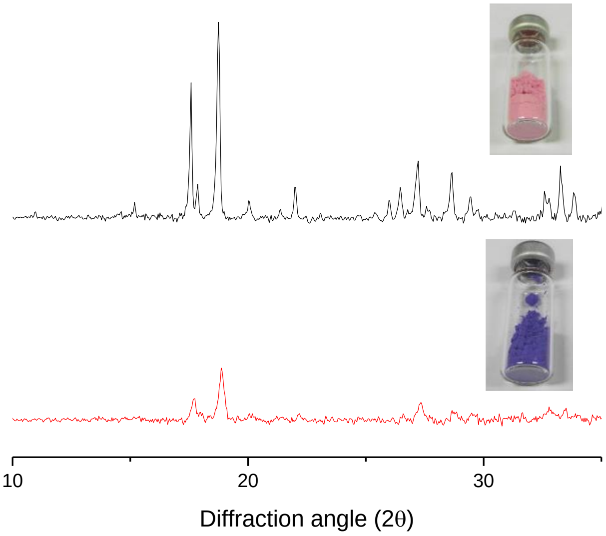

Figure A.3.4 XRD patterns and physical aspect of fresh Co-BTC (top) and Co-BTC dehydrated at 423 K (bottom)

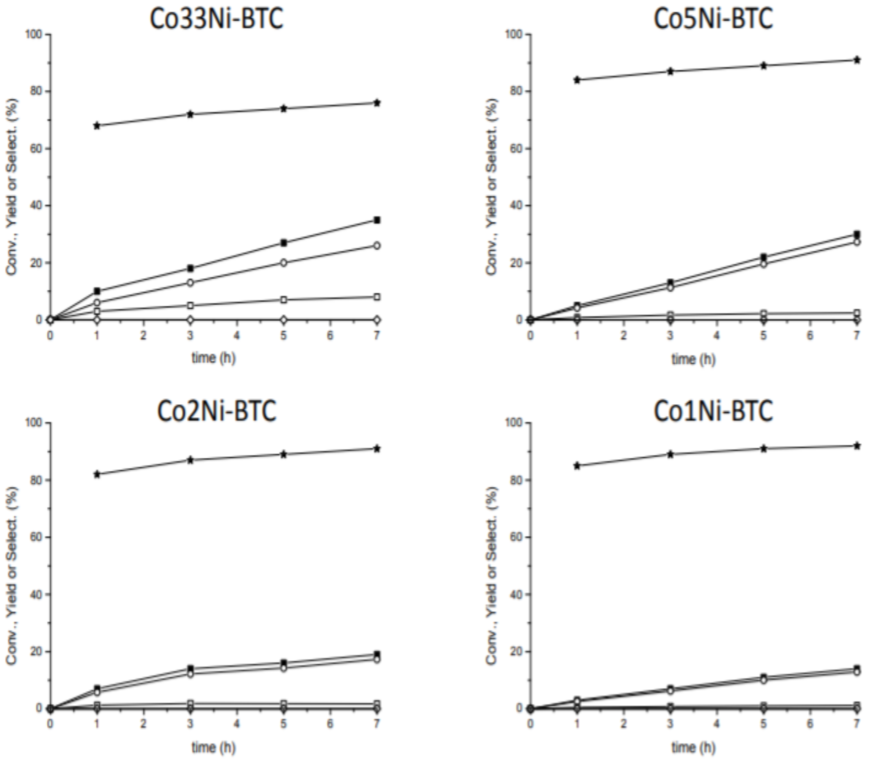

Figure A.3..4 Cumene conversion (-■-), yields of CHP (- ○-), PP (-□-), AP (-◇-) and selectivity to CHP (-*-) obtained over Co-Ni bimetallic compounds.

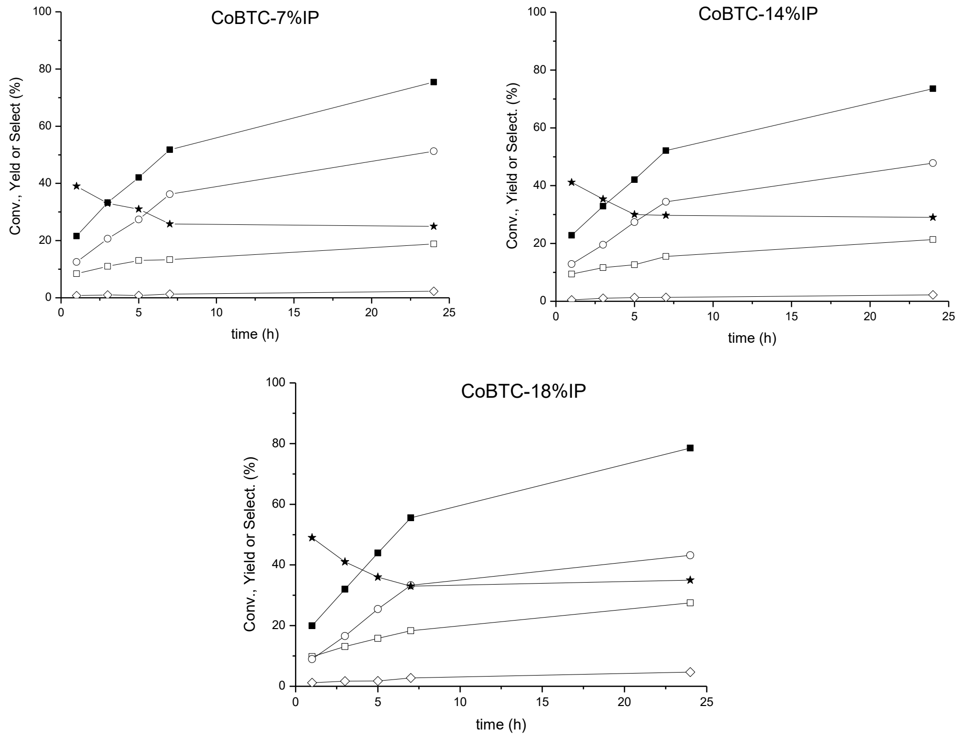

Figure A.3.6 Cumene conversion (-■-), yields of CHP (- ○-), PP (-□-), AP (-◇-) and selectivity to PP (-*-) obtained over mixed-ligand compounds

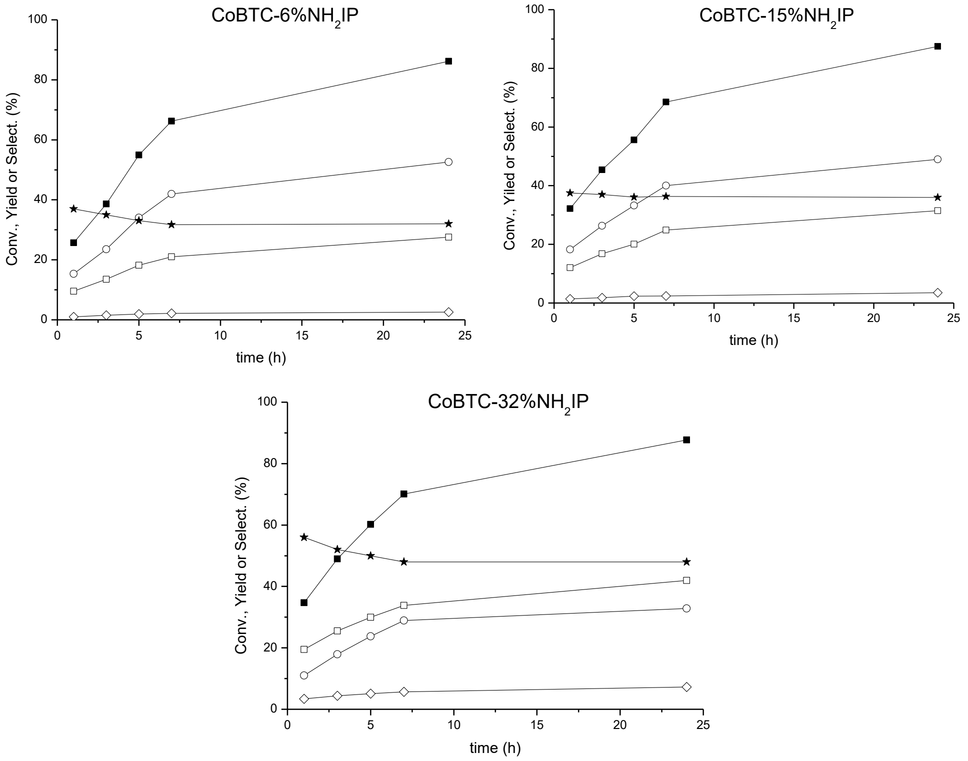

Figure A.3.7 Cumene conversion (-■-), yields of CHP (-○-), PP (-□-), AP (-◇-) and selectivity to PP (-*-) obtained over mixed-ligand compounds

Calculation of probabilities of different Co^{2+} arrangements in bimetallic CoxNi-BTC compounds as a function of total cobalt content

As we have already discussed in the M-BTC crystalline framework each metal ion in a terminal site is surrounded by 8 closest neighbours: 6 bridging atoms at distances $d_{term\text{-}bridg}$ = 5.89 Å (two sites), 5.63 Å (two sites) and 5.60 Å (two sites), and 2 terminal atoms at distances $d_{term\text{-}term}$ = 6.53 Å. Beyond these 8 closest neighbours, other metal-metal contacts are too distant (e.g., $d_{term\text{-}term}$ = 16.11 Å, $d_{term\text{-}bridg}$ = 10.40 Å and $d_{bridg\text{-}bridg}$ = 8.32 Å), so that they can be neglected.

Taking into account this spatial distribution of metal sites and the preferred site occupation of terminal sites by Co^{2+} ions, the probability to find an isolated Co^{2+} ion in a terminal site (i.e., surrounded by 8 Ni^{2+} ions) or surrounded by n-other Co ions and 8-2 Ni^{2+} ions, can be calculated using a binomial distribution (see for instance: a) *Schaums Outline of Statistics*, Fourth Edition, Schaum's Outline Series, 2011, by Murray R Spiegel and Larry J. Stephens; b) *Introduction to Probability and Random Variables,* McGraw-Hill, 1960, by G. P. Wadsworth). More precisely, the calculations of statistical occupation of neighbour sites around a terminal site have been performed using a python script provided in a separate file.

Thus, the probability of occupation on a terminal site (P_{term}) has been set equal to 1 for molar fractions of Co (X_{Co}) above 33% and $3*X_{Co}$ below to take into account the preferential occupation (the factor 3 derive by the sum of relative site multiplicities 1 and 2 for terminal and bridging sites respectively). Meanwhile the probability of occupation of a site bridging site (P_{bridge}) has been defined as 0 below the 33% of Co and (X_{Co}-0.33)/0.66 to renormalize X_{Co} after that all the apical sites were occupied.

Chapter 5

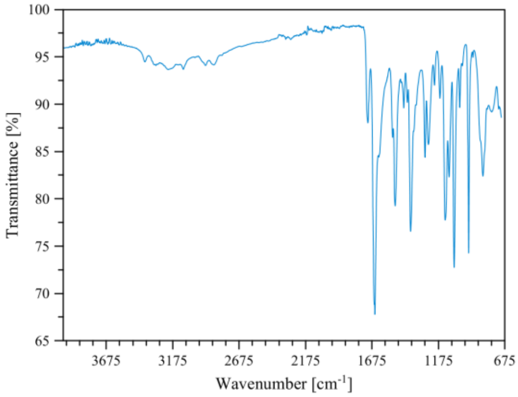

Figure A.3.8 Infrared spectrum of Co(BPZNH$_2$)·DMF

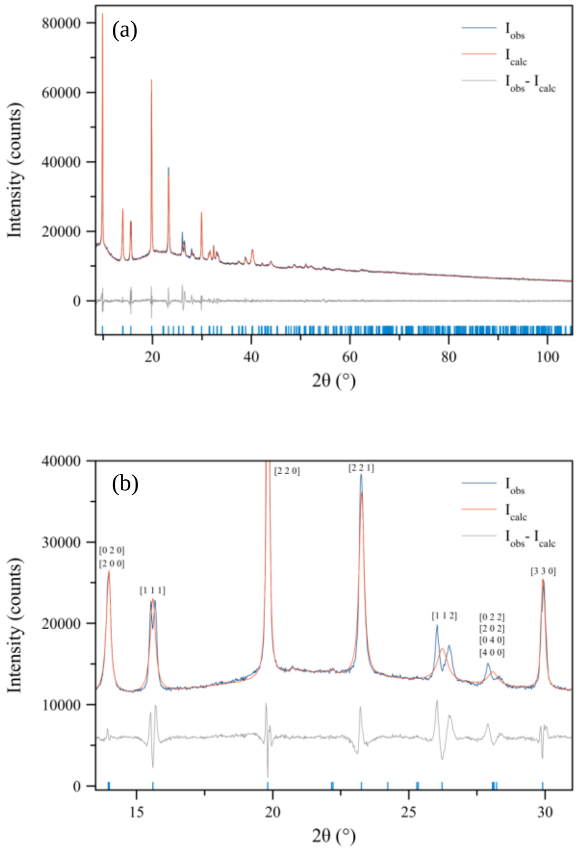

Figure A.3.9 (a) Result of the whole powder pattern refinement carried out with the Le Bail approach on the PXRD pattern of $Co(BPZNH_2)\cdot DMF$ in terms of experimental, calculated and difference traces (black, red and grey, respectively; $R_p = 0.016$; $R_{wp} = 0.027$), assuming the existence of a (supposedly) unique orthorhombic *Cccm* phase. The positions of the Bragg reflections are indicated by blue ticks. (b) Magnification of the low-angle portion of (a): the [*hhl*], [0*kl*] and [*h*0*l*] reflections doubling or right-side anisotropic broadening are clearly visible.

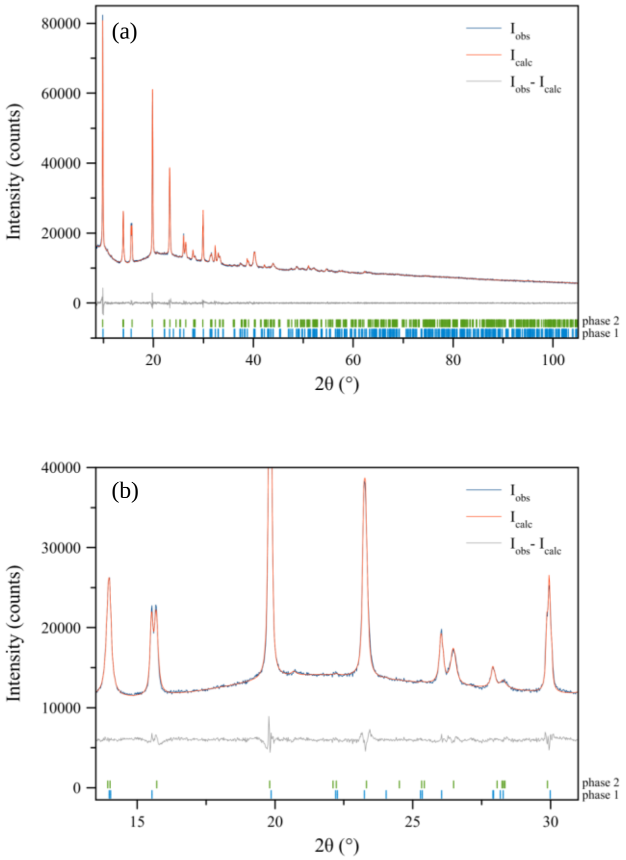

Figure A.3.10 (a) Result of the whole powder pattern refinement carried out with the Le Bail approach on the PXRD pattern of $Co(BPZNH_2)\cdot DMF$ in terms of experimental, calculated and difference traces (black, red and grey, respectively; $R_p = 0.010$; $R_{wp} = 0.015$), assuming the existence of two orthorhombic *Cccm* phases with slightly different unit cell parameters (Table S1). The positions of the Bragg reflections of the two phases are indicated by blue or green ticks. (b) Magnification of the low-angle portion of (a).

Table A.2.3 Unit cell parameters of the two orthorhombic *Cccm* phases present in a batch of Co(BPZNH$_2$)·DMF.

# Phase	*a* (Å)	*b* (Å)	*c* (Å)	*V* (Å^3)	*V*/*Z*’ (Å^3)
1	12.610(2)	12.658(2)	7.4005(5)	1181.3(3)	295.3
2	12.631(4)	12.712(5)	7.2569(6)	1165.2(6)	291.3

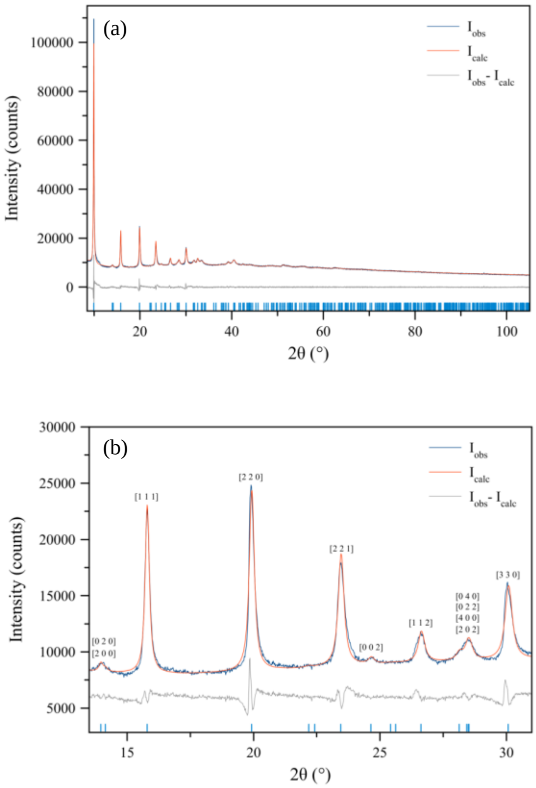

Figure A.3.11 (a) Result of the whole powder pattern refinement carried out with the Le Bail approach on the PXRD pattern of *activated* Co(BPZNH$_2$) in terms of experimental, calculated and difference traces (black, red and grey, respectively; R_p = 0.017; R_{wp} = 0.026), assuming the existence of a (supposedly) unique orthorhombic *Cccm* phase. The positions of the Bragg reflections are indicated by blue ticks. (b) Low-angle portion of (a): the [*hhl*], [0*kl*] and [*h*0*l*] right-side anisotropic broadening is clearly visible.

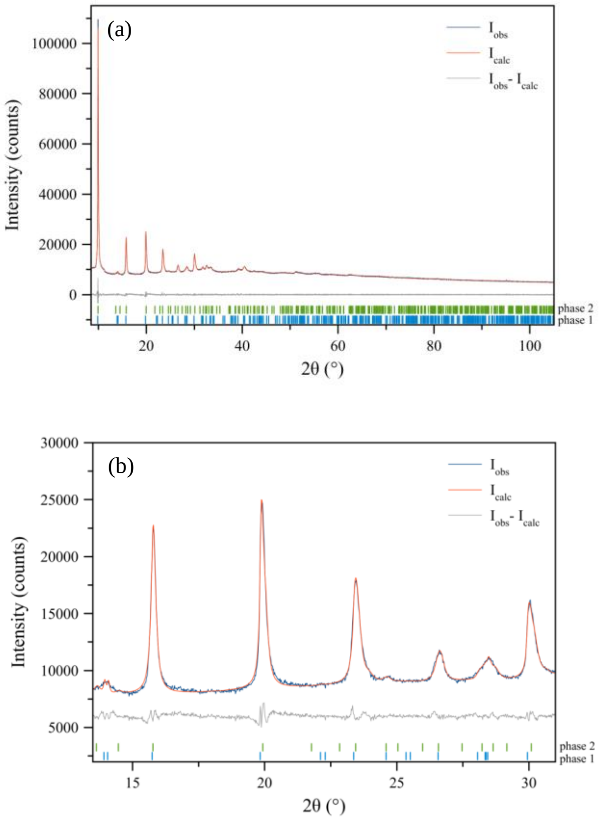

Figure A.3.12 (a) Result of the whole powder pattern refinement carried out with the Le Bail approach on the PXRD pattern of *activated* Co(BPZNH$_2$) in terms of experimental, calculated and difference traces (black, red and grey, respectively; *R*$_{\mathrm{p}}$ = 0.010; *R*$_{\mathrm{wp}}$ = 0.015), assuming the presence of two orthorhombic *Cccm* phases with slightly different unit cell parameters. The positions of the Bragg reflections of the two phases are indicated by blue or green ticks. (b) Low-angle portion of (a).

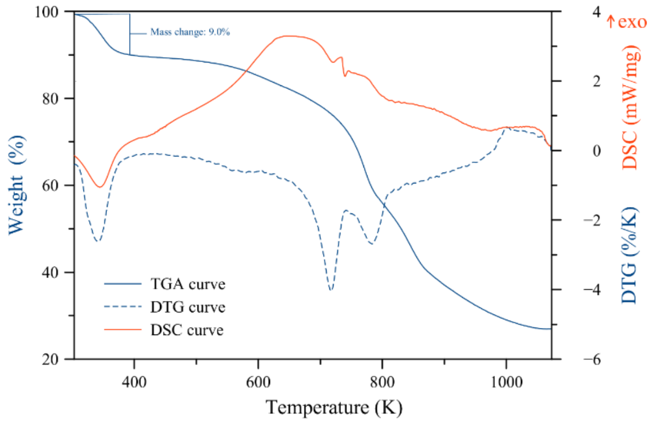

Figure A.3.13 TGA (blue continuous line), DTG (blue dashed line) and DSC (red line) traces measured under a flow of N_2 on *activated* Co(BPZNH$_2$).

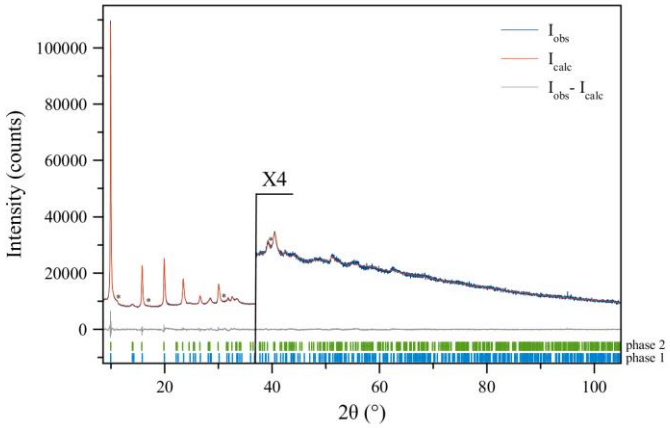

Figure A.3.14 Graphical result of the final Rietveld refinement carried out on Co(BPZNH$_2$) in terms of experimental, calculated and difference traces (blue, red and grey, respectively). The blue and green markers at the bottom indicate the positions of the Bragg reflections of phase 1 and phase 2, respectively. Horizontal axis, 2ϴ (°); vertical axis, intensity (counts). The portion above ~40° (2ϴ) has been magnified. The asterisks indicate peaks ascribed to impurities.

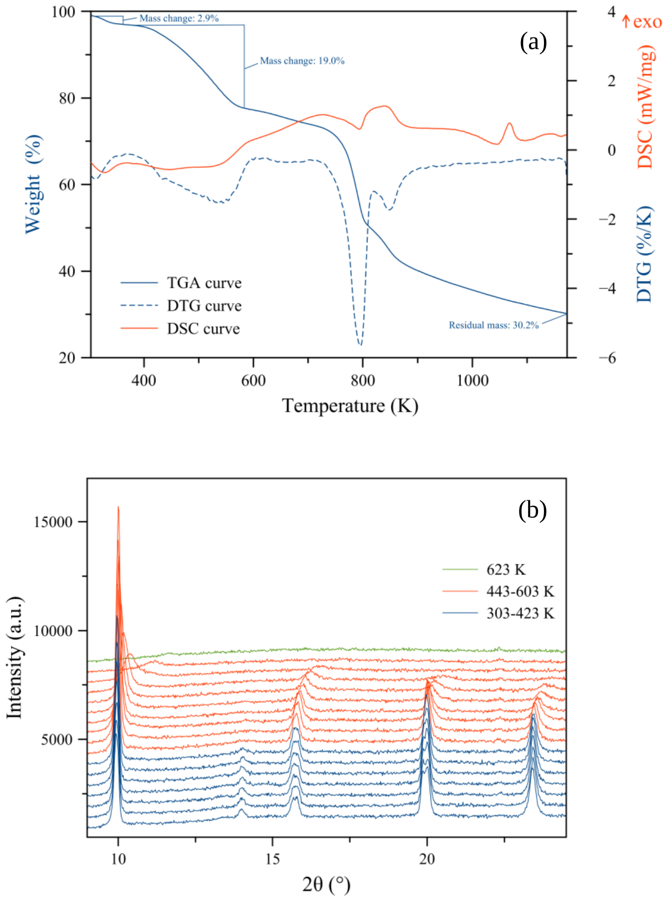

Figure A.3.15 (a) TGA (blue continuous line), DTG (blue dashed line) and DSC (red line) traces acquired under a flow of N_2 on Co(BPZNH$_2$)·DMF. (b) Variable-temperature powder X-ray diffraction patterns measured in air on Co(BPZNH$_2$)·DMF in the temperature range 303-623 K (with steps of 20 K).

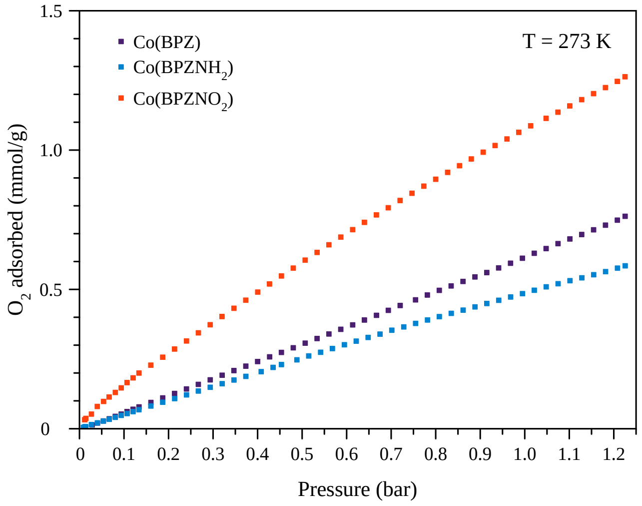

Figure A.3.16 O_2 adsorption isotherms measured at 273 K on Co(BPZX).

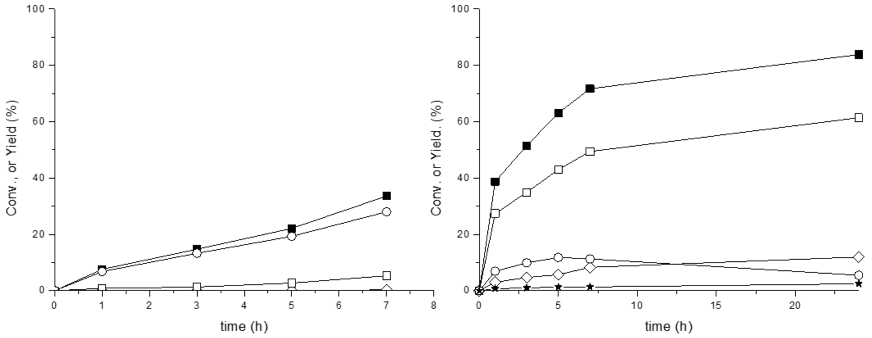

Figure A.3.17 CM conversion (-■-) and yields of CHP (-○-), PP (-□-), AP(-◊-) and CMD (-*-) obtained over CoBPZ (*Left*) and CoBPZ-NH2 (*Right*).

Chapter 6

a)

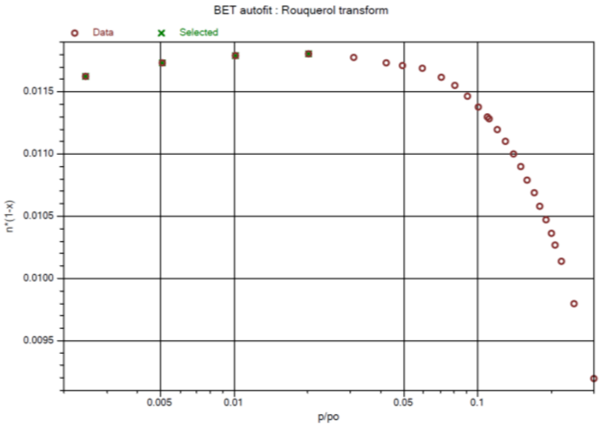

b)

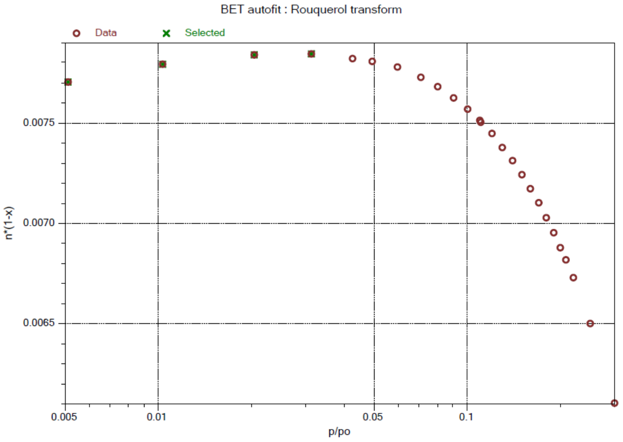

Figure A.3.18 (Part I) BET data points satisfying the Rouquerol consistency criterion (a) M-1 (b) HM-1 and (c) HM-2

c)

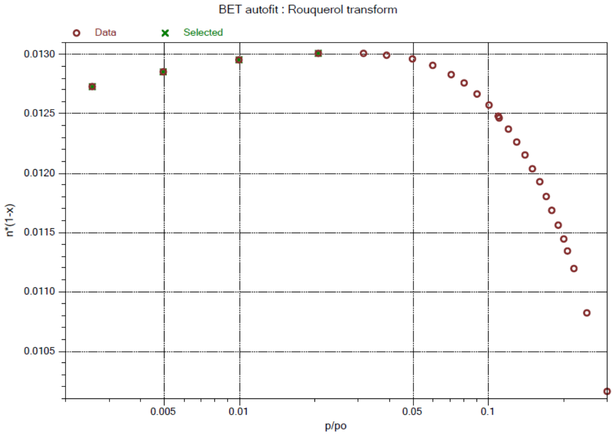

Figure A.3.18 (Part II) BET data points satisfying the Rouquerol consistency criterion (a) M-1 (b) HM-1 and (c) HM-2

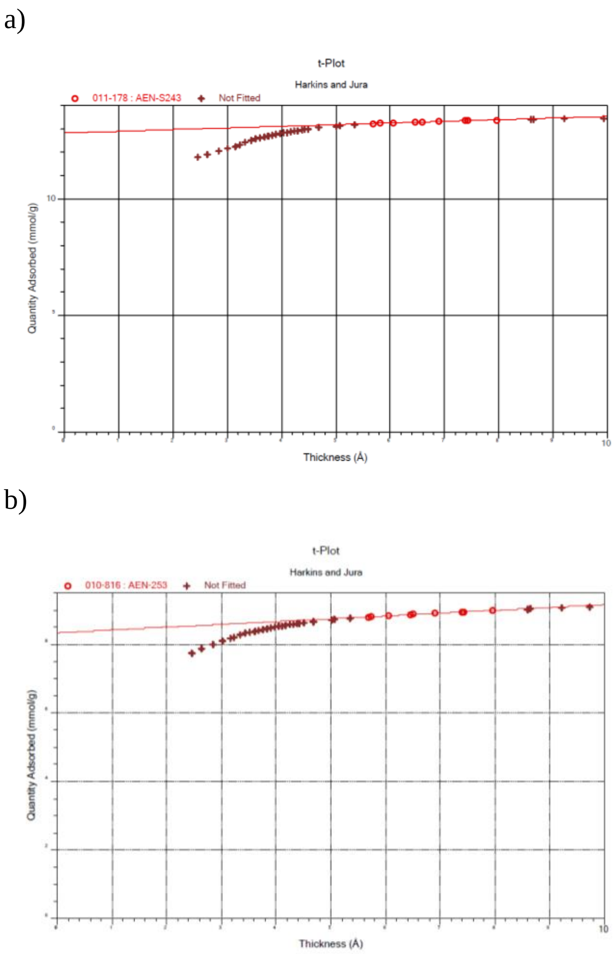

Figure A.3.19 (Part I) t-plot graphs for (a) M-1 (b) HM-1 and (c) HM-2

c)

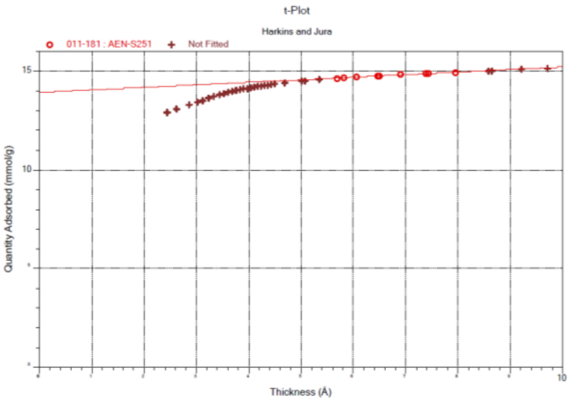

Figure A.3.19 (Part II) t-plot graphs for (a) M-1 (b) HM-1 and (c) HM-2

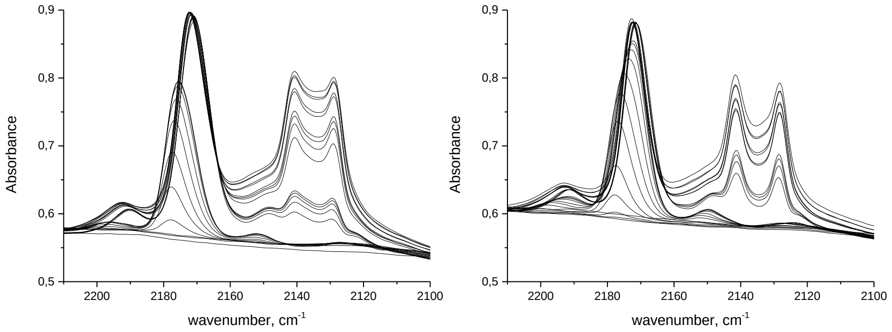

Figure A.3.20 FTIR spectra of adsorbed CO (at 77 K) onto M-1 (*left*) and HM-2 (*right*).

A.4. References

(1) Petříček, V.; Dušek, M.; Palatinus, L. Crystallographic Computing System JANA2006: General Features. *Zeitschrift für Krist. - Cryst. Mater.* **2014**, *229* (5), 345–352.

(2) Le Bail, A. Whole Powder Pattern Decomposition Methods and Applications: A Retrospection. *Powder Diffr.* **2005**, *20* (04), 316–326.

(3) Rodríguez-Carvajal, J. Recent Advances in Magnetic Structure Determination by Neutron Powder Diffraction. *Phys. B Condens. Matter* **1993**, *192* (1–2), 55–69.

(4) Bérar, J. F.; Lelann, P. E.s.d.'s and Estimated Probable Error Obtained in Rietveld Refinements with Local Correlations. *J. Appl. Crystallogr.* **1991**, *24* (1), 1–5.

(5) Sheldrick, G. M. SHELXT – Integrated Space-Group and Crystal-Structure Determination. *Acta Crystallogr. Sect. A Found. Adv.* **2015**, *71* (1), 3–8.

(6) Sheldrick, G. M. Crystal Structure Refinement with SHELXL. *Acta Crystallogr. Sect. C Struct. Chem.* **2015**, *71* (1), 3–8.

(7) Dolomanov, O. V.; Bourhis, L. J.; Gildea, R. J.; Howard, J. A. K.; Puschmann, H. OLEX2 : A Complete Structure Solution, Refinement and Analysis Program. *J. Appl. Crystallogr.* **2009**, *42* (2), 339–341.

(8) Pettinari, C.; Tăbăcaru, A.; Boldog, I.; Domasevitch, K. V.; Galli, S.; Masciocchi, N. Novel Coordination Frameworks Incorporating the 4,4′-Bipyrazolyl Ditopic Ligand. *Inorg. Chem.* **2012**, *51* (9), 5235–5245.

(9) Mosca, N.; Vismara, R.; Fernandes, J. A.; Tuci, G.; Di Nicola, C.; Domasevitch, K. V.; Giacobbe, C.; Giambastiani, G.; Pettinari, C.; Aragones-Anglada, M.; et al. Nitro-Functionalized Bis(Pyrazolate) Metal-Organic Frameworks as Carbon Dioxide Capture Materials under Ambient Conditions. *Chem. - A Eur. J.* **2018**, *24* (50), 13170–13180.

(10) Vismara, R.; Tuci, G.; Mosca, N.; Domasevitch, K. V.; Di Nicola, C.; Pettinari, C.; Giambastiani, G.; Galli, S.; Rossin, A. Amino-Decorated Bis(Pyrazolate) Metal-Organic Frameworks for Carbon Dioxide Capture and Green Conversion into Cyclic Carbonates. *Inorg. Chem. Front.* **2019**, *6* (2), 533–545.